

**Isotopic signatures in seafloor  
hydrothermal systems:  
from crust creation to  
subduction**

Dissertation

---

zur Erlangung des  
Doktorgrades der Naturwissenschaften  
(Dr. rer. nat.)

im Fachbereich Geowissenschaften  
der Universität Bremen

vorgelegt von  
Lucy Emilie Marie Schlicht

Bremen, 20. Mai 2020



Einreichung: 20. Mai 2020

Promotionskolloquium: 23. Juli 2020

Erstgutachter: Prof. Dr. Wolfgang Bach,  
Fachbereich Geowissenschaften, Universität Bremen

Zweitgutachter: Prof. Dr. Horst R. Marschall,  
Institut für Geowissenschaften, Goethe-Universität Frankfurt



## **Versicherung an Eides Statt / Affirmation in lieu of an oath**

gem. § 5 Abs. 5 der Promotionsordnung vom 18.06.2018 /

*according to § 5 (5) of the Doctoral Degree Rules and Regulations of 18 June, 2018*

---

Ich/ I, **Lucy Schlicht**, [REDACTED]

versichere an Eides Statt durch meine Unterschrift, dass ich die vorliegende Dissertation selbständig und ohne fremde Hilfe angefertigt und alle Stellen, die ich wörtlich dem Sinne nach aus Veröffentlichungen entnommen habe, als solche kenntlich gemacht habe, mich auch keiner anderen als der angegebenen Literatur oder sonstiger Hilfsmittel bedient habe und die zu Prüfungszwecken beigelegte elektronische Version (PDF) der Dissertation mit der abgegebenen gedruckten Version identisch ist. / *With my signature I affirm in lieu of an oath that I prepared the submitted dissertation independently and without illicit assistance from third parties, that I appropriately referenced any text or content from other sources, that I used only literature and resources listed in the dissertation, and that the electronic (PDF) and printed versions of the dissertation are identical.*

Ich versichere an Eides Statt, dass ich die vorgenannten Angaben nach bestem Wissen und Gewissen gemacht habe und dass die Angaben der Wahrheit entsprechen und ich nichts verschwiegen habe. / *I affirm in lieu of an oath that the information provided herein to the best of my knowledge is true and complete.*

Die Strafbarkeit einer falschen eidesstattlichen Versicherung ist mir bekannt, namentlich die Strafandrohung gemäß § 156 StGB bis zu drei Jahren Freiheitsstrafe oder Geldstrafe bei vorsätzlicher Begehung der Tat bzw. gemäß § 161 Abs. 1 StGB bis zu einem Jahr Freiheitsstrafe oder Geldstrafe bei fahrlässiger Begehung. / *I am aware that a false affidavit is a criminal offence which is punishable by law in accordance with § 156 of the German Criminal Code (StGB) with up to three years imprisonment or a fine in case of intention, or in accordance with § 161 (1) of the German Criminal Code with up to one year imprisonment or a fine in case of negligence.*

Bremen/ Place, Datum/ Date (20<sup>th</sup> May, 2020)

[REDACTED]  
(Unterschrift/ Signature)



*The deepest sin against the human mind is to  
believe things without evidence.*  
— Thomas H. Huxley



## PREFACE

---

This thesis is submitted to achieve the degree of *Doctor rerum naturalium* (Dr. rer. nat.) at the Faculty of Geosciences, University of Bremen. The studies presented in this thesis were conducted in close collaboration with a researcher group at the Ben Gurion University of the Negev in Be'er Sheva, Israel under the supervision of Prof. Dr. Yaron Katzir. Both projects were facilitated by a joined research grant that was provided by the *German-Israeli Foundation for Scientific Research and Development* (GIF) to promote the cooperation of German and Israeli scientists. The aim of the shared research was to investigate the characteristics of hydrothermal activity in the modern and ancient oceanic crust. The German studies focused on hydrothermal systems in the modern crust based on hydrothermal fluid and altered rock samples from various geological settings of fluid-rock exchange. The findings are compiled in the cumulative format of this thesis that comprises three individual manuscripts that are embedded in a joint introductory and concluding frame. In total, this thesis contains six chapters:

**Chapter 1:** The first chapter describes the fundamental principles and the high impact of hydrothermal activity in different settings of fluid-rock exchange on geochemical budgets. Furthermore, the first chapter highlights the importance of boron, lithium, strontium and oxygen isotopes as proxies for hydrothermal processes and emphasizes the motivation to investigate their systematics within this thesis.

**Chapter 2:** The second chapter differentiates the scientific contributions of the listed authors to the studies conducted within this thesis. Further, an overview of my contributions to other publications that are related to the content of this thesis is given.

**Chapter 3:** The third chapter contains the manuscript “Boron hydrothermal mass flux and isotope signatures in different plate margin settings” that is in preparation for submission to the journal *Geology*. The manuscript presents new hydrothermal fluid boron and boron isotope data from four ultramafic hosted fluid discharge sites (Logatchev, Semenov, Irinovskoe, and Ashadze) along the Mid-Atlantic Ridge and evaluates them in the light of new and previous experimental data on boron and boron isotope exchange between ultramafic materials and seawater-like fluids. Furthermore, the impact of ultramafic compared to basaltic and felsic hosted vent systems on the boron hydrothermal mass flux and its boron isotopic composition is estimated.

**Chapter 4:** The fourth chapter presents the manuscript “Boron, lithium and strontium isotopes in a low-temperature ridge flank hydrothermal system: Implications for marine geochemical budgets” that was submitted to the journal *Geochimica et Cosmochimica Acta*. The manuscript examines potential shifts in the boron, lithium and strontium isotopic composition of seafloor weathered

basalts from Dorado Outcrop that is located on 18.5 to 23 Myr old crust of the Cocos Plate. In addition, the lithium and strontium isotopic compositions of discharging fluids at Dorado Outcrop were investigated to estimate the impact of ridge flank hydrothermal circulation on the lithium and strontium isotopic budget of seawater based on data of a “typical” example of low-temperature ridge flank circulation.

**Chapter 5:** The fifth chapter contains the manuscript “Boron, lithium, strontium and oxygen isotope systematics of two hydrothermal systems in modern back-arc and arc crust (PACManus and Brothers volcano, W-Pacific)” that is in preparation for submission to a special issue in the journal *Economic Geology* with focus on hydrothermal activity at the Brothers volcano. Boron isotope data of altered rock samples that were recovered from the basement of the eastern Manus Basin (ODP Leg 193) and boron, lithium, strontium and oxygen isotope data that were received from the basement of the Brothers volcano (IODP Expedition 376) were investigated to reconstruct the alteration histories at both locations, regarding fluid sources, alteration temperatures and water-to-rock-ratios.

**Chapter 6:** The sixth chapter summarizes the results of this thesis and gives an outlook to potential research in future studies.

The appendix contains the supplements for the individual manuscripts and a record of the reference standards that were measured along the sample materials in the scope of this thesis. The electronic appendix includes additional information on spot measurements that were performed by electron microprobe analyses (EMPA), scanning electron microscopy (SEM), secondary ion mass spectrometry (SIMS), and laser ablation inductively coupled plasma mass spectrometry (LA-ICP-MS). Further, a documentation of the measurements by alternating gradient field magnetometry (AGFM) is included.

Lucy Schlicht  
Bremen, May 2020

# TABLE OF CONTENTS

---

<b>PREFACE</b>	<b>IX</b>
<b>ABBREVIATIONS AND DEFINITIONS</b>	<b>XV</b>
<b>ABSTRACT</b>	<b>XVII</b>
<b>KURZFASSUNG</b>	<b>XXI</b>
<b>CHAPTER 1: INTRODUCTION</b>	<b>1</b>
<b>1.1. Significance and discovery of seafloor hydrothermal systems</b>	<b>1</b>
<b>1.2. Basic principles of seafloor hydrothermal activity</b>	<b>3</b>
1.2.1. Hydrothermal circulation and seawater-derived alteration	3
1.2.2. Phase separation and segregation	5
1.2.3. Magma degassing and advanced argillic alteration	6
<b>1.3. Diversity of seafloor hydrothermal systems at different geological settings</b>	<b>8</b>
1.3.1. Hydrothermal systems at mid ocean ridges	8
1.3.1.1. Fast-spreading ridges	9
1.3.1.2. Slow- to ultra-slow-spreading ridges	9
1.3.1.3. Examples of ultramafic rock hosted vent sites along the Mid-Atlantic Ridge	12
Logatchev	13
Semenov	14
Irinovskoe	15
Ashadze	15
1.3.2. Hydrothermal systems at ridge flanks	16
1.3.2.1. Example of a ridge flank hydrothermal system	18
Dorado Outcrop	18
1.3.3. Hydrothermal systems at subduction zones	19
1.3.3.1. Examples of seafloor hydrothermal systems influenced by subduction processes	20
Brothers arc volcano	20
Snowcap, Manus Back-Arc Basin	22
<b>1.4. Trace elements and their isotope signatures in seafloor hydrothermal systems</b>	<b>24</b>
1.4.1. Boron and boron isotopes	24
1.4.1.1. Boron isotope determination techniques	24
1.4.1.2. Boron distribution and isotopic fractionation systematics	25
1.4.1.3. Boron and boron isotopes in natural reservoirs	28
1.4.2. Lithium and lithium isotopes	30
1.4.2.1. Lithium isotope determination techniques	31
1.4.2.2. Lithium distribution and isotopic fractionation systematics	32
1.4.2.3. Lithium and lithium isotopes in natural reservoirs	32
1.4.3. Strontium isotopes	35
1.4.4. Oxygen isotopes	36
<b>1.5. Motivation and research objectives</b>	<b>37</b>
<b>References</b>	<b>39</b>
<b>CHAPTER 2: SCIENTIFIC CONTRIBUTIONS</b>	<b>57</b>
<b>2.1. First author manuscripts</b>	<b>57</b>

2.2.	<i>Contributions to related publications</i>	59
2.3.	<i>Contributions to conferences</i>	60
	<i>References</i>	60
<b>CHAPTER 3: BORON HYDROTHERMAL MASS FLUX AND ISOTOPE SIGNATURES IN DIFFERENT PLATE MARGIN SETTINGS</b>		<b>61</b>
	<i>Abstract</i>	61
3.1.	<i>Introduction</i>	63
3.2.	<i>Materials and methods</i>	63
3.3.	<i>Boron distribution and isotopic fractionation</i>	63
3.4.	<i>Boron and boron isotope signatures of peridotite versus volcanic hosted systems</i>	65
3.5.	<i>Global hydrothermal boron mass fluxes and boron isotopic compositions</i>	67
	<i>Acknowledgments</i>	69
	<i>References</i>	69
<b>CHAPTER 4: BORON, LITHIUM AND STRONTIUM ISOTOPES IN A LOW-TEMPERATURE RIDGE FLANK HYDROTHERMAL SYSTEM: IMPLICATIONS FOR MARINE GEOCHEMICAL BUDGETS</b>		<b>73</b>
	<i>Abstract</i>	73
4.1.	<i>Introduction</i>	75
4.2.	<i>Sample locations</i>	77
4.3.	<i>Methods</i>	78
4.3.1.	<i>Sampling and sample preparation</i>	78
4.3.2.	<i>Scanning electron microscopy (SEM)</i>	79
4.3.3.	<i>Electron microprobe analyses (EMPA)</i>	79
4.3.4.	<i>Laser ablation inductively coupled plasma mass spectrometry (LA-ICP-MS)</i>	79
4.3.5.	<i>Concentration and isotope analyses</i>	80
4.3.5.1.	<i>Lithium concentrations and isotope analyses</i>	80
4.3.5.2.	<i>Boron concentrations and isotope analyses</i>	81
4.3.5.3.	<i>Strontium isotope analyses</i>	82
4.4.	<i>Estimates on the oceanic lithium and lithium isotopic budget</i>	83
4.5.	<i>Results</i>	85
4.5.1.	<i>Lithium concentrations and Li and Sr isotopes of hydrothermal fluid samples</i>	85
4.5.2.	<i>Rock samples</i>	87
4.5.2.1.	<i>Petrographic characteristics and alteration types</i>	87
4.5.2.2.	<i>Lithium and boron concentrations and isotopic compositions of rock samples</i>	92
4.6.	<i>Discussion</i>	93
4.6.1.	<i>Impact of reverse weathering in ridge flanks on ocean geochemical budgets</i>	93
4.6.1.1.	<i>Lithium</i>	93
4.6.1.2.	<i>Strontium</i>	95
4.6.2.	<i>Low-temperature basalt alteration and uptake of lithium and boron</i>	95
4.6.3.	<i>Impact of variations in past isotopic seawater composition on altered basalts</i>	97

4.7. <i>Summary and conclusions</i>	101
<i>Acknowledgements</i>	103
<i>References</i>	103
<b>CHAPTER 5: BORON, LITHIUM, STRONTIUM AND OXYGEN ISOTOPE SYSTEMATICS OF TWO HYDROTHERMAL SYSTEMS IN MODERN BACK-ARC AND ARC CRUST</b>	<b>109</b>
<i>Abstract</i>	109
<b>5.1. Introduction</b>	<b>111</b>
<b>5.2. Geological setting</b>	<b>112</b>
5.2.1. <i>Snowcap, Manus Basin</i>	112
5.2.2. <i>Brothers volcano, Kermadec arc</i>	113
<b>5.3. Sample material</b>	<b>114</b>
5.3.1. <i>Snowcap, Manus Basin</i>	114
5.3.2. <i>Brothers volcano, Kermadec arc</i>	116
<b>5.4. Methods</b>	<b>121</b>
5.4.1. <i>Preparation of rock powders</i>	121
5.4.2. <i>Boron, lithium and strontium concentrations</i>	122
5.4.3. <i>Boron isotopes</i>	123
5.4.4. <i>Lithium isotopes</i>	123
5.4.5. <i>Strontium isotopes</i>	125
5.4.6. <i>Quartz separate preparation and cathodoluminescence (CL) spectroscopy</i>	125
5.4.7. <i>In-situ oxygen isotope measurements</i>	126
<b>5.5. Results</b>	<b>126</b>
5.5.1. <i>Unaltered rocks</i>	126
5.5.2. <i>Altered rocks</i>	127
5.5.3. <i>Quartz separates and temperature constraints</i>	130
<b>5.6. Discussion</b>	<b>130</b>
5.6.1. <i>Signatures of unaltered rocks and sample preservation</i>	133
<i>Brothers volcano</i>	134
<i>Snowcap, PACMANUS</i>	134
5.6.2. <i>Signatures of altered oceanic crust</i>	135
5.6.2.1. <i>Lithium concentrations and isotopes</i>	135
5.6.2.2. <i>Strontium concentrations and isotopes</i>	136
5.6.2.3. <i>Boron concentrations and isotopes</i>	138
5.6.2.4. <i>Oxygen isotopes and temperature constraints</i>	142
5.6.3. <i>Implications for subsurface processes in hydrothermal systems</i>	143
<b>5.7. Conclusions</b>	<b>146</b>
<i>Acknowledgements</i>	146
<i>References</i>	147
<b>CHAPTER 6: CONCLUSIONS AND OUTLOOK</b>	<b>153</b>
<i>References</i>	157

<b>ACKNOWLEDGMENTS</b>	<b>159</b>
<b>APPENDIX</b>	<b>161</b>
<b>A.1. Supplementary material to thesis chapter 3</b>	<b>161</b>
A.1.1 Materials and methods	161
A.1.2 Results of the natural fluid samples	169
A.1.3 Results of the experiment	172
A.1.4 Summary of the experimental results of this and the previous study	180
<b>References</b>	<b>183</b>
<b>A.2. Procedures and isotopic reference materials</b>	<b>187</b>
A.2.1 Purification procedures	187
A.2.2 Reference materials	190
<b>References</b>	<b>191</b>
<b>A.3. Overview of the electronic appendix</b>	<b>192</b>

## ABBREVIATIONS AND DEFINITIONS

---

### *Chemical definitions*

$$\delta^{11}\text{B} (\text{‰}) = \left\{ \left[ \frac{(^{11}\text{B}/^{10}\text{B})_{\text{sample}}}{(^{11}\text{B}/^{10}\text{B})_{\text{NIST SRM 951}}} - 1 \right] \times 1000 \right\}$$

$$\delta^7\text{Li} (\text{‰}) = \left\{ \left[ \frac{(^7\text{Li}/^6\text{Li})_{\text{sample}}}{(^7\text{Li}/^6\text{Li})_{\text{NIST RM 8545}}} - 1 \right] \times 1000 \right\}$$

$$\delta^{18}\text{O} (\text{‰}) = \left\{ \left[ \frac{(^{18}\text{O}/^{16}\text{O})_{\text{sample}}}{(^{18}\text{O}/^{16}\text{O})_{\text{VSMOW}}} - 1 \right] \times 1000 \right\}$$

$$\text{pH} = -\log_{10} a(\text{H}^+)$$

### *General terms*

BAB	Back-arc basin
EM	End-member
HFSE	High field strength element
LILE	Large ion lithophile element
mbsf/ mbsl	meters below seafloor/ meters below sea level
MOR/MORB	Mid ocean ridge/ Mid ocean ridge basalt
OCC	Oceanic core complex
REE/LREE	Rare earth elements/ Light rare earth elements
RFHS	Ridge flank hydrothermal system
sd/ sd <sub>mean</sub> /se	Standard deviation/ Standard deviation of the mean/ Standard error
T	Temperatures
w/r	Water-to-rock

### *Specific locations and tectonic structures*

CNSC	Cococ-Naszca Spreading Center
CR	Cocos Ridge
DT	Djaul Transform
EPR	East Pacific Rise
JFR	Juan de Fuca Ridge
LHF/SHF/IHF/AHF	Logatchev/ Semenov/ Irinovskoe/ Ashadze hydrothermal field
MAR	Mid Atlantic Ridge
MAT	Middle America Trench
METZ	Manus Extensional Transform Zone
MMP	Manus Microplate
MSC	Manus Spreading Center
PACMANUS	Papua New Guinea-Australia-Canada-Manus
SAT	South America trench
SER	Southeastern rifts
SWIR	Southwest Indian Ridge
WIT	Willaumez Transform
WT	Weitin Transform

### *Organizations and Institutes*

DSDP	Deep Sea Drilling Project
GEOMAR	Geomar Helmholtz-Zentrum für Ozeanforschung Kiel
GFZ	Geo Forschungszentrum
GIF	German-Israeli Foundation for Scientific Research and Development
GLOMAR	Bremen International Graduate School for Marine Sciences
IODP	International/Integrated Ocean Discovery Program
MARUM	Center for Marine Environmental Sciences
ODP	Ocean Drilling Program
PSO	Pôle Spectrométrie Océan

### *Measuring and sampling techniques*

AGFM	Alternating gradient field magnetometry
AUV	Autonomous underwater vehicle
CL microscopy	Cathodoluminescence microscopy
CTD logger	Conductivity-temperature-depth logger
EDX spectroscopy	Energy dispersive X-ray spectroscopy
EMPA	Electron microprobe analysis
HDPE bottle	High-density polyethylene bottle
ICP-MS	Inductively coupled plasma mass spectrometry
ICP-OES	Inductively coupled plasma optical emission spectrometry
IGT samplers	Isobaric gas-tight samplers
LA-ICP-MS	Laserablation Inductively coupled plasma mass spectrometry
MC-ICP-MS	Multicollector inductively coupled plasma mass spectrometry
ROV	Remotely operating vehicle
SEM	Scanning electron microscopy
SIMS	Secondary ion mass spectrometry
SIS	Stable introduction system
TG/DSC	Thermogravimetry/ Differential scanning calorimetry
TIMS	Thermal ionization mass spectrometry
XRF	X-Ray fluorescence

### *Mineral abbreviations*

anh	anhydrite	dsp	diaspora	plg	plagioclase
ba	barite	gp	gypsum	prl	pyrophyllite
bei	beidellite	ill	illite	py	pyrite
brc	brucite	mgt	magnetite	qtz	quartz
cal	calcite	mnt	montmorillonite	rt	rutile
ccp	chalcopyrite	mor	mordenite	smc	smectite
chl	chlorite	natro	natroalunite	sph	sphalerite
chr	chrysotile	ol	olivine	zeo	zeolite
crr	corrensite	op	opal	zun	zuniyite
crs	cristobalite	php	phillipsite		

## ABSTRACT

---

The geochemical exchange of seawater and rocks in seafloor hydrothermal systems has large impacts on the composition of seawater and oceanic crust, and also on the mantle composition once the altered oceanic crust is recycled back to the mantle at subduction zones. Indeed, the characteristics of hydrothermal circulation vastly change over the life time of the oceanic crust but also strongly vary at different plate marginal settings.

New crust is created by partial melting of the underlying mantle, mainly at mid-ocean ridge axes. In young oceanic crust that is still influenced by the axial volcanic activity, high-temperature (150 to >350 °C) hydrothermal circulation is therefore very common that stands out by the growth of sulfide-rich chimneys and discharge of particle-rich fluids that occur as “black smoke” in the directly overlain water column. The formation of large ore deposits that are highly enriched in precious metals (e.g. copper and gold) also often occurs. Indeed, the rate of new crust production that is sensitively coupled to the rate of mid-ocean ridge spreading additionally influences the characteristics of hydrothermal activity at the axes. A decrease in magma production rates at slow-spreading ridges, thus leads to subsidence of the axis and to an increase in tectonic activity that in turn can result in the exposure of mantle material at the seafloor. Hydrothermal interaction between seawater and mantle rocks results typically in an increase in fluid alkalinity due to the serpentinization of the major host mineral olivine compared to interaction with basaltic crust at fast spreading ridges that is characterized by highly acidic conditions. The differing host rock compositions also strongly influence the elemental exchange between seawater and rocks and have a critical impact on the rock alteration patterns at the seafloor.

The magmatic heat supply that drives high-temperature hydrothermal activity however diminishes with further distance of the crust to the axis and fluid circulation becomes increasingly inhibited because of sedimentation of impermeable marine clays on top of the crust and due to sealing of fractures and pore spaces by newly formed minerals. Nevertheless, especially in so called “ridge flank hydrothermal systems” extremely large amounts of seawater can still circulate through tens of million years old oceanic crust between basaltic structures that reach above the impermeable sediment cover and due to mining of lithospheric heat. The fluid temperatures in these systems are usually very low (mostly <25 °C) and the absolute changes in the discharging fluid compositions are relatively minor compared to seawater. However, due to the very high water fluxes and the large areas that are affected by circulation, hydrothermal activity in the ridge flanks also importantly changes ocean and ocean crust chemistry.

Another class of high-temperature hydrothermal systems is closely connected with the destruction of the aged and altered oceanic crust at subduction zones. The recycling of altered crust and

sediments that are enriched in hydrous mineral phases lowers the melting point and triggers volcanic activity in the overlain mantle wedge at subduction zones. These complex volcanic processes are expressed by the eruption of more evolved, felsic lavas at volcanic arcs that are very frequently associated with high-temperature hydrothermal vent systems. Furthermore, also in the back-arc region hydrothermal activity is quite common because the extensional stress in the back arc allows ascent and partial melting of mantle that provides heat for the circulation of fluids. The melts in subduction influenced settings are usually very rich in dissolved volatiles (e.g. CO<sub>2</sub>, SO<sub>2</sub>) and the relatively shallow water depth at volcanic arcs and back-arcs further accelerate the degassing of magmatic fluids from the subjacent magma chamber. The disproportionation of the sulfur gases that are dissolved in these magmatic fluids and mixing with seawater leads to the formation of “acid-sulfate” fluids of extremely high acidity (pH<2) that discharge at the seafloor in form of milky white smoke that is rich in native sulfur droplets. Magmatic fluids are further believed to transport significant amounts of metals like copper and gold directly from the underlying magma chamber up to shallower levels of the hydrothermal system and to enhance formation of large ore bodies that are comparable to porphyry- and epithermal-type ore deposits on-land.

The most useful approach to study the diverse alteration histories and the particular contributions of different settings of hydrothermal fluid-rock interactions on geochemical budgets is the combination of multiple proxies with differing sensitivities for specific aspects. The highly fluid mobile elements boron and lithium are very helpful tracers to investigate seafloor hydrothermal systems because the elemental partitioning and isotopic fractionation between fluids and rocks of both are very sensitive to changing alteration temperatures, water-to-rock-ratios, and are affected by the type of primary as well as secondary mineral phases that occur; boron isotopes also react sensitive to pH shifts. Furthermore, the boron and lithium elemental and isotopic compositions of the interacting reservoirs (mainly seawater and oceanic crust or rather mantle rocks) are very different and lead to distinct signature shifts between seawater and hydrothermal fluids, as well as between fresh and altered rocks. The additional appraisal of other tracers like strontium isotopic compositions that are sensitive for changing water-to-rock ratios and oxygen isotopes that are commonly used as paleo-thermometer, further helps to reconstruct the local alteration histories of specific vent sites.

In the scope of this thesis, hydrothermal fluids and fresh as well as altered rocks from four very diverse settings of fluid-rock interaction were investigated by using boron and/or lithium elemental and isotopic compositions, partly combined with strontium and oxygen isotopic systematics. The studied locations span the whole range from high-temperature hydrothermal systems that are (1) hosted in mantle rocks at the slow-spreading Mid Atlantic Ridge, over (2) a low-temperature ridge flank hydrothermal circulation system at 18.5 to 23 million years old crust of the eastern flank of the East Pacific Rise, up to high-temperature hydrothermal activity that is associated with (3) an

active arc volcano in the southern Kermadec Arc close to New Zealand and (4) with a hydrothermal system at the eastern part of the Manus back-arc basin that is close to Papua New Guinea. In addition, an experimental study was conducted to investigate the boron partitioning and isotopic fractionation between seawater and mantle materials.

The experimental data confirmed the general assumption that mantle lithologies favor the uptake of boron even at elevated temperatures (300 °C) and that an increased abundance of the same boron species in fluid and rock due to changing pH conditions leads to a decrease in boron isotopic fractionation. Indeed, the decrease in boron isotopic fractionation in our experiments was significantly more intense than assumed based on previous experimental results and theoretical predictions. The boron isotope data of the natural fluids from four mantle rock hosted vent sites along the Mid Atlantic Ridge were furthermore the first ones measured for this class of systems and therefore gave some new insights to the differences of mantle rock compared to basaltic and felsic hosted vent systems. As expected, the natural fluids were depleted in boron compared to seawater due to the preferred boron uptake of ultramafic mantle rocks even at elevated temperatures, while the boron isotope signatures were only moderately fractionated compared to seawater. Our compilation of boron isotope fluid data from basaltic hosted vent systems at slow- and fast-spreading ridges further indicated a stronger fractionated boron isotope signal (versus seawater) at slow-spreading compared to fast-spreading settings, potentially due to the longer fluid pathways and lower water-to-rock-ratios at the strongly structure controlled slow-spreading ridges. This difference may also have important implications for the boron isotopic composition of past seawater. It is assumed that several pulses of globally increased spreading rates occurred over the Phanerozoic that could have led to an increased boron isotopic composition of the hydrothermal mass flux, in case that the more rapid ridge spreading resulted in less tectonic activity at the axes. A well-constrained boron isotopic composition of paleo-seawater is important for reconstructions of potential seawater acidity changes in the past.

The lithium isotopic fluid data from the ridge flank hydrothermal discharge site “Dorado Outcrop” pointed to a significant contribution of basalt weathering in the ridge flanks on the lithium isotopic composition of seawater but also highlighted the importance of seawater-sediment exchange on lithium isotopic budgets. The strontium isotopic composition of the fluids was indistinguishable from seawater and could not confirm a major impact of ridge flank systems on the strontium isotopic composition of seawater. The lithium isotopic composition of the altered rocks indicated potential interaction with paleo-seawater shortly after formation of the outcrop 18.5 to 23 million years ago that most likely had a lower lithium isotopic signature compared to modern seawater. This suggests a potential applicability of lithium isotopes in low-temperature basalt alteration products as proxy for changing seawater lithium isotopic compositions in the past.

The boron isotope data from the Manus back-arc basin and boron, lithium, strontium and oxygen isotope data from the Brothers arc volcano pointed to large differences in water-to-rock-ratios and alteration temperatures between superposed rock layers of contrasting permeability in the basement of seafloor hydrothermal systems. More coherent lavas flows seemed to act as permeability barriers of lower water-to-rock-ratios but increased alteration temperatures, while less permeable underlying volcanoclastic rocks were affected by higher water-to-rock-ratios and overall lower alteration temperatures. This relation may also have important implications for the mobilization, transport and precipitation of others elements, e.g. precious metals.

## KURZFASSUNG

---

Der geochemische Stoffaustausch von Meerwasser und Gesteinen in Hydrothermalsystemen am Meeresboden hat großen Einfluss auf die Zusammensetzung der Ozeane und der ozeanischen Kruste, und beeinflusst auch die Mantelzusammensetzung im Zuge von Wiederaufarbeitungsvorgängen an Subduktionszonen. Die Ausprägung der hydrothermalen Zirkulation verändert sich stark über die Lebenszeit der ozeanischen Kruste, aber unterscheidet sich auch zwischen verschiedenen Arten von Plattengrenzen.

Die Entstehung neuer Kruste wird eingeleitet durch das partielle Aufschmelzen des unterliegenden Mantels, im Besonderen entlang der mittelozeanischen Spreizungsachsen. In junger ozeanischer Kruste, die noch im Einflussbereich der axialen magmatischen Aktivität steht, findet daher häufig Zirkulation von Fluiden unter hohen Temperaturen (150 bis >350 °C) statt. Diese zeichnet sich aus durch die Bildung von sulfid-reichen Schloten am Meeresboden und dem Ausstoß von partikelreichen Fluiden, die als schwarzer Rauch in der direkt überlagernden Wassersäule erscheinen. Zudem ist auch die Ausbildung von Erzlagerstätten häufig, die angereichert sind an wertvollen Metallen, wie Kupfer und Gold. Die Art der hydrothermalen Zirkulation an den divergierenden Plattengrenzen hängt allerdings auch stark ab von der Produktionsrate von neuer Kruste, die wiederum in direkter Abhängigkeit zur Spreizungsrate steht. Eine Verringerung der Magmaproduktion an langsam spreizenden Rücken führt demzufolge zum Absinken der Rückenachse und dadurch zur Zunahme der tektonischen Aktivität, wodurch es wiederum zur Freilegung von Mantelgesteinen am Meeresboden kommen kann. Hydrothermaler Austausch zwischen Meerwasser und Mantelgesteinen führt zu einer Erhöhung der Fluid-Alkalinität durch die Serpentinisierung des Mantelminerals Olivine, im Gegensatz zum Auftreten von typischerweise sehr sauren Bedingungen in basaltischen Hydrothermalsystemen an schnell spreizenden Rücken. Dies hat auch Auswirkung auf die Elementfracht der austretenden Fluide, die mit dem jeweiligen Gestein interagiert haben und verändert die Alterationsmuster der Gesteine.

Die magmatische Wärmezufuhr, die die hydrothermale Zirkulation unter hohen Temperaturen nahe der mittelozeanischen Rücken ermöglicht, verringert sich drastisch mit zunehmender Entfernung von den Rücken und die Fluidzirkulation wird weiter gehemmt durch Sedimentation von undurchlässigen Schichten von marinen Tonen und durch die Verschließung von Porenräumen und Rissen mit neugebildeten Mineralphasen. Nichtsdestotrotz findet die Zirkulation von sehr großen Wassermengen auch noch in Zehner Millionen Jahre alter Kruste und in großer Entfernung zu den Rücken statt, besonders in so genannten „Rückenflanken-Hydrothermalsystemen“. In den Rückenflanken tritt Zirkulation zwischen basaltischen Strukturen auf, die über die sie umgebende deutlich impermeablere Sedimentschicht hinausragen und die durch den Verbrauch von lithosphärischer Wärme angetrieben wird. Die Temperaturen der austretenden Fluide sind

vergleichsweise niedrig (typischerweise  $<25^{\circ}\text{C}$ ) und auch die chemische Modifikation im Vergleich zu Meerwasser ist recht gering. Die extrem großen Wasserströme und die Größe der beeinflussten Bereiche der Kruste führen dennoch dazu, dass hydrothermale Aktivität in den Rückenflanken einen entscheidenden Einfluss auf die Chemie der Ozeane und der ozeanischen Kruste hat.

Eine weitere Klasse an hydrothermalen Systemen steht in enger Verbindung zur Zerstörung der gealterten ozeanischen Kruste in Subduktionszonen. Die Wiederaufarbeitung von gealterter Kruste und den aufliegenden Sedimenten, die beide angereichert sind an wasserhaltigen Mineralphasen, führt zur Erniedrigung des Schmelzpunktes und fördert die Entstehung von vulkanischer Aktivität im überliegenden Mantelkeil in Subduktionszonen. Diese komplexen vulkanischen Vorgänge führen zur Eruption von höher differenzierten, felsischen Laven in vulkanischen Inselbögen und sind häufig verbunden mit der Ausbildung von Hochtemperatur-Hydrothermalsystemen. Zudem kommt es auch in der Region hinter dem eigentlichen Inselbogen („back-arc“) häufig zu magmatischer und somit auch hydrothermaler Aktivität, ausgelöst durch Dehnungsprozesse und Aufstieg sowie partielles Aufschmelzen von Mantelmaterial hinter dem Inselbogen. Die Schmelzen in subduktionsbeeinflussten Bereichen sind gemeinhin stark angereichert an gelösten flüchtigen Bestandteilen (z.B.  $\text{CO}_2$ ,  $\text{SO}_2$ ) und des Weiteren führt die relativ geringe Wassertiefe in und hinter vulkanischen Inselbögen dazu, dass magmatische Fluide leicht von der unterliegenden Magmakammer entgasen können. Die Disproportionierung von Schwefelgasen, die in diesen magmatischen Fluiden angereichert sind, und das Mischen mit Meerwasser führen zur Ausbildung von „sulfat-sauren“ Wässern. Diese Wässer sind extrem sauer ( $\text{pH}<2$ ) und erscheinen am Meeresboden als milchig-weißer Rauch, der reich ist an elementarem Schwefel Tröpfchen. Es wird zudem angenommen, dass magmatische Fluide fähig sind größere Mengen an Metallen wie Kupfer und Gold direkt von der unterliegenden Magmakammer hoch zu flacheren Ebenen des hydrothermalen Systems zu transportieren und daher mit der Entstehung von besonders großen und kupfer- und gold-reichen Lagerstätten in Verbindung stehen; vergleichbar zu porphyrischen und epithermalen Lagerstätten an Land.

Der sinnvollste Ansatz um die sehr unterschiedlichen Alterationsabläufe in verschiedenen Umgebungen von hydrothermaler Zirkulation zu untersuchen und deren jeweiligen Einfluss auf globale geochemische Bilanzen abzuschätzen, ist die Kombination von mehreren Indikatoren, die unterschiedlich sensitive auf verschiedene Interaktionsaspekte reagieren. Die sehr fluid-mobilen Elemente Bor und Lithium sind sehr geeignet zur Untersuchung von Hydrothermalsystemen, weil die elementare Verteilung sowie auch die Isotopenfraktionierung zwischen interagierenden Fluiden und Gesteinen stark abhängen von Änderungen der Temperatur, der Wasser-Gesteins-Verhältnisse, und beeinflusst werden durch die primäre und sekundäre Mineralogie; Bor Isotope reagieren zu dem empfindlich auf pH Veränderungen. Des Weiteren zeigen die interagierenden Reservoirs (hauptsächlich Meerwasser und ozeanische Kruste bzw. Mantelgesteine) sehr unterschiedliche Bor

und Lithium elementare und isotopische Zusammensetzungen, wodurch größere Verschiebungen in den Signaturen zwischen Meerwasser und hydrothermale Fluid, sowie zwischen dem frischen und gealterten Gestein zu erwarten sind. Die zusätzliche Untersuchung weiterer geochemischer Indikatoren, wie Strontium Isotopen mit einer Empfindlichkeit für Wasser-Gesteins-Verhältnisse und Sauerstoff Isotopen als Geothermometer, ermöglicht eine noch präzisere Rekonstruktion der Alterationsgeschichte von spezifischen Lokationen.

Im Rahmen dieser Dissertation wurden hydrothermale Fluide und frische sowie alterierte Gesteine von vier sehr unterschiedlichen Umgebungen der Wasser-Gesteins-Interaktion untersucht, unter zur Hilfenahme von Bor und Lithium elementaren und isotopischen Zusammensetzungen, und zum Teil ergänzt mit Strontium und Sauerstoff Isotopen. Die untersuchten Lokationen reichen von (1) Hydrothermalsystemen in Mantelgesteinen entlang des langsam spreizenden Mittelatlantischen Rückens, über (2) ein Rückenflanken-Hydrothermalsystem in 18.5 bis 23 Millionen Jahre alter Kruste in der östlichen Flanke des Ostpazifischen Rückens, bis hin zu hydrothermaler Aktivität in Verbindung mit (3) einem aktiven untermeerischen Vulkan im südlichen Teil des Kermadec Inselbogens nahe Neuseelands und (4) dem östlichen Manus back-arc Beckens in der Nähe von Papua Neuguinea. Zusätzlich wurde eine experimentelle Studie durchgeführt, um die elementare Verteilung und Isotopenfraktionierung von Bor im Austausch zwischen Meerwasser und Mantelgesteinen zu untersuchen.

Die experimentelle Studie konnte die generelle Annahme bestätigen, dass Mantelgesteine auch bei hohen Temperaturen (300 °C) bevorzugt Bor aufnehmen und dass eine Annäherung der Bor Spezifikation im Fluid an die Bor Spezifikation im Gestein durch Änderungen des pH Wertes im Fluid zu einer Verringerung der Bor Isotopenfraktionierung führt. Die beobachtete Verringerung war allerdings deutlich stärker als vermutet auf Grundlage von vorherigen experimentellen Versuchen und theoretischen Berechnungen. Die Bor Isotopendaten der natürlichen Fluide von hydrothermalen Systemen in Mantelgesteinen am Mittelatlantischen Rücken repräsentieren die ersten Daten dieser System-Klasse und liefern daher wichtige Information über die Unterschiede zwischen hydrothermaler Aktivität in Mantelgesteinen im Vergleich zu basaltischen und felsischen Systemen. Die Fluide haben wie erwartet eine Verringerung in der Bor Konzentration im Vergleich zum Meerwasser gezeigt und ein moderat fraktioniertes Bor-Isotopensignal. Des Weiteren konnte die Zusammenstellung von Bor-Isotopendaten von basaltischen System aufzeigen, dass hydrothermale Fluide an langsam spreizenden Rücken deutlich fraktioniertere Bor-Isotopensignaturen tragen als an schnell spreizenden Rücken und dass dieser Zusammenhang potentielle durch die längeren Zirkulationswege an den tektonisch geprägten langsam spreizenden Rücken erklärt werden kann. Diese Beobachtung könnte auch weitreichende Bedeutung für die Bor-Isotopenzusammensetzung von Meerwasser in der früheren Erdgeschichte gehabt haben. Es wird vermutet, dass es innerhalb des Phanerozoikums mehrere Pulse von beschleunigter globaler

Spreizungsrate gegeben hat, die folglich mit einer Erhöhung der Bor-Isotopenzusammensetzung des hydrothermalen Flusses verbunden gewesen sein könnten, unter der Annahme dass eine höhere Spreizungsrate in der Vergangenheit mit geringer tektonischen Aktivität an den Spreizungsachsen in Erscheinung getreten ist. Eine genaue Bestimmung der Bor-Isotopenzusammensetzung des Meerwassers in der Vergangenheit ist essentiell für die Rekonstruktion von möglichen Änderungen im Säuregehalt des Meerwassers über geologische Zeitskalen.

Die Lithium-Isotopenzusammensetzungen von hydrothermalen Fluiden, die an der Rückenflanken-Austrittsstelle „Dorado Outcrop“ aufsteigen deuten darauf hin, dass die Alteration von Basalten unter niedrigen Temperaturen einen wesentlichen Einfluss auf die Lithium-Isotopenzusammensetzung des Meerwasser hat, zeigen aber auch die potentiell große Rolle von Meerwasser-Sediment-Interaktionen auf die Meerwasserzusammensetzung auf. Die Strontium-Isotopenzusammensetzung der Fluide war ununterscheidbar von der Meerwassersignatur und es konnte daher kein größerer Effekt von Rückenflankensystemen auf die Strontium-Isotopenzusammensetzung des Meerwassers bestätigt werden. Die Lithium-Isotopenzusammensetzung der alterierten Gesteine resultiert möglicherweise von der Interaktion mit Meerwasser kurz nach der Entstehung der basaltischen Struktur vor 18.5 bis 23 Million Jahren, das eine niedrigere Lithium-Isotopenzusammensetzung hatte als modernes Meerwasser. Dies weist auf die mögliche Anwendbarkeit von Lithiumisotopen in alterierten Basalten als Anzeiger für Veränderungen der Lithiumisotopie des Meerwassers in der Vergangenheit hin.

Die Bor-Isotopendaten vom Manus Becken und die Bor-, Lithium-, Strontium-, und Sauerstoff-Isotopendaten vom Brothers Inselbogen Vulkan weisen auf große Unterschiede im Wasser-Gesteins-Verhältnis und der Alterationstemperatur zwischen übereinanderliegenden Gesteinschichten mit variierenden Permeabilitäten im Untergrund von Hydrothermalsystemen hin. Strukturell einheitlichere Lavaströme bilden scheinbar Zonen verringerter Permeabilität, die geringere Wasser-Gesteins-Verhältnisse aber erhöhte Alterationstemperaturen aufweisen, im Vergleich zu strukturell heterogeneren vulkaniklastischen Gesteinslagen mit erhöhter Permeabilität, die durch höhere Wasser-Gesteins-Verhältnisse und niedrigere Alterationstemperaturen beeinflusst werden. Dieser Zusammenhang hat potentiell auch weiterreichende Auswirkungen auf die Mobilisierung, den Transport und die Ablagerung anderer Elemente, wie z. B. Edelmetallen.

# CHAPTER 1:

## INTRODUCTION

---

### *1.1. Significance and discovery of seafloor hydrothermal systems*

Seafloor hydrothermal activity is expressed by the exchange between seawater and oceanic crust under increased temperatures, often accompanied by the formation of sulfide-rich chimneys and discharge of metal-rich fluids that appear as black smoke in the overlying water column due to sulfide precipitation in contact with seawater. This process results in major changes in ocean and oceanic crust chemistry (German & Von Damm, 2003), facilitates the formation of high-grade ore deposits (German *et al.*, 2016) and generates unique environments for the development of highly specialized life-forms that potentially are comparable to the earliest forms of life (Holm, 1992; Fisher *et al.*, 2007). The investigation of seafloor hydrothermal systems by a multitude of techniques is required for a deeper understanding of the processes controlling hydrothermal fluid-rock exchange, like for example fluid temperature and pH, structural features and water-to-rock-ratios, as well as host rock and alteration phase mineralogy and geochemical compositions.

The heat that facilitates high-temperature hydrothermal circulation in the oceanic crust derives from magma chambers that are associated with tectonic plate margins, and following hydrothermal circulation has a direct relation to plate tectonic processes. The existence of plate movements over long geological timescales was already supposed by Alfred Wegener in the early 20<sup>th</sup> century (Wegener, 1929) but was at first widely unaccepted by the scientific community. General confirmation on that plate tectonic activity was actually a constant process through earth history and led as well as leads to continuous creation of new oceanic crust at mid-ocean ridges that is followed by the destruction of matured crust at subduction zones came not before the 1960<sup>th</sup>. Evidence for this processes derived amongst others from investigations of rocks from deeper portions of the oceanic crust that could be recovered by scientific drilling since the start of the Deep Sea Drilling Project (DSDP) in 1968. The final most convincing argument for the existence of plate tectonics was indeed the discovery of periodic paleo-magnetic stripe-patterns at the seafloor that indicated a systematic increase in the age of oceanic crust with further distance to the ridges in a symmetrical manner on both sides (Vine & Matthews, 1963). The first evidence for hydrothermal activity at the seafloor already emerged in the middle of the 1960<sup>th</sup> only slightly after general agreement on the existence of plate tectonic processes by the identification of metalliferous brines and iron-rich deposits in marine sediments at the Atlantis II Deep of the Red Sea (Miller, 1964; Miller *et al.*, 1966). Widespread affection of oceanic crust by fluid circulation was then assumed since the 1970<sup>th</sup> due to discovery of fluid discharge at the Galapagos Rift (Corliss *et al.*, 1979) and because a significant discrepancy between expected heat flow of oceanic crust based on plate cooling models and actually measured heat flow was recognized (Lister, 1972). Later, amongst others Stein & Stein

(1994) further explicated constraints on oceanic crust heat flow and proposed that hydrothermal circulation in high- and low-temperature systems is associated with a heat flow of 11 TW that represents approximately 34% of the total oceanic heat flux of 32 TW. Recovery of ore-rich chimney fragments and isotope data derived from the Troodos Ophiolite that represents a section of Cretaceous oceanic crust exposed on-land today also indicated that hydrothermal fluid circulation already occurred in ancient times (Chapman & Spooner, 1977; Oudin & Constantinou, 1984).

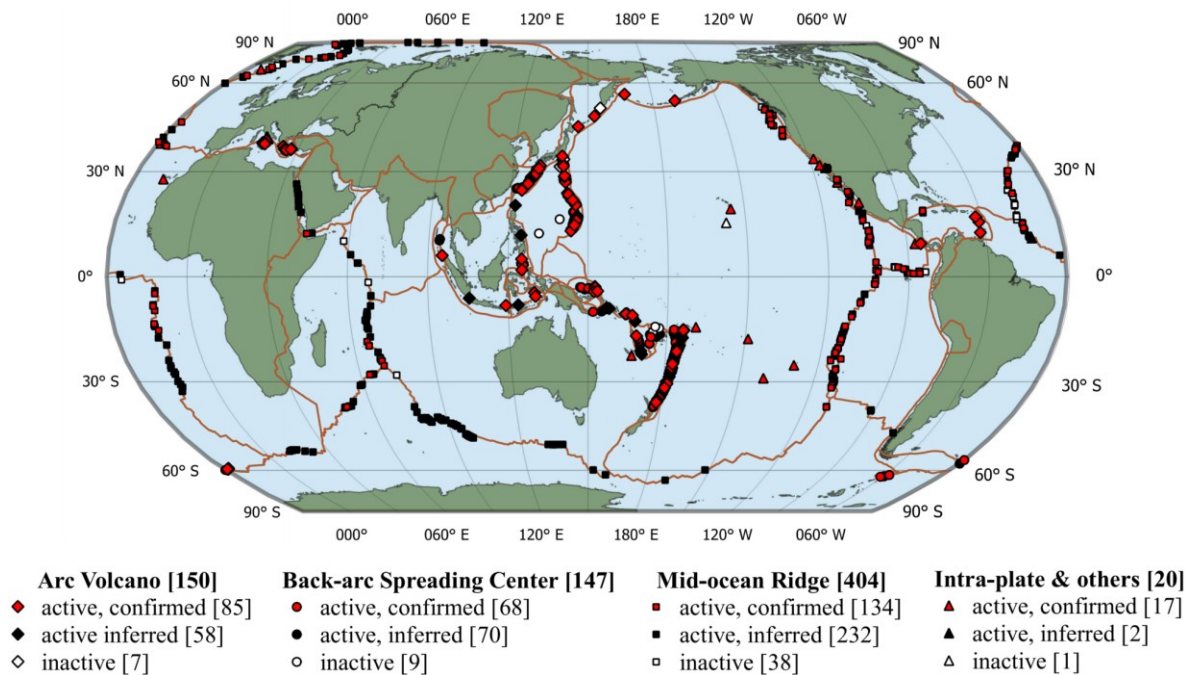


**Figure 1.1-1:** Global abundance of high-temperature hydrothermal systems in various geological settings based on the Inter Ridge Data Base Ver.3.4 (Beaulieu & Szafranski, 2019). In brackets the number of vent fields of a specific type is given. Plate boundaries were taken from Bird (2003).

Ever since, a large number of seafloor hydrothermal systems was discovered and studied (**Figure 1.1-1**, Beaulieu & Szafranski, 2019): at mid ocean ridges over the total range of spreading rates (e.g. Von Damm *et al.*, 1985; Rona *et al.*, 1987; Charlou *et al.*, 1991; Kelley *et al.*, 2001; Tao *et al.*, 2012), and close to subduction zones in submarine volcanic arcs (e.g. Stoffers *et al.*, 1999) and back-arc basins (e.g. Both *et al.*, 1986; Gamo *et al.*, 2004). Furthermore, the crucial importance of low-temperature ridge flank circulation systems on geochemical budgets gained increasing attention over the past decades (Mottl *et al.*, 1998; Wheat & Fisher, 2008). Development of more elaborated detection techniques significantly improved the number of vent system discoveries; e.g. by detection of methane (CH<sub>4</sub>) and He anomalies in the water column (e.g. Sudarikov & Roumiantsev, 2000; Schmale *et al.*, 2012; Lough *et al.*, 2019), heat flow measurements (e.g. Hutnak *et al.*, 2008) or by direct observations of ore bodies or active fluid discharge at the seafloor.

The fluid-rock interaction processes at the seafloor and in the basement of particular hydrothermal vent sites were also studied from various geochemical and mineralogical (German & Von Damm,

2003), hydrogeological (Fisher *et al.*, 2014), structural (e.g. Embley *et al.*, 2012) and geophysical (e.g. Jacobson, 1992) perspectives. The applicability of B, Li, and Sr isotopes as tracers in hydrothermally altered rocks as well as fluids, and O isotopes in quartz separates as paleothermometer in seafloor hydrothermal systems in diverse settings of marine fluid-rock exchange is the essential focus of this thesis.

## **1.2. Basic principles of seafloor hydrothermal activity**

### *1.2.1. Hydrothermal circulation and seawater-derived alteration*

The fundamental principles of hydrothermal circulation were studied in detail over the last decades and a large number of well written reviews on these systematics were already published (e.g. Chester, 1990; Alt, 1995; Lowell *et al.*, 1995; German & Von Damm, 2003; Staudigel, 2003; Shanks III, 2012; Bach *et al.*, 2013; Fisher *et al.*, 2014). In the following chapter, the most important aspects will be summarized.

Hydrothermal activity at the seafloor is characterized by circulation of fluids through the oceanic crust driven by a heat source that is at plate margins represented by a subjacent magma chamber. Simplified, hydrothermal fluid circulation can be subdivided into four main stages (**Figure 1.2-1**):

- (1) recharge of seawater through permeable zones and fault systems into the upper crust, accompanied by initial fluid-rock interaction under low-temperatures (<150 °C),
- (2) interaction between seawater and oceanic crust under increased pressures and temperatures (> 400 °C) close to the brittle-ductile boundary leads to compositional modifications of seawater (a so-called hydrothermal fluid forms) and the oceanic crust, typically expressed by enrichment of the fluid phase in volatiles and base metals as well as by a decrease in fluid pH and replacement of primary minerals by hydrous alteration phases,
- (3) the increase in fluid temperatures leads to reduced buoyancy and ascent of the hydrothermal fluid, and finally
- (4) the discharge of high-temperature (> 350 °C) fluids at the seafloor occurs, accompanied by the precipitation of metal-rich sulfides due to the contact of hot and metal-rich fluids with cold and oxygen-rich seawater.

The precipitation of sulfides from the metal enriched hydrothermal fluid can occur in differing forms: it can emerge by precipitation of sulfide particles within the upper few meters of the overlying water column in form of “black smoke” that arises from the vent site, but also by formation of sulfide- and sulfate-rich chimneys of several meters height or by formation of massive ore bodies directly on the seafloor (e.g. Tivey, 2007). Vent systems that are characterized by the discharge of fluids of low metal concentrations, also show precipitation of calcium sulfate (anhydrite) in form of “white smoke” (e.g. Gamo *et al.*, 2004). Indeed, the precipitation of particles that are optical visible by black or white smoke ends maximal a few tens of meters above the vent

site. Nevertheless, the buoyant hydrothermal outflow continues to rise up to hundreds of meters within the water column in form of hydrothermal plumes of still shifted signatures (e.g. high CH<sub>4</sub> and He values) relative to unmodified seawater until their density finally equalizes with the ambient seawater density (Schmale *et al.*, 2012). Hydrothermal plumes are therefore important indicators for the existence of hydrothermal activity within a certain area, also hundreds of meters above the actual vent site.

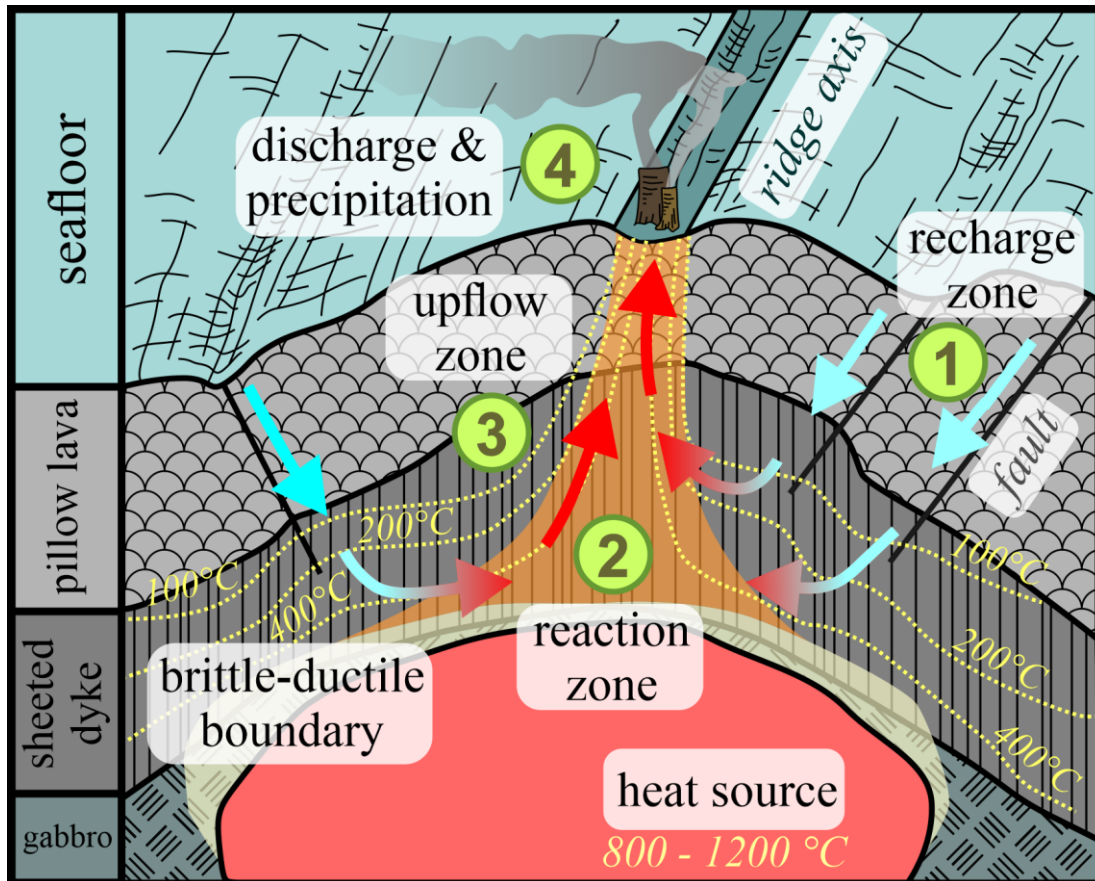


**Figure 1.2-1:** Diagram of the four main stages of high-temperature hydrothermal circulation in the oceanic crust (modified after Alt, 1995; Foustoukos & Seyfried, 2007a) and the upper part of the simplified sequence of oceanic rock layers after the Penrose model (on the left). The numbered stages (green circles) are explained in further detail in **Chapter 1.2**.

Hydrothermal fluid circulation shifts the interacting fluid composition but also leads to major changes in the chemical and mineralogical composition of the affected oceanic crust. The increased temperatures (up to >400 °C) and highly acidic conditions (typically pH<4) that commonly occur during fluid-rock reactions in the seafloor result in thermodynamic instability of primary mineral phases and to replacement processes by secondary minerals that are in equilibrium with the new ambient conditions. The extent of alteration, the type of secondary minerals that form, their relative proportions and the distinct composition of these newly formed minerals mainly depend on the temperatures, fluid pH, water-to-rock-ratios, initially composition of the basement rocks as well as on the mobilization and availability of elements in the circulating fluid. These conditions indeed

change along the fluid pathway. Close to the fluid recharge site, reaction temperatures are still low (<150 °C) and fluids are less acidic. In the early stages, low-temperature reactions between basalt (most common host rock in the oceanic crust) and fluids close to the recharge site leads to the formation of secondary Mg-rich clay minerals (Mg-smectites) due to uptake of Mg from the circulating fluid, precipitation of Fe-oxyhydroxides (e.g. goethite) due to mobilization of Fe caused by the breakdown of primary Fe-hosting phases (pyroxene and olivine), and to the formation of zeolites; the latter gave this alteration mineral assemblage the name “zeolite-facies” (e.g. Bach *et al.*, 2013). Under the increased alteration temperatures (>400 °C) in greater depth, the uptake of Mg from the fluid continuous and leads to nearly complete removal of Mg from the fluid but in this case the formation of Mg-rich clay minerals (chlorite) adapted to the increased temperatures occurs, typical for the “green-schist-facies” (e.g. Bach *et al.*, 2013). Further, mineral phases indicative for “green-schist-facies” up to “amphibolite-facies” are common at the reaction zone of high-temperature hydrothermal systems, like K-rich phyllosilicates (e.g. illite, muscovite), albite, actinolite, and quartz, as well as mineral phases like sulfates (anhydrite, barite), and sulfides (e.g. pyrite, chalcopyrite, sphalerite, Bach *et al.*, 2013). Sulfides precipitate not only directly at the seafloor surface as described above but also in the sub-surface due to entrainment of cold oxygen-rich unmodified seawater through faults and permeable zones. In particular, the directly underlying zone in the basement of hydrothermal discharge sites typically exhibits a complex network of altered rock fragments and thick, metal-sulfide-rich and sulfate-rich veins that is denoted as “stockwork zone”. Continuous closure of veins and fractures due to mineral precipitations also can have major impacts on alteration extents and conditions in the basement because of a more restricted and potentially channelized fluid flow (e.g. Dobson *et al.*, 2003; Heap *et al.*, 2017).

### 1.2.2. Phase separation and segregation

The interaction of heated seawater with the host rock strongly affects the composition of altered rocks and fluids in seafloor hydrothermal systems. An additional commonly observed process is the separation of seawater in a low-density and chloride-poor fluid phase (‘vapor’) and a high-density and chloride-rich fluid phase (‘brine’). This process leads to variations in fluid composition and also transports heat to shallower levels of the hydrothermal system (Foustoukos & Seyfried, 2007a).

Pure H<sub>2</sub>O separates in a vapor and a coexisting liquid phase along the boiling curve until it reaches the critical point at 374 °C and 220 bars (Haar *et al.*, 1984). Beyond the critical point only one supercritical fluid phase exists because the densities of the gaseous and liquid phase convergent. However, the addition of NaCl to the solution shifts the critical point towards higher temperatures and pressures and allows phase separation to occur over a wide range of P-T-conditions (Foustoukos & Seyfried, 2007a). The extension of the boiling curve beyond the critical point of H<sub>2</sub>O in a binary H<sub>2</sub>O-NaCl-system is defined as the critical curve, linking the critical point of seawater to the critical point of NaCl at 3568 °C and 182 bars (Driesner & Heinrich, 2007). For

example, a solution that equals seawater salinity (~3.2 wt% NaCl) reaches the critical point at 407 °C and 298 bars, hence at elevated P-T conditions compared to pure H<sub>2</sub>O.

Based on a classification first established by Welhan & Craig (1979), phase separation processes of seawater can be subdivided in ‘supercritical’ and ‘subcritical’ in dependence on the relative position to the critical point of seawater. Supercritical phase separation forms a small quantity of brine, while subcritical phase separation forms a small quantity of vapor. However, Foustoukos & Seyfried (2007b) highlighted that this discrimination is only significant if phase separation occurs in very close approximation to the two-phase-boundary because otherwise the vapor phase volumetrically dictates the whole system and also the partitioning behavior of trace elements (like lithium and boron) becomes equal for both subdivisions of phase separation.

In natural seafloor hydrothermal systems, the presence of phase separation were detected in a variety of geological settings and spreading rates, however a greater variability and higher frequency of observations were recognized at intermediate and fast spreading axes compared to slower spreading velocities. The most convincing evidence for phase separation is the strong deviation of dissolved NaCl concentrations in discharging hydrothermal fluids (e.g. Charlou *et al.*, 2002; Reeves *et al.*, 2011) and in fluid inclusions (e.g. Vanko, 1988; Nehlig, 1991) compared to seawater composition. Furthermore, the distribution and concentration of dissolved volatiles give hints for the occurrence of phase separation processes in the sub-seafloor (e.g. Welhan & Craig, 1979; Reeves *et al.*, 2011). The chloride-rich, high-density ‘brines’ produced by phase separation tend to descend and accumulate in deeper regions, also reported from fluid inclusion studies of fossil hydrothermal systems (Kelley & Robinson, 1990) and oceanic fracture zones (Kelley & Delaney, 1987). Investigations of modern back-arc basins at the Lau Basin (e.g. Vanko *et al.*, 2004) however also display high-salinity brine inclusions within the upper hundred meters of the hydrothermal systems and indicate that the brine phase is not imperatively restricted to lower parts of the crust. In general, it has to be recognized that phase separation and segregation process in the sub-seafloor are often complex and for example pass through multiple separation and segregation stages or might be influenced by mixing processes, mineral-fluid buffering reactions or the abundance of polyatomic ionic species (Foustoukos & Seyfried, 2007a). Phase separation under such extreme P-T-conditions that reach the halite stability field for example can lead to even stronger shifts of the fluid composition (Berndt & Seyfried, 1997; Foustoukos & Seyfried, 2007b).

### *1.2.3. Magma degassing and advanced argillic alteration*

Magma degassing is characterized by the ascent of high-temperature supercritical fluids enriched in magmatic volatiles (e.g. CO<sub>2</sub>, CH<sub>4</sub>, H<sub>2</sub>O, H<sub>2</sub>, SO<sub>2</sub>, H<sub>2</sub>S) that are directly liberating from the underlying magma chamber and potentially lead to significant modifications in fluid chemistry and rock alteration signatures in seafloor hydrothermal systems (Hedenquist & Lowenstern, 1994; Butterfield *et al.*, 2011). The degassing itself and the composition of the magmatic fluids mainly

depend on the magma composition and the depth of the magma chamber or rather the depressurization (Monecke *et al.*, 2014) but also can evolve with continuously degassing of fluids. For example, in the initial phase the exsolving magmatic fluid is typically enriched in carbon species (e.g. CO<sub>2</sub>), while ascent of a silicic magma body to shallower crust levels leads to an increase in the H<sub>2</sub>O component with ongoing degassing (Yang & Scott, 2006). Degassing of CO<sub>2</sub> in greater depth and under higher pressure conditions of extremely high CO<sub>2</sub>-enriched magmas can locally even cause the appearance of viscous, liquid CO<sub>2</sub> at the seafloor (e.g. at the Champagne vent field, Eifuku volcano, Mariana arc, Lupton *et al.*, 2006). The disproportionation of sulfur gases (e.g. SO<sub>2</sub> and H<sub>2</sub>S, Butterfield *et al.*, 2011) that are commonly present in magmatic fluids and mixing with seawater-derived hydrothermal fluids leads to the formation of extremely low pH acid-sulfate fluids and precipitation of native sulfur, both frequently observed in seafloor magmatic-hydrothermal systems (e.g. Resing *et al.*, 2007; de Ronde *et al.*, 2011; Reeves *et al.*, 2011; Seewald *et al.*, 2015; de Ronde *et al.*, 2019b; Kleint *et al.*, 2019). The formation of sulfate-rich fluids and mineral deposits that are related to magmatic fluids is already well-known from continental hydrothermal systems, like volcanic fumaroles (e.g. Stoiber & Rose, 1974; Bernard *et al.*, 1990), and subaerial volcanic hydrothermal systems (e.g. Hedenquist & Lowenstern, 1994). At the seafloor, acid-sulfate fluids typically appear as low-temperature (<120 °C), low-pH (occasionally as low as pH=1.2, Kleint *et al.*, 2019), milky white plumes due to the ascent of native sulfur droplets, sulfate particles (e.g. natroalunite), silica, and Fe-oxyhydroxides (de Ronde *et al.*, 2005; Resing *et al.*, 2007) that issue from low-relief mounds or small chimneys comprising of alunite, silica, native sulfur, clay minerals and sulfides (de Ronde & Stucker, 2015). The volcanic host rocks affected by alteration of acid-sulfate fluids become extensively altered and are replaced by an advanced argillic alteration mineral assemblage of typically i.a. natroalunite, alunite, pyrophyllite, kaolinite, diaspora, and dickite (e.g. de Ronde *et al.*, 2019b; Seewald *et al.*, 2019). The extensive leaching of the host rocks gives them a nearly white appearance after alteration.

Beside the highly acidic and volatile-rich nature, magmatic fluids are also supposed to be highly enriched in metals and suggested to enhance the formation of especially large and Cu- and Au-rich ore bodies at the seafloor. It was assumed that ore forming processes are comparable to porphyry- and epithermal-type ore deposits like they are found at fumaroles and subaerial volcanoes (e.g. Hedenquist & Lowenstern, 1994; Möller *et al.*, 2003). The assumption that ascending magmatic fluids transport metals from the subjacent magma chamber to shallower levels of seafloor hydrothermal systems was mainly derived from experimental data (review in Williams-Jones & Heinrich, 2005), fluid- and melt inclusion studies (review in Yang & Scott, 2006), and modeling results (Gruen *et al.*, 2014). Phase separation experiments demonstrated that enrichment of metals not only occurs in the hypersaline liquid phase that is usually trapped at deeper portions of magmatic-hydrothermal systems due to its high-density but showed that metal enrichment can also occur in the low-density volatile phase in form of chloride and sulfate complexes that are capable to

ascent towards the seafloor surface (e.g. Ballhaus *et al.*, 1994; Simon *et al.*, 2004; Zajacz *et al.*, 2011). In particular, the partitioning of Cu towards the vapor phase in presence of sulfur was suggested based on fluid inclusion data (Heinrich *et al.*, 1992), and was also assumed for Au (Ulrich *et al.*, 1999). Indeed, the metal concentrations in magmatic fluids additionally depend on the magma composition and may also on the stage of ore formation. Yang & Scott (2002) assumed that the vapors of basaltic to basaltic-andesitic melts display high concentrations of Ni, Cu, Zn, and Fe but that vapors of andesitic, dacitic, and rhyolitic melts are more enriched in Cu, Zn, Fe, and Mn inferred from precipitates within vesicles of melt inclusions and matrix glasses derived from a back-arc hosted hydrothermal system. Gruen *et al.* (2014) further suggested that the early degassing stage of dacitic magmas at Brothers volcano is dominated by the vapor phase and formation Cu-Au-rich deposits, while at later stages the hypersaline liquid phase may expel at the seafloor that is also enriched in other metals (e.g. Fe, Zn) based on modeling results.

In general, the degassing of magmatic fluids and formation of acid-sulfate fluids in association with metal transport from the magma chamber are much more frequently associated with vent systems in arc volcanoes and back-arc settings (**Chapter 1.3.3**) than with systems at mid-ocean ridges (**Chapter 1.3.1**). This relation results from the intensified volatile enrichment of arc and back-arc magmas and the enhanced depressurization at these locations due to relatively shallow water depth (de Ronde & Stucker, 2015).

### ***1.3. Diversity of seafloor hydrothermal systems at different geological settings***

The world map (**Figure 1.1-1**) highlights the widespread abundance of vent systems. High-temperature hydrothermal discharge occurs at any type of plate margins, at mid ocean ridges as well as subduction zones, and at any spreading rate, from ultra-slow- to fast-spreading. Further, even in the sediment buried mid ocean ridge flanks that are not directly underlain by a magmatic heat source, low-temperature hydrothermal circulation occurs due to mining of lithospheric heat by outcrop-to-outcrop circulation between volcanic seamounts reaching above the sediment cover. The characteristics of hydrothermal activity in these highly diverse geological settings vary and are further described in the following subchapters (overview in **Figure 1.3-1**).

#### ***1.3.1. Hydrothermal systems at mid ocean ridges***

At mid ocean ridges (MOR), also described as divergent plate boundaries, new oceanic crust is formed by ascent of magmas that are derived from partial melting of the subjacent lithospheric mantle (Wilson, 2007). MOR span a total length of approximately 60.000 km across the world ocean floors and host a large number of hydrothermal vent systems (Beaulieu *et al.*, 2015). The mid-ocean ridge spreading rates vary from ultra-slow (<20 mm/year, e.g. the Southwest Indian Ridge), over slow- (20-40 mm/year, e.g. the Mid Atlantic Ridge) to fast-spreading rates (>40 mm/year, e.g. East Pacific Rise), controlled by the oceanic crust production rates and the thermal structure in the basement (German & Lin, 2004). In addition, differing spreading rates are

accompanied with great variance in the tectonic structures of ridges, also influencing the characteristics of hydrothermal activity at fast- versus slow-spreading ridges.

#### *1.3.1.1. Fast-spreading ridges*

At fast-spreading ridges (>40mm/year), the production rate of new oceanic crust is relatively high and constant over time, resulting in development of a rather even ridge crest topography (**Figure 1.3-1(1)**). The sequence of consecutive rock layers with depth at fast-spreading ridges is relatively undisturbed and follows more or less closely the simplified model of the oceanic crust structure (Vine & Moores, 1972):

- (1) a sediment cap superimposes
- (2) an up to 1 km thick layer of basaltic pillow lavas, lava flows and volcanic breccias, that is underlain
- (3) by an around 1 km thick layer of the basaltic sheeted dyke complex, and then
- (4) by a several km thick layer of gabbroic intrusive rocks that are subordinated
- (5) by the peridotitic mantle.

The magma chamber, as an important driver of hydrothermal circulation, is situated at comparable shallow depth of around 1-4 km beneath the seafloor at fast-spreading ridges (e.g. Detrick *et al.*, 1987, Detrick *et al.*, 1993, Carbotte *et al.*, 2006). Therefore, hydrothermal circulation is narrowed to the topmost part of the crust and fluid pathways are relatively short at fast spreading rates (Baker, 2007). The mode of hydrothermal circulation and change in fluid and rock chemistry, as well as the rock alteration patterns are well-described by the basic principles of hydrothermal activity, explicated in **Chapter 1.2.1**.

#### *1.3.1.2. Slow- to ultra-slow-spreading ridges*

At ultra-slow- (<20 mm/year) and slow-spreading (20-40 mm/year) ridges the magma supply is much less continuous, more irregular distributed along the axis (German & Lin, 2004), and the magma chamber is around twice as deep-seated (5-8 km depth, Hannington *et al.*, 2005) than at fast-spreading ridges (**Figure 1.3-1(2)**). The lack in continuous magma supply results in subsidence of the axial crust and development of a highly jointed rift valley in an extension dominated tectonic setting (German & Lin, 2004). Commonly observed at slow-spreading ridges is an asymmetrical spreading mode and the formation of very large-scale, shallow dipping normal faults that often show tens of km displacement, denoted as detachment faults (Smith *et al.*, 2006; Smith *et al.*, 2008). Detachment faults are originally high-angle ( $65\pm 10^\circ$ ) normal faults that flatten to low-angles (ca.  $30^\circ$ ) as a consequence of flexural unloading (MacLeod *et al.*, 2009; Escartín *et al.*, 2017). Detachment faults uplift the footwall and therefore exhume upper as well as lower oceanic crust and mantle material (ultramafic rocks) onto the seafloor; especially, but not only, in association with axial discontinuities at ridge segment extremities (Smith *et al.*, 2006; Smith *et al.*, 2008). The lower

crustal rocks and mantle lithologies exposed at the seafloor form gently curved, corrugated surfaces and often elevated massifs that are elongated up to several km parallel to the axis, denoted as oceanic core complexes (OCCs, e.g. Cann *et al.*, 1997; Tucholke *et al.*, 1998; MacLeod *et al.*, 2009). The intrusion of gabbroic magma bodies into OCCs is also frequently described (e.g. MacLeod *et al.*, 2009). The structure control and irregularity in volcanic and intrusive events at slow-spreading ridges results in disturbance of the classically assumed structure of oceanic crust that exists at fast-spreading ridges (**Chapter 1.3.1.1**).

All so far discovered OCCs along the Mid-Atlantic Ridge show evidence for active or formerly active hydrothermal processes of great extent (Escartín *et al.*, 2017, and references therein), and also ultra-slow-spreading ridges host a significant number of vent systems (e.g. Bach *et al.*, 2002; Edmonds *et al.*, 2003; Harding *et al.*, 2017). In addition, both are commonly associated with especially large and Cu-Au-rich ore deposits (Fouquet *et al.*, 2010; German *et al.*, 2016). This is somehow surprising, since earlier studies (Baker *et al.*, 1996) predicted that hydrothermal activity is directly proportional to the heat flux and crustal production rate of particular ridge segments that are relatively low at slow- and even lower at ultra-slow-spreading ridges. Hydrothermal circulation at slow- and ultra-slow-spreading ridges can be driven by deep penetration of seawater along the extensively developed fault systems down to the deeply seated axial magma chamber (Allen & Seyfried, 2004) or by channelization of lithospheric heat along deep rooted faults (Lowell, 2017). But furthermore, heat to drive hydrothermal circulation can also be provided by the gabbroic bodies intruding into the footwall of detachment faults (e.g. McCaig *et al.*, 2007, **Figure 1.3-1(2)**). One further and rather unique potential heat source that occurs in ultramafic hosted vent systems results from the alteration of ultramafic rocks by serpentinization (replacement of olivine by serpentine, brucite and magnetite) because this is an exothermic reaction that on its own terms leads to the release of heat and may drive hydrothermal circulation (Lowell & Rona, 2002; Früh-Green *et al.*, 2003; German & Lin, 2004). Nevertheless, Allen & Seyfried (2004) concluded that not much more than an increase in fluid temperatures of around 50 °C can be explained by the exothermic serpentinization reaction, even under ideal conditions. This increase is not sufficient to explain the high-temperature (>350 °C) fluids found at slow- and ultra-slow-spreading ridges, and additional heat supply by the axial magma chamber or gabbroic intrusions is needed to drive the circulation in those kind of systems.

Serpentinization of ultramafic material is nevertheless a common process associated with OCCs and leads to distinct changes in fluid composition, e.g. towards higher pH, increased methane (CH<sub>4</sub>) and higher hydrogen (H<sub>2</sub>) concentrations (e.g. Seyfried & Dibble, 1980; Janecky & Seyfried, 1986; Charlou *et al.*, 1991). Indeed, hydrothermal fluids issuing from some ultramafic hosted vent systems buffer pH at relatively low, more acidic conditions (pH≤5, e.g. Logatchev, Seyfried *et al.*, 2013). The low fluid pH may be caused by interaction with gabbroic intrusions (McCaig *et al.*, 2007) or by

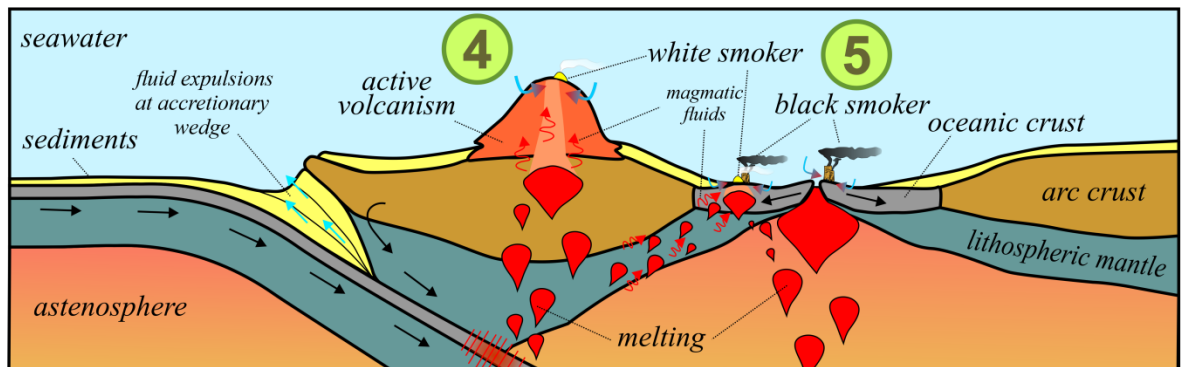
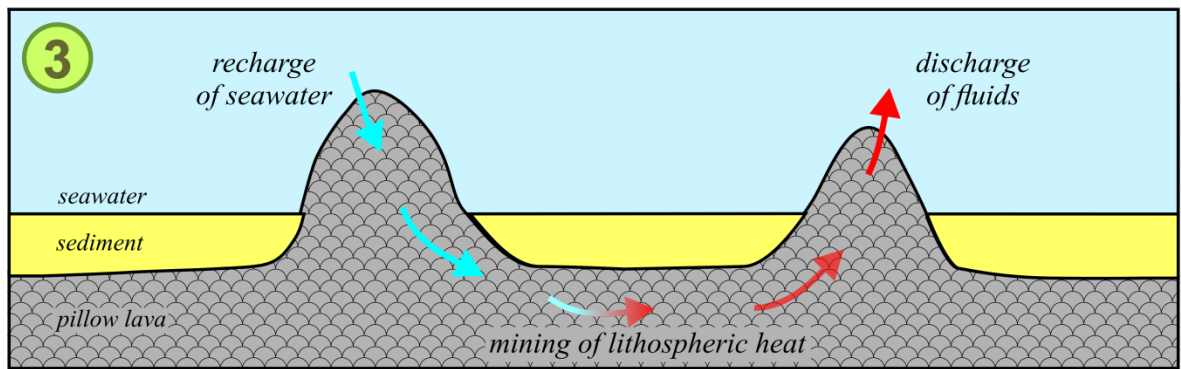
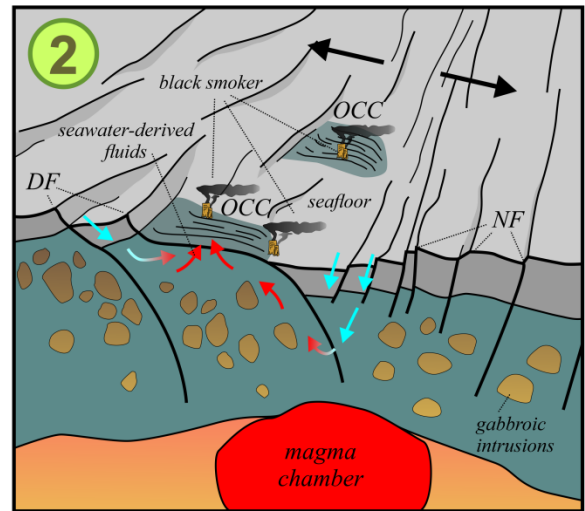
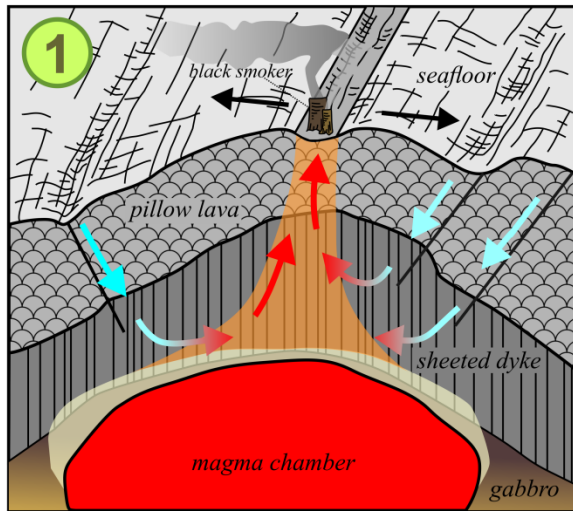
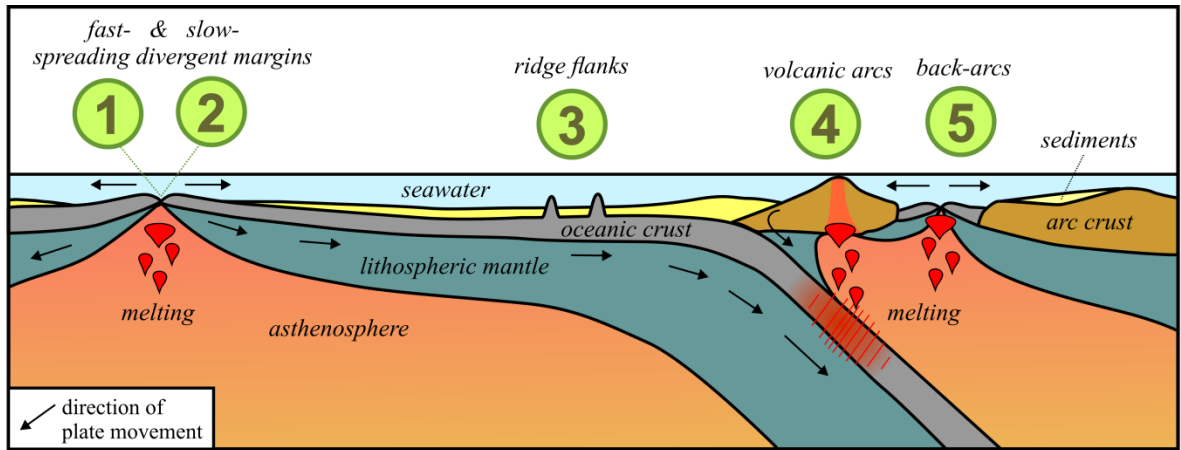


**Figure 1.3-1 (previous page):** The topmost section of the figure shows a schematic illustration of the five main geological settings of magmatic and/or hydrothermal activity (cf. Yang & Scott, 2006). The following pictures show fluid circulation at the specific locations in more detail, in correspondence to the green numbers given in the topmost picture. Not to scale. (1) Fluid circulation at fast-spreading divergent margins (cf. Alt, 1995; Foustoukos & Seyfried, 2007a). The constant magma supply creates a relatively homogenous relief at the seafloor, resulting in a channelized high-temperature ( $>350$  °C) fluid discharge at the axis from black smoker chimneys. (2) Fluid circulation at slow-spreading divergent margins (cf. Carbotte & Canales, 2019) is strongly controlled by the tectonic structure that is characterized by subsidence of the spreading axis, development of steep dipping ( $65\pm 10^\circ$ ) normal faults (NF) and large-scale, shallow dipping ( $\sim 30^\circ$ ) detachment faults (DF). At DF, lower crustal and mantle rocks become exposed to the seafloor in so-called oceanic core complexes (OCC), often associated with high-temperature ( $<350$  °C) hydrothermal vents. Intrusion of gabbroic magma bodies to the footwall of DFs is supposed to be an important heat source that gives rise to hydrothermal circulation. (3) Fluid circulation in low-temperature (most usual  $<25$  °C) ridge flank hydrothermal systems between basaltic structures of higher permeability in contrast to the sounding sediments that is driven by mining of lithospheric heat (cf. Fisher & Wheat, 2010). (4) Fluids at submarine arc volcanoes can have two characteristics: seawater-derived hydrothermal fluids that form by re- and discharge of seawater through more permeable parts at the summit of the volcano, or magmatic fluids that ascent from the underlying magma chamber (cf. Yang & Scott, 2006). Magmatic fluid contribution can lead to the formation of acid-sulfate fluids and discharge at the seafloor in form of native sulfur-rich white smoke. (5) In back-arc basins (BAB), the fluid circulation systematics strongly depend on the stage of rifting and spreading and the distance to the subducting slab. If arc magmatism still strongly contributes, hydrothermal activity at BAB is often very similar to arc systems. In later stages of spreading, hydrothermal signatures at BAB are more comparable to fast-spreading ridges as it is shown in picture (1). Also integrated in the lowermost picture is the fluid expulsion by diagenetic processes at the accretionary wedge in the fore-arc region of subduction zones.

---

a decrease in pH because of stability of talc-tremolite under increased temperatures ( $>340$  °C) that are produced by alteration of pyroxenes (beside olivine an abundant mineral in ultramafic mantle rocks). The alteration to a talc-tremolite-bearing alteration mineral assemblage leads to a release of  $H^+$  ions and therefore to a decrease in fluid pH, in contrast to  $H^+$  ion consumption and an increase in fluid pH that is accompanied with the serpentinization of olivine (Allen & Seyfried, 2003). Mantle rocks that show replacement of talc-tremolite were already found at several sites at slow-spreading ridges (e.g. Bach *et al.*, 2004; Boschi *et al.*, 2008; Petersen *et al.*, 2009). Some vent sites hosted in ultramafic lithologies are potentially also affected by phase separation or magma degassing processes (e.g. Semenov, Melekestseva *et al.*, 2014; Melekestseva *et al.*, 2017; details on phase separation and magma degassing are given in **Chapter 1.2.2** and **1.2.3**).

#### *1.3.1.3. Examples of ultramafic rock hosted vent sites along the Mid-Atlantic Ridge*

The ridge segment between the Marathon and  $15^\circ 20' N$  Fracture Zones along the Mid-Atlantic Ridge (MAR) is especially hydrothermally active. It was assumed (Smith *et al.*, 2006; Smith *et al.*, 2008) that up to 35% of the ridge segment between the  $13^\circ$  to  $15^\circ N$  along the MAR is influenced

by detachment faulting and potential formation of OCCs. The number of vent sites is even comparable to the abundance of vent sites at fast-spreading ridges (Beaulieu & Szafranski, 2019).

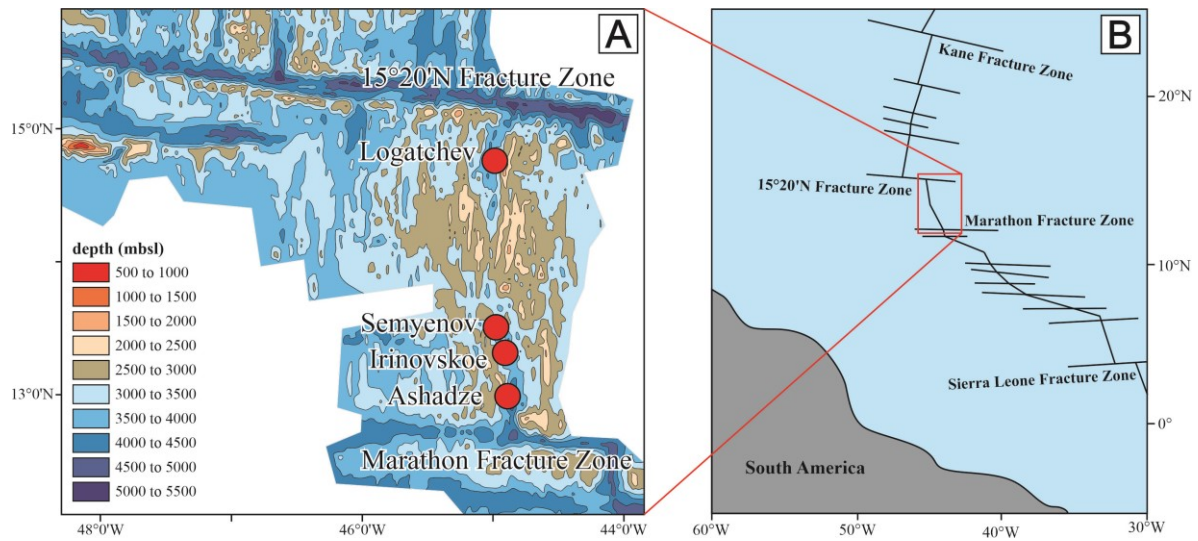


**Figure 1.3-2:** Locations of hydrothermal fields along the MAR between the Marathon and 15°20'N Fracture Zones. (A) The bathymetric map was modified after Ondréas *et al.* (2012), and (B) the overview map showing the progression of the MAR ridge axis and fracture zones was modified after Melekestseva *et al.* (2010).

Details on four hydrothermal vent fields (Logatchev, Semenov, Irinovskoe, Ashadze, **Figure 1.3-2**) hosted in this area are given in the following subchapters.

### Logatchev

The Logatchev hydrothermal field (LHF) at 14°45'N on the MAR were discovered by a Russian expedition in 1993 (Batuev *et al.*, 1994). It actually comprises of four hydrothermal fields (LHF-1 to -4) roughly oriented along an E-SE transect in maximal distance of 9 km apart from each other; LHF-1 and -2 show active fluid discharge while LHF-3 and -4 are inactive nowadays (Petersen *et al.*, 2009). Hydrothermal activity is already lasting for at least 60,000 years within the LHF based on the  $^{230}\text{Th}/^{234}\text{U}$  dating method carried out for massive sulfide precipitates (Lalou *et al.*, 1996; Kuznetsov *et al.*, 2006). LHF-1 is the most detailed studied field at Logatchev and is made up of seven high-temperature (up to 360 °C) fluid discharge sites (Site 'A' and 'B', IRINA, IRINA II, QUEST, CANDELABRA, and ANNA-LOUISE). It is hosted on the eastern rift flank approximately 7 km apart from the MAR axis on a plateau beneath a 350 m elevated cliff in 3060 to 2910 mbsl (Petersen *et al.*, 2009). The LHF-1 depicts two characteristic fluid discharge types. The first type (Site 'A' and IRINA II) comprises of up to 15 m high, mound-shaped edifices of serpentinized rock talus that are crested by up to 5 m high black smoker chimneys rich in Zn- and Fe-sulfides and minor Cu-sulfides (Petersen *et al.*, 2009; Augustin *et al.*, 2012). The second type (Site 'B', IRINA, QUEST, CANDELABRA, and ANNA-LOUISE) is represented by venting of fluids resigning from 2 to 5 m deep local depressions in the seafloor ('smoking craters') that are

rimmed by 1 to > 5 m high craters of serpentinites and weathered sulfide talus that are mostly devoid of anhydrite (Petersen *et al.*, 2009). Some small (maximum 0.6 m high) black smoker chimneys were reported from the rims of the craters (Petersen *et al.*, 2009). The second type was so far solely described from ultramafic hosted seafloor hydrothermal systems but the formation processes are poorly understood so far.

The basement underlying the LHF consists of dunites and harzburgites that are extensively serpentinitized and replaced by serpentine (primarily the lizardite polymorph) and fine grained magnetite; but brucite, another mineral typically formed by serpentinitization, is lacking (Augustin *et al.*, 2008; Petersen *et al.*, 2009). The absence of brucite in altered ultramafic rocks collected from the seafloor surface was linked to potential destabilization of brucite due to exchange with ambient seawater by other authors (e.g. Snow & Dick, 1995; Augustin *et al.*, 2012). Beside ultramafic lithologies, the basement of the LHF contains a fraction of 20-40 % made up of gabbroic rocks classified as gabbro-norites (Kelemen *et al.*, 2004; Petersen *et al.*, 2009). Low-temperature hydrothermal exchange seems also to affect the system to a certain extent, i.a. based on high Sr, Rb, U, and Pb concentrations that some altered rocks display compared to fresh mantle rocks (Augustin *et al.*, 2012).

The discharging fluids at the LHF show characteristics typical for serpentinitization processes like very high concentrations of dissolved CH<sub>4</sub> and H<sub>2</sub> and a depletion in B relative to ambient seawater (Schmidt *et al.*, 2007). An increase in CH<sub>4</sub> and He relative to ambient seawater was also detected in gas plumes in the water column above the LHF (Schmale *et al.*, 2012).

#### *Semenov*

The Semenov hydrothermal district (SHD) is hosted within a OCC at 13°31'N and 44°55'W west of the MAR in a water depth of 2400 to 2950 mbsl and was discovered by a Russian expedition in 2007 (Beltenev *et al.*, 2007). It consists of five hydrothermal fields (SHF-1 to -5), in which only one of them (SHF-2) shows active fluid discharge of white smoke up to 313 °C (***Thesis Chapter 5***). The other four fields are inactive but show abundant massive sulfides (Beltenev *et al.*, 2007; Beltenev *et al.*, 2009). Data received from <sup>230</sup>Th/U dating of massive sulfides point to that several pulses of hydrothermal activity took place at the SHD in a minimum range of 124 to 37 ka (Kuznetsov *et al.*, 2011). The ages of sulfide deposits at the eastern part of the SHD are variable but contain the oldest measured samples compared to overall younger ages towards the west and may indicate a westward shift of hydrothermal activity over time (Kuznetsov *et al.*, 2011).

The OCC underlying the SHD comprises of serpentinitized harzburgite that were replaced by serpentine and magnetite, and partly further modified by talc replacement, and by gabbroic rocks (gabbro, olivine gabbro, gabbro-norite, and ferrogabbro) that were affected by actinolitization, prehnitization, and chloritization; locally also amphibolites and altered silicic igneous rock types

(plagiogranites, tonalite, and diorite) occur (Beltenev *et al.*, 2007; Beltenev *et al.*, 2009; Pertsev *et al.*, 2012). Furthermore, exposures of unaltered to moderately altered basaltic rocks and dolerites are present (Pertsev *et al.*, 2012). The actively venting SHF-2 (13°31.13'N and 44°58.03'W) in the NW of the OCC in 2500 to 2600 mbsl is hosted in altered basaltic rocks based on investigations of the seafloor surface (Beltenev *et al.*, 2007). Indeed, as described before the OCC comprises of a mixture of ultramafic, mafic and silicic rock types and the rock compositions in greater depth are unknown. Geochemical signatures of massive sulfide of the SHF-2 deposits give evidence for both, affection of hydrothermal activity by ultramafic rocks (i.a. very high Au and Ag contents, Melekestseva *et al.*, 2010; Melekestseva *et al.*, 2017) as well as by mafic lithologies (enrichment in SiO<sub>2</sub>, Melekestseva *et al.*, 2017). Melekestseva *et al.* (2014) and (2017) suggested that the very high metal (e.g. Au, Ag) concentrations at SHF-2 could also result from magmatic fluid contributions based on thermodynamic modeling results, the abundance of silicic rock types, and based on the high volatile contents of fluid inclusions at the SHD.

#### *Irinovskoe*

The Irinovskoe hydrothermal field (IHF) is located at 13°20'N, within an OCC in 5 km distance to the neovolcanic zone of the MAR and in water depth between 2700 to 2850 (Escartín *et al.*, 2017). It was studied by AUV (autonomous underwater vehicle) and ROV (remotely operating vehicles) during the ODEMAR research cruise in 2013 (Jamieson *et al.*, 2014). The IHF has two active vent sites of high-temperature (up to 365 °C) black smoke discharging from cauldron-shaped edifices that are both situated at the summit of the OCC; Active Pot and Pinnacle Ridge (Escartín *et al.*, 2017). The basement of the OCC consists of ultramafic and gabbroic rocks that were hydrothermally altered to varying extents. Dating by <sup>230</sup>Th/U of massive sulfides from the IHF (Cherkashov *et al.*, 2016; Kuznetsov *et al.*, 2018) indicated that three pulses of hydrothermal activity occurred in a total age range between 8 and 58 ka.

#### *Ashadze*

The Ashadze hydrothermal district (AHD) at 12°58'N along the MAR and around 30 km north of the Marathon Fracture Zone was first discovered by a Russian expedition in 2003 (Beltenev *et al.*, 2003). Further investigations were made amongst others by ROV during the French-German 'Serpentine' cruise in 2007 (Fouquet *et al.*, 2008). The AHD is associated with the corrugated surface of an OCC that is located west of the MAR axial valley and characterized by slope failure associated with distinctive landslides (Beltenev *et al.*, 2003). Four individual hydrothermal fields (AHF-1 to -4) were assigned to the AHD. Two of them (AHF-1 and -2) show active discharge of fluids highly enriched in H<sub>2</sub> in form of black smoke (Charlou *et al.*, 2010). The active AHF-1 lies 4 km west from the MAR rift valley and in 1 km distance to the contact zone of ultramafic-gabbroic lithologies of the detachment and basaltic rocks at a water depth of 4100 mbsl (Ondréas *et al.*, 2012). Hydrothermal discharge of fluids at temperatures up to 372 °C led to precipitation of Cu-Zn

sulfides (Firstova *et al.*, 2016). The AHF-2 is situated in 5 km distance from the AHF-1 and 9 km apart from the axial valley in a water depth of 3260 mbsl and within a N-S trending narrow (around 70 m wide) linear depression that is restricted to the east by a faulted gabbroic body and to the west by a N-S oriented ridge (Fouquet *et al.*, 2010; Ondréas *et al.*, 2012). At AHF-2, the mineralization dominantly consists of pyrite and Cu-sulfides of high Cu, Au and Co contents (Cherkashev *et al.*, 2013) and the maximum measured fluid temperatures of escaping fluids were 296 °C (Ondréas *et al.*, 2012). Indeed, temperature measurements at AHF-2 were complicated because fluid discharges arises from up to 5 m deep and 40 m wide hydrothermal craters that made the investigations by ROV difficult and the in-situ temperatures directly at the discharge were probably higher than the measured ones (Fouquet *et al.*, 2008). Ondréas *et al.* (2012) suggested that those craters, like they were already observed e.g. at the Logatchev hydrothermal fields, result from geyser-like explosions on the seafloor. The AHF-1 and -2 are both hosted in serpentinized peridotites that are partly further replaced by talc, altered gabbroic rocks and trondhjemites (Silantyev *et al.*, 2011). Silantyev *et al.* (2011) assumed that the trondhjemites represent partial melting products of gabbroids that could form due to the ingress of hydrothermal fluids towards the root zone of the hydrothermal system. A further discovered hydrothermal field in the rift valley of the Ashadze district (AHF-4) that is inactive nowadays but was identified by the occurrence of extinct Zn- rich sulfide chimneys is hosted in basaltic rocks in 4530 mbsl (Ondréas *et al.*, 2012). During another Russian expedition in 2005 (Beltenev *et al.*, 2005) an additional inactive hydrothermal field (AHF-3) located 1.8 km north from AHF-1 were described. However, the existence of the AHF-3 could not be confirmed during the following cruise in 2007 (Ondréas *et al.*, 2012). The timeframe of hydrothermal activity at the AHD were investigated by using the  $^{230}\text{Th}/\text{U}$  dating method for massive sulfide deposits. The method delivered maximum ages of  $7.2 \pm 1.8$  ka for the AHF-1 that point to a recent start of hydrothermal activity, and a more mature age of  $27.3 \pm 1.8$  ka for the AHF-2, respectively (Cherkashev *et al.*, 2013). The inactive AHF-4 indicates onset of hydrothermal activity around  $63.5 \pm 10.8$  ka in the deeper rift valley of the district (Cherkashev *et al.*, 2013).

### 1.3.2. Hydrothermal systems at ridge flanks

High-temperature (>350 °C) hydrothermal circulation at the seafloor is restricted to the region of direct heat supply that is provided by a subjacent magma chamber. Besides, also the permeability of the crust becomes increasingly smaller due to sealing of pore spaces and fractures by newly formed minerals and inhibits fluid circulation. The oceanic crust is additionally increasingly buried by impermeable marine sediments that prohibit exchange between oceanic crust and seawater away from the ridge axes (Fisher & Wheat, 2010). Nevertheless, Stein & Stein (1994) estimated that off-axis, low-temperature (<150 °C) fluid circulation accounts for approximately 70% of the total hydrothermal heat loss from oceanic crust of 11 TW, and following transports very large amounts of water through the oceanic crust. The low-temperature seawater-crust exchange either occurs before the crust is completely sealed by sediments or in so-called “ridge flank hydrothermal

systems” (RFHS, *Figure 1.3-1(3)*). In RFHS, fluids are transported by outcrop-to-outcrop circulation between tens of km distant basaltic seamounts and edifices that reach above the surrounding sediment cover and show an increased permeability in contrast to the highly impermeable sediments (Mottl *et al.*, 1998; Hutnak *et al.*, 2008; Fisher & Wheat, 2010; Le Gal *et al.*, 2018; Villinger *et al.*, 2019). Mining of lithospheric heat provides the heat supply that is needed for hydrothermal circulation (Hutnak *et al.*, 2008; Fisher & Wheat, 2010; Winslow *et al.*, 2016). During the fluid pathway from the recharging to the discharging outcrop, distinct changes in fluid and crust chemistry occur due to interactions between basaltic crust and fluids, diffusive exchange with the sediment covering the crust, and microbial activities (Wheat *et al.*, 2019). The absolute change in discharging fluid versus seawater chemistry is rather small compared to high-temperature hydrothermal systems due to the low reaction temperatures (<150 °C, but more usual <25 °C) but the very high water fluxes and large areas affected by low-temperature circulation resulting in a nevertheless large impact of low-temperature hydrothermal exchange on oceanic crust as well as seawater chemistry (Mottl & Wheat, 1994; Wheat *et al.*, 2017a); especially for fluid mobile elements like lithium and boron (Lemarchand *et al.*, 2002; Misra & Froelich, 2012).

Estimates on the element mass fluxes at RFHS are nevertheless difficult because of the issues to detect the relatively diffusive outflow of fluids of only slightly elevated temperatures (<150 °C, but more typical < 25 °C), compared to ambient seawater (2 °C). To date, sampling of fluids could only be conducted for two RFHS discharge sites that are in first order controlled by mining of lithospheric heat; Baby Bare Outcrop close to the Juan de Fuca Ridge (Mottl *et al.*, 1998) and Dorado Outcrop close to the East Pacific Rise (Wheat & Fisher, 2008). Furthermore, only Dorado Outcrop exhibits an exchange environment typical for RFHS, regarding basement temperatures (13.2°C), fluid residence times (a few years), and surrounding sediment cover (approximately 500m), while Baby Bare Outcrop shows unusual high basement reaction temperatures of discharging fluids (64 °C) due to very rapid burying and sealing of crust by sediments shortly after crust formation (Mottl *et al.*, 1998; Wheat *et al.*, 2004). The higher fluid temperatures at Baby Bare Outcrop lead to intensified alteration and seawater-rock exchange in the basement and potentially to stronger shifts in altered rock and fluid chemistry, and therefore may not be representative to make assumptions on global elemental fluxes at RFHS.

Typical alteration mineral phases of the low-temperature basaltic crust at RFHS are Mg-smectites (e.g. saponite), K-rich clay minerals (e.g. celadonite), zeolites (e.g. phillipsite, clinoptilolite), and Fe-oxyhydroxides (e.g. Wheat *et al.*, 2019), very similar to the alteration patterns at the recharge zone of high-temperature hydrothermal systems (*Chapter 1.2.1*). Ridge flank systems are also important host-environments for specialized microbial communities (Edwards *et al.*, 2012; Lee *et al.*, 2015; Baquiran *et al.*, 2016).

### 1.3.2.1. Example of a ridge flank hydrothermal system

#### Dorado Outcrop

Dorado Outcrop (**Figure 1.3-5**) is a northwest-southeast striking basaltic edifice of 0.5 km width and 2 km length that reaches approximately 150m above the surrounding sediment cover (around 500m thick) and is located at 18.5 to 23 Myr old crust of the Cocos Plate, east of the East Pacific Rise (Wheat & Fisher, 2008). The region around Dorado Outcrop of a size of 14.500 km<sup>2</sup> stands out by its 10-40% lower measured than predicted heat flow that was expected based on lithospheric models (Fisher, 2003; Hutnak & Fisher, 2007), pointing to extensive advective removal of heat by outcrop-to-outcrop fluid circulation (as described in **Chapter 1.3.2**). In the region, several basaltic seamounts and other edifices of active fluid recharge or discharge were identified by swath bathymetry, seismic data and heat flow measurements (Fisher, 2003; Hutnak & Fisher, 2007) that are believed to be formed by off-axis volcanism (Barckhausen *et al.*, 2001; Wheat *et al.*, 2019). Dorado Outcrop was identified to be a fluid discharge site with a predicted discharge rate in a range from 100 to 10,000 L/s based on chemical and thermal data, hydrological modeling, and dye experiments (Hutnak *et al.*, 2008; Wheat & Fisher, 2008; Lauer *et al.*, 2018; Wheat *et al.*, 2019). The large range in discharge rates inferred from different methods might be also influenced by the strong tidal pressure effects that influence fluid flow in the region around Dorado Outcrop (Fisher, 2003; Hutnak & Fisher, 2007; Hutnak *et al.*, 2008). Discharging fluid temperatures at Dorado Outcrop are 12.3 °C, slightly cooled by ascent compared to the basement fluid temperatures of around 13.2 °C (Wheat & Fisher, 2008; Wheat *et al.*, 2017a). The most closely located recharging basaltic structure is called Tengosed Seamount, in around 20 km distance to Dorado Outcrop.

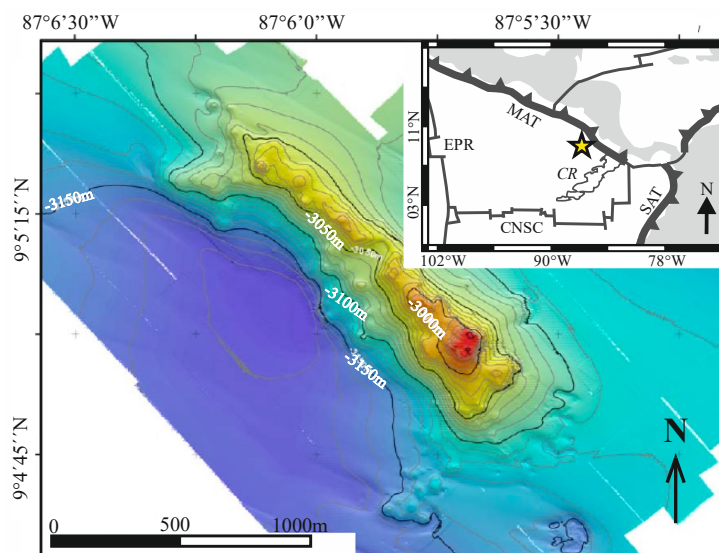


**Figure 1.3-3:** Topographic map of Dorado Outcrop (modified after Wheat *et al.*, 2017b). Upper right corner: location of Dorado Outcrop (yellow star) on 18.5 to 23 Myr old crust of the Cocos Plate, west of Costa Rica. CNSC – Cocos-Nazca Spreading Center, CR – Cocos Ridge, EPR – East Pacific Rise, MAT – Middle America Trench, SAT – South America Trench.

Data on pore-water profiles (Wheat & Fisher, 2008) and spring fluids (Wheat *et al.*, 2017a) collected at Dorado Outcrop revealed some slight but significant changes in chemical composition of certain elements (i.a. lithium) compared to seawater that highlighted that RFHS potential have an important impact on seawater composition. Alteration mineralogy of altered basalts collected at the surface of Dorado Outcrop corresponds to the typical low-temperature mineral assemblage, consisting of Mg-smectites, K-rich clay minerals, zeolites and Fe-oxyhydroxides (Wheat *et al.*, 2019).

### 1.3.3. Hydrothermal systems at subduction zones

The continued cooling of the oceanic crust due to heat loss with increasing distance from the ridges results in a density increase with aging (Stein & Stein, 1994). At subduction zones, also denoted as convergent plate boundaries, the aged oceanic lithosphere (oceanic crust and rigid upper mantle material) and the overlying sediments are subducted beneath an adjacent tectonic plate of lower density due to gravitational sinking; the overriding plate can be oceanic or continental (**Figure 1.3-1(4)**). The subducted oceanic lithosphere sinks down to the high-temperature (>1300 °C), ductile and lower density upper mantle (asthenosphere) and then becomes recycled further into deeper mantle portions. Magma generation and volcanic activity within the overlain mantle wedge results from a lowering of the melting point by water that derives from dehydration of the subducted altered oceanic crust and marine sediments that became enriched in hydrous mineral phases by seawater alteration since crust creation at the ridge axis (Sisson & Grove, 1993; Arculus, 2004; Grove *et al.*, 2012). The magmatic activity at subduction zones of two colliding oceanic plates leads to the formation of submarine (e.g. Kermadec Arc) and potentially also subaerial volcanic or island arcs (e.g. the Philippines), especially in the Western Pacific area. The composition of arc lavas is highly diverse but commonly more evolved and felsic in composition (typically dacites, andesites or even rhyolites) and more enriched in volatiles (e.g. CO<sub>2</sub>, H<sub>2</sub>O, SO<sub>2</sub>) and large-ion-lithophile elements (LILE, e.g. Rb, Cs, Ba, Sr, U) compared to MORB because of slab recycling processes. In contrast, high-field strength elements (HFSE, e.g. Nb, Ti, Zr) show depletion relative to elements of similar compatibility in arc lavas relative to MORB (McCulloch & Gamble, 1991; Arculus, 2004).

Another form of magmatic activity associated with subduction zones is back-arc magmatism (**Figure 1.3-1(5)**). The back arc is the region behind the volcanic arc seen from the viewpoint of the subduction zone and experiences significant extensional stress during subduction due oceanic trench rollback (Gill *et al.*, 1984; Parson & Wright, 1996; Taylor & Martinez, 2003; Pearce & Stern, 2006; Watanabe *et al.*, 2010). This extensional stress leads to rifting within the plate behind the volcanic arc, to ascent and decompression melting of mantle material at relatively shallow depth, and finally to the creation of a new spreading system in the back-arc. The composition of back-arc lavas is usually in transition between the enriched arc lava composition, especially in early stages of back-arc rifting, and the mid ocean ridge basalt composition, especially with further development of the

back-arc spreading system and further distance to the slab (Gill, 1976; Hawkins & Melchior, 1985; Taylor & Martinez, 2003). Oceanic convergent boundaries that comprise volcanic arcs and back-arc basins from the stages of rifting to spreading span a total length of around 17,500 km that corresponds to approximately one third of the global mid ocean ridge length (Bird, 2003).

High-temperature hydrothermal activity is a common phenomenon at volcanic arcs (submarine and subaerial) as well as at back-arc basins in different stages from rifting to spreading and significantly contribute to global hydrothermal discharge (Ishibashi & Urabe, 1995; de Ronde *et al.*, 2001; de Ronde & Stucker, 2015). Baker *et al.* (2008) estimated that hydrothermal flux at submarine arcs is equivalent to 10 % of the fluid discharge at mid-ocean ridges. The general processes of hydrothermal fluid circulation is very similar to mid-ocean ridge systems (details are given in **Chapter 1.2.1**) but is in addition frequently accompanied by phase separation (**Chapter 1.2.2**) and magma degassing (**Chapter 1.2.3**) processes due to the high volatile contents of magmas (e.g. CO<sub>2</sub>, H<sub>2</sub>O, SO<sub>2</sub>, H<sub>2</sub>S) and the shallow water depth at subduction zones. A study of a hydrothermal systems at the Tonga arc (Stoffers *et al.*, 2006) for example described an extreme form of fluid discharge by “flame-like jets” due to the intensified depressurization at the shallow water depth present there. It was assumed (de Ronde & Stucker, 2015, Baker *et al.*, 2008) that 70 % of the arc related hydrothermal sites are affected by phase separation and magma degassing processes, as well as a significant number of back-arc systems (e.g. Seewald *et al.*, 2019). Resulting, hydrothermal fluids at back-arc and arc settings show a tendency to especially low pH and high volatile contents, in which the signatures of back-arc fluids tend to equalize with mid-ocean ridge fluid signatures with increasing distance to the subducting slab (de Ronde & Stucker, 2015).

Rock alteration patterns in arc and back-arc settings are highly variable and can reach from green-schist to amphibolite-facies mineral assemblages (i.a. chlorite, illite, silica, sulfides) like they are typical in seawater dominated systems (**Chapter 1.2.1**), up to strongly leached advanced argillic alteration mineral assemblages (i.a. natroalunite, pyrophyllite) due to contribution of acid-sulfate fluids that are produced by the disproportionation of magmatic fluid derived sulfur gases (SO<sub>2</sub>, H<sub>2</sub>S) in contact with seawater (for details see **Chapter 1.2.3**). Hydrothermal systems at subduction zones are furthermore often associated with especially high-grade and Cu-Au-rich ore deposits that are assumed to be promoted by ascent of metal-rich magmatic fluids (Monecke *et al.*, 2014), similar to porphyry- and epithermal-type ore deposits on-land (e.g. Hedenquist & Lowenstern, 1994).

#### *1.3.3.1. Examples of seafloor hydrothermal systems influenced by subduction processes*

##### *Brothers arc volcano*

Brothers volcano is an active submarine caldera volcano of 3 to 3.5 km basal width at the southern intra-oceanic Kermadec Arc that is produced by subduction processes of the Pacific under the Australian Plate (**Figure 1.3-4A**). The caldera rim is hosted at 1320 to 1540 meters below sea-level

(mbsl), the base of the caldera at around 2200 mbsl and in the center of the caldera two neovolcanic cones arise; the more recently formed Upper Cone (crest at 1220 mbsl) that partly converges to the northeast with the earlier erupted Lower Cone (crest at 1340 mbsl; de Ronde *et al.*, 2011; Embley *et al.*, 2012, **Figure 1.3-4B**). The host rocks at all three sites (Caldera rim, Upper and Lower Cone) are dacitic lavas and volcanoclastic material, in which the caldera floor and the crests of the cone sites are buried under loads of talus.

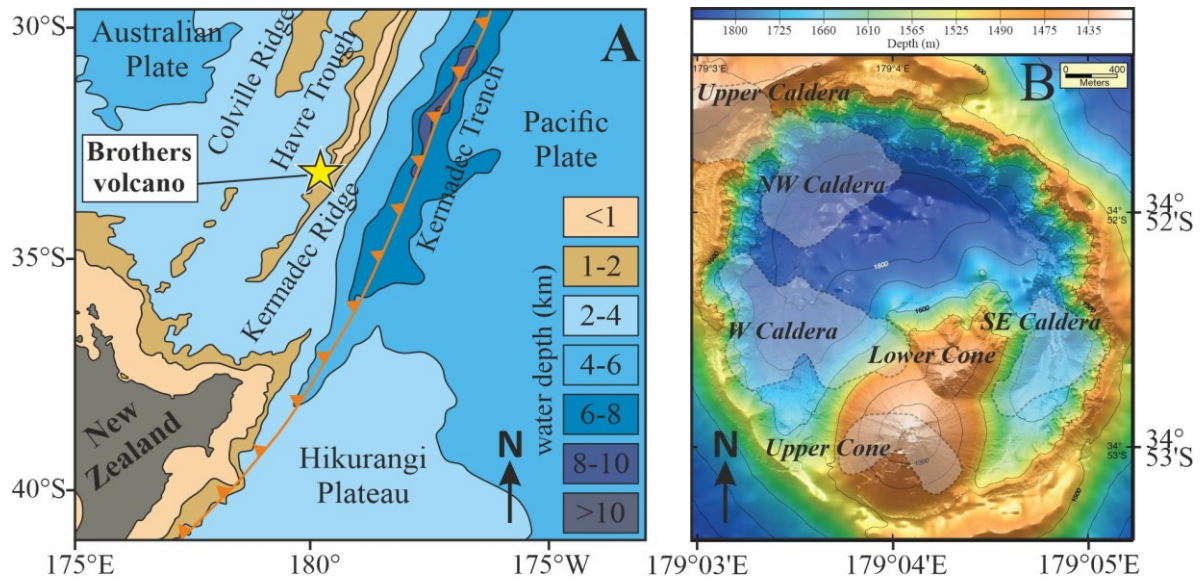


**Figure 1.3-4:** Geological setting of the Southern Kermadec Arc. (A) Location of Brothers volcano within the Southern Kermadec Arc, modified after Ballance *et al.* (1999). (B) Map of Brothers volcano taken from Embley *et al.* (2012) based on high-resolution (2m) autonomous underwater vehicle (AUV) data and a ship-derived bathymetry (25m resolution). The map is complemented by zones of low magnetization intensity (Caratori Tontini *et al.*, 2012) shown in light gray that are suggested to represent active or extinct high-temperature fluid up flow zones.

In total, the Kermadec arc hosts 34 volcanic structures and 26 of them show hydrothermal activity (de Ronde *et al.*, 2001; de Ronde *et al.*, 2003). Brothers volcano is the most hydrothermally active site within the southern Kermadec arc and exhibits five main locations of active fluid discharge (Upper Caldera, NW Caldera, W Caldera, Upper Cone, Lower Cone) and one site of extinct hydrothermal activity (SE Caldera) based on observed fluid discharge and/or sulfide deposits at the seafloor (de Ronde *et al.*, 2005; de Ronde *et al.*, 2011) and zones of low magnetization assumed to be produced by hydrothermal circulation (Caratori Tontini *et al.*, 2012). At the caldera rims, fluid re- and discharge occurs through ring fault systems developed at the slopes of the caldera rim, in contrast to the cone sites that show fluid discharge directly at the summits through loads of talus (de Ronde *et al.*, 2005).

The characteristics of the issuing fluids are highly contrasting although they are driven by the same magma source based on  $^3\text{He}/^4\text{He}$  fluid data (de Ronde *et al.*, 2011). The NW Caldera, W Caldera

and Upper Caldera (and most likely once also the SE Caldera) sites are dominated by seawater derived black-smoker-type fluids of moderate acidity (pH=3), high temperatures ( $\leq 320$  °C) and moderate volatile contents (13-40 mM), while at the Upper and Lower Cone the influence of magmatic fluids enhances formation of hydrothermal fluids that have a milky color, are highly acidic (down to pH=1.8) and volatile rich ( $\text{CO}_2 \leq 206$  mM) but show lower temperatures ( $\leq 120$  °C; Massoth *et al.*, 2003; de Ronde *et al.*, 2005; de Ronde *et al.*, 2011; de Ronde *et al.*, 2019b; McDermott *et al.*, 2019). Seawater-derived fluid dominated vent sites develop Cu-Zn-Au-rich chimneys, in contrast to sites of magmatic fluid contribution that show formation of smaller mounds ( $\leq 0.5$ m) and chimneys of native sulfur and massive Fe-oxyhydroxide crusts (de Ronde *et al.*, 2011).

Similarly, also host rock alteration characteristics strongly differ, inferred from altered rock mineral assemblages of surfaces rock samples (de Ronde *et al.*, 2005) and from drill-core rock samples at the NW Caldera, Upper Cone and Lower Cone site that were taken during IODP Expedition 376 from March to July 2018 (de Ronde *et al.*, 2019a; de Ronde *et al.*, 2019b). The seawater controlled rock alteration at the caldera shows a typical green-schist facies secondary mineral assemblage of mainly chlorite, illite, silica polymorphes and sulfides indicative for high-temperature alteration ( $\leq 250$  °C), partly overprinted by low-temperature ( $< 150$  °C) alteration minerals, like smectites, Fe-oxyhydroxides, and zeolites (cf. **Chapter 1.2.1**). The magmatic fluid affected rocks at the cone sites are in contrast replaced by an advanced argillic mineral assemblage of mainly pyrophyllite, natroalunite, silica polymorphs, diaspora, zunyite, rutile, pyrite and native sulfur (cf. **Chapter 1.2.3**) that is in part intensively entangled with an illite dominated, probably seawater-derived alteration mineral assemblage. Indeed, drill-core rock samples showed that at deeper portions of the NW Caldera a magmatic fluid influenced alteration mineral assemblage occurs, similar to the Upper Cone site, that was interpreted to represent an earlier stage of volcanism and magmatic fluid ascent before caldera collapse (de Ronde *et al.*, 2005; de Ronde *et al.*, 2019b).

#### *Snowcap, Manus Back-Arc Basin*

The Manus Basin is a rapidly spreading (approximately 10 cm/year) back-arc basin within the Bismarck Sea close to Papua New Guinea that lies adjacent to two subduction zone systems (**Figure 1.3-5**); the nowadays extinct Manus Trench to the north that once produced the lavas of the New Ireland volcanic island arc, and the New Britain Trench to the south that shows active subduction of the Solomon plate beneath the New Britain island arc (Taylor, 1979; Martinez & Taylor, 1996). The switch in subduction geometry and initial formation of the now present Manus Back-arc spreading system occurred in the Oligocene because the Ontong Java Plateau started to move in direction of the Manus Trench (Martinez & Taylor, 1996).

The central part of the Manus spreading system is already further developed and in greater distance to the subducting slab and following characterized by basaltic lavas with highly comparable compositions to MORB (Sinton, 2003). In contrast, the eastern parts of the Manus Basin, the

southeastern rifts (SER), are still in an earlier stage of rifting and stronger influenced by recycling processes at the actively subducting plate margin. This is expressed in variable rock types (basalts over basaltic-andesites, andesites and dacites) and more arc-like signatures of the lavas at the SER (e.g. high abundance of LILE and Pb) compared to the central part of the BAB (Sinton, 2003; Park *et al.*, 2010).

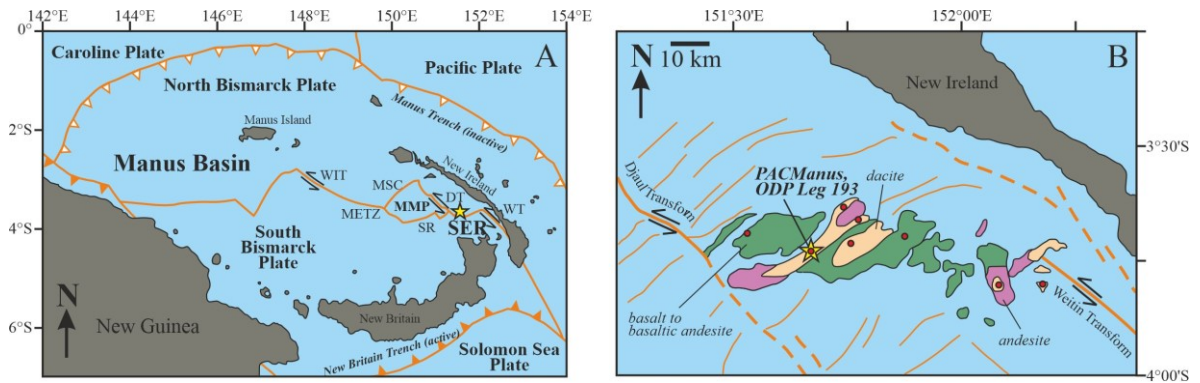


**Figure 1.3-5:** Geological setting of the Manus Basin. (A) Tectonic features of the basin, modified after Thal *et al.* (2014). The yellow star shows the position of ODP Leg 193, PACManus. (B) Rock types at Pual Ridge, sites of hydrothermal activity (red dots) and location of PACManus, modified after Shipboard Scientific Party (2002b). The thick orange lines represent plate boundaries. Lines complemented by open triangles symbolize inactive subduction, while closed triangles stand for active subduction. Thin orange lines in (B) show extensional faults. The parallel arrows represent the movement at transform faults (WIT=Willaumez Transform; METZ=Manus Extensional Transform Zone; DT=Djaul Transform; WT=Weitin Transform). MMP=Manus Microplate; MSC=Manus Spreading Center; SER=Southeast Ridges.

The Manus Back-arc basin shows widespread hydrothermal activity; at the central spreading center as well as within the SER. The hydrothermal fluids issuing from the central part show more MOR-like black-smoker-type signatures compared to a stronger arc influence of fluids at the SER, predominantly expressed by higher volatile contents and acidity than at the central part (Gamo *et al.*, 1997; Reeves *et al.*, 2011; Seewald *et al.*, 2015; Seewald *et al.*, 2019). Resulting, also the rocks show either a typical seawater dominated alteration signature (e.g. chlorite, illite) or advanced argillic alteration patterns (e.g. pyrophyllite, alunite, cf. **Chapter 1.2.3**). Fluid and melt inclusion studies conducted for dredged rocks of the SER indicated that the ascending magmatic fluids that caused the argillic alteration patterns are also capable to transport significant amounts of metals (Cu, Au, Zn, Pb, Ag) from the magma chamber towards shallower rock levels (Yang & Scott, 1996; Yang & Scott, 2002; Yang & Scott, 2006).

The vent site Snowcap (water depth of 1640 mbsl) is an example of an arc influenced hydrothermal system within the SER, regarding diffusively discharging fluid compositions (pH=3.4-5.0, CO<sub>2</sub>=102-112 mM, Reeves *et al.*, 2011) and fluid temperatures (180 °C at the surface but probably >300 °C within the basement; Shipboard Scientific Party, 2002a; Reeves *et al.*, 2011) and the argillic alteration patterns (in particular pyrophyllite and locally native sulfur, e.g. Lackschewitz *et*

*al.*, 2004; Paulick & Bach, 2006), intercalated with seawater dominated alteration mineral assemblages with depth (e.g. chlorite, illite). Snowcap is part of the Papua New Guinea-Australia-Canada-Manus (PACMANUS) hydrothermal field that has several active as well as inactive vent sites and is hosted at the crest of the elongated neovolcanic structure Pual Ridge (approximately 20 km long, 1-1.5 km wide and 500-600m above the surrounding seafloor), in the SER between the Djaul and the Weitin Transforms (Thal *et al.*, 2014, **Figure 1.3-5B**).

Pual Ridge consists of basaltic to dacitic volcanics, in which Snowcap is situated in unaltered to extensively altered dacitic lavas and volcanisclastic material (Paulick *et al.*, 2004; Thal *et al.*, 2014). In particular at the very top of Snowcap, a relatively unaltered dacitic lava cap occurs that is directly underlain by an alteration zone strongly affected by magmatic fluids. Following, it was suggested that the more coherent lava flow on top serves as permeability barrier that traps the magmatic fluids under its seal (Paulick & Bach, 2006). Paulick *et al.* (2004) suggested that at least three additional paleo-seafloor levels of more coherent lava flows exist in the basement of Snowcap based on facies reconstruction of drill-core material of ODP Leg 193. Paulick & Bach (2006) following interpreted that this former seafloor levels of more coherent lava flows also act as barriers for the upcoming magmatic fluids during past magmatic-hydrothermal activity and can explain the intercalation of magmatic fluid- and seawater-typical alteration mineral assemblages with depth that occur at Snowcap.

#### **1.4. Trace elements and their isotope signatures in seafloor hydrothermal systems**

##### **1.4.1. Boron and boron isotopes**

Boron is a fluid mobile element with a moderately volatile character and has two stable isotopes ( $^{11}\text{B}$  and  $^{10}\text{B}$ , with relative abundances of 80 and 20%) that fractionate in primarily dependence on temperatures, mineralogy and on the B coordination of interacting phases that is strongly controlled by pH in aqueous solutions. Further, natural reservoirs (e.g. seawater, oceanic and continental crust, as well as the mantle) span a wide range in B concentrations and  $\delta^{11}\text{B}$  compositions. Due to the high sensitivity of B and B isotopes for a variety of parameters that potential affect hydrothermal seawater-rock reactions and the diversity in compositions of exchanging reservoirs, B and B isotopes are useful proxies to investigate seafloor hydrothermal processes.

##### **1.4.1.1. Boron isotope determination techniques**

The determination of B isotopes is a challenging task, in particular in low B concentrated samples because of the sensitivity for contamination within the laboratory, the light mass of both isotopes and the potential isotopic fractionation during the purification procedures. Nevertheless, B purification and  $\delta^{11}\text{B}$  measuring techniques vastly developed over the two last decades and today a variety of different determination options are available, e.g. including positive and negative ion thermal ionization mass spectrometry (P- and N-TIMS; Ramakumar *et al.*, 1985; Zeininger &

Heumann, 1983), multi-collector inductively coupled plasma MS (MC-ICP-MS; e.g. Walder & Freedman, 1992; Aggarwal *et al.*, 2003), and also in-situ determination techniques by secondary-ion MS (SIMS; Straub & Layne, 2002) or laser ablation ICP-MS (LA-ICP-MS; Lécuyer *et al.*, 2002).

Within the frame of this thesis,  $\delta^{11}\text{B}$  compositions were determined for hydrothermal solutions and different silicate phases at the Isotope Geochemistry Laboratory at the Center for Marine Environmental Sciences (MARUM), University of Bremen. Purification of B from silicates was performed by alkali fusion ( $\text{K}_2\text{CO}_3$  as fusion agent), followed by a two-step column exchange procedure (Amberlit IRA 743 and AG-50W-X8) and the addition of mannitol for complexation, adapted after Romer *et al.* (2014) that was already modified after Tonarini *et al.* (1997) and Kasemann *et al.* (2001), see **Appendix A.2.1**. Fluid samples were either purified by performing only the cation exchange step (AG-50W-X8) adapted after Romer *et al.* (2014) or by a sublimation technique following Wang *et al.* (2010). Measurements of  $\delta^{11}\text{B}$  compositions were performed by a Thermo-Fisher Scientific Neptune Plus MC-ICP-MS in the standard-sample-standard bracketing mode with NIST SRM 951 (Catanzaro *et al.*, 1970) as standard solution (usually 50 ppb). More detailed descriptions of the procedures are given in the respective manuscript chapters (**Thesis Chapter 3, 4, and 5**).

The B isotopic values are expressed in the conventional delta-notation:

$$\delta^{11}\text{B} (\text{‰}) = \left( \frac{{}^{11}\text{B}/{}^{10}\text{B}_{\text{sample}}}{{}^{11}\text{B}/{}^{10}\text{B}_{\text{NIST SRM 951}}} - 1 \right) \times 1000 \quad (\text{Eq.1.4-1})$$

The long-term reproducibility of NIST SRM 951 was  $-0.1 \pm 0.2 \text{ ‰}$  ( $2\text{sd}_{\text{mean}}$ ,  $n=8$ ). The basaltic reference materials showed B contents and  $\delta^{11}\text{B}$  values of: BHVO-2 ( $2.36 \pm 0.02 \text{ } \mu\text{g/g}$ ;  $-2.8 \pm 0.3 \text{ ‰}$ ,  $2\text{sd}$ ,  $n=1$ ) and IAEA-B5 ( $8.73 \pm 2.48 \text{ } \mu\text{g/g}$ ;  $-4.1 \pm 0.7 \text{ ‰}$ ,  $2\text{sd}_{\text{mean}}$ ,  $n=5$ ), the granitic reference material IAEA-GM ( $4.81 \pm 0.29 \text{ } \mu\text{g/g}$ ;  $0.0 \pm 0.6 \text{ ‰}$ ,  $2\text{sd}_{\text{mean}}$ ,  $n=4$ ) and a laboratory internal pacific bottom seawater standard ( $4.97 \pm 0.30 \text{ } \mu\text{g/g}$ ;  $+39.7 \pm 0.1 \text{ ‰}$ ,  $2\text{sd}_{\text{mean}}$ ,  $n=4$ ). A compilation of the B and  $\delta^{11}\text{B}$  compositions of the standard solutions and the reference materials is given in the **Appendix A.2**.

#### 1.4.1.2. Boron distribution and isotopic fractionation systematics

Boron distribution between solid and fluid phases is in first order controlled by the reaction temperatures and the mineralogy of the initial and newly formed solid phases. The reaction of fluids with mafic (e.g. basalts) or felsic (e.g. dacites) rocks under increased temperatures ( $\geq 150 \text{ } ^\circ\text{C}$ ) leads to partitioning of B towards the fluid phase and B loss from the solid phase (e.g. Ishikawa & Nakamura, 1992) that is typically replaced by clay minerals (e.g. chlorite, illite), silica polymorphs (e.g. quartz) and sulfides (e.g. pyrite). In contrast, reaction with mafic or felsic rocks at lower temperatures ( $< 150 \text{ } ^\circ\text{C}$ ) results in partitioning of B towards the solid phase, especially incorporated into the lattice or adsorbed onto the charged mineral surfaces of the newly formed clay minerals (e.g. Mg-smectites and K-rich clay minerals, Donnelly *et al.*, 1979; Spivack & Edmond, 1987,

Smith *et al.*, 1995), potentially also taken up by zeolites (e.g. Yamaoka *et al.*, 2015b) or adsorbed to the charged surfaces of Fe-oxyhydroxides and oxides (e.g. Goldberg *et al.*, 1993; Lemarchand *et al.*, 2007).

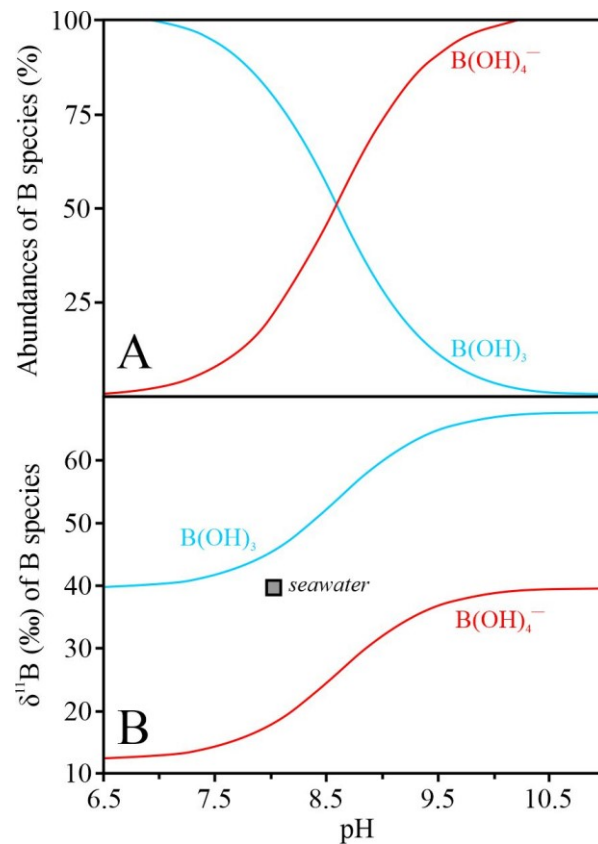


**Figure 1.4-1:** Boron and  $\delta^{11}B$  composition of seawater in dependence on pH, modified after Foster *et al.* (2016). (A) Abundances of  $B^{[3]}$  species (here solely  $B(OH)_3$ ) and  $B^{[4]}$  species (here solely  $B(OH)_4^-$ ) ( $T=25$  °C;  $P=1$  atm; salinity=35 psu), and (B)  $\delta^{11}B$  composition of B species in seawater with changing pH. In addition, the composition of modern ocean seawater is shown (Foster *et al.*, 2010).

In contrast, the alteration of ultramafic mantle rocks by serpentinization occurs over a wide temperature range (typically 50-350 °C, McCollom & Bach, 2009) and results even at elevated temperatures (300 °C) in an uptake of B by the solid phase due to the high B uptake preference of the alteration dominating clay mineral phase serpentine (Foustoukos *et al.*, 2008, and references therein; Hansen *et al.*, 2017). The serpentinization of ultramafic rocks also leads to an increase in fluid pH because  $H^+$  ions are consumed during reaction. An important effect for B systematics with increasing fluid pH is an accompanied increase in the abundance of tetrahedral coordinated B species ( $B^{[4]}$ ) relative to the trigonal coordinated B species ( $B^{[3]}$ ) in aqueous solution (**Figure 1.4-1A**; seawater contains around 80%  $B^{[3]}$  versus 20%  $B^{[4]}$  species), while clay minerals (e.g. serpentine) always host solely the  $B^{[4]}$  species (e.g. Palmer *et al.*, 1987). Foustoukos *et al.* (2008) assumed that an increase in  $B^{[4]}$  species in solution due to increasing fluid pH leads to a preferred uptake of B from the equally  $B^{[4]}$  coordinated serpentine based on experimental results of Seyfried & Dibble (1980), Janecky (1982), Janecky & Seyfried (1986). Indeed, the supposed dependence

could not be confirmed based on ultramafic batch reaction experiments that were conducted in the framework of this thesis (*Thesis Chapter 3*) and by Hansen *et al.* (2017); instead a strong temperature dependent relation was indicated.

Nevertheless, it is well-established that the B speciation and the exchange of different B species in rocks and fluids is crucial for B isotopic fractionation (e.g. Kakihana *et al.*, 1977; Spivack & Edmond, 1987; Palmer *et al.*, 1987). The fundamental B isotopic exchange reaction between main B<sup>[3]</sup> species B(OH)<sub>3(aq)</sub> and the main B<sup>[4]</sup> species B(OH)<sub>4</sub><sup>-</sup> can be expressed as follows:



The preference of the heavier <sup>11</sup>B isotope for the stronger inter-atomic bonds of the B<sup>[3]</sup> species leads to a passive enrichment of <sup>10</sup>B in the B<sup>[4]</sup> species and to significant isotopic fractionation between the interacting phases (*Figure 1.4-1B*, e.g. Kakihana *et al.*, 1977; Palmer *et al.*, 1987; Spivack & Edmond, 1987). Boron isotope exchange experiments between various B<sup>[4]</sup> coordinated solid phases (e.g. smectites, boromuscovite, melts) and B<sup>[3]</sup>-bearing fluids point to a linear relation of decreasing B isotopic fractionation with increasing temperatures that seems to be largely independent from the specific type of solid phase and only regards the abundant B species (Palmer *et al.*, 1987; Williams *et al.*, 2001; Hervig *et al.*, 2002; Wunder *et al.*, 2005). In contrast, experiments that were conducted for mineral phases that are B<sup>[3]</sup> coordinate (e.g. tourmaline; Palmer *et al.*, 1992; Meyer *et al.*, 2008; Marschall *et al.*, 2009) and experiments that were performed under higher pH conditions (pH>8) and resulting contained B<sup>[3]</sup> and B<sup>[4]</sup> in the fluid phase (Wunder *et al.*, 2005; Hansen *et al.*, 2017; *Thesis Chapter 3*) showed significantly deviating trends, also in agreement with ab-initio calculations (Kowalski *et al.*, 2013). Indeed, in NaCl-bearing saline aqueous solutions (like seawater), also additional B species like NaB(OH)<sub>4(aq)</sub> and B(OH)<sub>3</sub>Cl<sup>-</sup> can form (e.g. Pokrovski *et al.*, 1995; Akinfiyev *et al.*, 2006; Foustoukos *et al.*, 2008). The specific impact of additional B species in saline solutions on B isotopic fractionation are still poorly understood but Hansen *et al.* (2017) suggested that they may be significant for fluid-rock B isotopic exchange reactions.

Furthermore, B and B isotopes not only partition between fluids and solids but also are potentially affected by phase separation processes (*Chapter 1.2.2*) due to the moderately volatile character of B. Phase separation leads to the separation of a fluid in a high-density brine phase and a low-density vapor phase. Experiments showed that boron prefers to partition towards the low-salinity vapor phase, especially if halite stability is reached in the co-existing brine phase (Foustoukos & Seyfried, 2007b). Some previous experiments (Berndt & Seyfried, 1990; Liebscher *et al.*, 2005) estimated more variable B partitioning directions and even a more pronounced partitioning of B towards the brine phase but Foustoukos & Seyfried (2007b) and (Foustoukos & Seyfried, 2007a) concluded that

this effects resulted from exceptional low bulk Cl concentrations. Boron isotopic fractionation between vapor and brine phase seems to be minimal based on experimental data (Spivack *et al.*, 1990; Liebscher *et al.*, 2005). The authors supposed this is potentially caused by same dominance of B<sup>[3]</sup> species in vapor as well as brine phase.

#### 1.4.1.3. Boron and boron isotopes in natural reservoirs

The B and  $\delta^{11}\text{B}$  composition of natural materials spans a wide range from -50 to +60 ‰ (Barth, 1993), and also the B and  $\delta^{11}\text{B}$  composition of reservoirs related to hydrothermal circulation is highly diverse as recently highlighted in a comprehensive review by Marschall (2018) and illustrated in **Figure 1.4-2**.

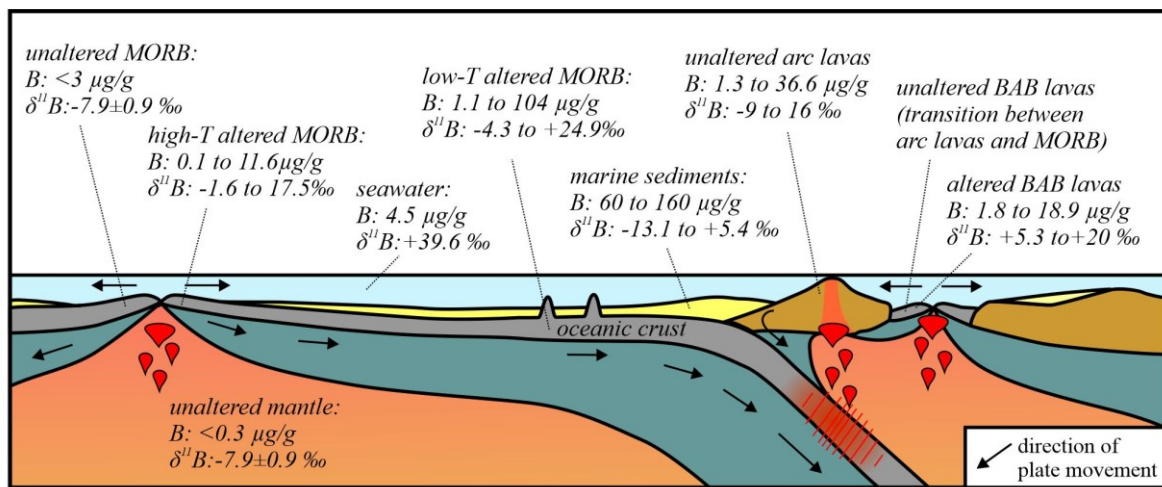


**Figure 1.4-2:** Boron and  $\delta^{11}\text{B}$  compositions of natural reservoirs. References: unaltered mantle (Chaussidon & Libourel, 1993; Leeman & Sisson, 1996; Marschall *et al.*, 2017); unaltered MORB (Spivack & Edmond, 1987; Marschall *et al.*, 2017); altered MORB (Spivack & Edmond, 1987; Ishikawa & Nakamura, 1992; Smith *et al.*, 1995; Yamaoka *et al.*, 2012; Yamaoka *et al.*, 2015b); unaltered arc lavas (De Hoog & Savoy, 2018); unaltered back-arc basin lavas (Chaussidon & Jambon, 1994; Ishikawa & Nakamura, 1994; Wilckens *et al.*, 2018); altered BAB lavas (Wilckens *et al.*, 2018); marine sediments (Spivack & Edmond, 1987; Ishikawa & Nakamura, 1993; Tonarini *et al.*, 2011); seawater (Spivack & Edmond, 1987; Foster *et al.*, 2010).

Modern open oceans show a globally uniform B concentration (4.5  $\mu\text{g/g}$ ) and  $\delta^{11}\text{B}$  composition (+39.6; Spivack & Edmond, 1987; Foster *et al.*, 2010) due to the long residence time of B in seawater ( $10^7$  years, Lemarchand *et al.*, 2002) compared to global ocean mixing times ( $10^3$  years). In contrast, the unaltered basaltic crust that forms at mid-ocean ridges displays relatively low B contents (<3  $\mu\text{g/g}$ ) and  $\delta^{11}\text{B}$  values compared to seawater ( $\delta^{11}\text{B}$  range from -12 to 0 ‰; e.g. Spivack & Edmond, 1987; Chaussidon & Jambon, 1994; Roy-Barman *et al.*, 1998; Marschall *et al.*, 2017), in which especially the higher measured MORB  $\delta^{11}\text{B}$  values most likely reflect contamination by seawater-rock interactions. Marschall *et al.* (2017) investigated a large data set of 56 basaltic glass samples from the Mid-Atlantic Ridge, East Pacific Rise and Southwest Indian Ridge, including a careful consideration of potential overprint by fluid-rock reactions and concluded that the global

average MORB  $\delta^{11}\text{B}$  composition is  $-7.1 \pm 0.9$  ‰, indistinguishable at all investigated ridge segments. The mantle shows even lower B contents ( $<0.3$   $\mu\text{g/g}$ , Chaussidon & Libourel, 1993; Leeman & Sisson, 1996) than MORB due to the high incompatibility of B during partial mantle melting. It is generally estimated that the  $\delta^{11}\text{B}$  composition of the mantle equals MORB composition ( $-7.1 \pm 0.9$ ‰) because B isotopic fractionation is negligible at magmatic temperatures (Chaussidon & Jambon, 1994; Chaussidon & Marty, 1995; Marschall *et al.*, 2017). Direct measurement of B and  $\delta^{11}\text{B}$  values of the mantle was not achieved so far due to the difficulties to determine the very low B contents and the sensitivity of the low B concentrated mantle rocks for contamination by fluid-rock interactions.

Volcanic arc lavas usually show significantly higher B concentrations (on average 12  $\mu\text{g/g}$ , in range from 1.3 to 36.6  $\mu\text{g/g}$ ) and  $\delta^{11}\text{B}$  values (on average  $+4.1 \pm 6.2$  ‰, in a range from -9 to +16 ‰) than mantle and MORB rocks, compiled by De Hoog & Savov (2018) based on a comprehensive collection of published data sets by various authors (see publication for details) of in total 75 selected rock samples (only data of  $\text{MgO} > 4\text{wt.}\%$ ). The B and  $\delta^{11}\text{B}$  composition of BAB lavas lies commonly between the enriched arc-like signatures and converges to more MORB-like signatures with greater distance to the subducting slab in later stages of rifting and spreading (e.g. Chaussidon & Jambon, 1994; Ishikawa & Nakamura, 1994; Wilckens *et al.*, 2018). The enriched B and  $\delta^{11}\text{B}$  values of arc and immature BAB lavas originate from dehydration processes of the subducting slab that carries a highly enriched B and  $\delta^{11}\text{B}$  signature and contributes to melting processes at convergent plate boundaries.

The high B values of the aged oceanic crust and also of the sediments that are subducted at convergent margins result from uptake of B by low-temperature alteration of the basaltic oceanic crust (1 to 104  $\mu\text{g/g}$ ; e.g. Spivack & Edmond, 1987; Smith *et al.*, 1995) and adsorption of B to marine clay minerals (typically 60 to 160  $\mu\text{g/g}$ ; e.g. Spivack & Edmond, 1987; Ishikawa & Nakamura, 1993), for example prominent in ridge flank hydrothermal systems (**Chapter 1.3.2**). Furthermore, altered ultramafic lithologies that are also subducted at convergent margins often show highly enriched B concentrations (up to 91  $\mu\text{g/g}$ ; e.g. Thompson & Melson, 1970; Spivack & Edmond, 1987; Boschi *et al.*, 2008; Vils *et al.*, 2009) that can be produced by low- and high-temperature alteration (**Chapter 1.4.1.2**). Although, additional Si-metasomatism associated with a talc-tremolite mineral assemblage can also lead to a release of B from altered ultramafic rocks (e.g. Boschi *et al.*, 2008; Harvey *et al.*, 2014). The high  $\delta^{11}\text{B}$  values of altered basaltic (range from -4.3 to +24.9 ‰; Spivack & Edmond, 1987; Ishikawa & Nakamura, 1992; Smith *et al.*, 1995; Yamaoka *et al.*, 2012; Yamaoka *et al.*, 2015a) and ultramafic rocks (mainly in a range from +8 to +20 ‰; e.g. Spivack & Edmond, 1987; Boschi *et al.*, 2008; Harvey *et al.*, 2014), and marine sediments (main range from -13.1 to +5.4 ‰; Spivack & Edmond, 1987; Ishikawa & Nakamura, 1993; Tonarini *et al.*, 2011) can be produced by low- and high-temperature hydrothermal alteration due to interaction

with seawater-derived fluids of high  $\delta^{11}\text{B}$  composition. Altered dacitic lavas from subduction influenced settings in the Western Pacific of already initially high B (1.2 to 28.9  $\mu\text{g/g}$ ) and  $\delta^{11}\text{B}$  values (-0.5 to +9.0 ‰) showed B concentrations up to 18.9  $\mu\text{g/g}$  and  $\delta^{11}\text{B}$  values up to +20 ‰ (Wilckens *et al.*, 2018). In general, high-temperature hydrothermal fluid-rock interaction tends to produce higher  $\delta^{11}\text{B}$  signatures in altered rocks than low-temperature alteration because the reduced B isotopic fractionation at higher temperatures results in a less fractionated and originally high  $\delta^{11}\text{B}$  seawater signature (+39.6 ‰) that is adopted by the newly formed alteration mineral phases.

High-temperature fluids issuing from mafic or felsic hosted hydrothermal systems at MOR, arc or back-arc settings are enriched in B compared to seawater (or show similar values) due to the leaching of B from the host rocks by fluid-rock interaction at elevated temperatures (>150 °C, e.g. Spivack & Edmond, 1987; James *et al.*, 1995; Kleint *et al.*, 2019; Wilckens *et al.*, 2018). High-temperature fluids collected from ultramafic hosted systems in comparison show depletion in B versus seawater because of the B uptake preference of alteration phases (serpentine) even at elevated temperatures (at least 300 °C; e.g. Schmidt *et al.*, 2007; Foustoukos *et al.*, 2008; Seyfried *et al.*, 2011; Tao *et al.*, 2020). The  $\delta^{11}\text{B}$  signature of high-temperature fluids in all settings is depleted compared to seawater due to low the initial  $\delta^{11}\text{B}$  values of the interacting oceanic crust and mantle lithologies relative to seawater, most distinct in arc and back-arc settings because of additionally also relatively high B contents of the primary lavas (e.g. Spivack & Edmond, 1987; James *et al.*, 1995; Yamaoka *et al.*, 2015a; Wilckens *et al.*, 2018). In arc and back-arc settings it was furthermore suggested that phase separation and magma degassing processes may shift the B and B isotopic systematics of fluids (Wilckens *et al.*, 2018), comparable to processes at fumaroles and thermal springs (e.g. Leeman *et al.*, 2005; Foustoukos & Seyfried, 2007a; Zhao *et al.*, 2019).

Another location of fluid discharge at the seafloor impacting B and  $\delta^{11}\text{B}$  seawater composition is the expulsion of fluids at the fore-arc of subduction zones due to early diagenetic processes within the accretionary prism (e.g. Kastner *et al.*, 1991). The expelled fluids in the fore-arc region have highly variable B and  $\delta^{11}\text{B}$  patterns but show a tendency to relatively high B concentrations (up to 5,000  $\mu\text{M}$ ) and  $\delta^{11}\text{B}$  values (+24  $\pm$  5‰) based on observations of interstitial pore fluids, mud volcanoes and seafloor seeps in various locations (e.g. Kastner *et al.*, 2014; Saffer & Kopf, 2016).

Summarized, high- and low-temperature hydrothermal processes have major implications for B and  $\delta^{11}\text{B}$  systematics of seawater and altered oceanic crust as well as for volcanic and fluid expulsion processes at convergent plate boundaries, and once the altered crust is subducted may also impact the composition of the mantle.

#### 1.4.2. Lithium and lithium isotopes

Lithium is a highly fluid mobile element and has two stable isotopes,  ${}^7\text{Li}$  (92.4%) and  ${}^6\text{Li}$  (7.6 %), that show a mass dependent isotopic fractionation between solids and fluids that is mainly

influenced by variations in temperature and mineralogy. Lithium and  $\delta^7\text{Li}$  systematics are useful proxies for hydrothermal processes due to the sensitivity for changing alteration conditions and also because of the large range in composition of natural reservoirs related to seafloor hydrothermal processes (Chan & Edmond, 1988). Recent reviews on these Li and  $\delta^7\text{Li}$  systematics were given by Penniston-Dorland *et al.* (2017) and Tomascak *et al.* (2016a).

#### 1.4.2.1. Lithium isotope determination techniques

Similar to  $\delta^{11}\text{B}$  systematics, the interest in  $\delta^7\text{Li}$  signatures as a proxy for a variety of Earth processes drastically increased with further development of more efficient purification (mainly by cation exchange chromatography) and higher resolution measuring techniques (including MC-ICP-MS, TIMS and SIMS) over the last decades (reviewed by Tomascak *et al.*, 2016b).

Lithium isotopic measurements related to this thesis were performed on hydrothermal solutions and silicate phases at the Isotope Geochemistry Laboratory at MARUM, University of Bremen. Silicates were dissolved in minimum five consecutive steps to bring all components into solution by adding: a HF-HNO<sub>3</sub> mixture (5:1), a concentrated HCl-HNO<sub>3</sub> mixture (2:1), a HNO<sub>3</sub>-H<sub>2</sub>O<sub>2</sub> mixture (2:1) to remove potential organic components, 2.5M HNO<sub>3</sub> and finally 4N HCl for chloride conversion to avoid matrix effects during purification by column separation (based on 0.15M HCl). Lithium purification prior to measuring of dissolved silicates and hydrothermal fluid samples was reached by two consecutive column separation steps (both based on cation exchange resin AG-50W-X8), modified after Moriguti & Nakamura (1998), see *Appendix A.2.1*. Measurements of  $\delta^7\text{Li}$  compositions were performed by a Thermo-Fisher Scientific Neptune Plus MC-ICP-MS in the standard-sample-standard bracketing mode with NIST RM 8545 (L-SVEC, Flesch *et al.*, 1973) as standard solution (usually 25 ppb). More detailed descriptions of the procedures are given in the respective manuscript chapters (*Thesis Chapter 4 and 5*).

The Li isotopic values are expressed in the conventional delta-notation:

$$\delta^7\text{Li} (\text{‰}) = \left( \frac{{}^7\text{Li}/{}^6\text{Li}_{\text{sample}}}{{}^7\text{Li}/{}^6\text{Li}_{\text{L-SVEC}}} - 1 \right) \times 1000 \quad (\text{Eq.1.4-3})$$

The long-term reproducibility of NIST RM 8545 was  $-0.2 \pm 0.2 \text{ ‰}$  ( $2\text{sd}_{\text{mean}}$ ,  $n=7$ ). The basaltic reference materials showed Li contents and  $\delta^7\text{Li}$  values of: BHVO-2 ( $4.39 \pm 0.00 \text{ ‰}$ ;  $+4.3 \pm 0.2 \text{ ‰}$ ,  $2\text{sd}_{\text{mean}}$ ,  $n=2$ ) and IAEA-B5 ( $8.12 \pm 0.19 \text{ ‰}$ ;  $+4.5 \pm 1.1 \text{ ‰}$ ,  $2\text{sd}_{\text{mean}}$ ,  $n=3$ ), the granitic reference material IAEA-GM ( $45.57 \pm 0.82 \text{ ‰}$ ;  $-0.7 \pm 0.1 \text{ ‰}$ ,  $2\text{sd}$ ,  $n=1$ ) and a laboratory internal Pacific bottom seawater standard ( $0.18 \pm 0.01 \text{ ‰}$ ;  $+30.9 \pm 0.7 \text{ ‰}$ ,  $2\text{sd}_{\text{mean}}$ ,  $n=2$ ). A compilation of the Li and  $\delta^7\text{Li}$  compositions of the standard solutions and the reference materials is given in the *Appendix A.2*.

#### 1.4.2.2. Lithium distribution and isotopic fractionation systematics

Lithium preferentially substitutes for Mg in octahedral coordination due to the similarity in ionic radius of  $\text{Li}^+$  (0.76 Å) and  $\text{Mg}^{2+}$  (0.72 Å) and therefore shows often exchange with Mg-rich silicate phases in six-fold, octahedral coordination (Shannon, 1976; Vigier *et al.*, 2008); in seafloor hydrothermal systems in particular with Mg-rich clay minerals. In aqueous solutions, Li forms four-fold hydration shells with  $\text{H}_2\text{O}$  in tetrahedral coordination ( $[\text{Li}(\text{H}_2\text{O})_4]^+$ ; Lyubartsev *et al.*, 2001; Yamaji *et al.*, 2001), at least within the temperature range that is relevant for seafloor hydrothermal systems (2 to 450 °C). Beside mineralogical preferences, also temperature conditions strongly influence the extent and the direction of Li partitioning during fluid-rock interactions. Thus, the alteration of oceanic crust and mantle material at low-temperatures (<150°C) leads to partitioning of Li towards the newly formed solid phases (e.g. Mg-smectites, serpentine), while at higher-temperatures (>150°C) Li favors partitioning towards the fluid phase (e.g. Seyfried *et al.*, 1984; Chan *et al.*, 1992; Seyfried *et al.*, 1998; Brenan *et al.*, 1998b; Chan *et al.*, 2002; Decitre *et al.*, 2002; Caciagli *et al.*, 2011; Hansen *et al.*, 2017). Furthermore, Li has a moderately incompatible character during melting processes in most igneous systems (e.g. Brenan *et al.*, 1998a).

Lithium isotopic fractionation between solid and fluid phases strongly depends on the Li bonding environment of the interacting phases and the reaction temperatures. Regarding the bonding environment, mineral phases that host Li in lower coordination have higher bond energies compared to phases of higher coordination (Wunder *et al.*, 2011). Furthermore, the heavier  $^7\text{Li}$  isotope favors partitioning towards the phase of stronger bonding, resulting in a passive enrichment of the lighter  $^6\text{Li}$  isotope in the corresponding phase (Schauble, 2004). In case of seafloor hydrothermal systems this is commonly expressed in fractionation of  $^7\text{Li}$  towards the fluid phase (in tetrahedral coordination) and passive enrichment of  $^6\text{Li}$  in the solid phase (mainly in octahedral coordination). The linear temperature dependence that is expressed by an increase in Li isotopic fractionation with decreasing temperatures during solid-fluid exchange was shown in a number of experimental studies at various temperatures and by using different solid phases (e.g. Williams & Hervig, 2005; Vigier *et al.*, 2008; Millot *et al.*, 2010; Hindshaw *et al.*, 2019; Pogge von Strandmann *et al.*, 2019) as well as was suggested based on theoretical predictions (e.g. Kowalski & Jahn, 2011; Dupuis *et al.*, 2017). Indeed, recently published experimental data by Hindshaw *et al.* (2019) suggested that the abundance of other dissolved components (e.g. Mg and Na) may significantly affect Li isotopic fractionation, at least at the low temperatures (25 °C) that were chosen for their experiments.

#### 1.4.2.3. Lithium and lithium isotopes in natural reservoirs

Seawater has a globally uniform Li (0.18 µg/g) and  $\delta^7\text{Li}$  composition (on average +31‰ ± 0.1 ‰, Millot *et al.*, 2004) due to the long residence time of Li in seawater ( $10^6$  years, Huh *et al.*, 1998) versus ocean mixing times ( $10^3$  years, **Figure 1.4-3**). In comparison to seawater, the unaltered upper mantle shows relatively high Li contents ( $\leq 2$  µg/g; e.g. Ryan & Langmuir, 1987; Marschall *et al.*,

2017) and the Li contents of mantle derived MORB are typically even higher (4 to 8  $\mu\text{g/g}$ , e.g. Chan *et al.*, 1992). The  $\delta^7\text{Li}$  composition of the upper mantle ( $+3.5 \pm 1.0$  ‰; Magna *et al.*, 2008; Pogge von Strandmann *et al.*, 2011; Lai *et al.*, 2015) and MORB ( $+3$  to  $5$  ‰, Chan *et al.*, 1992; Nishio *et al.*, 2007; Tomascak *et al.*, 2008; Marschall *et al.*, 2017) is in contrast significantly lower than seawater. Consequently, fluid-rock interaction in seafloor hydrothermal systems leads to vast shifts in fluid and altered rock Li and  $\delta^7\text{Li}$  compositions, in which the signatures represent a mixture of Li that was derived from the host rock mineral phases and seawater derived Li.

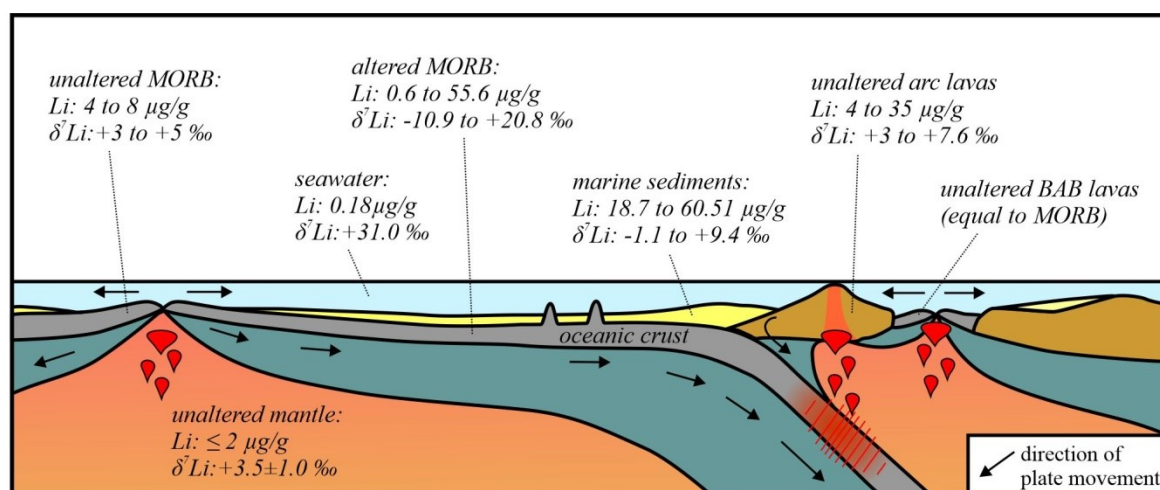


**Figure 1.4-3:** Lithium and  $\delta^7\text{Li}$  compositions of natural reservoirs. References: unaltered mantle (Ryan & Langmuir, 1987; Magna *et al.*, 2008; Pogge von Strandmann *et al.*, 2011; Lai *et al.*, 2015; Marschall *et al.*, 2017); unaltered MORB (Chan *et al.*, 1992; Nishio *et al.*, 2007; Tomascak *et al.*, 2008); altered MORB (Chan *et al.*, 1992; Chan *et al.*, 2002; Brant *et al.*, 2012; Gao *et al.*, 2012; Marschall *et al.*, 2017); unaltered arc lavas (Moriguti & Nakamura, 1998; Tomascak *et al.*, 2002; Moriguti *et al.*, 2004; Magna *et al.*, 2006); marine sediments (Plank, 2014); seawater (Millot *et al.*, 2004).

Low-temperature ( $<150$  °C) altered oceanic crust and mantle rocks are enriched in Li compared to unaltered material due to the preferred partitioning of Li towards the solid phase at low-temperatures (**Chapter 1.4.2.2**). Low-temperature altered MORB recovered from the seafloor showed Li contents in a range from 5.6 to 55.6  $\mu\text{g/g}$  (Chan *et al.*, 1992; Chan *et al.*, 2002) and low-temperature altered basalts collected from four former ridge flank settings of the Troodos Ophiolite had values even up to 118.8  $\mu\text{g/g}$  (Coogan *et al.*, 2017). In contrast, high-temperature ( $>150$  °C) alteration leads to removal of Li from the host rocks due to the fluid mobile character of Li, even if the alteration extents appears only minor (Brant *et al.*, 2012). High-temperature altered rocks from the sheeted dyke complex of ODP Site 504B near the Costa Rica Rift showed Li contents as low as 0.6  $\mu\text{g/g}$  (Chan *et al.*, 2002). The  $\delta^7\text{Li}$  composition of low- and high-temperature altered basalts is highly variable in a range from  $-10.9$  to  $+20.8$  ‰ (Chan *et al.*, 1992; Chan *et al.*, 2002; Brant *et al.*, 2012; Gao *et al.*, 2012; Coogan *et al.*, 2017). High-temperature hydrothermal fluids show higher Li concentrations (2.8 to 9.1  $\mu\text{g/g}$ ; Von Damm, 1990) and lower  $\delta^7\text{Li}$  values ( $+3$  to  $+11$  ‰; Chan *et al.*,

1993; Chan *et al.*, 1994; Foustoukos *et al.*, 2004) compared to seawater due to mobilization of Li from oceanic crust that have comparable low  $\delta^7\text{Li}$  compositions.

In case of serpentinized mantle material the differentiation in low- and high-temperature altered rocks is more complicated than for basalts because a similar mineral assemblage is formed over a wide temperature range but serpentinites collected from the Mariana forearc and the Southwest Indian Ridge showed Li contents lower as well as higher (0.6 to 8.2  $\mu\text{g/g}$ ) and  $\delta^7\text{Li}$  values similar to or higher (+2.9 to +14.2 ‰) than unaltered mantle (Decitre *et al.*, 2002; Benton *et al.*, 2004). Indeed, serpentinites recovered during ODP 209 at the Mid-Atlantic Ridge showed more extreme Li concentrations of 0.07 to 1.13  $\mu\text{g/g}$  and  $\delta^7\text{Li}$  values of -28.4 to +7.17 ‰ that were suggested to result from interaction with a more evolved fluid that should have a  $\delta^7\text{Li}$  value of -2 to +12 ‰ that existence still needs to be proofed (Vils *et al.*, 2009).

Marine sediments can have very variable Li and  $\delta^7\text{Li}$  compositions. Plank (2014) published a comprehensive review on the composition of subducting sediments and based on this compiled data set of in total 29 subduction trench settings the bulk sedimentary input at convergent margins has a Li concentration in a range from 18.70 to 60.51  $\mu\text{g/g}$  and a  $\delta^7\text{Li}$  composition ranging from -1.1 to +9.4 ‰.

At convergent plate boundaries the oceanic crust, the mantle rocks and marine sediments that are most typical enriched in  $\delta^7\text{Li}$  due to diagenetic and alteration effects are subducted beneath an adjacent tectonic plate. In the fore-arc region, the compaction of the accretionary wedge in the early stage of subduction commonly leads to expulsion of fluids enriched in Li (on average 2  $\mu\text{g/g}$ ) and lowered in  $\delta^7\text{Li}$  (on average +18 ‰) compared to seawater (Benton *et al.*, 2004; Scholz *et al.*, 2010; Kastner *et al.*, 2014). This early stage is followed by prograde metamorphic dehydration of the slab with further subduction that potentially also impacts melt generation processes and arc lava composition at convergent margins (e.g. Zack *et al.*, 2003; Marschall *et al.*, 2007a; Marschall *et al.*, 2007b). For some arc lavas indeed an across arc variation towards high  $\delta^7\text{Li}$  values compared to MORB was found, for example at the Izu arc of up to +7.6 ‰ (Moriguti & Nakamura, 1998) and the southern Cascadia subduction zone of up to +6.4 ‰ (Magna *et al.*, 2006). In contrast, at other arc settings the  $\delta^7\text{Li}$  signatures of lavas are indistinguishable of MORB values and show no across arc variation (e.g. Tomascak *et al.*, 2002; Moriguti *et al.*, 2004). The reasons for this differing  $\delta^7\text{Li}$  systematics at arcs are still strongly debated. In the review by Tomascak *et al.* (2016a) a differentiated consideration of this issue was given and they concluded that potential reasons for the  $\delta^7\text{Li}$  discrepancies at different arcs could be variability in the sedimentary inputs, local similarities in  $\delta^7\text{Li}$  signatures of the subduction component and MORB, isotopic disequilibrium during slab dehydration due to kinetic processes or isotopic re-equilibration of the melt with further ascent. Unaltered lavas associated with back-arc basins in the southern Washington Cascades, (Leeman *et al.*, 2004), Lau basin (Brens *et al.*, 2019), and Manus basin (Wilckens *et al.*, 2019) showed

undistinguishable  $\delta^7\text{Li}$  values compared to unaltered MORB and point to minor impact of slab recycling processes on back-arc  $\delta^7\text{Li}$  systematics.

### 1.4.3. Strontium isotopes

The mass difference between the radiogenic isotope  $^{87}\text{Sr}$  (product of the radioactive decay of  $^{87}\text{Rb}$ , half-life period of  $4.88 \times 10^{10}$  years; Faure & Powell, 1972) and the stable isotope  $^{86}\text{Sr}$  is relatively small and results in a negligible mass depended isotope fractionation between the interacting phases. Instead, the  $^{87}\text{Sr}/^{86}\text{Sr}$  compositions of fluids and altered rocks in seafloor hydrothermal systems are controlled by the host rock and source fluid (mainly seawater) Sr isotopic composition.

The  $^{87}\text{Sr}/^{86}\text{Sr}$  ratio in global modern seawater is uniformly  $0.709175 \pm 0.000015$  (Scher *et al.*, 2014), in consistent with a steady-state Sr ocean residence time of  $10^6$  years (McArthur, 1994) versus  $10^3$  years of ocean mixing times. The Sr isotopic composition of unaltered MORB (0.7023 to 0.7033, Ito *et al.*, 1987; Rubín & Macdougall, 1992) is relatively low compared to seawater. Arc lavas show locally enriched Sr isotopic signatures compared to MORB in dependence on the  $^{87}\text{Sr}/^{86}\text{Sr}$  ratios of the subducted altered crust and sediments (e.g. Haase *et al.*, 2002) but nevertheless are still significantly lower than seawater. Following, typical  $^{87}\text{Sr}/^{86}\text{Sr}$  values of hydrothermal fluids (0.7037; Bach & Humphris, 1999) mimic the host rock values, while altered rocks show distinctly increased  $^{87}\text{Sr}/^{86}\text{Sr}$  ratios up to seawater-like compositions (e.g. Alt *et al.*, 1996; Gillis *et al.*, 2005; Vils *et al.*, 2009).

The Sr isotopic composition is furthermore influenced by the w/r-ratio during interaction and is a well-established proxy for w/r-ratio estimates in seafloor hydrothermal systems. The relation for closed-system conditions that is valid up to extreme high w/r-ratios can be described as follows (McCulloch *et al.*, 1980; Marks *et al.*, 2015):

$$w/r \approx \frac{C_{rock(i)}^{Sr} \cdot ((^{87}\text{Sr}/^{86}\text{Sr}_{rock(f)}) - (^{87}\text{Sr}/^{86}\text{Sr}_{rock(i)}))}{C_{fluid(i)}^{Sr} \cdot ((^{87}\text{Sr}/^{86}\text{Sr}_{fluid(i)}) - (^{87}\text{Sr}/^{86}\text{Sr}_{rock(i)}))} \quad (\text{Eq.1.4-4})$$

where  $C_{rock(i)}^{Sr}$  and  $C_{fluid(i)}^{Sr}$  are the Sr concentrations of the fresh rock and initial fluid, and  $^{87}\text{Sr}/^{86}\text{Sr}_{rock(i)}$ ,  $^{87}\text{Sr}/^{86}\text{Sr}_{fluid(i)}$ , and  $^{87}\text{Sr}/^{86}\text{Sr}_{rock(f)}$  describe the Sr isotopic composition of the fresh rock, initial fluid and the altered rock. A typical range of w/r-ratios within the oceanic crust is <0.5 to 2 (e.g. Albarède *et al.*, 1981; Alt *et al.*, 1996; Harris *et al.*, 2015) but also significantly higher values may locally occur (Reeves *et al.*, 2011; Marks *et al.*, 2015).

For calculations of the w/r-ratios based on altered rock  $^{87}\text{Sr}/^{86}\text{Sr}$  ratios it is necessary to estimate the Sr isotopic composition of the interacting fluid. Commonly, seawater is assumed as initial fluid phase. Indeed, errors may result from further modification of seawater during recharge prior to equilibration with deeper rock portions that lead to incorrect w/r-ratio estimates. Another problem can arise from precipitation or dissolution of mineral phases that equilibrated with a fluid of

differing Sr isotopic composition than the bulk rocks and therefore have shifted Sr isotopic signatures. In particular, precipitation and dissolution of sulfates (e.g. anhydrite) often results in shifts in Sr isotopic compositions of the bulk rocks and should be regarded for w/r-ratio estimates based on  $^{87}\text{Sr}/^{86}\text{Sr}$  ratios (e.g. Reeves *et al.*, 2011).

The  $^{87}\text{Sr}/^{86}\text{Sr}$  measurements in the scope of this thesis were conducted by using a Thermo Scientific TRITON Plus TIMS, either at the Isotope Geochemistry group at the MARUM (University of Bremen, Germany) or the Pôle Spectrométrie Océan (PSO, Brest, France). Purification before measurements was reached by exchange with the Sr specific resin Sr.spec<sup>TM</sup> adapted after Deniel & Pin (2001), *Appendix A.2.1*. Details are given in *Thesis Chapter 4 and 5*. The long-term reproducibility of NIST SRM 987 was  $0.710247 \pm 0.000005$  (2se, n=3, *Appendix A.2*).

#### 1.4.4. Oxygen isotopes

Oxygen has three stable isotopes ( $^{16}\text{O}=99.762\%$ ,  $^{17}\text{O}=0.038\%$ ,  $^{18}\text{O}=0.2\%$ ). The  $\delta^{18}\text{O}$  notation describes the ratio of the two most abundant oxygen isotopes ( $^{16}\text{O}$  and  $^{18}\text{O}$ ) of a sample relative to the ratio of the Vienna Standard Mean Ocean Water (VSMOW):

$$\delta^{18}\text{O} = \left( \frac{{}^{18}\text{O}/{}^{16}\text{O}_{\text{sample}}}{{}^{18}\text{O}/{}^{16}\text{O}_{\text{VSMOW}}} - 1 \right) \times 1000 \quad (\text{Eq.1.4-5})$$

Oxygen isotopes are part of the “light stable isotopes” group and show a mass dependent isotopic fractionation that is sensitive for changes in temperature. The oxygen isotopic fractionation is also sensitive for mineralogy but can be calibrated over a temperature range for a specific oxygen-bearing mineral phase by experimental, empirical or theoretical approaches (e.g. Valley, 2001; Hoefs, 2018). The oxygen isotopic fractionation between equilibrated quartz-water pairs is frequently used as a paleo-thermometer to investigate the thermal history of fluid-rock interactions due to the widespread occurrence of quartz in natural systems and the well characterized fractionation systematics (e.g. Sharp & Kirschner, 1994; Hu & Clayton, 2003; Pollington *et al.*, 2016). The relation can be expressed by a linear, one-coefficient equation that is valid for moderate to high temperatures (Valley, 2001):

$$1000 \ln \alpha_{\text{qtz-water}} = \frac{A_{\text{qtz-water}} \times 10^6}{T^2} \quad (\text{Eq.1.4-6})$$

where the isotopic fractionation factor is defined as  $\alpha_{\text{qtz-water}} = ({}^{18}\text{O}/{}^{16}\text{O})_{\text{qtz}}/({}^{18}\text{O}/{}^{16}\text{O})_{\text{water}}$ ,  $A_{\text{qtz-water}}$  is a constant, and  $T$  is the temperature (in Kelvin).

For temperature calculations based on  $\delta^{18}\text{O}$  values of quartz from natural systems the  $\delta^{18}\text{O}$  signature of the equilibrating fluid has to be estimated. Inaccurate  $\delta^{18}\text{O}$  fluid assumptions or not reached equilibrium between quartz and fluid can therefore result in wrong temperature estimates. For low-temperatures (<50 °C), problems could also result from poor calibration of the thermometer because

experiments are usually conducted under higher-temperatures (>400 °C) to ensure isotopic equilibration of the phases and extrapolation to significantly lower temperatures potentially leads to errors. Pollington *et al.* (2016) compared the oxygen isotopic fractionation calibrations for the quartz-water pair of nine experimental and theoretical studies and found a large variance of 16 ‰ at 50 °C between the published equations. Further, temperature calibrations are commonly conducted between a mineral phase and pure water but in saline solutions (like seawater) other dissolved species may disturb the isotopic fractionation. Indeed, Hu & Clayton (2003) assumed a relatively small effect of other dissolved species on oxygen isotopic fractionation and supposed a maximum shift in  $\delta^{18}\text{O} < 1\text{‰}$ .

The  $\delta^{18}\text{O}$  measurements on quartz separates that were conducted within the frame of this thesis were performed by a CAMECA ims-1280 secondary ion mass spectrometer (SIMS) at the Wisc-SIMS (Wisconsin Secondary Ion Mass Spectrometry) Laboratory, Department of Geoscience at the University of Wisconsin-Madison. Details on the procedure are given in *Thesis Chapter 5*. Analyses were performed in the standard-sample-standard bracketing mode by using the standard UWQ-1. The reproducibility of the  $\delta^{18}\text{O}$  bracketing-standard measurements was on average  $\pm 0.2\text{‰}$  (2sd, n=27, see the *Appendix A.3*).

### **1.5. Motivation and research objectives**

Seafloor hydrothermal systems have a critical influence on the geochemical budgets of seawater and altered rocks and also impacting the mantle composition once the altered lithologies are recycled at subduction zones (German & Von Damm, 2003). Further, hydrothermal systems often host high-grade ore deposits that are enriched in precious ore-metals and show many similarities to ore deposits mined on-land (German *et al.*, 2016). Hydrothermal activity is common in various submarine environments, reaching from the whole range of ultra-slow- to fast-spreading mid-ocean ridges (*Chapter 1.3.1*), over ridge flank hydrothermal systems (*Chapter 1.3.2*) to subduction influenced settings at volcanic arcs and back-arc basins (*Chapter 1.3.3*). The characteristics of hydrothermal activity in these settings are highly diverse, regarding the host rock lithology and alteration mineralogy, the structural and thermal regime, the fluid acidity and volatile contents, and also the dissolved metal concentrations in the circulation fluids can strongly vary, to name only a few of the significantly differing parameters. Boron and Li are both very fluid mobile elements and the B (*Chapter 1.4.1*) and Li (*Chapter 1.4.2*) elemental and isotopic systematics are very sensitive for potentially changing fluid-rock interaction parameters in hydrothermal circulation systems, e.g. like temperatures, w/r-ratios and B also for pH shifts. In addition, the combination of B,  $\delta^{11}\text{B}$ , Li and  $\delta^7\text{Li}$  signatures with additional fluid-rock sensitive tracers like Sr (*Chapter 1.4.3*) and O (*Chapter 1.4.4*) isotopic values allows creating an even more differentiated picture of hydrothermal processes at vent sites in different marine environments and to make constraints on the alteration history and geochemical budgets.

The main research objectives that are related to this thesis are:

- (1) Constraining the influence of increased fluid pH conditions in ultramafic versus mafic and felsic hosted vent sites on the B isotopic fractionation systematics.
  - Is an increase in fluid pH and B<sup>[4]</sup> species indeed linked to a decrease in B isotopic fractionation between fluid and B<sup>[4]</sup> coordinated mineral phases as it is generally estimated (e.g. Kakihana *et al.*, 1977; Wunder *et al.*, 2005; Kowalski *et al.*, 2013; Hansen *et al.*, 2017)?
  - And if so, how strong is the decrease in B isotopic fractionation with relative increase in B<sup>[4]</sup> species in solution?
  
- (2) Estimating the contributions of particular fluid discharge settings to the total B hydrothermal mass flux and its  $\delta^{11}\text{B}$  composition.
  - What are differences between ultramafic and mafic hosted vent sites at slow- and fast-spreading ridges?
  - How contribute arc and back-arc related vent sites?
  - And what are potentially implications for paleo-seawater B and  $\delta^{11}\text{B}$  signatures during periods of globally increased seafloor production and spreading rates that were predicted to exist over different time intervals in the Phanerozoic (Conrad & Lithgow-Bertelloni, 2007; Seton *et al.*, 2009)?
  
- (3) Evaluating the change in modern seawater  $\delta^7\text{Li}$  and  $^{87}\text{Sr}/^{86}\text{Sr}$  compositions due to low-temperature fluid-rock exchange in ridge flank hydrothermal systems.
  - How large is the impact on seawater  $\delta^7\text{Li}$  of basalt weathering versus marine sediment diagenesis?
  - And has basalt weathering in the flanks an impact on seawater Sr isotopic composition as estimated by Butterfield *et al.* (2001) based on data of an unusual warm ridge flank system at the eastern flank of the Juan de Fuca Ridge?
  
- (4) Investigating the potential impact of changes in paleo-seawater  $\delta^7\text{Li}$  and  $\delta^{11}\text{B}$  compositions on basalt weathering alteration products.
  - Can the relatively low  $\delta^7\text{Li}$  signature of weathered basalts of 18.5 to 23 Myr old crust of the Dorado Outcrop potentially be explained by lower  $\delta^7\text{Li}$  seawater values at the time of the formation of the edifice as previously assumed for altered rocks from the Cretaceous Troodos Ophiolite (Coogan *et al.*, 2017)?

- (5) Investigating the potential imprint of magmatic fluid  $\delta^{11}\text{B}$  signatures on hydrothermally altered rocks in the basement of arc and back-arc settings.
- Fluids affected by magma degassing from the Manus basin showed distinct shifts towards lower  $\delta^{11}\text{B}$  values compared to solely seawater-derived fluids (Wilckens *et al.*, 2018). Is a systematic shift towards lower  $\delta^{11}\text{B}$  values also present in altered rocks influenced by magmatic fluids compared to solely seawater altered rocks?
- (6) Constraining the impact of changing w/r-ratios and/or temperatures during alteration on the B,  $\delta^{11}\text{B}$ , Li,  $\delta^7\text{Li}$ ,  $^{87}\text{Sr}/^{86}\text{Sr}$  and  $\delta^{18}\text{O}$  systematics at the basement of hydrothermal systems at back-arc and arc settings.
- What is the impact of permeability contrasts between coherent lava flows and more heterogeneous volcanoclastics on w/r-ratios and temperatures?
  - Can the data confirm a more channelized fluid flow within volcanoclastic rocks that are sealed by less permeable lava flows, as it was previously supposed to occur at the Snowcap vent site within the Manus back-arc basin based on volcanic facies reconstruction and alteration patterns with depth (Paulick & Bach, 2006)?

## References

- Aggarwal J. K., Sheppard D., Mezger K. and Pernicka E. (2003) Precise and accurate determination of boron isotope ratios by multiple collector ICP-MS. *Chem. Geol.* **199**, 331–342.
- Akinfiyev N. N., Voronin M. V., Zotov A. V. and Prokof'ev V. Y. (2006) Experimental investigation of the stability of a chloroborate complex and thermodynamic description of aqueous species in the B-Na-Cl-O-H system up to 350°C. *Geochem. Int.* **44**, 867–878.
- Albarède F., Michard A., Minster J. F. and Michard G. (1981)  $^{87}\text{Sr}/^{86}\text{Sr}$  ratios in hydrothermal waters and deposits from the East Pacific Rise at 21°N. *Earth Planet. Sci. Lett* **55**, 229–236.
- Allen D. E. and Seyfried W. E. (2003) Compositional controls on vent fluids from ultramafic-hosted hydrothermal systems at mid-ocean ridges. *Geochim. Cosmochim. Acta* **67**, 1531–1542.
- Allen D. E. and Seyfried W. E. (2004) Serpentinization and heat generation. *Geochim. Cosmochim. Acta* **68**, 1347–1354.
- Alt J. (1995) Subseafloor Processes in Mid-Ocean Ridge Hydrothermal Systems. In *Seafloor Hydrothermal Systems* (eds. S. E. Humphris, R. A. Zierenberg, L. S. Mullineaux and R. E. Thomson). American Geophysical Union, Washington, D. C., pp. 85–114.
- Alt J. C., Teagle D. A. H., Bach W., Halliday A. N. and Erzinger J. (1996) Stable and Strontium Isotopic Profiles Through Hydrothermally Altered Upper Oceanic Crust, Hole 504B. In *Proceedings of the Ocean Drilling Program, Scientific Results Vol. 148* (eds. J. C. Alt, H. Kinoshita, L. B. Stokking and P. J. Michael).
- Arculus R. J. (2004) Evolution of Arc Magmas and Their Volatiles. In *The State of the Planet* (eds. R. S. J. Sparks and C. J. Hawkesworth). American Geophysical Union, Washington, D. C., pp. 95–108.
- Augustin N., Lackschewitz K. S., Kuhn T. and Devey C. W. (2008) Mineralogical and chemical mass changes in mafic and ultramafic rocks from the Logatchev hydrothermal field (MAR 15°N). *Mar. Geol.* **256**, 18–29.
- Augustin N., Paulick H., Lackschewitz K. S., Eisenhauer A., Garbe-Schönberg D., Kuhn T., Botz R. and Schmidt M. (2012) Alteration at the ultramafic-hosted Logatchev hydrothermal field. *Geochem. Geophys. Geosyst.* **13**.

- Bach W., Banerjee N. R., Dick H. J. B. and Baker E. T. (2002) Discovery of ancient and active hydrothermal systems along the ultra-slow spreading Southwest Indian Ridge 10°-16°E. *Geochem. Geophys. Geosyst.* **3**, 1–14.
- Bach W., Garrido C. J., Paulick H., Harvey J. and Rosner M. (2004) Seawater-peridotite interactions. *Geochem. Geophys. Geosyst.* **5**.
- Bach W. and Humphris S. E. (1999) Relationship between the Sr and O isotope compositions of hydrothermal fluids and the spreading and magma-supply rates at oceanic spreading centers. *Geology* **27**, 1067.
- Bach W., Jöns N. and Klein F. (2013) Metasomatism Within the Ocean Crust. In *Metasomatism and the Chemical Transformation of Rock* (eds. D. E. Harlov and H. Austrheim). Springer Berlin Heidelberg. Berlin, Heidelberg, pp. 253–288.
- Baker E. T. (2007) Hydrothermal cooling of midocean ridge axes. *Earth Planet. Sci. Lett* **263**, 140–150.
- Baker E. T., Chen Y. J. and Phipps Morgan J. (1996) The relationship between near-axis hydrothermal cooling and the spreading rate of mid-ocean ridges. *Earth Planet. Sci. Lett* **142**, 137–145.
- Baker E. T., Embley R. W., Walker S. L., Resing J. A., Lupton J. E., Nakamura K.-i., de Ronde C. E. J. and Massoth G. J. (2008) Hydrothermal activity and volcano distribution along the Mariana arc. *J. Geophys. Res.* **113**, 47.
- Ballance P. F., Ablaev A. G., Pushchin I. K., Pletnev S. P., Biryulina M. G., Itaya T., Follas H. A. and Gibson G. W. (1999) Morphology and history of the Kermadec trench–arc–backarc basin–remnant arc system at 30 to 32°S. *Mar. Geol.* **159**, 35–62.
- Ballhaus C., Ryan C., Mernagh T. and Green D. (1994) The partitioning of Fe, Ni, Cu, Pt, and Au between sulfide, metal, and fluid phases. *Geochim. Cosmochim. Acta* **58**, 811–826.
- Baquiran J.-P. M., Ramírez G. A., Haddad A. G., Toner B. M., Hulme S., Wheat C. G., Edwards K. J. and Orcutt B. N. (2016) Temperature and Redox Effect on Mineral Colonization in Juan de Fuca Ridge Flank Subsurface Crustal Fluids. *Front. Microbiol.* **7**, 396.
- Barckhausen U., Ranero C. R., Huene R. von, Cande S. C. and Roeser H. A. (2001) Revised tectonic boundaries in the Cocos Plate off Costa Rica. *J. Geophys. Res.* **106**, 19207–19220.
- Barth S. (1993) Boron isotope variations in nature. *Geol. Rundsch.* **82**.
- Batuev B. N., Krotov A. G., Markov V. F., Cherkashev G. A., Krasnov S. G. and Lisitzin Y. D. (1994) Massive sulfide deposits discovered at 14°45'N, Mid-Atlantic Ridge. *BRIDGE Newsletter* **6**, 6–10.
- Beaulieu S. E., Baker E. T. and German C. R. (2015) Where are the undiscovered hydrothermal vents on oceanic spreading ridges? *Deep Sea Research Part II: Topical Studies in Oceanography* **121**, 202–212.
- Beaulieu S. E. and Szafranski K. (2019) InterRidge Global Database of Active Submarine Hydrothermal Vent Fields, Version 3.4. *World Wide Web electronic publication available from <http://vents-data.interridge.org> (accessed 2020-04-06)*.
- Beltenev V., Ivanov V., Rozhdestvenskaya I., Cherkashov G., Stepanova T., Shilov V., Davydov M., Laiba A., Kaylio V., Narkevsky E., Pertsev A., Dobretzova I., Gustaytis A., Popova Y., Amplieva Y., Evrard C., Moskalev L. and Gebruk A. (2009) New data about hydrothermal fields on the Mid-Atlantic Ridge between 11° - 14°N: 32nd Cruise of R/V Professor Logatchev. *InterRidge News* **18**, 13–17.
- Beltenev V., Ivanov V., Rozhdestvenskaya I., Cherkashov G., Stepanova T., Shilov V., Pertsev A., Davydov M., Egorov I., Melekesteva I., Narkevsky E. and Ignatov V. (2007) A new hydrothermal field at 13°30' N on the Mid-Atlantic Ridge. *InterRidge News* **16**, 9–10.
- Beltenev V., Ivanov V., Shagin A., Sergeyev M., Rozhdestvenskaya I. I., Shilov V., Debretzova I., Cherkashev G. A., Samovarov M. and Poroshina I. M. (2005) New hydrothermal sites at 13°N, Mid-Atlantic-Ridge. *InterRidge News* **14**, 14–16.
- Beltenev V., Nescheretov A., Shilov V., Ivanov V., Shagin A., Stepanova T., Cherkashev G., Batuev B., Samovarov M., Rozhdestvenskaya I., Andreeva I., Fedorov I., Davydov M., Romanova L., Rumyantsev A., Zaharov V., Luneva N. and Artemeva O. (2003) New discoveries at 12°58'N, 44°52'W, MAR: Professor Logatchev-22 cruise, initial results. *InterRidge News* **12**, 13–14.
- Benton L. D., Ryan J. G. and Savov I. P. (2004) Lithium abundance and isotope systematics of forearc serpentinites, Conical Seamount, Mariana forearc. *Geochem. Geophys. Geosyst.* **5**, 123.

- Bernard A., Symonds R. B. and Rose W. I. (1990) Volatile transport and deposition of Mo, W and Re in high temperature magmatic fluids. *Appl. Geochemistry* **5**, 317–326.
- Berndt M. E. and Seyfried W. E. (1990) Boron, bromine, and other trace elements as clues to the fate of chlorine in mid-ocean ridge vent fluids. *Geochim. Cosmochim. Acta* **54**, 2235–2245.
- Berndt M. E. and Seyfried W. E. (1997) Calibration of fractionation during subcritical phase separation of seawater. *Geochim. Cosmochim. Acta* **61**, 2849–2854.
- Bird P. (2003) An updated digital model of plate boundaries. *Geochem. Geophys. Geosyst.* **4**, 1.
- Boschi C., Dini A., Früh-Green G. L. and Kelley D. S. (2008) Isotopic and element exchange during serpentinization and metasomatism at the Atlantis Massif (MAR 30°N). *Geochim. Cosmochim. Acta* **72**, 1801–1823.
- Both R., Crook K., Taylor B., Brogan S., Chappell B., Frankel E., Liu L., Sinton J. and Tiffin D. (1986) Hydrothermal chimneys and associated fauna in the Manus Back-Arc Basin, Papua New Guinea. *Eos Trans. AGU* **67**, 489.
- Brant C., Coogan L. A., Gillis K. M., Seyfried W. E., Pester N. J. and Spence J. (2012) Lithium and Li-isotopes in young altered upper oceanic crust from the East Pacific Rise. *Geochim. Cosmochim. Acta* **96**, 272–293.
- Brenan J. M., Neroda E., Lundstrom C. C., Shaw H. F., Ryerson F. J. and Phinney D. L. (1998a) Behaviour of boron, beryllium, and lithium during melting and crystallization. *Geochim. Cosmochim. Acta* **62**, 2129–2141.
- Brenan J. M., Ryerson F. J. and Shaw H. F. (1998b) The role of aqueous fluids in the slab-to-mantle transfer of boron, beryllium, and lithium during subduction. *Geochim. Cosmochim. Acta* **62**, 3337–3347.
- Brens R., Liu X.-M., Turner S. and Rushmer T. (2019) Lithium isotope variations in Tonga-Kermadec arc-Lau back-arc lavas and Deep Sea Drilling Project (DSDP) Site 204 sediments. *Island Arc* **28**, e12276.
- Butterfield D. A., Nakamura K.-i., Takano B., Lilley M. D., Lupton J. E., Resing J. A. and Roe K. K. (2011) High SO<sub>2</sub> flux, sulfur accumulation, and gas fractionation at an erupting submarine volcano. *Geology* **39**, 803–806.
- Butterfield D. A., Nelson B. K., Wheat C., Mottl M. J. and Roe K. K. (2001) Evidence for basaltic Sr in midocean ridge-flank hydrothermal systems and implications for the global oceanic Sr isotope balance. *Geochim. Cosmochim. Acta* **65**, 4141–4153.
- Caciagli N., Brenan J. M., McDonough W. F. and Phinney D. (2011) Mineral–fluid partitioning of lithium and implications for slab–mantle interaction. *Chem. Geol.* **280**, 384–398.
- Cann J. R., Blackman D. K., Smith D. K., McAllister E., Janssen B., Mello S., Avgerinos E., Pascoe A. R. and Escartin J. (1997) Corrugated slip surfaces formed at ridge–transform intersections on the Mid-Atlantic Ridge. *Nature* **385**, 329–332.
- Caratori Tontini F., Davy B., Ronde C. E. J. de, Embley R. W., Leybourne M. and Tivey M. A. (2012) Crustal Magnetization of Brothers Volcano, New Zealand, Measured by Autonomous Underwater Vehicles. *Econ. Geol.* **107**, 1571–1581.
- Carbotte S. M. and Canales J. P. (2019) Tectonics. In *Encyclopedia of Ocean Sciences*. Elsevier, pp. 455–471.
- Carbotte S. M., Detrick R. S., Harding A., Canales J. P., Babcock J., Kent G., van Ark E., Nedimovic M. and Diebold J. (2006) Rift topography linked to magmatism at the intermediate spreading Juan de Fuca Ridge. *Geology* **34**, 209.
- Catanzaro E. J., Champion C. E., Garner E. L., Marinemko G., Sappenfield K. M. and Shields W. R. (1970) *Boric assay; isotopic, and assay standard reference materials*. National Bureau of Standards Special Publication 260-17.
- Chan L., Edmond J. M., Thompson G. and Gillis K. (1992) Lithium isotopic composition of submarine basalts. *Earth Planet. Sci. Lett* **108**, 151–160.
- Chan L., Gieskes J. M., You C.-F. and Edmond J. M. (1994) Lithium isotope geochemistry of sediments and hydrothermal fluids of the Guaymas Basin, Gulf of California. *Geochim. Cosmochim. Acta* **58**, 4443–4454.
- Chan L.-H., Alt J. C. and Teagle D. A. (2002) Lithium and lithium isotope profiles through the upper oceanic crust. *Earth Planet. Sci. Lett* **201**, 187–201.

- Chan L.-H. and Edmond J. M. (1988) Variation of lithium isotope composition in the marine environment. *Geochim. Cosmochim. Acta* **52**, 1711–1717.
- Chan L.-H., Edmond J. M. and Thompson G. (1993) A lithium isotope study of hot springs and metabasalts from Mid-Ocean Ridge Hydrothermal Systems. *J. Geophys. Res.* **98**, 9653.
- Chapman H. and Spooner E. (1977) <sup>87</sup>Sr enrichment of ophiolitic sulphide deposits in Cyprus confirms ore formation by circulating seawater. *Earth Planet. Sci. Lett* **35**, 71–78.
- Charlou J., Bougault H., Appriou P., Nelsen T. and Rona P. (1991) Different TDM/CH<sub>4</sub> hydrothermal plume signatures. *Geochim. Cosmochim. Acta* **55**, 3209–3222.
- Charlou J., Donval J., Fouquet Y., Jean-Baptiste P. and Holm N. (2002) Geochemistry of high H<sub>2</sub> and CH<sub>4</sub> vent fluids issuing from ultramafic rocks at the Rainbow hydrothermal field (36°14'N, MAR). *Chem. Geol.* **191**, 345–359.
- Charlou J. L., Donval J. P., Kohn C., Ondréas H. and Fouquet Y. (2010) High Production and Fluxes of H<sub>2</sub> and CH<sub>4</sub> and Evidence of Abiotic Hydrocarbon Synthesis by Serpentinization in Ultramafic-Hosted Hydrothermal Systems on the Mid-Atlantic Ridge. *Geophys. Monogr. Ser.* **188**, 265–296.
- Chaussidon M. and Jambon A. (1994) Boron content and isotopic composition of oceanic basalts. *Earth Planet. Sci. Lett* **121**, 277–291.
- Chaussidon M. and Libourel G. (1993) Boron partitioning in the upper mantle. *Geochim. Cosmochim. Acta* **57**, 5053–5062.
- Chaussidon M. and Marty B. (1995) Primitive boron isotope composition of the mantle. *Science (New York, N.Y.)* **269**, 383–386.
- Cherkashev G. A., Ivanov V. N., Bel'tenev V. I., Lazareva L. I., Rozhdestvenskaya I. I., Samovarov M. L., Poroshina I. M., Sergeev M. B., Stepanova T. V., Dobretsova I. G. and Kuznetsov V. Y. (2013) Massive sulfide ores of the northern equatorial Mid-Atlantic Ridge. *Oceanology* **53**, 607–619.
- Cherkashov G., Kuznetsov V., Kuksa K., Tabuns E., Maksimov F. and Bel'tenev V. (2016) Sulfide geochronology along the Northern Equatorial Mid-Atlantic Ridge. *Ore Geol. Rev.* **87**, 147–154.
- Chester R. (1990) The transport of material to the oceans: the hydrothermal pathway. In *Marine Geochemistry* (ed. R. Chester). Springer Netherlands. Dordrecht, pp. 135–148.
- Conrad C. P. and Lithgow-Bertelloni C. (2007) Faster seafloor spreading and lithosphere production during the mid-Cenozoic. *Geology* **35**, 29.
- Coogan L. A., Gillis K. M., Pope M. and Spence J. (2017) The role of low-temperature (off-axis) alteration of the oceanic crust in the global Li-cycle. *Geochim. Cosmochim. Acta* **203**, 201–215.
- Corliss J. B., Dymond J., Gordon L. I., Edmond J. M., Herzen R. P. von, Ballard R. D., Green K., Williams D., Bainbridge A., Crane K. and van Andel T. H. (1979) Submarine thermal springs on the galapagos rift. *Science (New York, N.Y.)* **203**, 1073–1083.
- De Hoog J. and Savov I. P. (2018) Boron Isotopes as a Tracer of Subduction Zone Processes. In *Boron Isotopes - The Fifth Element* (eds. H. Marschall and G. Foster). Springer, Cham, pp. 216–247.
- de Ronde C. E. J., Baker E. T., Massoth G. J., Lupton J. E., Wright I. C., Feely R. A. and Greene R. R. (2001) Intra-oceanic subduction-related hydrothermal venting, Kermadec volcanic arc, New Zealand. *Earth Planet. Sci. Lett* **193**, 359–369.
- de Ronde C. E. J., Cornel E. J., Massoth G. J., Butterfield D. A., Christenson B. W., Ishibashi J., Ditchburn R. G., Hannington M. D., Brathwaite R. L., Lupton J. E., Kamenetsky V. S., Graham I. J., Zellmer G. F., Dziak R. P., Embley R. W., Dekov V. M., Munnik F., Lahr J., Evans L. J. and Takai K. (2011) Submarine hydrothermal activity and gold-rich mineralization at Brothers Volcano, Kermadec Arc, New Zealand. *Miner. Deposita* **46**, 541–584.
- de Ronde C. E. J., Faure K., Bray C. J., Chappell D. A. and Wright I. C. (2003) Hydrothermal fluids associated with seafloor mineralization at two southern Kermadec arc volcanoes, offshore New Zealand. *Miner. Deposita* **38**, 217–233.
- de Ronde C. E. J., Hannington M. D., Stoffers P., Wright I. C., Ditchburn R. G., Reyes A. G., Baker E. T., Massoth G. J., Lupton J. E., Walker S. L., Greene R. R., Soong C. W. R., Ishibashi J., Lebon G. T., Bray C. J. and Resing J. A. (2005) Evolution of a Submarine Magmatic-Hydrothermal System. *Econ. Geol.* **100**, 1097–1133.

- de Ronde C. E. J., Humphris S. E., Höfig T. W. and the Expedition 376 Scientists (2019a) *Brothers Arc Flux*. International Ocean Discovery Program.
- de Ronde C. E. J., Humphris S. E., Höfig T. W., Reyes A. G. and the Shipboard Scientists of IODP Expedition 376 (2019b) Critical role of caldera collapse in the formation of seafloor mineralization. *Geology* **47**, 762–766.
- de Ronde C. E. J. and Stucker V. K. (2015) Seafloor Hydrothermal Venting at Volcanic Arcs and Backarcs. In *The Encyclopedia of Volcanoes* (ed. H. Sigurdsson). Elsevier, pp. 823–849.
- Decitre S., Deloué E., Reisberg L., James R., Agrinier P. and Mével C. (2002) Behavior of Li and its isotopes during serpentinization of oceanic peridotites. *Geochem. Geophys. Geosyst.* **3**, 1–20.
- Deniel C. and Pin C. (2001) Single-stage method for the simultaneous isolation of lead and strontium from silicate samples for isotopic measurements. *Anal. Chim. Acta* **426**, 95–103.
- Detrick R. S., Buhl P., Vera E., Mutter J., Orcutt J., Madsen J. and Brocher T. (1987) Multi-channel seismic imaging of a crustal magma chamber along the East Pacific Rise. *Nature* **326**, 35–41.
- Detrick R. S., Harding A. J., Kent G. M., Orcutt J. A., Mutter J. C. and Buhl P. (1993) Seismic structure of the southern East Pacific Rise. *Science (New York, N.Y.)* **259**, 499–503.
- Dobson P. F., Kneafsey T. J., Hulen J. and Simmons A. (2003) Porosity, permeability, and fluid flow in the Yellowstone geothermal system, Wyoming. *J. Volcanol. Geoth. Res.* **123**, 313–324.
- Donnelly T. W., Thompson G. and Salisbury M. H. (1979) The chemistry of altered basalts at site 417, Deep Sea Drilling Project 51. *Init. Rep. DSDP* **51-53**.
- Driesner T. and Heinrich C. A. (2007) The system H<sub>2</sub>O–NaCl. Part I. *Geochim. Cosmochim. Acta* **71**, 4880–4901.
- Dupuis R., Benoit M., Tuckerman M. E. and Méheut M. (2017) Importance of a Fully Anharmonic Treatment of Equilibrium Isotope Fractionation Properties of Dissolved Ionic Species As Evidenced by Li<sup>+</sup>(aq). *Acc. Chem. Res.* **50**, 1597–1605.
- Edmonds H. N., Michael P. J., Baker E. T., Connelly D. P., Snow J. E., Langmuir C. H., Dick H. J. B., Mühe R., German C. R. and Graham D. W. (2003) Discovery of abundant hydrothermal venting on the ultraslow-spreading Gakkel ridge in the Arctic Ocean. *Nature* **421**, 252–256.
- Edwards K. J., Fisher A. T. and Wheat C. G. (2012) The deep subsurface biosphere in igneous ocean crust. *Front. Microbiol.* **3**, 8.
- Embley R. W., Ronde C. E. J. de, Merle S. G., Davy B. and Tontini F. C. (2012) Detailed Morphology and Structure of an Active Submarine Arc Caldera. *Econ. Geol.* **107**, 1557–1570.
- Escartín J., Mével C., Petersen S., Bonnemaïn D., Cannat M., Andreani M., Augustin N., Bezos A., Chavagnac V., Choi Y., Godard M., Haaga K., Hamelin C., Ildefonse B., Jamieson J., John B., Leleu T., MacLeod C. J., Massot-Campos M., Nomikou P., Olive J. A., Paquet M., Rommevaux C., Rothenbeck M., Steinfuhrer A., Tominaga M., Triebe L., Campos R., Gracias N. and Garcia R. (2017) Tectonic structure, evolution, and the nature of oceanic core complexes and their detachment fault zones (13°20'N and 13°30'N, Mid Atlantic Ridge). *Geochem. Geophys. Geosyst.* **18**, 1451–1482.
- Faure G. and Powell J. L. (1972) *Strontium Isotope Geology*. Springer, Berlin.
- Firstova A., Stepanova T., Cherkashov G., Goncharov A. and Babaeva S. (2016) Composition and Formation of Gabbro-Peridotite Hosted Seafloor Massive Sulfide Deposits from the Ashadze-1 Hydrothermal Field, Mid-Atlantic Ridge. *Minerals* **6**, 19.
- Fisher A. and Wheat C. G. (2010) Seamounts as Conduits for Massive Fluid, Heat, and Solute Fluxes on Ridge Flanks. *Oceanog.* **23**, 74–87.
- Fisher A. T. (2003) Abrupt thermal transition reveals hydrothermal boundary and role of seamounts within the Cocos Plate. *Geophys. Res. Lett.* **30**, 522.
- Fisher A. T., Alt J. and Bach W. (2014) Hydrogeologic Properties, Processes, and Alteration in the Igneous Ocean Crust. In *Earth and Life Processes Discovered from Subseafloor Environments - A Decade of Science Achieved by the Integrated Ocean Drilling Program (IODP)* (eds. R. Stein, D. K. Blackman, F. Inagaki and H.-C. Larsen). Elsevier, pp. 507–551.
- Fisher C., Takai K. and Le Bris N. (2007) Hydrothermal Vent Ecosystems. *Oceanog.* **20**, 14–23.

- Flesch G. D., Anderson A. R. and Svec H. J. (1973) A secondary isotopic standard for  $6\text{Li}/7\text{Li}$  determinations. *Int. J. Mass Spectrom. Ion Phys.* **12**, 265–272.
- Foster G. L., Lécuyer C. and Marschall H. R. (2016) Boron Stable Isotopes. In *Encyclopedia of Geochemistry* (ed. W. M. White). Springer International Publishing. Cham.
- Foster G. L., Pogge von Strandmann P. A. E. and Rae J. W. B. (2010) Boron and magnesium isotopic composition of seawater. *Geochem. Geophys. Geosyst.* **11**.
- Fouquet Y., Cambon P., Etoubleau J., Charlou J. L., Ondréas H., Barriga, Fernando J. A. S., Cherkashev G., Semkova T., Poroshina I., Bohn M., Donval J. P., Henry K., Murphy P. and Rouxel O. (2010) Geodiversity of Hydrothermal Processes Along the Mid-Atlantic Ridge and Ultramafic-Hosted Mineralization: a New Type Of Oceanic Cu-Zn-Co-Au Volcanogenic Massive Sulfide Deposit. *Geophys. Monogr. Ser.* **188**, 321–367.
- Fouquet Y., Cherkashov G., Charlou J. L., Ondréas H., Birot D., Cannat M., Bortnikov N. S., Silantyev S., Sudarikov S., Cambon-Bonavita M. A., Desbruyères D., Fabri M. C., Querellou J., Hourdez S., Gebruk A., Sokolova T., Hoisé E., Mercier E., Kohn C., Donval J. P., Etoubleau J., Normand A., Stephan M., Briand P., Crozon J., Fernagu P. and Buffier E. (2008) Serpentine cruise - ultramafic hosted hydrothermal deposits on the Mid-Atlantic Ridge: First submersible studies on Ashadze 1 and 2, Logatchev 2 and Krasnov vent fields. *InterRidge News* **17**, 16–21.
- Foustoukos D. I., James R. H., Berndt M. E. and Seyfried W. E. (2004) Lithium isotopic systematics of hydrothermal vent fluids at the Main Endeavour Field, Northern Juan de Fuca Ridge. *Chem. Geol.* **212**, 17–26.
- Foustoukos D. I., Savov I. P. and Janecky D. R. (2008) Chemical and isotopic constraints on water/rock interactions at the Lost City hydrothermal field,  $30^\circ\text{N}$  Mid-Atlantic Ridge. *Geochim. Cosmochim. Acta* **72**, 5457–5474.
- Foustoukos D. I. and Seyfried W. E. (2007a) Fluid Phase Separation Processes in Submarine Hydrothermal Systems. *Rev. Mineral. Geochem.* **65**, 213–239.
- Foustoukos D. I. and Seyfried W. E. (2007b) Trace element partitioning between vapor, brine and halite under extreme phase separation conditions. *Geochim. Cosmochim. Acta* **71**, 2056–2071.
- Früh-Green G. L., Kelley D. S., Bernasconi S. M., Karson J. A., Ludwig K. A., Butterfield D. A., Boschi C. and Proskurowski G. (2003) 30,000 years of hydrothermal activity at the lost city vent field. *Science (New York, N.Y.)* **301**, 495–498.
- Gamo T., Masuda H., Yamanaka T., Okamura K., Ishibashi J., Nakayama E., Obata H., Shitashima K., Nishio Y., Hasumoto H., Watanabe M., Mitsuzawa K., Seama N., Tsunogai U., Kouzuma F. and Sano Y. (2004) Discovery of a new hydrothermal venting site in the southernmost Mariana Arc. *Geochem. J.* **38**, 527–534.
- Gamo T., Okamura K., Charlou J.-L., Urabe T., Auzende J.-M., Ishibashi J., Shitashima K., Chiba H. and Cruise S. S. P. o. t. M. (1997) Acidic and sulfate-rich hydrothermal fluids from the Manus back-arc basin, Papua New Guinea. *Geology* **25**, 139–142.
- Gao Y., Vils F., Cooper K. M., Banerjee N., Harris M., Hoefs J., Teagle D. A. H., Casey J. F., Elliott T., Laverne C., Alt J. C. and Muehlenbachs K. (2012) Downhole variation of lithium and oxygen isotopic compositions of oceanic crust at East Pacific Rise, ODP Site 1256. *Geochem. Geophys. Geosyst.* **13**.
- German C. R. and Lin J. (2004) The Thermal Structure of the Oceanic Crust, Ridge-Spreading and Hydrothermal Circulation: How Well do we Understand their Inter-Connections? In *Mid-Ocean Ridges* (eds. C. R. German, J. Lin and L. M. Parson). American Geophysical Union. Washington, D. C., pp. 1–18.
- German C. R., Petersen S. and Hannington M. D. (2016) Hydrothermal exploration of mid-ocean ridges. *Chem. Geol.* **420**, 114–126.
- German C. R. and Von Damm K. L. (2003) Hydrothermal Processes. In *Treatise on Geochemistry* (eds. H. D. Holland and K. K. Turekian). Elsevier, pp. 181–222.
- Gill J. B. (1976) Composition and age of Lau Basin and Ridge volcanic rocks. *Geol. Soc. Am. Bull.* **87**, 1384.
- Gill J. B., Stork A. L. and Whelan P. M. (1984) Volcanism accompanying back-arc basin development in the southwest Pacific. *Tectonophysics* **102**, 207–224.
- Gillis K. M., Coogan L. A. and Pedersen R. (2005) Strontium isotope constraints on fluid flow in the upper oceanic crust at the East Pacific Rise. *Earth Planet. Sci. Lett* **232**, 83–94.

- Goldberg S., Forster H. S. and Heick E. L. (1993) Boron Adsorption Mechanisms on Oxides, Clay Minerals, and Soils Inferred from Ionic Strength Effects. *Soil Sci. Soc. Am. J.* **57**, 704–708.
- Grove T. L., Till C. B. and Krawczynski M. J. (2012) The Role of H<sub>2</sub>O in Subduction Zone Magmatism. *Annu. Rev. Earth Planet. Sci.* **40**, 413–439.
- Gruen G., Weis P., Driesner T., Heinrich C. A. and Ronde C. E. de (2014) Hydrodynamic modeling of magmatic–hydrothermal activity at submarine arc volcanoes, with implications for ore formation. *Earth Planet. Sci. Lett* **404**, 307–318.
- Haar L., Gallagher J. S. and Kell G. (1984) *NBS/NRC Steam Tables: Thermodynamic and transport properties and computer programs for vapor and liquid states of water in SI units*. Washington, Hemisphere.
- Haase K. M., Worthington T. J., Stoffers P., Garbe-Schönberg D. and Wright I. (2002) Mantle dynamics, element recycling, and magma genesis beneath the Kermadec Arc-Havre Trough. *Geochem. Geophys. Geosyst.* **3**, 1–22.
- Hannington M. D., de Ronde C. E. J. and Petersen S. (2005) Sea-Floor Tectonics and Submarine Hydrothermal Systems. In *One Hundredth Anniversary Volume* (eds. J. W. Hedenquist, J. F. H. Thompson, R. J. Goldfarb and J. P. Richards). Society of Economic Geologists.
- Hansen C. T., Meixner A., Kasemann S. A. and Bach W. (2017) New insight on Li and B isotope fractionation during serpentinization derived from batch reaction investigations. *Geochim. Cosmochim. Acta* **217**, 51–79.
- Harding J. L., van Avendonk H. J., Hayman N. W., Grevemeyer I., Peirce C. and Dannowski A. (2017) Magmatic-tectonic conditions for hydrothermal venting on an ultraslow-spread oceanic core complex. *Geology* **45**, 839–842.
- Harris M., Coggon R. M., Smith-Duque C. E., Cooper M. J., Milton J. A. and Teagle D. A. (2015) Channelling of hydrothermal fluids during the accretion and evolution of the upper oceanic crust. *Earth Planet. Sci. Lett* **416**, 56–66.
- Harvey J., Savov I. P., Agostini S., Cliff R. A. and Walshaw R. (2014) Si-metasomatism in serpentinized peridotite. *Geochim. Cosmochim. Acta* **126**, 30–48.
- Hawkins J. W. and Melchior J. T. (1985) Petrology of Mariana Trough and Lau Basin basalts. *J. Geophys. Res.* **90**, 11431.
- Heap M. J., Kennedy B. M., Farquharson J. I., Ashworth J., Mayer K., Letham-Brake M., Reuschlé T., Gilg H. A., Scheu B., Lavallée Y., Siratovich P., Cole J., Jolly A. D., Baud P. and Dingwell D. B. (2017) A multidisciplinary approach to quantify the permeability of the Whakaari/White Island volcanic hydrothermal system (Taupo Volcanic Zone, New Zealand). *J. Volcanol. Geoth. Res.* **332**, 88–108.
- Hedenquist J. W. and Lowenstern J. B. (1994) The role of magmas in the formation of hydrothermal ore deposits. *Nature* **370**, 519–527.
- Heinrich C. A., Ryan C. G., Mernagh T. P. and Eadington P. J. (1992) Segregation of ore metals between magmatic brine and vapor; a fluid inclusion study using PIXE microanalysis. *Econ. Geol.* **87**, 1566–1583.
- Hervig R. L., Moore G. M., Williams L. B., Peacock S. M., Holloway J. R. and Roggensack K. (2002) Isotopic and elemental partitioning of boron between hydrous fluid and silicate melt. *Amer. Miner.* **87**, 769–774.
- Hindshaw R. S., Tosca R., Goût T. L., Farnan I., Tosca N. J. and Tipper E. T. (2019) Experimental constraints on Li isotope fractionation during clay formation. *Geochim. Cosmochim. Acta* **250**, 219–237.
- Hoefs J. (2018) *Stable Isotope Geochemistry*. Springer International Publishing, Cham.
- Holm N. G. (1992) *Marine Hydrothermal Systems and the Origin of Life*. Springer Netherlands, Dordrecht.
- Hu G. and Clayton R. N. (2003) Oxygen isotope salt effects at high pressure and high temperature and the calibration of oxygen isotope geothermometers. *Geochim. Cosmochim. Acta* **67**, 3227–3246.
- Huh Y., Chan L.-H., Zhang L. and Edmond J. M. (1998) Lithium and its isotopes in major world rivers. *Geochim. Cosmochim. Acta* **62**, 2039–2051.
- Hutnak M. and Fisher A. T. (2007) Influence of sedimentation, local and regional hydrothermal circulation, and thermal rebound on measurements of seafloor heat flux. *J. Geophys. Res.* **112**, 1813.

- Hutnak M., Fisher A. T., Harris R., Stein C., Wang K., Spinelli G., Schindler M., Villinger H. and Silver E. (2008) Large heat and fluid fluxes driven through mid-plate outcrops on ocean crust. *Nature Geosci* **1**, 611–614.
- Ishibashi J. and Urabe T. (1995) Hydrothermal activity related to arc-backarc magmatism in the Western Pacific. In *Backarc Basins: Tectonics and Magmatism* (ed. B. Taylor). Plenum Press, pp. 451–495.
- Ishikawa T. and Nakamura E. (1992) Boron isotope geochemistry of the oceanic crust from DSDP/ODP Hole 504B. *Geochim. Cosmochim. Acta* **56**, 1633–1639.
- Ishikawa T. and Nakamura E. (1993) Boron isotope systematics of marine sediments. *Earth Planet. Sci. Lett* **117**, 567–580.
- Ishikawa T. and Nakamura E. (1994) Origin of the slab component in arc lavas from across-arc variation of B and Pb isotopes. *Nature* **370**, 205–208.
- Ito E., White W. M. and Göpel C. (1987) The O, Sr, Nd and Pb isotope geochemistry of MORB. *Chem. Geol.* **62**, 157–176.
- Jacobson R. S. (1992) Impact of crustal evolution on changes of the seismic properties of the uppermost ocean crust. *Rev. Geophys.* **30**, 23.
- James R. H., Elderfield H. and Palmer M. R. (1995) The chemistry of hydrothermal fluids from the Broken Spur site, 29°N Mid-Atlantic ridge. *Geochim. Cosmochim. Acta* **59**, 651–659.
- Jamieson J., Petersen S., Augustin N., Steinführer A., Escartin J. and ODEMAR Scientific Party (2014) AUV- and ROV-based exploration of active and inactive seafloor massive sulfide deposits at the Semyenov and Irinovskoe sites on the Mid-Atlantic Ridge. *Proceedings of the 43rd Underwater Mining Institute: Harvesting Seabed Mineral Resources in Harmony with Nature*, 189–196.
- Janecky D. R. (1982) Serpentinization of peridotite within the oceanic crust; experimental and theoretical investigations of seawater-peridotite interaction at 200C and 300C, 500 bars. *Thesis, University of Minnesota at Minneapolis, MN, USA*.
- Janecky D. R. and Seyfried W. E. (1986) Hydrothermal serpentinization of peridotite within the oceanic crust. *Geochim. Cosmochim. Acta* **50**, 1357–1378.
- Kakihana H., Kotaka M., Satoh S., Nomura M. and Okamoto M. (1977) Fundamental Studies on the Ion-Exchange Separation of Boron Isotopes. *B. Chem. Soc. Jpn.* **50**, 158–163.
- Kasemann S., Meixner A., Rocholl A., Vennemann T., Rosner M., Schmitt A. K. and Wiedenbeck M. (2001) Boron and Oxygen Isotope Composition of Certified Reference Materials NIST SRM 610/612 and Reference Materials JB-2 and JR-2. *Geostand. Geoanal. Res.* **25**, 405–416.
- Kastner M., Elderfield H. and Martin J. B. (1991) Fluids in convergent margins. *Phil. Trans. R. Soc. Lond. A* **335**, 243–259.
- Kastner M., Solomon E. A., Harris R. N. and Torres M. E. (2014) Fluid Origins, Thermal Regimes, and Fluid and Solute Fluxes in the Forearc of Subduction Zones. In *Earth and Life Processes Discovered from Subseafloor Environments - A Decade of Science Achieved by the Integrated Ocean Drilling Program (IODP)* (eds. R. Stein, D. Blackman, F. Inagaki and H.-C. Larsen). Elsevier, pp. 671–733.
- Kelemen P. B., Kikawa E. and Miller D. J. (2004) *Proceedings of the Ocean Drilling Program, 209 Initial Reports*. Ocean Drilling Program.
- Kelley D. S. and Delaney J. R. (1987) Two-phase separation and fracturing in mid-ocean ridge gabbros at temperatures greater than 700°C. *Earth Planet. Sci. Lett* **83**, 53–66.
- Kelley D. S., Karson J. A., Blackman D. K., Früh-Green G. L., Butterfield D. A., Lilley M. D., Olson E. J., Schrenk M. O., Roe K. K., Lebon G. T. and Rivizzigno P. (2001) An off-axis hydrothermal vent field near the Mid-Atlantic Ridge at 30 degrees N. *Nature* **412**, 145–149.
- Kelley D. S. and Robinson P. T. (1990) Development of a brine-dominated hydrothermal system at temperatures of 400–500°C in the upper level plutonic sequence, Troodos ophiolite, Cyprus. *Geochim. Cosmochim. Acta* **54**, 653–661.
- Kleint C., Bach W., Diehl A., Fröhberg N., Garbe-Schönberg D., Hartmann J. F., de Ronde C. E. J., Sander S. G., Strauss H., Stucker V. K., Thal J., Zitoun R. and Koschinsky A. (2019) Geochemical characterization of highly diverse hydrothermal fluids from volcanic vent systems of the Kermadec intraoceanic arc. *Chem. Geol.* **528**, 119289.

- Kowalski P. M. and Jahn S. (2011) Prediction of equilibrium Li isotope fractionation between minerals and aqueous solutions at high P and T. *Geochim. Cosmochim. Acta* **75**, 6112–6123.
- Kowalski P. M., Wunder B. and Jahn S. (2013) Ab initio prediction of equilibrium boron isotope fractionation between minerals and aqueous fluids at high P and T. *Geochim. Cosmochim. Acta* **101**, 285–301.
- Kuznetsov V., Cherkashev G. A., Lein A., Shilov V., Maksimov F., Arslanov K., Stepanova T., Baranova N., Chernov S. and Tarasenko D. (2006) <sup>230</sup>Th/U dating of massive sulfides from the Logatchev and Rainbow hydrothermal fields (Mid-Atlantic Ridge). *Geochronometria* **25**, 51–55.
- Kuznetsov V., Maksimov F., Zheleznov A., Cherkashov G., Beltenev V. and Lazareva L. (2011) <sup>230</sup>Th/U Chronology of ore formation within the Semenov hydrothermal district (13°31'N). *Geochronometria* **38**, 72–76.
- Kuznetsov V. Y., Tabuns E. V., Cherkashev G. A., Bel'tenev V. E., Maksimov F. E., Kuksa K. A., Lazareva L. I., Levchenko S. B. and Zherebtsov I. E. (2018) <sup>230</sup>Th/U Chronology and Geochemistry of Irinovskoe Hydrothermal Field (Mid-Atlantic Ridge). *Dokl. Earth Sc.* **478**, 26–30.
- Lackschewitz K. S., Devey C. W., Stoffers P., Botz R., Eisenhauer A., Kummert M., Schmidt M. and Singer A. (2004) Mineralogical, geochemical and isotopic characteristics of hydrothermal alteration processes in the active, submarine, felsic-hosted PACMANUS field, Manus Basin, Papua New Guinea. *Geochim. Cosmochim. Acta* **68**, 4405–4427.
- Lai Y.-J., Pogge von Strandmann P. A., Dohmen R., Takazawa E. and Elliott T. (2015) The influence of melt infiltration on the Li and Mg isotopic composition of the Horoman Peridotite Massif. *Geochim. Cosmochim. Acta* **164**, 318–332.
- Lalou C., Reyss J. L., Brichet E., Krasnov S., Stepanova T., Cherkashev G. and Markov V. (1996) Initial chronology of a recently discovered hydrothermal field at 14°45'N, Mid-Atlantic Ridge. *Earth Planet. Sci. Lett* **144**, 483–490.
- Lauer R. M., Fisher A. T. and Winslow D. M. (2018) Three-dimensional models of hydrothermal circulation through a seamount network on fast-spreading crust. *Earth Planet. Sci. Lett* **501**, 138–151.
- Le Gal V., Lucazeau F., Cannat M., Poort J., Monnin C., Battani A., Fontaine F., Goutorbe B., Rolandone F., Poitou C., Blanc-Valleron M.-M., Piedade A. and Hipólito A. (2018) Heat flow, morphology, pore fluids and hydrothermal circulation in a typical Mid-Atlantic Ridge flank near Oceanographer Fracture Zone. *Earth Planet. Sci. Lett* **482**, 423–433.
- Lécuyer C., Grandjean P., Reynard B., Albarède F. and Telouk P. (2002) <sup>11</sup>B/<sup>10</sup>B analysis of geological materials by ICP–MS Plasma 54. *Chem. Geol.* **186**, 45–55.
- Lee M. D., Walworth N. G., Sylvan J. B., Edwards K. J. and Orcutt B. N. (2015) Microbial Communities on Seafloor Basalts at Dorado Outcrop Reflect Level of Alteration and Highlight Global Lithic Clades. *Front. Microbiol.* **6**, 1470.
- Leeman W. P. and Sisson V. B. (1996) Geochemistry of boron and its implications for crustal and mantle processes. In *Boron: mineralogy, petrology and geochemistry* (eds. E. S. Grew and L. M. Anovitz), pp. 645–695.
- Leeman W. P., Tonarini S., Chan L. H. and Borg L. E. (2004) Boron and lithium isotopic variations in a hot subduction zone—the southern Washington Cascades. *Chem. Geol.* **212**, 101–124.
- Leeman W. P., Tonarini S., Pennisi M. and Ferrara G. (2005) Boron isotopic variations in fumarolic condensates and thermal waters from Vulcano Island, Italy. *Geochim. Cosmochim. Acta* **69**, 143–163.
- Lemarchand D., Gaillardet J., Lewin É. and Allègre C. (2002) Boron isotope systematics in large rivers. *Chem. Geol.* **190**, 123–140.
- Lemarchand E., Schott J. and Gaillardet J. (2007) How surface complexes impact boron isotope fractionation. *Earth Planet. Sci. Lett* **260**, 277–296.
- Liebscher A., Meixner A., Romer R. L. and Heinrich W. (2005) Liquid-vapor fractionation of boron and boron isotopes. *Geochim. Cosmochim. Acta* **69**, 5693–5704.
- Lister C. R. B. (1972) On the Thermal Balance of a Mid-Ocean Ridge. *Geophys. J. Int.* **26**, 515–535.
- Lough A., Homoky W. B., Connelly D. P., Comer-Warner S. A., Nakamura K., Abyaneh M. K., Kaulich B. and Mills R. A. (2019) Soluble iron conservation and colloidal iron dynamics in a hydrothermal plume. *Chem. Geol.* **511**, 225–237.

- Lowell R. P. (2017) A fault-driven circulation model for the Lost City Hydrothermal Field. *Geophys. Res. Lett.* **44**, 2703–2709.
- Lowell R. P. and Rona P. A. (2002) Seafloor hydrothermal systems driven by the serpentinization of peridotite. *Geophys. Res. Lett.* **29**.
- Lowell R. P., Rona P. A. and Herzen R. P. von (1995) Seafloor hydrothermal systems. *J. Geophys. Res.* **100**, 327–352.
- Lupton J., Butterfield D., Lilley M., Evans L., Nakamura K.-i., Chadwick W., Resing J., Embley R., Olson E., Proskurowski G., Baker E., Ronde C. de, Roe K., Greene R., Lebon G. and Young C. (2006) Submarine venting of liquid carbon dioxide on a Mariana Arc volcano. *Geochem. Geophys. Geosyst.* **7**.
- Lyubartsev A. P., Laasonen K. and Laaksonen A. (2001) Hydration of Li<sup>+</sup> ion. An ab initio molecular dynamics simulation. *J. Chem. Phys.* **114**, 3120–3126.
- MacLeod C. J., Searle R. C., Murton B. J., Casey J. F., Mallows C., Unsworth S. C., Achenbach K. L. and Harris M. (2009) Life cycle of oceanic core complexes. *Earth Planet. Sci. Lett* **287**, 333–344.
- Magna T., Ionov D. A., Oberli F. and Wiechert U. (2008) Links between mantle metasomatism and lithium isotopes. *Earth Planet. Sci. Lett* **276**, 214–222.
- Magna T., Wiechert U., Grove T. L. and Halliday A. N. (2006) Lithium isotope fractionation in the southern Cascadia subduction zone. *Earth Planet. Sci. Lett* **250**, 428–443.
- Marks N., Zierenberg R. A. and Schiffman P. (2015) Strontium and oxygen isotopic profiles through 3 km of hydrothermally altered oceanic crust in the Reykjanes Geothermal System, Iceland. *Chem. Geol.* **412**, 34–47.
- Marschall H. (2018) Boron Isotopes in the Ocean Floor Realm and the Mantle. In *Boron Isotopes - The Fifth Element* (eds. H. Marschall and G. Foster). Springer, Cham, pp. 189–216.
- Marschall H. R., Altherr R. and Rüpke L. (2007a) Squeezing out the slab — modelling the release of Li, Be and B during progressive high-pressure metamorphism. *Chem. Geol.* **239**, 323–335.
- Marschall H. R., Meyer C., Wunder B., Ludwig T. and Heinrich W. (2009) Experimental boron isotope fractionation between tourmaline and fluid. *Contr. Mineral. and Petrol.* **158**, 675–681.
- Marschall H. R., Pogge von Strandmann P. A., Seitz H.-M., Elliott T. and Niu Y. (2007b) The lithium isotopic composition of orogenic eclogites and deep subducted slabs. *Earth Planet. Sci. Lett* **262**, 563–580.
- Marschall H. R., Wanless V. D., Shimizu N., Pogge von Strandmann P. A., Elliott T. and Monteleone B. D. (2017) The boron and lithium isotopic composition of mid-ocean ridge basalts and the mantle. *Geochim. Cosmochim. Acta* **207**, 102–138.
- Martinez F. and Taylor B. (1996) Backarc spreading, rifting, and microplate rotation, between transform faults in the Manus Basin. *Mar. Geophys. Res.* **18**, 203–224.
- Massoth G. J., Ronde C. E. de, Lupton J. E., Feely R. A., Baker E. T., Lebon G. T. and Maenner S. M. (2003) Chemically rich and diverse submarine hydrothermal plumes of the southern Kermadec volcanic arc (New Zealand). *Geological Society, London, Special Publications* **219**, 119–139.
- McArthur J. M. (1994) Recent trends in strontium isotope stratigraphy. *Terra Nova* **6**, 331–358.
- McCaig A. M., Cliff R. A., Escartin J., Fallick A. E. and MacLeod C. J. (2007) Oceanic detachment faults focus very large volumes of black smoker fluids. *Geology* **35**, 935.
- McCullom T. M. and Bach W. (2009) Thermodynamic constraints on hydrogen generation during serpentinization of ultramafic rocks. *Geochim. Cosmochim. Acta* **73**, 856–875.
- McCulloch M. T. and Gamble J. A. (1991) Geochemical and geodynamical constraints on subduction zone magmatism. *Earth Planet. Sci. Lett* **102**, 358–374.
- McCulloch M. T., Gregory R. T., Wasserburg G. and Taylor H. P. (1980) A neodymium, strontium, and oxygen isotopic study of the Cretaceous Samail ophiolite and implications for the petrogenesis and seawater-hydrothermal alteration of oceanic crust. *Earth Planet. Sci. Lett* **46**, 201–211.
- McDermott J., Rouxel O., Stucker V. K., de Ronde C. E. J. and Massiot C. (2019) Insights into the controls on acid sulfate fluid geochemistry at arc and back arc systems from Brothers volcano. *Amer. Geophys. Union, Fall Meeting 2019*.

- Melekestseva I. Y., Kotlyarov V. A., Khvorov P. V., Ivanov V. N., Beltenev V. E. and Dobretsova I. G. (2010) Noble-metal mineralization in the Semenov-2 hydrothermal field (13°31'N), mid-atlantic ridge. *Geol. Ore Deposits* **52**, 800–810.
- Melekestseva I. Y., Maslennikov V. V., Tret'yakov G. A., Nimis P., Beltenev V. E., Rozhdestvenskaya I. I., Maslennikova S. P., Belogub E. V., Danyushevsky L., Large R., Yuminov A. M. and Sadykov S. A. (2017) Gold- and Silver-Rich Massive Sulfides from the Semenov-2 Hydrothermal Field, 13°31.13'N, Mid-Atlantic Ridge. *Econ. Geol.* **112**, 741–773.
- Melekestseva I. Y., Tret'yakov G. A., Nimis P., Yuminov A. M., Maslennikov V. V., Maslennikova S. P., Kotlyarov V. A., Beltenev V. E., Danyushevsky L. V. and Large R. (2014) Barite-rich massive sulfides from the Semenov-1 hydrothermal field (Mid-Atlantic Ridge, 13°30.87' N). *Mar. Geol.* **349**, 37–54.
- Meyer C., Wunder B., Meixner A., Romer R. L. and Heinrich W. (2008) Boron-isotope fractionation between tourmaline and fluid. *Contr. Mineral. and Petrol.* **156**, 259–267.
- Miller A. (1964) High Salinity in Sea Water. *Nature* **203**, 590–591.
- Miller A., Densmore C., Degens E., Hathaway J., Manheim F., McFarlin P., Pocklington R. and Jokela A. (1966) Hot brines and recent iron deposits in deeps of the Red Sea. *Geochim. Cosmochim. Acta* **30**, 341–359.
- Millot R., Guerrot C. and Vigier N. (2004) Accurate and High-Precision Measurement of Lithium Isotopes in Two Reference Materials by MC-ICP-MS. *Geostand Geoanalyt Res* **28**, 153–159.
- Millot R., Scaillet B. and Sanjuan B. (2010) Lithium isotopes in island arc geothermal systems. *Geochim. Cosmochim. Acta* **74**, 1852–1871.
- Misra S. and Froelich P. N. (2012) Lithium isotope history of Cenozoic seawater. *Science (New York, N.Y.)* **335**, 818–823.
- Möller P., Dulski P. and Morteani G. (2003) Partitioning of rare earth elements, yttrium, and some major elements among source rocks, liquid and vapor of Larderello-Travale geothermal field, Tuscany (Central Italy). *Geochim. Cosmochim. Acta* **67**, 171–183.
- Monecke T., Petersen S. and Hannington M. D. (2014) Constraints on Water Depth of Massive Sulfide Formation. *Econ. Geol.* **109**, 2079–2101.
- Moriguti T. and Nakamura E. (1998) Across-arc variation of Li isotopes in lavas and implications for crust/mantle recycling at subduction zones. *Earth Planet. Sci. Lett* **163**, 167–174.
- Moriguti T., Shibata T. and Nakamura E. (2004) Lithium, boron and lead isotope and trace element systematics of Quaternary basaltic volcanic rocks in northeastern Japan. *Chem. Geol.* **212**, 81–100.
- Mottl M. J. and Wheat C. (1994) Hydrothermal circulation through mid-ocean ridge flanks. *Geochim. Cosmochim. Acta* **58**, 2225–2237.
- Mottl M. J., Wheat G., Baker E., Becker N., Davis E., Feely R., Grehan A., Kadko D., Lilley M., Massoth G., Moyer C. and Sansone F. (1998) Warm springs discovered on 3.5 Ma oceanic crust, eastern flank of the Juan de Fuca Ridge. *Geology* **26**, 51.
- Nehlig P. (1991) Salinity of oceanic hydrothermal fluids. *Earth Planet. Sci. Lett* **102**, 310–325.
- Nishio Y., Nakai S., Ishii T. and Sano Y. (2007) Isotope systematics of Li, Sr, Nd, and volatiles in Indian Ocean MORBs of the Rodrigues Triple Junction. *Geochim. Cosmochim. Acta* **71**, 745–759.
- Ondréas H., Cannat M., Fouquet Y. and Normand A. (2012) Geological context and vents morphology of the ultramafic-hosted Ashadze hydrothermal areas (Mid-Atlantic Ridge 13°N). *Geochem. Geophys. Geosyst.* **13**, 6.
- Oudin E. and Constantinou G. (1984) Black smoker chimney fragments in Cyprus sulphide deposits. *Nature* **308**, 349–353.
- Palmer M. R., London D., Morgan G. B. and Babb H. A. (1992) Experimental determination of fractionation of <sup>11</sup>B/<sup>10</sup>B between tourmaline and aqueous vapor: A temperature- and pressure-dependent isotopic system. *Chem. Geol.*, 123–129.
- Palmer M. R., Spivack A. J. and Edmond J. M. (1987) Temperature and pH controls over isotopic fractionation during adsorption of boron on marine clay. *Geochim. Cosmochim. Acta* **51**, 2319–2323.

- Park S.-H., Lee S.-M., Kamenov G. D., Kwon S.-T. and Lee K.-Y. (2010) Tracing the origin of subduction components beneath the South East rift in the Manus Basin, Papua New Guinea. *Chem. Geol.* **269**, 339–349.
- Parson L. M. and Wright I. C. (1996) The Lau-Havre-Taupo back-arc basin. *Tectonophysics* **263**, 1–22.
- Paulick H. and Bach W. (2006) Phyllosilicate Alteration Mineral Assemblages in the Active Subsea-Floor Pacmanus Hydrothermal System, Papua New Guinea, ODP Leg 193. *Econ. Geol.* **101**, 633–650.
- Paulick H., Vanko D. and Yeats C. (2004) Drill core-based facies reconstruction of a deep-marine felsic volcano hosting an active hydrothermal system (Pual Ridge, Papua New Guinea, ODP Leg 193). *J. Volcanol. Geoth. Res.* **130**, 31–50.
- Pearce J. A. and Stern R. J. (2006) Origin of Back-Arc Basin Magmas: Trace Element and Isotope Perspectives. In *Back-Arc Spreading Systems: Geological, Biological, Chemical, and Physical Interactions* (eds. D. M. Christie, C. R. Fisher, S.-M. Lee and S. Givens), pp. 63–86.
- Penniston-Dorland S., Liu X.-M. and Rudnick R. L. (2017) Lithium Isotope Geochemistry. *Rev. Mineral. Geochem.* **82**, 165–217.
- Pertsev A. N., Bortnikov N. S., Vlasov E. A., Beltenev V. E., Dobretsova I. G. and Ageeva O. A. (2012) Recent massive sulfide deposits of the Semenov ore district, Mid-Atlantic Ridge, 13°31' N. *Geol. Ore Deposits* **54**, 334–346.
- Petersen S., Kuhn K., Kuhn T., Augustin N., Hékinian R., Franz L. and Borowski C. (2009) The geological setting of the ultramafic-hosted Logatchev hydrothermal field (14°45'N, Mid-Atlantic Ridge) and its influence on massive sulfide formation. *Lithos* **112**, 40–56.
- Plank T. (2014) The Chemical Composition of Subducting Sediments. In *Treatise on Geochemistry* (eds. K. K. Turekian and H. D. Holland). Elsevier, pp. 607–629.
- Pogge von Strandmann P. A., Elliott T., Marschall H. R., Coath C., Lai Y.-J., Jeffcoate A. B. and Ionov D. A. (2011) Variations of Li and Mg isotope ratios in bulk chondrites and mantle xenoliths. *Geochim. Cosmochim. Acta* **75**, 5247–5268.
- Pogge von Strandmann P. A., Fraser W. T., Hammond S. J., Tarbuck G., Wood I. G., Oelkers E. H. and Murphy M. J. (2019) Experimental determination of Li isotope behaviour during basalt weathering. *Chem. Geol.* **517**, 34–43.
- Pokrovski G. S., Schott J. and Sergeev A. S. (1995) Experimental determination of the stability constants of NaSO<sub>4</sub><sup>-</sup> and NaB(OH)<sub>4</sub><sup>0</sup> in hydrothermal solutions using a new high-temperature sodium-selective glass electrode — Implications for boron isotopic fractionation. *Chem. Geol.* **124**, 253–265.
- Pollington A. D., Kozdon R., Anovitz L. M., Georg R. B., Spicuzza M. J. and Valley J. W. (2016) Experimental calibration of silicon and oxygen isotope fractionations between quartz and water at 250 °C by in situ microanalysis of experimental products and application to zoned low δ<sup>30</sup>Si quartz overgrowths. *Chem. Geol.* **421**, 127–142.
- Ramakumar K. L., Parab A. R., Khodade P. S., Almaula A. I., Chitambar S. A. and Jain H. C. (1985) Determination of isotopic composition of boron. *J. Radioanal. Nucl. Ch. Lett.* **94**, 53–61.
- Reeves E. P., Seewald J. S., Saccoccia P., Bach W., Craddock P. R., Shanks W. C., Sylva S. P., Walsh E., Pichler T. and Rosner M. (2011) Geochemistry of hydrothermal fluids from the PACMANUS, Northeast Pual and Vienna Woods hydrothermal fields, Manus Basin, Papua New Guinea. *Geochim. Cosmochim. Acta* **75**, 1088–1123.
- Resing J. A., Lebon G., Baker E. T., Lupton J. E., Embley R. W., Massoth G. J., Chadwick W. W. and de Ronde C. E. J. (2007) Venting of Acid-Sulfate Fluids in a High-Sulfidation Setting at NW Rota-1 Submarine Volcano on the Mariana Arc. *Econ. Geol.* **102**, 1047–1061.
- Romer R. L., Meixner A. and Hahne K. (2014) Lithium and boron isotopic composition of sedimentary rocks — The role of source history and depositional environment. *Gondwana Res.* **26**, 1093–1110.
- Rona P. A., Widenfalk L. and Boström K. (1987) Serpentinized ultramafics and hydrothermal activity at the Mid-Atlantic Ridge crest near 15°N. *J. Geophys. Res.* **92**, 1417.
- Roy-Barman M., Wasserburg G., Papanastassiou D. and Chaussidon M. (1998) Osmium isotopic compositions and Re–Os concentrations in sulfide globules from basaltic glasses. *Earth Planet. Sci. Lett.* **154**, 331–347.

- Rubin K. H. and Macdougall J. D. (1992) ThSr isotopic relationships in MORB. *Earth Planet. Sci. Lett* **114**, 149–157.
- Ryan J. G. and Langmuir C. H. (1987) The systematics of lithium abundances in young volcanic rocks. *Geochim. Cosmochim. Acta* **51**, 1727–1741.
- Saffer D. M. and Kopf A. J. (2016) Boron desorption and fractionation in Subduction Zone Fore Arcs. *Geochem. Geophys. Geosyst.* **17**, 4992–5008.
- Schauble E. A. (2004) Applying Stable Isotope Fractionation Theory to New Systems. *Rev. Mineral. Geochem.* **55**, 65–111.
- Scher H. D., Griffith E. M. and Buckley W. P. (2014) Accuracy and precision of  $^{88}\text{Sr}/^{86}\text{Sr}$  and  $^{87}\text{Sr}/^{86}\text{Sr}$  measurements by MC-ICPMS compromised by high barium concentrations. *Geochem. Geophys. Geosyst.* **15**, 499–508.
- Schmale O., Walter M., Schneider von Deimling J., Sültenfuß J., Walker S., Rehder G. and Keir R. (2012) Fluid and gas fluxes from the Logatchev hydrothermal vent area. *Geochem. Geophys. Geosyst.* **13**.
- Schmidt K., Koschinsky A., Garbe-Schönberg D., Carvalho L. M. de and Seifert R. (2007) Geochemistry of hydrothermal fluids from the ultramafic-hosted Logatchev hydrothermal field, 15°N on the Mid-Atlantic Ridge. *Chem. Geol.* **242**, 1–21.
- Scholz F., Hensen C., Lange G. J. de, Haeckel M., Liebetrau V., Meixner A., Reitz A. and Romer R. L. (2010) Lithium isotope geochemistry of marine pore waters – Insights from cold seep fluids. *Geochim. Cosmochim. Acta* **74**, 3459–3475.
- Seewald J. S., Reeves E. P., Bach W., Saccocia P. J., Craddock P. R., Shanks W. C., Sylva S. P., Pichler T., Rosner M. and Walsh E. (2015) Submarine venting of magmatic volatiles in the Eastern Manus Basin, Papua New Guinea. *Geochim. Cosmochim. Acta* **163**, 178–199.
- Seewald J. S., Reeves E. P., Bach W., Saccocia P. J., Craddock P. R., Walsh E., Shanks W. C., Sylva S. P., Pichler T. and Rosner M. (2019) Geochemistry of hot-springs at the SuSu Knolls hydrothermal field, Eastern Manus Basin. *Geochim. Cosmochim. Acta* **255**, 25–48.
- Seton M., Gaina C., Muller R. D. and Heine C. (2009) Mid-Cretaceous seafloor spreading pulse. *Geology* **37**, 687–690.
- Seyfried W. E., Chen X. and Chan L.-H. (1998) Trace Element Mobility and Lithium Isotope Exchange During Hydrothermal Alteration of Seafloor Weathered Basalt. *Geochim. Cosmochim. Acta* **62**, 949–960.
- Seyfried W. E. and Dibble W. E. (1980) Seawater-peridotite interaction at 300°C and 500 bars. *Geochim. Cosmochim. Acta* **44**, 309–321.
- Seyfried W. E., Foustoukos D. I. and Allen D. E. (2013) Ultramafic-Hosted Hydrothermal Systems at Mid-Ocean Ridges: Chemical and Physical Controls on pH, Redox and Carbon Reduction Reactions. *Geophys. Monogr. Ser.* **148**, 267–284.
- Seyfried W. E., Janecky D. R. and Mottl M. J. (1984) Alteration of the oceanic crust. *Geochim. Cosmochim. Acta* **48**, 557–569.
- Seyfried W. E., Pester N. J., Ding K. and Rough M. (2011) Vent fluid chemistry of the Rainbow hydrothermal system (36°N, MAR). *Geochim. Cosmochim. Acta* **75**, 1574–1593.
- Shanks III P. (2012) Hydrothermal alteration in volcanogenic massive sulfide occurrence model. *U.S. Geol. Surv. Sci. Invest. Rep.* **2010-5070-C**, chap. 11.
- Shannon R. D. (1976) Revised effective ionic radii and systematic studies of interatomic distances in halides and chalcogenides. *Acta Cryst. A.* **32**, 751–767.
- Sharp Z. and Kirschner D. (1994) Quartz-calcite oxygen isotope thermometry. *Geochim. Cosmochim. Acta* **58**, 4491–4501.
- Shipboard Scientific Party (2002a) Leg 193 Summary. *Proc. Ocean Drill. Prog. Init. Repts.* **193**, edited by **R.A. Binns et al.**,
- Shipboard Scientific Party (2002b) Leg 193 Summary. In *Proceedings of the Ocean Drilling Program, Initial Reports* (eds. R. A. Binns, F. J. A. S. Barriga and D. J. Miller).

- Silantyev S. A., Krasnova E. A., Cannat M., Bortnikov N. S., Kononkova N. N. and Beltenev V. E. (2011) Peridotite-gabbro-trondhjemite association of the Mid-Atlantic Ridge between 12°58' and 14°45'N. *Geochem. Int.* **49**, 323–354.
- Simon A. C., Pettke T., Candela P. A., Piccoli P. M. and Heinrich C. A. (2004) Magnetite solubility and iron transport in magmatic-hydrothermal environments. *Geochim. Cosmochim. Acta* **68**, 4905–4914.
- Sinton J. (2003) Magma Genesis and Mantle Heterogeneity in the Manus Back-Arc Basin, Papua New Guinea. *J. Petrol.* **44**, 159–195.
- Sisson T. W. and Grove T. L. (1993) Experimental investigations of the role of H<sub>2</sub>O in calc-alkaline differentiation and subduction zone magmatism. *Contr. Mineral. and Petrol.* **113**, 143–166.
- Smith D. K., Cann J. R. and Escartín J. (2006) Widespread active detachment faulting and core complex formation near 13 degrees N on the Mid-Atlantic Ridge. *Nature* **442**, 440–443.
- Smith D. K., Escartín J., Schouten H. and Cann J. R. (2008) Fault rotation and core complex formation. *Geochem. Geophys. Geosyst.* **9**, n/a-n/a.
- Smith H., Spivack A. J., Staudigel H. and Hart S. R. (1995) The boron isotopic composition of altered oceanic crust. *Chem. Geol.* **126**, 119–135.
- Snow J. E. and Dick H. J. (1995) Pervasive magnesium loss by marine weathering of peridotite. *Geochim. Cosmochim. Acta* **59**, 4219–4235.
- Spivack A. and Edmond J. (1987) Boron isotope exchange between seawater and the oceanic crust. *Geochim. Cosmochim. Acta* **51**, 1033–1043.
- Spivack A. J., Berndt M. E. and Seyfried W. E. (1990) Boron isotope fractionation during supercritical phase separation. *Geochim. Cosmochim. Acta* **54**, 2337–2339.
- Staudigel H. (2003) Hydrothermal Alteration Processes in the Oceanic Crust. In *Treatise on Geochemistry* (eds. H. D. Holland and K. K. Turekian). Elsevier, pp. 511–535.
- Stein C. A. and Stein S. (1994) Constraints on hydrothermal heat flux through the oceanic lithosphere from global heat flow. *J. Geophys. Res.* **99**, 3081–3095.
- Stoffers P., Worthington T. J., Schwarz-Schampera U., Hannington M. D., Massoth G. J., Hekinian R., Schmidt M., Lundsten L. J., Evans L. J., Vaiomo'unga R. and Kerby T. (2006) Submarine volcanoes and high-temperature hydrothermal venting on the Tonga arc, southwest Pacific. *Geology* **34**, 453.
- Stoffers P., Wright I. C. and the Shipboard Scientific Party (1999) Cruise report Sonne 135, Havre Trough-Taupo Volcanic Zone: Tectonic, magmatic and hydrothermal processes, Suva-Fiji-Wellington, New Zealand, Sept.9-Oct. 15, 1998. *Berichte-Reports, Institut für Geowissenschaften, Universität Kiel.*
- Stoiber R. E. and Rose W. I. (1974) Fumarole incrustations at active Central American volcanoes. *Geochim. Cosmochim. Acta*, 495–516.
- Straub S. M. and Layne G. D. (2002) The systematics of boron isotopes in Izu arc front volcanic rocks. *Earth Planet. Sci. Lett* **198**, 25–39.
- Sudarikov S. and Roumiantsev A. (2000) Structure of hydrothermal plumes at the Logatchev vent field, 14°45'N, Mid-Atlantic Ridge. *J. Volcanol. Geoth. Res.* **101**, 245–252.
- Tao C., Lin J., Guo S., Chen Y. J., Wu G., Han X., German C. R., Yoerger D. R., Zhou N., Li H., Su X. and Zhu J. (2012) First active hydrothermal vents on an ultraslow-spreading center. *Geology* **40**, 47–50.
- Tao C., Seyfried W. E., Lowell R. P., Liu Y., Liang J., Guo Z., Ding K., Zhang H., Liu J., Qiu L., Egorov I., Liao S., Zhao M., Zhou J., Deng X., Li H., Wang H., Cai W., Zhang G., Zhou H., Lin J. and Li W. (2020) Deep high-temperature hydrothermal circulation in a detachment faulting system on the ultra-slow spreading ridge. *Nat. Commun.* **11**, 1300.
- Taylor B. (1979) Bismarck Sea. *Geology* **7**, 171.
- Taylor B. and Martinez F. (2003) Back-arc basin basalt systematics. *Earth Planet. Sci. Lett* **210**, 481–497.
- Thal J., Tivey M., Yoerger D., Jöns N. and Bach W. (2014) Geologic setting of PACManus hydrothermal area — High resolution mapping and in situ observations. *Mar. Geol.* **355**, 98–114.
- Thompson G. and Melson W. G. (1970) Boron contents of serpentinites and metabasalts in the oceanic crust. *Earth Planet. Sci. Lett* **8**, 61–65.

- Tivey M. (2007) Generation of Seafloor Hydrothermal Vent Fluids and Associated Mineral Deposits. *Oceanog.* **20**, 50–65.
- Tomascak P., Magna T. and Dohmen R. (eds.) (2016a) *Advances in Lithium Isotope Geochemistry*. Springer Cham.
- Tomascak P., Magna T. and Dohmen R. (2016b) Methodology of Lithium Analytical Chemistry and Isotopic Measurements. In *Advances in Lithium Isotope Geochemistry* (eds. P. Tomascak, T. Magna and R. Dohmen). Springer Cham, pp. 5–18.
- Tomascak P. B., Langmuir C. H., Le Roux P. J. and Shirey S. B. (2008) Lithium isotopes in global mid-ocean ridge basalts. *Geochim. Cosmochim. Acta* **72**, 1626–1637.
- Tomascak P. B., Widom E., Benton L. D., Goldstein S. L. and Ryan J. G. (2002) The control of lithium budgets in island arcs. *Earth Planet. Sci. Lett* **196**, 227–238.
- Tonarini S., Leeman W. P. and Leat P. T. (2011) Subduction erosion of forearc mantle wedge implicated in the genesis of the South Sandwich Island (SSI) arc. *Earth Planet. Sci. Lett* **301**, 275–284.
- Tonarini S., Pennisi M. and Leeman W. P. (1997) Precise boron isotopic analysis of complex silicate (rock) samples using alkali carbonate fusion and ion-exchange separation. *Chem. Geol.* **142**, 129–137.
- Tucholke B. E., Lin J. and Kleinrock M. C. (1998) Megamullions and mullion structure defining oceanic metamorphic core complexes on the Mid-Atlantic Ridge. *J. Geophys. Res.* **103**, 9857–9866.
- Ulrich T., Günther D. and Heinrich C. A. (1999) Gold concentrations of magmatic brines and the metal budget of porphyry copper deposits. *Nature* **399**, 676–679.
- Valley J. W. (2001) Stable Isotope Thermometry at High Temperatures. *Rev. Mineral. Geochem.* **43**, 365–413.
- Vanko D. A. (1988) Temperature, pressure, and composition of hydrothermal fluids, with their bearing on the magnitude of tectonic uplift at mid-ocean ridges, inferred from fluid inclusions in oceanic layer 3 rocks. *J. Geophys. Res.* **93**, 4595–4611.
- Vanko D. A., Bach W., Roberts S., Yeats C. and Scott S. D. (2004) Fluid inclusion evidence for subsurface phase separation and variable fluid mixing regimes beneath the deep-sea PACMANUS hydrothermal field, Manus Basin back arc rift, Papua New Guinea. *J. Geophys. Res.* **109**, 417.
- Vigier N., Decarreau A., Millot R., Carignan J., Petit S. and France-Lanord C. (2008) Quantifying Li isotope fractionation during smectite formation and implications for the Li cycle. *Geochim. Cosmochim. Acta* **72**, 780–792.
- Villinger H. W., Müller P., Bach W., Becker K., Orcutt B. N., Kaul N. and Wheat C. G. (2019) Evidence for Low-Temperature Diffuse Venting at North Pond, Western Flank of the Mid-Atlantic Ridge. *Geochem. Geophys. Geosyst.* **20**, 2572–2584.
- Vils F., Tonarini S., Kalt A. and Seitz H.-M. (2009) Boron, lithium and strontium isotopes as tracers of seawater–serpentinite interaction at Mid-Atlantic ridge, ODP Leg 209. *Earth Planet. Sci. Lett* **286**, 414–425.
- Vine F. J. and Matthews D. H. (1963) Magnetic Anomalies Over Oceanic Ridges. *Nature* **199**, 947–949.
- Vine F. J. and Moores E. M. (1972) A Model for the Gross Structure, Petrology, and Magnetic Properties of Oceanic Crust. In *Studies in Earth and Space Sciences* (eds. R. Shagam, R. B. Hargraves, W. J. Morgan, F. B. van Houtan, C. A. Burk, H. D. Holland and L. C. Hollister). Geological Society of America, pp. 195–206.
- Von Damm K. L. (1990) Seafloor Hydrothermal Activity. *Annu. Rev. Earth Planet. Sci.* **18**, 173–204.
- Von Damm K. L., Edmond J., Grant B., Measures C., Walden B. and Weiss R. (1985) Chemistry of submarine hydrothermal solutions at 21 °N, East Pacific Rise. *Geochim. Cosmochim. Acta* **49**, 2197–2220.
- Walder A. J. and Freedman P. A. (1992) Isotopic ratio measurement using a double focusing magnetic sector mass analyser with an inductively coupled plasma as an ion source. *J. Anal. At. Spectrom.* **7**, 571–575.
- Wang B.-S., You C.-F., Huang K.-F., Wu S.-F., Aggarwal S. K., Chung C.-H. and Lin P.-Y. (2010) Direct separation of boron from Na- and Ca-rich matrices by sublimation for stable isotope measurement by MC-ICP-MS. *Talanta* **82**, 1378–1384.

- Watanabe M., Okino K. and Kodera T. (2010) Rifting to spreading in the southern Lau Basin. *Tectonophysics* **494**, 226–234.
- Wegener A. (1929) *Die Entstehung der Kontinente und Ozeane*. Vieweg, Braunschweig.
- Welhan J. A. and Craig H. (1979) Methane and hydrogen in East Pacific Rise hydrothermal fluids. *Geophys. Res. Lett.* **6**, 829–831.
- Wheat C. G. and Fisher A. T. (2008) Massive, low-temperature hydrothermal flow from a basaltic outcrop on 23 Ma seafloor of the Cocos Plate. *Geochem. Geophys. Geosyst.* **9**, n/a-n/a.
- Wheat C. G., Fisher A. T., McManus J., Hulme S. M. and Orcutt B. N. (2017a) Cool seafloor hydrothermal springs reveal global geochemical fluxes. *Earth Planet. Sci. Lett.* **476**, 179–188.
- Wheat C. G., Fisher A. T., McManus J., Hulme S. M. and Orcutt B. N. (2017b) Cool Seafloor Hydrothermal Springs Reveal Global Geochemical Fluxes. *Earth Planet. Sci. Lett.* **476**, 1–10.
- Wheat C. G., Hartwell A. M., McManus J., Fisher A. T., Orcutt B. N., Schlicht L. E. M., Niedenzu S. and Bach W. (2019) Geology and Fluid Discharge at Dorado Outcrop, a Low Temperature Ridge-Flank Hydrothermal System. *Geochem. Geophys. Geosyst.* **20**, 487–504.
- Wheat C. G., Mottl M. J., Fisher A. T., Kadko D., Davis E. E. and Baker E. (2004) Heat flow through a basaltic outcrop on a sedimented young ridge flank. *Geochem. Geophys. Geosyst.* **5**, n/a-n/a.
- Wilckens F. K., Reeves E. P., Bach W., Meixner A., Seewald J. S., Koschinsky A. and Kasemann S. A. (2018) The influence of magmatic fluids and phase separation on B systematics in submarine hydrothermal vent fluids from back-arc basins. *Geochim. Cosmochim. Acta* **232**, 140–162.
- Wilckens F. K., Reeves E. P., Bach W., Seewald J. S. and Kasemann S. A. (2019) Application of B, Mg, Li, and Sr Isotopes in Acid-Sulfate Vent Fluids and Volcanic Rocks as Tracers for Fluid-Rock Interaction in Back-Arc Hydrothermal Systems. *Geochem. Geophys. Geosyst.* **20**, 5849–5866.
- Williams L. B. and Hervig R. L. (2005) Lithium and boron isotopes in illite-smectite. *Geochim. Cosmochim. Acta* **69**, 5705–5716.
- Williams L. B., Hervig R. L., Holloway J. R. and Hutcheon I. (2001) Boron isotope geochemistry during diagenesis. Part I. Experimental determination of fractionation during illitization of smectite. *Geochim. Cosmochim. Acta* **65**, 1769–1782.
- Williams-Jones A. E. and Heinrich C. A. (2005) 100th Anniversary Special Paper. *Econ. Geol.* **100**, 1287–1312.
- Wilson M. (2007) Partial melting processes in the Earth's upper mantle. In *Igneous Petrogenesis* (ed. M. Wilson). Springer Netherlands. Dordrecht, pp. 32–72.
- Winslow D. M., Fisher A. T., Stauffer P. H., Gable C. W. and Zvoloski G. A. (2016) Three-dimensional modeling of outcrop-to-outcrop hydrothermal circulation on the eastern flank of the Juan de Fuca Ridge. *J. Geophys. Res.* **121**, 1365–1382.
- Wunder B., Meixner A., Romer R. L. and Jahn S. (2011) Li-isotope fractionation between silicates and fluids. *Eur. J. Mineral.* **23**, 333–342.
- Wunder B., Meixner A., Romer R. L., Wirth R. and Heinrich W. (2005) The geochemical cycle of boron. *Lithos* **84**, 206–216.
- Yamaji K., Makita Y., Watanabe H., Sonoda A., Kanoh H., Hirotsu T. and Ooi K. (2001) Theoretical Estimation of Lithium Isotopic Reduced Partition Function Ratio for Lithium Ions in Aqueous Solution. *J. Phys. Chem. A* **105**, 602–613.
- Yamaoka K., Hong E., Ishikawa T., Gamo T. and Kawahata H. (2015a) Boron isotope geochemistry of vent fluids from arc/back-arc seafloor hydrothermal systems in the western Pacific. *Chem. Geol.* **392**, 9–18.
- Yamaoka K., Ishikawa T., Matsubaya O., Ishiyama D., Nagaishi K., Hiroyasu Y., Chiba H. and Kawahata H. (2012) Boron and oxygen isotope systematics for a complete section of oceanic crustal rocks in the Oman ophiolite. *Geochim. Cosmochim. Acta* **84**, 543–559.
- Yamaoka K., Matsukura S., Ishikawa T. and Kawahata H. (2015b) Boron isotope systematics of a fossil hydrothermal system from the Troodos ophiolite, Cyprus. *Chem. Geol.* **396**, 61–73.
- Yang K. and Scott S. D. (1996) Possible contribution of a metal-rich magmatic fluid to a sea-floor hydrothermal system. *Nature* **383**, 420–423.

- Yang K. and Scott S. D. (2002) Magmatic Degassing of Volatiles and Ore Metals into a Hydrothermal System on the Modern Sea Floor of the Eastern Manus Back-Arc Basin, Western Pacific. *Econ. Geol.* **97**, 1079–1100.
- Yang K. and Scott S. D. (2006) Magmatic Fluids as a Source of Metals in Seafloor Hydrothermal Systems. In *Back-Arc Spreading Systems: Geological, Biological, Chemical, and Physical Interactions* (eds. D. M. Christie, C. R. Fisher, S.-M. Lee and S. Givens), pp. 163–184.
- Zack T., Tomascak P. B., Rudnick R. L., Dalpé C. and McDonough W. F. (2003) Extremely light Li in orogenic eclogites. *Earth Planet. Sci. Lett* **208**, 279–290.
- Zajacz Z., Seo J. H., Candela P. A., Piccoli P. M. and Tossell J. A. (2011) The solubility of copper in high-temperature magmatic vapors. *Geochim. Cosmochim. Acta* **75**, 2811–2827.
- Zeininger H. and Heumann K. G. (1983) Boron isotope ratio measurement by negative thermal ionization mass spectrometry. *Int. J. Mass Spectrom. Ion Phys.* **48**, 377–380.
- Zhao R., Shan X., Wu C., Yi J., Hao G. and Wang P. (2019) Formation and evolution of the Changbaishan volcanic geothermal system in a convergent plate boundary back-arc region constrained by boron isotope and gas data. *J. Hydrol.* **569**, 188–202.



## CHAPTER 2:

### SCIENTIFIC CONTRIBUTIONS

---

#### 2.1. *First author manuscripts*

In the scope of this thesis I produced three stand-alone manuscripts (Chapter 3 to 5) as first author but with significant support by affiliated scientists. A brief overview of the research and the particular contributions of the other authors to the three manuscripts are emphasized in the following subchapter.

#### *Chapter 3:*

##### *Boron Hydrothermal Mass Flux and Isotope Signatures in Different Plate Margin Settings*

Lucy E.M. Schlicht<sup>1</sup>, Christian T. Hansen<sup>1,2</sup>, Eoghan P. Reeves<sup>3</sup>, Simone A. Kasemann<sup>1</sup>, Anette Meixner<sup>1</sup>, Wolfgang Bach<sup>1</sup>

<sup>1</sup>Faculty of Geosciences and MARUM-Center for Marine Environmental Sciences, University of Bremen

<sup>2</sup>ICBM- Institute for Chemistry and Biology of the Marine Environment, University of Oldenburg

<sup>3</sup>Department of Earth Science & K.G. Jebsen Centre for Deep Sea Research, University of Bergen

In the manuscript the B and  $\delta^{11}\text{B}$  values of hydrothermal fluids from four ultramafic hosted vents sites (Logatchev, Semenov, Irinovskoe, and Ashadze) at the Mid Atlantic Ridge were investigated. Furthermore, a hydrothermal batch experiment was conducted to study the B elemental partitioning or rather B isotopic fractionation between ultramafic material (fresh olivine) and a synthetic seawater-like fluid at 300 °C and 40 MPa, in analogy to experiments conducted by Hansen *et al.* (2017) at 100 and 200 °C, 40 MPa. Afterwards, the B and  $\delta^{11}\text{B}$  fluid data from ultramafic hosted systems were compared with fluid data of basaltic and felsic hosted vent systems to estimate the total B hydrothermal mass flux and its  $\delta^{11}\text{B}$  composition.

- |                 |  |
|-----------------|--|
| L.E.M. Schlicht | conducted the $\delta^{11}\text{B}$ measurements of the natural and experimental materials; evaluated and interpreted the data; literature review and mass flux constraints; drafted the text, tables and figures of the manuscript. |
| C.T. Hansen     | executed the batch experiment; helped evaluating the experimental data.  |
| E.P. Reeves     | provided the natural fluid samples and their Mg and B concentrations.  |
| S.A. Kasemann   | supervised the $\delta^{11}\text{B}$ measurements; helped with interpretations.  |
| A. Meixner      | supported the $\delta^{11}\text{B}$ measurements in the laboratory.  |
| W. Bach         | supervised the study; helped with the preparation of the manuscript.   |

Further, SEM measurements were performed by P. Witte and A. Türke; B concentrations of the experimental fluids were determined by P. Monien (ICP-MS); TG-DSC measurements were supported by M. Wendschuh; AGFM measurements were performed by T. Fredrichs.

## **Chapter 4:**

### *Boron, Lithium and Strontium Isotopes in a Low-Temperature Ridge Flank Hydrothermal System: Implications for Marine Geochemical Budgets*

Lucy E. M. Schlicht<sup>1</sup>, C. Geoffrey Wheat<sup>2</sup>, Simone A. Kasemann<sup>1</sup>, Anette Meixner<sup>1</sup>, Wolfgang Bach<sup>1</sup>

<sup>1</sup>Faculty of Geosciences and MARUM-Center for Marine Environmental Sciences, University of Bremen

<sup>2</sup>Institute of Marine Science, University of Alaska Fairbanks

In this manuscript the change in B,  $\delta^{11}\text{B}$ , Li,  $\delta^7\text{Li}$  and  $^{87}\text{Sr}/^{86}\text{Sr}$  compositions of low-temperature altered compared to fresh basalts from Dorado Outcrop at the eastern flank of the East Pacific Rise were studied to investigate the geochemical exchange during seafloor weathering. In addition, the  $\delta^7\text{Li}$  and  $^{87}\text{Sr}/^{86}\text{Sr}$  compositions of low-temperature (12.3 °C) fluids were analyzed that discharged at Dorado Outcrop and that is believed to represent a “typical” example of a ridge flank hydrothermal system. The fluid data were used to constrain the impact of ridge flank hydrothermal circulation on global seawater  $\delta^7\text{Li}$  and  $^{87}\text{Sr}/^{86}\text{Sr}$  budgets.

L.E.M. Schlicht	selected and prepared the rock samples; conducted the B and Li concentration measurements of the rock samples and the $\delta^{11}\text{B}$ , $\delta^7\text{Li}$ and $^{87}\text{Sr}/^{86}\text{Sr}$ measurements of the fluid samples; conducted the EMPA, SEM and LA-ICP-MS measurements; evaluated and interpreted the data; literature review; drafted the text, tables and figures of the manuscript.
C.G. Wheat	provided the sample material; supported the preparation of the manuscript.
S.A. Kasemann	supervised the isotope measurements; helped with interpretations.
A. Meixner	supported the isotope measurements in the laboratory.
W. Bach	supervised the study; helped with sample selection; supported the preparation of the manuscript.

The preparation of the rocks and part of the major and trace element measurements was conducted in collaboration with a master student (N. Niedenzu) that worked on the pre-altered characteristics of the basalts. Furthermore, the isotopic compositions of the rocks and fluids were already determined within my master thesis that was submitted in 2017 but the interpretation of the data significantly evolved during my time as a PhD student compared to the initial results. Additionally, P. Witte supported the SEM measurements; S. Sopke supported the EMPA measurements; and P. Monien supported the LA-ICP-MS analyses.

## **Chapter 5:**

### *Boron, Lithium, Strontium and Oxygen Isotope Systematics of Two Hydrothermal Systems in Modern Back-Arc and Arc Crust (PACManus and Brothers Volcano, W-Pacific)*

Lucy E.M. Schlicht<sup>1</sup>, Olivier Rouxel<sup>2</sup>, Jeremy R. Deans<sup>3</sup>, Stephen Fox<sup>4</sup>, Yaron Katzir<sup>4</sup>, Simone A. Kasemann<sup>1</sup>, Anette Meixner<sup>1</sup>, Wolfgang Bach<sup>1</sup>

<sup>1</sup>Faculty of Geosciences and MARUM-Center for Marine Environmental Sciences, University of Bremen

<sup>2</sup>IFREMER, Unité de Géosciences Marines

<sup>3</sup>School of Biological, Environmental, and Earth Sciences, the University of Southern Mississippi

<sup>4</sup>Department of Geological and Environmental Sciences, Ben Gurion University of the Negev

In the manuscript the B and  $\delta^{11}\text{B}$  signatures of altered rocks from drill cores of the eastern Manus back-arc basin (ODP 193) and a fresh rock collected from the surface (SO 216) were investigated. In addition, the B,  $\delta^{11}\text{B}$ , Li,  $\delta^7\text{Li}$  and  $^{87}\text{Sr}/^{86}\text{Sr}$  compositions of altered and fresh rocks received from a drill cruise (IODP 376) and from surface rocks (SO 253) of the Brothers arc volcano were investigated, accompanied by  $\delta^{18}\text{O}$  measurements on quartz separates (IODP 376). The data from both locations were used to make constraints on the effect of permeability contrasts between superposed lithologies on the fluid pathways, w/r-ratios and alteration temperature distributions with depth.

L.E.M. Schlicht	selected and prepared the rock samples; handpicked the quartz separates; conducted the $\delta^{11}\text{B}$ , $\delta^7\text{Li}$ and part of the $^{87}\text{Sr}/^{86}\text{Sr}$ measurements; evaluated and interpreted the data; drafted the text, tables and figures.
O. Rouxel	conducted the B, Li and Sr concentration measurements and part of the $^{87}\text{Sr}/^{86}\text{Sr}$ measurements.
J. R. Deans	helped with sample selection onboard and with manuscript preparation.
S. Fox	conducted the SEM and $\delta^{18}\text{O}$ measurements on the quartz separates.
Y. Katzir	supervised the $\delta^{18}\text{O}$ measurements; helped with interpretations.
S.A. Kasemann	supervised the isotope measurements; helped with interpretations.
A. Meixner	supported the isotope measurements in the laboratory.
W. Bach	supervised the study; helped with the preparation of the manuscript.

S. Fox was supported by J. valley to conduct the  $\delta^{18}\text{O}$  measurements. Two unaltered rock samples from the Brothers volcano and their Sr concentrations were provided by P. Brandl.

## 2.2. *Contributions to related publications*

Beside the three first author manuscripts, I also contributed to the following publications that are related to the research of the thesis:

deRonde C.E.J., Humphris S.E., Höfig T.W., Reyes A., Brandl P.A., Cai L., Cai .F, Caratori Tontini F., Deans J.R., Farough A., Jamieson J.W., Kolandaivelu K.P., Kutovaya A., Labonté J., Martin A.J., Massiot C., McDermott J.M., McIntosh I.M., Nozaki T., Pellizari V.H., Roberts S., Rouxel O., **Schlicht L.E.M.**, Seo J.H., Straub S.M., Strehlow K., Takai K., Tanner D., Tepley II F.J., Zhang C. (2019): Critical role of caldera collapse in the formation of seafloor mineralization: The case of Brothers volcano. *Geology* 47(8), 762-766. doi: 10.1130/G46047.1

deRonde C.E.J., Humphris S.E., Höfig T.W., and the Expedition 376 Scientists (2019): Brothers Arc Flux. *Proceedings of the International Ocean Discovery Program 376*. doi:10.14379/iodp.proc.376.2019

Wheat C.G., Hartwell A.M., McManus J., Fisher A.T., Orcutt B.N., **Schlicht L.E.M.**, Niedenzu S., Bach W. (2019): Geology and fluid discharge at Dorado Outcrop, a low temperature ridge-flank hydrothermal system. *Geochemistry, Geophysics, Geosystems* 20(1), 487-504. doi:10.1029/2018GC007933

### 2.3. Contributions to conferences

The following conference contributions were related to the research of this thesis:

**Schlicht L.E.M.**, Rouxel O., Meixner A., Kasemann S.A., Bach W., and Expedition 376 Scientists (2019): Boron isotopes in hydrothermally altered crust of the Brothers Volcano (Kermadec Arc, New Zealand). *Goldschmidt Conference 2019*, Barcelona, Spain (poster).

Hansen C.T., **Schlicht L.E.M.**, Reeves E.P., Meixner A., Kasemann S.A., Bach W. (2019): Boron isotope behavior in ultramafic-hosted hydrothermal systems: nature vs. experiment. *Goldschmidt Conference 2019*, Barcelona, Spain (poster).

McDermott J.M., Rouxel O., **Schlicht L.E.M.**, Bach W., Stucker V.K., de Ronde C.E.J., Massiot C., and Expedition 376 Scientists (2019): Geochemistry of deep seafloor hydrothermal fluids at Brothers volcano. *Goldschmidt Conference 2019*, Barcelona, Spain (oral presentation, keynote).

Rouxel O., **Schlicht L.E.M.**, Kutovaya A., McDermott J.M. and Expedition 376 Scientists (2019): Geochemical mass balance during hydrothermal alteration of seafloor volcanic rocks at Brothers Volcano, Kermadec Arc. *Goldschmidt Conference 2019*, Barcelona, Spain (poster).

**Schlicht L.E.M.**, Kasemann S.A., Meixner A., Bach W. (2018): Boron isotopes in hydrothermally altered rocks from the Manus basin. *Goldschmidt Conference 2018*, Boston, MA, United States (poster).

Fox S., Katzir Y., Bach W., **Schlicht L.E.M.** (2018): The Influence of Exsolved Magmatic Fluids in Back-Arc Crust: Epidiosites and Base Metals. *Goldschmidt Conference 2018*, Boston, MA, United States (poster).

**Schlicht L.E.M.**, Reeves E.P., Schaen A., Kasemann S.A., Meixner A., Bach W. (2018): Boron systematics of vent fluids from peridotite-hosted hydrothermal systems. *GeoBonn 2018*, Bonn, Germany.

**Schlicht L.E.M.**, Wheat C.G., Kasemann S., Bach W. (2017): Impact of ridge flank hydrothermal systems on the Li and  $\delta^7\text{Li}$  composition of seawater. *GeoBremen 2017*, Bremen, Germany.

### References

Hansen C. T., Meixner A., Kasemann S. A. and Bach W. (2017) New insight on Li and B isotope fractionation during serpentinization derived from batch reaction investigations. *Geochim. Cosmochim. Acta* **217**, 51–79.

# CHAPTER 3:

## BORON HYDROTHERMAL MASS FLUX AND ISOTOPE SIGNATURES IN DIFFERENT PLATE MARGIN SETTINGS

Lucy E.M. Schlicht<sup>1</sup>, Christian T. Hansen<sup>1,2</sup>, Eoghan P. Reeves<sup>3</sup>, Simone A. Kasemann<sup>1</sup>, Anette Meixner<sup>1</sup>, Wolfgang Bach<sup>1</sup>

<sup>1</sup>Faculty of Geosciences and MARUM-Center for Marine Environmental Sciences, University of Bremen, Leobener Str. 8, 28359 Bremen, Germany

<sup>2</sup>ICBM- Institute for Chemistry and Biology of the Marine Environment, University of Oldenburg, Ammerländer Heerstraße 114-118, 26129 Oldenburg, Germany

<sup>3</sup>Department of Earth Science & K.G. Jebsen Centre for Deep Sea Research, University of Bergen, Realfagbygget, Allégt. 41, Norway

---

Manuscript in preparation for submission to *Geology*

### ***Abstract***

Hydrothermal fluid B and  $\delta^{11}\text{B}$  systematics show distinct differences between fast- and slow-spreading divergent and convergent margins due to varying host rock compositions, temperatures, pH, and tectonic settings controlling the fluid pathways. We present new data on B and  $\delta^{11}\text{B}$  systematics in fluids from ultramafic hosted vent sites and assess the particular impact of different plate margin settings and host lithologies on the modern B hydrothermal mass flux and its  $\delta^{11}\text{B}$  composition. Our estimates indicate that mafic hosted systems provide the largest portion of the total hydrothermal B mass flux but also reveal on trend lower  $\delta^{11}\text{B}$  signals in slow-spreading environments due to longer fluid pathways and lower water-to-rock ratios in the strongly tectonic controlled settings. Predicting the past, earlier episodes of accelerated seafloor spreading therefore potentially caused rises in total B hydrothermal mass flux and its  $\delta^{11}\text{B}$ , also important for paleo-seawater  $\delta^{11}\text{B}$  reconstructions.



### 3.1. Introduction

The  $\delta^{11}\text{B}$  record of biogenic carbonates is an important proxy for paleo-seawater pH reconstructions (e.g. Foster & Rae, 2016) but also reflects changes in  $\delta^{11}\text{B}$  of seawater due to varying B input and output fluxes and their  $\delta^{11}\text{B}$  systematics in the past. A careful assessment of these fluxes and  $\delta^{11}\text{B}$  is therefore essential. High-temperature (T) fluid discharge is, beside river flux and expulsion of fluids at convergent margins, one of the major input fluxes controlling seawater B and  $\delta^{11}\text{B}$  signals. Current estimates of the high-T fluid B flux and  $\delta^{11}\text{B}$  are based on altered basalt data (Smith *et al.*, 1995, Lemarchand *et al.*, 2002), which locally show high variability in B and  $\delta^{11}\text{B}$  and are prone to low-T overprints. Hydrothermal fluid B and  $\delta^{11}\text{B}$  data in contrast represent an integrated record of sub-seafloor processes over the whole affected basement and resulting are more suitable for global flux estimates. Indeed, the B and  $\delta^{11}\text{B}$  hydrothermal systematics distinctly vary in different margin settings and due to changing interaction conditions. A full assessment of the role of differing high-T fluid discharge settings on the B and  $\delta^{11}\text{B}$  signals of the hydrothermal mass flux is nevertheless currently missing. In particular,  $\delta^{11}\text{B}$  fluid data on ultramafic hosted systems are lacking, although distinct shifts in B partitioning and isotopic fractionation compared to mafic and felsic hosted systems were assumed (e.g. Foustoukos *et al.*, 2008).

We present B and  $\delta^{11}\text{B}$  data of natural and experimental fluids affected by high-T reactions between ultramafic rocks and seawater, and compare them with published data on basaltic and felsic hosted systems from divergent and convergent margins to assess the relative roles of vent systems in different settings on B and  $\delta^{11}\text{B}$  systematics of modern seawater. This analysis then lets us make predictions for past variations.

### 3.2. Materials and methods

We analyzed the B and  $\delta^{11}\text{B}$  values of fluids from four ultramafic hosted vent sites along the Mid-Atlantic Ridge (MAR) between 12 and 15°N (Logatchev, Semyenov-2, Irinovskoe, Ashadze-2, **Figure A. 1-1**, **Table A. 1-1**). Fluid end member values were calculated by projecting to zero-Mg (**Figure A. 1-2**; **Figure A. 1-3**; **Table A. 1-2**). Further, we used an experimental setup in analogy to Hansen *et al.* (2017) and reacted olivine with a seawater-like fluid (300°C, 40MPa) to investigate mineral alteration (**Figure A. 1-4**; **Table A. 1-3**; **Table A. 1-4**; **Table A. 1-5**), shifts in fluid B and  $\delta^{11}\text{B}$  (**Figure A. 1-5**; **Table A. 1-6**; **Table A. 1-7**), differences in modeled fluid  $\text{pH}_{\text{in situ}}$  and B species (**Figure A. 1-6**), and to compare the results (**Figure A. 1-7**; **Table A. 1-8**). Detailed descriptions of fluid collection, experimental setups and B and  $\delta^{11}\text{B}$  measurements are given in the **Appendix A.1**.

### 3.3. Boron distribution and isotopic fractionation

The partitioning of B between solids and fluids ( $D_{\text{S-F}}^{\text{B}}$ ) strongly depends on T and mineralogy. Mafic and felsic rocks take up B at low-T (<150°C) and release B at high-T (>150°C) during fluid-rock exchange (Spivack & Edmond, 1987). Reaction experiments (Hansen *et al.*, 2017; this study)

between seawater-like fluids and ultramafic material (olivine) also showed a decrease in  $D_{S-F}^B$  with increasing  $T$  (**Figure 3.3-1A**) but in contrast to mafic and felsic rocks the uptake of B by ultramafic alteration products (mainly serpentine) is even at  $T=300^\circ\text{C}$  still significant. Fluid pH seems to have a minor effect on  $D_{S-F}^B$  based on the similar  $D_{S-F}^B$  derived from experiments involving ultramafics over a range of differing pH (4.2 to 7.9, **Figure 3.3-1A**).

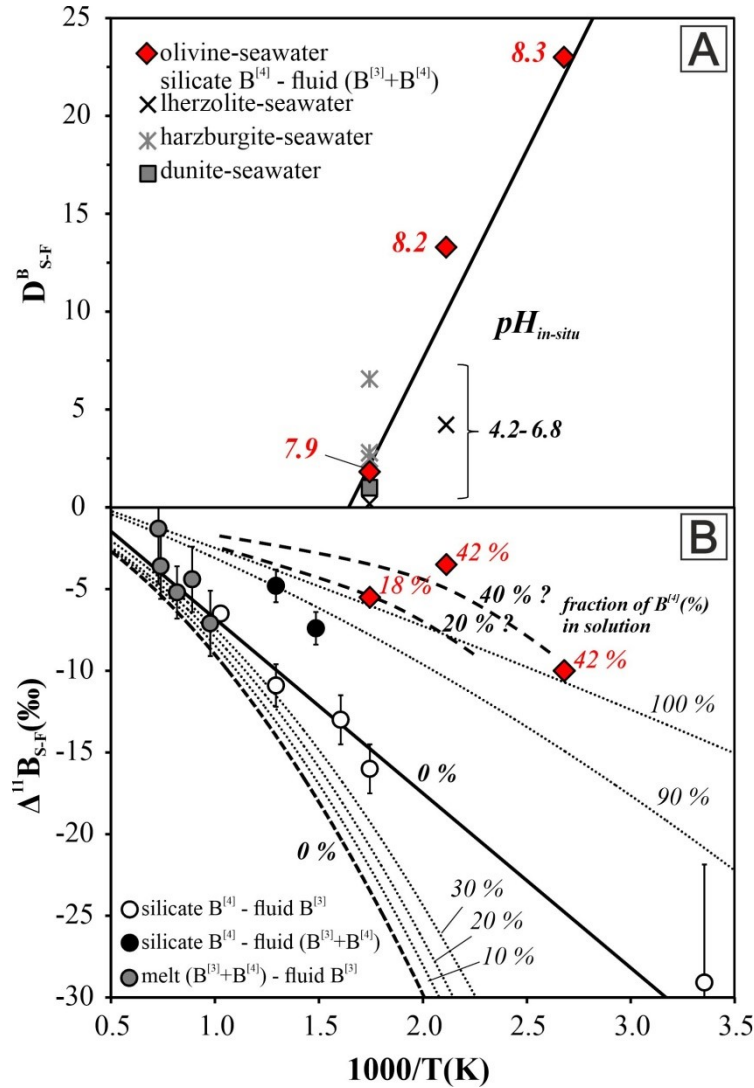


**Figure 3.3-1:** Experimental results of this study and Hansen et al. (2017) (red diamonds), compared to literature data. (A)  $D_{S-F}^B$  versus  $T$ . Italic numbers show the fluid pH. The linear regression ( $r^2=0.85$ ,  $p<0.05$ ) gives  $D_{S-F}^B=21.293 \cdot 1000/T(K) - 35.028$  (valid up to  $334^\circ\text{C}$ ). Literature data were compiled by Foustoukos et al. (2008) based on studies by Seyfried & Dibble (1980), Janecky (1982), and Janecky & Seyfried (1986). (B)  $\Delta^{11}B_{S-F}$  between solids ( $B^{[4]}$ ) and fluids with differing fractions of  $B^{[4]}$  (italic numbers) versus  $T$ . The bold solid line shows  $\Delta^{11}B_{S-F}=-10.60 \cdot 1000/T(K)+3.88$ , after Wunder et al. (2005) based on experimental data also shown in here (Palmer et al., 1987; Williams et al., 2001; Hervig et al., 2002; Wunder et al., 2005). The dotted and lower dashed lines show the  $\Delta^{11}B_{S-F}$  with varying  $T$  and  $B^{[4]}$  fractions in solution based on ab initio predictions by Kowalski et al. (2013). The upper dashed lines show the suggested  $\Delta^{11}B_{S-F}$  for 20 and 40 %  $B^{[4]}$  fractions based on this results.

The  $\delta^{11}\text{B}$  fractionation between solids and fluids intensifies with decreasing  $T$  (**Figure 3.3-1B**). But further,  $\delta^{11}\text{B}$  fractionation is also sensitive for fluid pH shifts because the pH in solutions controls

the B species abundances of differing  $\delta^{11}\text{B}$ ; such that the low-pH  $\text{B}^{[3]}$  species has  $^{11}\text{B}$  enriched whereas the high-pH  $\text{B}^{[4]}$  species is passively enriched in  $^{10}\text{B}$  (Spivack & Edmond, 1987). The  $\delta^{11}\text{B}$  fractionation occurs by exchange of opposite coordinated B species in the interacting fluid and solid. Typical B alteration host minerals in hydrothermal systems (phyllosilicates) are  $\text{B}^{[4]}$  but fluid pH and related B speciation in fluids vary between host lithologies. Mafic hosted systems show low fluid pH ( $\leq 4$ ) and a dominance of  $\text{B}^{[3]}$  in the fluid whereas serpentinization of ultramafics can lead to high fluid pH (Foustoukos *et al.*, 2008) and to a relative increase in  $\text{B}^{[4]}$  fraction in the fluid. Therefore, a decreased  $\delta^{11}\text{B}$  fractionation in ultramafic versus basaltic systems can be expected.

Several B isotope exchange experiments between various mafic silicates ( $\text{B}^{[4]}$ ) and acidic fluids ( $\text{B}^{[3]}$ ) were conducted that show a linear correlation of  $\delta^{11}\text{B}$  fractionation and T with minor variance between the differing mineral phases (**Figure 3.3-1B**). Experiments on  $\delta^{11}\text{B}$  fractionation that were conducted under more alkaline conditions are very sparse (Wunder *et al.*, 2005) but point to the expected lowering in fractionation with increasing fractions of  $\text{B}^{[4]}$  in solution, further confirmed by ab initio calculations (Kowalski *et al.*, 2013). Our experiments under alkaline conditions (18 to 42%  $\text{B}^{[4]}$  fractions in fluid) are in line with these suggestions although the obtained absolute  $\delta^{11}\text{B}$  fractionations are even lower than predicted by ab initio calculations under the assumption that solely  $\text{B}^{[4]}$  is present (**Figure 3.3-1B**). This indicates that the factors controlling  $\delta^{11}\text{B}$  fractionation as a function of B speciation in solution are still incompletely understood.

#### **3.4. Boron and boron isotope signatures of peridotite versus volcanic hosted systems**

Our vent fluid data of ultramafic hosted systems and experimentally derived  $D_{\text{S-F}}^{\text{B}}$  and  $\Delta^{11}\text{B}_{\text{S-F}}$  values allow us to quantify B partitioning and isotope fractionation for this class of vents and to compare them to other classes, i.e. basalt hosted vents along ridges and felsic rock hosted systems in arcs. Based on these comparisons, we derive constraints on the impact of host lithology, T, w/r ratios and pH in different margin settings on fluid B and  $\delta^{11}\text{B}$  systematics.

High-T fluids (up to 362 °C) from ultramafic-hosted vents at the MAR show depletion in B relative to seawater (**Figure 3.4-1**), in agreement with  $D_{\text{S-F}}^{\text{B}}$  towards the solid (**Figure 3.3-1A**). Basalt-hosted high-T fluids are in contrast enriched in B relative to seawater due to enhanced  $D_{\text{S-F}}^{\text{B}}$  into fluids at elevated temperatures (**Figure 3.4-1**). The slight decrease in B in fluids from the TAG hydrothermal vents can either be explained by interaction with ultramafic rocks hidden under the basaltic cap exposed at the seafloor or by mixing with fluids depleted in B due to previous low-T basalt-fluid interaction during recharge (Palmer, 1996). The fluid  $\delta^{11}\text{B}$  values of both classes of systems are lower than seawater because of exchange with mantle material or basaltic crust of low  $\delta^{11}\text{B}$  (both  $-7.1 \pm 0.9\%$ , Marschall *et al.*, 2017). The similar range in  $\delta^{11}\text{B}$  of fluids reacted with ultramafic rocks and basalts further points to similar  $\Delta^{11}\text{B}_{\text{S-F}}$  values for both host lithologies. This can be explained by the low pH ( $\leq 6.7$ ) of the peridotite hosted fluids, which is due to fluid-rock reactions in the basement at temperatures ( $>340^\circ\text{C}$ ) where talc-tremolite alteration of pyroxene and

not serpentinization of olivine set the fluid pH to values similar to fluid reactions with basalts (Allen & Seyfried, 2003), and certainly well within the field of  $B^{[3]}$  dominance in solution.

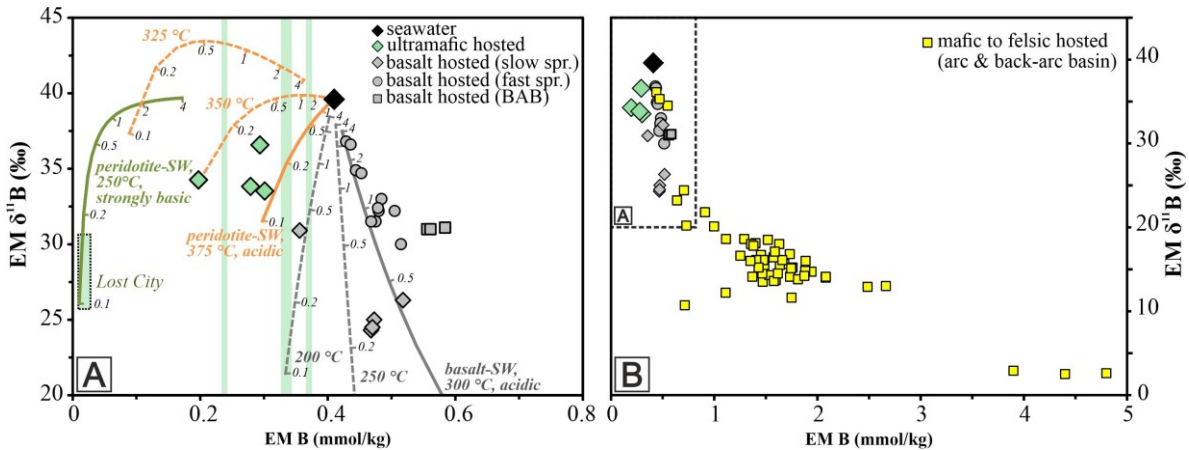


**Figure 3.4-1:** EM B and  $\delta^{11}B$  of seawater, and fluids from ultramafic (this study), basalt hosted (slow and fast spreading (spr.) rates) and arc/back-arc vents (BAB, Spivack & Edmond, 1987; James *et al.*, 1995; Yamaoka *et al.*, 2015; Wilckens *et al.*, 2018). (A) Vertical bars show additional fluid EM B of ultramafic systems (Schmidt *et al.*, 2007; Seyfried *et al.*, 2011; Tao *et al.*, 2020). The green box shows the fluid B and  $\delta^{11}B$  of Lost City estimated by Foustoukos *et al.* (2008). The lines predict the fluid B and  $\delta^{11}B$  variation for reaction of seawater (0.41 mmol/kg, 39.6 ‰) with basalt (1  $\mu\text{g/g}$ , -7.1 ‰) or ultramafics (0.2  $\mu\text{g/g}$ , -7.1 ‰) for different w/r ratios (italic numbers), calculated after Yamaoka *et al.* (2015). For reaction with acidic fluids, we assumed fluids only contain  $B^{[3]}$  and used the equation by Wunder *et al.* (2005) to estimate  $\Delta^{11}B_{S-F}$  (Figure 3.3-1B). For basaltic systems, we assumed a  $D_{S-F}^B$  of 0.1 (300 °C), 0.2 (250 °C), and 0.3 (200 °C) after Yamaoka *et al.* (2012). For ultramafic systems, we used the equation resulting from Figure 3.3-1A to estimate the  $D_{S-F}^B$  if  $T \leq 334$  °C; further we assumed 0.1 (375 °C), and 0.2 (350 °C). In addition, we calculated the fluid values for a Lost City-like system,  $T=250$  °C (Foustoukos *et al.*, 2008) and strongly basic fluids ( $pH_{in-situ} > 9$ ), predicting  $B^{[4]}$  is the only present species in solution and assuming a minimal  $\Delta^{11}B_{S-F}$  of -1 ‰. (B) shows fluids from arc/back-arc basins in addition.

Fluids from basalt-hosted vents at slow-spreading ridges show on average a more fractionated  $\delta^{11}B$  signature relative to seawater and larger variation than at fast-spreading ridges. Calculations after Yamaoka *et al.* (2015) combined with  $T$ ,  $D_{S-F}^B$  and  $\Delta^{11}B_{S-F}$  constraints from this work demonstrate that a stronger  $\delta^{11}B$  fractionation can result from reactions at lower  $T$  or from a lower w/r ratios and the associated rock-dominated  $\delta^{11}B$  fluid signature (Figure 3.4-1A). A higher variability in  $T$  and w/r ratios at the more tectonically controlled slow-spreading versus fast-spreading ridges is likely to cause the larger spread in  $\delta^{11}B$  due to a more heterogeneous thermal regime, deeper infiltration of fluids, longer reaction pathways and large contrasts in w/r ratios between block interiors and faults (cf. Palmer, 1996). The calculations also indicate that the higher  $\delta^{11}B$  values of high- $T$  fluids from ultramafic-hosted vents in comparison with the basalt-hosted ones at slow-spreading ridges are likely caused by the extremely low initial B contents of the mantle rocks (<0.2  $\mu\text{g/g}$ ) relative to basalts (1  $\mu\text{g/g}$ ), leading to a more seawater dominated signal of high  $\delta^{11}B$  (+39.6 ‰) in the fluids. Our calculations further show that stronger B depletion and isotopic fractionation can be reached for

a Lost-City-like hydrothermal system at  $T=250^{\circ}\text{C}$  (Foustoukos *et al.*, 2008), although absolute isotopic fractionation is likely smaller than for higher-T systems due to the high fluid  $\text{pH}\geq 9$  and the dominance of  $\text{B}^{[4]}$  in solution (**Figure 3.3-1B**).

Fluids from subduction-influenced settings show higher B and  $\delta^{11}\text{B}$  signatures than those from ridges and mature back-arc spreading centers (**Figure 3.4-1B**). This is due to higher B contents of more felsic host rocks in arcs (up to  $30\ \mu\text{g/g}$ , Palmer, 1991) compared to mid-ocean ridge basalts, caused by B influx from the subducting slab. Beside highly variable B and  $\delta^{11}\text{B}$  host rock compositions, parameters like T, water depth, and fluid acidity are also much more variable at arcs than ridges and further facilitate the wide range in fluid B and  $\delta^{11}\text{B}$  at arcs.

### 3.5. Global hydrothermal boron mass fluxes and boron isotopic compositions

The B and  $\delta^{11}\text{B}$  composition of seawater ( $433\pm 34\ \mu\text{mol/kg}$ ;  $+39.6\text{‰}$ ) is globally uniform due to the long residence time of B in seawater ( $10^7$  years) compared to mixing time in the oceans ( $10^3$  years), but it may change over time because of fluctuating input and output fluxes (Lemarchand *et al.*, 2002). Input fluxes to the oceans are from rivers, high-T hydrothermal discharge, and fluid expulsions at convergent margins and are balanced by output fluxes due to uptake of B by crustal weathering, adsorption to marine sediments, and co-precipitation in carbonates, biogenic silica and evaporites (Lemarchand *et al.*, 2002; Simon *et al.*, 2006). In the following chapter, we use B and  $\delta^{11}\text{B}$  data of natural fluids and water flux constraints for different settings of fluid discharge to assess the individual impacts on global B hydrothermal mass flux and  $\delta^{11}\text{B}$  compositions on modern seawater and make some assumptions for past variations.

**Table 3.5-1: Boron input fluxes to seawater and their  $\delta^{11}\text{B}$  values. Errors are 2sd.**

	B ( $\mu\text{mol/kg}$ )	B flux $\times 10^9$ (mol/yr)	$\delta^{11}\text{B}$ ( $\text{‰}$ )
<b>Input fluxes (weighted average)</b>		<b>50.7</b>	<b>15</b>
<b>Hydrothermal fluids (weighted average)</b>		<b>11.4</b>	<b>29 <math>\pm</math> 6</b>
at divergent margins (spreading $\leq 40\text{mm/year}$ )			
ultramafic hosted	$283 \pm 122^{\text{a,b,c}}$	$0.7 \pm 0.3^{\text{d,e}}$	$35 \pm 3^{\text{c}}$
basaltic hosted	$448 \pm 167^{\text{f}}$	$2.5 \pm 0.9^{\text{d,e}}$	$27 \pm 7^{\text{f}}$
at divergent margins (spreading $\geq 40\text{mm/year}$ )	$470 \pm 55^{\text{f,g}}$	$6.5 \pm 0.7^{\text{d}}$	$33 \pm 4^{\text{f,g}}$
at convergent margins (submarine arcs)	$800^{\text{h,i}}$	$1.7^{\text{j}}$	$17 \pm 11^{\text{i}}$
<b>Rivers</b>		<b>35.1<sup>k</sup></b>	<b>10<sup>k</sup></b>
<b>Fluid expulsions at convergent margins</b>		<b>4.2<sup>l</sup></b>	<b>24 <math>\pm</math> 5<sup>m</sup></b>
Modern seawater	$433 \pm 34^{\text{n,o}}$		$39.61 \pm 0.04^{\text{o}}$

References: (a) Schmidt *et al.* (2007), (b) Seyfried *et al.* (2011), Tao *et al.* (2020), (c) this study, (d) Baker (2007), (e) Beaulieu & Szafranski (2019), (f) James *et al.* (1995), (g) Spivack & Edmond (1987), (h) Kleint *et al.* (2019), (i) Yamaoka *et al.* (2015), Wilckens *et al.* (2018), (j) Baker *et al.* (2008), (k) Gaillardet & Lemarchand (2018), and references therein, (l) Kastner *et al.* (2014), (m) Saffer & Kopf (2016), (n) Lee *et al.* (2010), (o) Foster *et al.* (2010).

For our hydrothermal B mass flux and  $\delta^{11}\text{B}$  constraints, we discriminated four different settings of fluid discharge (references are listed in **Table 3.5-1**): slow- and ultra-slow-spreading ( $\leq 40\text{mm/year}$ ) ridges with (1) ultramafic, and (2) basaltic basement; (3) fast-spreading ( $\geq 40\text{mm/year}$ ) ridges; and (4) submarine volcanic arcs and back-arc crust with arc-like basement composition. The B mass flux for each separate setting was calculated based on the average fluid B values combined with published heat flux estimates, assuming  $T=350^\circ\text{C}$  and a specific heat capacity of seawater of  $4\text{kJ}/(\text{kg}\cdot\text{K})$ . The estimated  $800\mu\text{mol}/\text{kg}$  B for setting (4) is between ‘black smoker’-type fluids with high B values (up to  $2664\mu\text{mol}/\text{kg}$ , Wilckens *et al.*, 2018) and ‘acid sulfate’-type fluids with more seawater-like B signatures (around  $450\mu\text{mol}/\text{kg}$ ); both types are common in subduction related systems but with unknown relative abundance. For settings (1)-(3), Baker (2007) estimated a total minimal heat flux of  $1.1\text{TW}$ ;  $0.7\text{TW}$  at fast-spreading ( $\geq 40\text{mm/year}$ ) and  $0.4\text{TW}$  at slow-spreading ( $\leq 40\text{mm/year}$ ) axis. The proportions of heat flux at ultramafic (30%) versus mafic (70%) hosted systems at slow-spreading margins were estimated based on the confirmed abundance of ultramafic and mafic hosted vent fields at slow ( $\leq 40\text{mm/year}$ ) spreading margins (Beaulieu & Szafranski, 2019) and by assuming a similar heat flux for both types. The latter assumption is supported by the similarity in heat flux estimates for individual sites of ultramafic ( $1320\pm 600\text{MW}$ , Rainbow, Jean-Baptiste *et al.*, 2004) and mafic ( $1700\text{MW}$ , TAG, Wichers *et al.*, 2005) hosted systems along the MAR. However, Beaulieu *et al.* (2015) suggested that 75% of global vent systems are still undiscovered, and half of them are suggested to be hosted at slow- and ultra-slow-spreading margins. Further, the mass flux of Lost-City-type vent sites of unique B and  $\delta^{11}\text{B}$  signatures (**Figure 3.4-1A**) is still difficult to assess due to challenges to detect the low-T and particle poor discharge sites (Larson *et al.*, 2015). Nevertheless, the existing B and  $\delta^{11}\text{B}$  fluid data give first clues for estimating the impact of four different settings on the magnitude and  $\delta^{11}\text{B}$  composition of hydrothermal B flux.

Our calculations (**Table 3.5-1**) indicate a total weighted average B flux of  $11.4\times 10^9\text{mol}/\text{year}$ , which corresponds to  $\sim 30\%$  of the river flux. The  $\delta^{11}\text{B}$  of hydrothermal discharge into the oceans is  $+29\pm 6\%$ . Basalt hosted systems account for the largest portion of B high-T fluid flux (total of 79%), with 57% related to venting at fast-spreading and 22% related to venting at slow-spreading ridges. Ultramafic hosted systems deliver the smallest B portion (6%) towards seawater of the four settings due to the removal of B from fluids even at high-T (**Figure 3.3-1A**, **Figure 3.4-1**) and the smallest estimated contribution to global heat flux. The calculated B mass flux (15%) from arcs and back-arcs probably represents a lower estimate because of the high variance in host rock types, influence of the subducting slab, and still unresolved relative abundance of black smoker- and acid-sulfate type fluids that all could result in a significant shift in B concentrations of fluids.

The average  $\delta^{11}\text{B}$  value of high-T fluids from hydrothermal systems hosted in ultramafic crust is very similar to fluids from basalt-hosted vents at fast-spreading ridges. This average could be lower

if Lost City-like systems were more abundant than they currently appear to be. Because these systems are more difficult to detect they may indeed be underrepresented in our compilation. In contrast, the  $\delta^{11}\text{B}$  composition of hydrothermal B flux from basalt-hosted systems at slow-spreading margins shows more variability and a tendency towards lower  $\delta^{11}\text{B}$  compared to fast-spreading settings. The average  $\delta^{11}\text{B}$  estimated for fluids from arcs and back-arcs is the lowest of the four settings and therefore leads to distinct lowering of the  $\delta^{11}\text{B}$  of the total weighted average of the high-T fluid B flux.

The observed variance in high-T B fluxes and  $\delta^{11}\text{B}$  for different settings and especially fast- versus slow-spreading rates also have potential implications for past seawater composition, given that spreading rates may have been greater for most parts of the Late Phanerozoic (e.g. Conrad & Lithgow-Bertelloni, 2007; Seton *et al.*, 2009). For example, an increase in global average spreading rates in the Early Cretaceous (92 mm/a, Seton *et al.*, 2009) versus today (60 mm/a) would mean an increase in total B hydrothermal mass flux and  $\delta^{11}\text{B}$  from  $11.4 \cdot 10^9$  mol/year and +29 ‰ (today) to  $17.9 \cdot 10^9$  mol/year and +31 ‰ (Early Cretaceous). The assumptions underlying this estimate are: (1) all oceanic spreading ridges were fast and the total heat flux was 1.65 TW, and (2) the heat flux at convergent settings was 10 % of the heat flux at divergent margins, and (3) the average fluid B concentrations was uniform in time. The increase in total heat flux at divergent plate boundaries from 1.1 TW (today) to 1.65 TW (Cretaceous) was assumed based on the minimal heat flux of approximately 25 MW/(km of axis) given for a spreading rate of 92 mm/a (Baker, 2007) matching the Cretaceous, combined with assuming equal total length of divergent axis 66.000 km (today) and 64.000 km (Seton *et al.*, 2009).

Our estimates highlight the importance of the margin setting of fluid discharge on the hydrothermal B fluxes and  $\delta^{11}\text{B}$  values. One important aspect is the indicated impact of fluctuating seafloor spreading rates in the geological past on high-T fluid B fluxes and  $\delta^{11}\text{B}$  compositions.

### ***Acknowledgments***

The authors thank the shipboard participants of *RV METEOR M126*, including the crews and pilots of *MARUM QUEST*. We also thank P. Witte, A. Türke, M. Wendschuh, T. Frederichs, and P. Monien for support performing the measurements. This research was funded by the GIF Grant I-1357-301.8/2016.

### ***References***

- Allen D. E. and Seyfried W. E. (2003) Compositional controls on vent fluids from ultramafic-hosted hydrothermal systems at mid-ocean ridges. *Geochim. Cosmochim. Acta* **67**, 1531–1542.
- Baker E. T. (2007) Hydrothermal cooling of midocean ridge axes. *Earth Planet. Sci. Lett* **263**, 140–150.
- Baker E. T., Embley R. W., Walker S. L., Resing J. A., Lupton J. E., Nakamura K.-i., de Ronde C. E. J. and Massoth G. J. (2008) Hydrothermal activity and volcano distribution along the Mariana arc. *J. Geophys. Res.* **113**, 47.

- Beaulieu S. E., Baker E. T. and German C. R. (2015) Where are the undiscovered hydrothermal vents on oceanic spreading ridges? *Deep Sea Research Part II: Topical Studies in Oceanography* **121**, 202–212.
- Beaulieu S. E. and Szafranski K. (2019) InterRidge Global Database of Active Submarine Hydrothermal Vent Fields, Version 3.4. *World Wide Web electronic publication available from <http://vents-data.interridge.org>* (accessed 2020-04-06).
- Conrad C. P. and Lithgow-Bertelloni C. (2007) Faster seafloor spreading and lithosphere production during the mid-Cenozoic. *Geology* **35**, 29.
- Foster G. L., Pogge von Strandmann P. A. E. and Rae J. W. B. (2010) Boron and magnesium isotopic composition of seawater. *Geochem. Geophys. Geosyst.* **11**.
- Foster G. L. and Rae J. W. (2016) Reconstructing Ocean pH with Boron Isotopes in Foraminifera. *Annu. Rev. Earth Planet. Sci.* **44**, 207–237.
- Foustoukos D. I., Savov I. P. and Janecky D. R. (2008) Chemical and isotopic constraints on water/rock interactions at the Lost City hydrothermal field, 30°N Mid-Atlantic Ridge. *Geochim. Cosmochim. Acta* **72**, 5457–5474.
- Gaillardet J. and Lemarchand D. (2018) Boron in the Weathering Environment. In *Boron Isotopes - The Fifth Element* (eds. H. Marschall and G. Foster). Springer, Cham, pp. 163–188.
- Hansen C. T., Meixner A., Kasemann S. A. and Bach W. (2017) New insight on Li and B isotope fractionation during serpentinization derived from batch reaction investigations. *Geochim. Cosmochim. Acta* **217**, 51–79.
- Hervig R. L., Moore G. M., Williams L. B., Peacock S. M., Holloway J. R. and Roggensack K. (2002) Isotopic and elemental partitioning of boron between hydrous fluid and silicate melt. *Amer. Miner.* **87**, 769–774.
- James R. H., Elderfield H. and Palmer M. R. (1995) The chemistry of hydrothermal fluids from the Broken Spur site, 29°N Mid-Atlantic ridge. *Geochim. Cosmochim. Acta* **59**, 651–659.
- Janecky D. R. (1982) Serpentinization of peridotite within the oceanic crust; experimental and theoretical investigations of seawater-peridotite interaction at 200C and 300C, 500 bars. *Thesis, University of Minnesota at Minneapolis, MN, USA*.
- Janecky D. R. and Seyfried W. E. (1986) Hydrothermal serpentinization of peridotite within the oceanic crust. *Geochim. Cosmochim. Acta* **50**, 1357–1378.
- Jean-Baptiste P., Fourné E., Charlou J.-L., German C. R. and Radford-Knoery J. (2004) Helium isotopes at the Rainbow hydrothermal site (Mid-Atlantic Ridge, 36°14'N). *Earth Planet. Sci. Lett* **221**, 325–335.
- Kastner M., Solomon E. A., Harris R. N. and Torres M. E. (2014) Fluid Origins, Thermal Regimes, and Fluid and Solute Fluxes in the Forearc of Subduction Zones. In *Earth and Life Processes Discovered from Subseafloor Environments - A Decade of Science Achieved by the Integrated Ocean Drilling Program (IODP)* (eds. R. Stein, D. Blackman, F. Inagaki and H.-C. Larsen). Elsevier, pp. 671–733.
- Kleint C., Bach W., Diehl A., Fröhberg N., Garbe-Schönberg D., Hartmann J. F., de Ronde C. E. J., Sander S. G., Strauss H., Stucker V. K., Thal J., Zitoun R. and Koschinsky A. (2019) Geochemical characterization of highly diverse hydrothermal fluids from volcanic vent systems of the Kermadec intraoceanic arc. *Chem. Geol.* **528**, 119289.
- Kowalski P. M., Wunder B. and Jahn S. (2013) Ab initio prediction of equilibrium boron isotope fractionation between minerals and aqueous fluids at high P and T. *Geochim. Cosmochim. Acta* **101**, 285–301.
- Larson B. I., Lang S. Q., Lilley M. D., Olson E. J., Lupton J. E., Nakamura K. and Buck N. J. (2015) Stealth export of hydrogen and methane from a low temperature serpentinization system. *Deep Sea Research Part II: Topical Studies in Oceanography* **121**, 233–245.
- Lee K., Kim T.-W., Byrne R. H., Millero F. J., Feely R. A. and Liu Y.-M. (2010) The universal ratio of boron to chlorinity for the North Pacific and North Atlantic oceans. *Geochim. Cosmochim. Acta* **74**, 1801–1811.
- Lemarchand D., Gaillardet J., Lewin É. and Allègre C. (2002) Boron isotope systematics in large rivers. *Chem. Geol.* **190**, 123–140.
- Marschall H. R., Wanless V. D., Shimizu N., Pogge von Strandmann P. A., Elliott T. and Monteleone B. D. (2017) The boron and lithium isotopic composition of mid-ocean ridge basalts and the mantle. *Geochim. Cosmochim. Acta* **207**, 102–138.

- Palmer M. R. (1991) Boron-isotope systematics of Halmahera arc (Indonesia) lavas. *Geology* **19**, 215.
- Palmer M. R. (1996) Hydration and uplift of the oceanic crust on the Mid-Atlantic Ridge associated with hydrothermal activity. *Geophys. Res. Lett.* **23**, 3479–3482.
- Palmer M. R., Spivack A. J. and Edmond J. M. (1987) Temperature and pH controls over isotopic fractionation during adsorption of boron on marine clay. *Geochim. Cosmochim. Acta* **51**, 2319–2323.
- Saffer D. M. and Kopf A. J. (2016) Boron desorption and fractionation in Subduction Zone Fore Arcs. *Geochem. Geophys. Geosyst.* **17**, 4992–5008.
- Schmidt K., Koschinsky A., Garbe-Schönberg D., Carvalho L. M. de and Seifert R. (2007) Geochemistry of hydrothermal fluids from the ultramafic-hosted Logatchev hydrothermal field, 15°N on the Mid-Atlantic Ridge. *Chem. Geol.* **242**, 1–21.
- Seton M., Gaina C., Muller R. D. and Heine C. (2009) Mid-Cretaceous seafloor spreading pulse. *Geology* **37**, 687–690.
- Seyfried W. E. and Dibble W. E. (1980) Seawater-peridotite interaction at 300°C and 500 bars. *Geochim. Cosmochim. Acta* **44**, 309–321.
- Seyfried W. E., Pester N. J., Ding K. and Rough M. (2011) Vent fluid chemistry of the Rainbow hydrothermal system (36°N, MAR). *Geochim. Cosmochim. Acta* **75**, 1574–1593.
- Simon L., Lécuyer C., Maréchal C. and Coltice N. (2006) Modelling the geochemical cycle of boron. *Chem. Geol.* **225**, 61–76.
- Smith H., Spivack A. J., Staudigel H. and Hart S. R. (1995) The boron isotopic composition of altered oceanic crust. *Chem. Geol.* **126**, 119–135.
- Spivack A. and Edmond J. (1987) Boron isotope exchange between seawater and the oceanic crust. *Geochim. Cosmochim. Acta* **51**, 1033–1043.
- Tao C., Seyfried W. E., Lowell R. P., Liu Y., Liang J., Guo Z., Ding K., Zhang H., Liu J., Qiu L., Egorov I., Liao S., Zhao M., Zhou J., Deng X., Li H., Wang H., Cai W., Zhang G., Zhou H., Lin J. and Li W. (2020) Deep high-temperature hydrothermal circulation in a detachment faulting system on the ultra-slow spreading ridge. *Nat. Commun.* **11**, 1300.
- Wichers S., Reves-Sohn R. and Terray G. (2005) New constraints on the thermal power of the TAG hydrothermal system and the dynamics of the water column plume. *Eos Trans. AGU 86 Fall Meet. Suppl. (Abstract OS33A-1466)*.
- Wilckens F. K., Reeves E. P., Bach W., Meixner A., Seewald J. S., Koschinsky A. and Kasemann S. A. (2018) The influence of magmatic fluids and phase separation on B systematics in submarine hydrothermal vent fluids from back-arc basins. *Geochim. Cosmochim. Acta* **232**, 140–162.
- Williams L. B., Hervig R. L., Holloway J. R. and Hutcheon I. (2001) Boron isotope geochemistry during diagenesis. Part I. Experimental determination of fractionation during illitization of smectite. *Geochim. Cosmochim. Acta* **65**, 1769–1782.
- Wunder B., Meixner A., Romer R. L., Wirth R. and Heinrich W. (2005) The geochemical cycle of boron. *Lithos* **84**, 206–216.
- Yamaoka K., Hong E., Ishikawa T., Gamo T. and Kawahata H. (2015) Boron isotope geochemistry of vent fluids from arc/back-arc seafloor hydrothermal systems in the western Pacific. *Chem. Geol.* **392**, 9–18.
- Yamaoka K., Ishikawa T., Matsubaya O., Ishiyama D., Nagaishi K., Hiroyasu Y., Chiba H. and Kawahata H. (2012) Boron and oxygen isotope systematics for a complete section of oceanic crustal rocks in the Oman ophiolite. *Geochim. Cosmochim. Acta* **84**, 543–559.



## CHAPTER 4: BORON, LITHIUM AND STRONTIUM ISOTOPES IN A LOW- TEMPERATURE RIDGE FLANK HYDROTHERMAL SYSTEM: IMPLICATIONS FOR MARINE GEOCHEMICAL BUDGETS

Lucy E. M. Schlicht<sup>1</sup>, C. Geoffrey Wheat<sup>2</sup>, Simone A. Kasemann<sup>1</sup>, Anette Meixner<sup>1</sup>,  
Wolfgang Bach<sup>1</sup>

<sup>1</sup>Faculty of Geosciences and MARUM-Center for Marine Environmental Sciences, University of Bremen,  
Leobener Str. 8, 28359 Bremen, Germany

<sup>2</sup>Institute of Marine Science, University of Alaska Fairbanks, PO Box 475, Moss Landing, CA 95039, USA

---

Manuscript submitted to *Geochimica et Cosmochimica Acta*  
on the 10<sup>th</sup> of January, 2020 (manuscript reference no. *GCA-D-20-00035*)

### **Abstract**

Low-temperature alteration of basaltic crust in ridge-flank hydrothermal systems (RFHS) is believed to be one of the major sinks for Li and B in the oceans, but the magnitude of this removal flux is poorly constrained. We present Li and Sr isotopic compositions of hydrothermal fluids and Li, Sr and B contents and isotopic compositions of fresh glass, low-temperature altered basalts and a vein separate that were collected at the discharge site of a RFHS at the Cocos Plate, named Dorado Outcrop. The hydrothermal end-member fluid is depleted in Li ( $25.0 \pm 0.3 \mu\text{mol Li/kg}$  (1sd)) with a higher  $\delta^7\text{Li}$  value ( $+31.9 \text{ ‰}$ ) relative to bottom seawater ( $26.2 \pm 0.3 \mu\text{mol Li/kg}$  (1sd), and  $+31.2 \pm 0.2 \text{ ‰}$ ). The higher  $\delta^7\text{Li}$  value of the fluid is sufficient to explain 7 to 27 % of the observed shift in  $\delta^7\text{Li}$  seawater composition ( $+31 \text{ ‰}$  vs.  $+16.5 \text{ ‰}$ ) and potentially flank alteration has an even higher impact on seawater composition if globally representative reaction temperatures in RFHS are lower than at Dorado Outcrop ( $\sim 12.3 \text{ °C}$ ). The  $^{87}\text{Sr}/^{86}\text{Sr}$  composition of fluids at Dorado Outcrop is identical to ambient seawater and gives no indication of exchange with the basaltic crust at pertinent timescales ( $< 10$  years) and at the measured temperatures. The  $\delta^7\text{Li}$  values of altered rocks and a vein separate point to an alteration end-member composition close to  $+8 \text{ ‰}$  and are higher than fresh glass of  $+4.3 \pm 0.2 \text{ ‰}$ . However, altered rock  $\delta^7\text{Li}$  values at Dorado Outcrop are low compared to previously published data of seafloor weathered rocks and potentially indicate interaction with isotopically light paleo-seawater ( $+27 \text{ ‰}$ ), shortly after formation of the outcrop (18.5 to 23 Ma). The altered rocks show a uniform  $\delta^{11}\text{B}$  value of approximately  $+4 \text{ ‰}$  and are enriched in the heavy isotope compared to fresh glass of  $-2.4 \pm 0.1 \text{ ‰}$ , in agreement with assumptions of minor  $\delta^{11}\text{B}$  seawater variations over the last 20 Myr. A vein separate (phillipsite + smectites + Fe-OOH) shows slightly lower  $\delta^{11}\text{B}$  values of  $+1.7 \pm 0.1 \text{ ‰}$  than the whole rocks, most likely due to mineralogical differences.



#### 4.1. Introduction

The geochemical composition of global open oceans is controlled by the interaction of seawater and adjacent geological reservoirs. Some of the most important oceanic input fluxes are continental runoff and the discharge of high-temperature ( $> 300\text{ }^{\circ}\text{C}$ ) hydrothermal fluids at divergent plate boundaries. For some elements, a significant imbalance in ocean geochemical budgets was recognized. Mackenzie & Garrels (1966) offered a solution to resolve these geochemical imbalances through reverse weathering processes. Mottl & Wheat (1994) and Elderfield & Schultz (1996) and many deep-sea rock alteration studies (e.g. Donnelly *et al.*, 1980; Humphris *et al.*, 1980; Seyfried *et al.*, 1984; Alt *et al.*, 1996) suggested that a significant portion of this reverse weathering may occur in low-temperature ridge flank hydrothermal systems (RFHS). Given the small (several to tens of degrees) temperature increase within RFHS and the redistribution of  $\sim 8.1$  TW of the lithospheric heat (Stein & Stein, 1994; Mottl, 2003), the resulting discharge flux of water is similar to the riverine flux. Thus, RFHS have the potential to affect seawater composition, even with compositional changes that are only a few percent different than seawater (Wheat *et al.*, 2017). Potential mass sources and sinks in the RFHS stem from (1) abiotic water-rock reactions in the basaltic section, (2) exchange with the overlying sediment pore waters, and (3) microbial metabolic processes (Wheat *et al.*, 2019). However, the small number of sufficiently studied and sampled RFHS makes quantification of fluxes from such systems largely unconstrained.

**Table 4.1-1: Lithium and Li isotope budget of modern seawater. Uncertainties are 2sd. See Chapter 4.4. for further explanations.**

	Li ( $\mu\text{M}$ )	Li flux $\times 10^9$ (mol/yr)	$\delta^7\text{Li}$ (‰)	references
<i>Input fluxes(total)</i>		<b>34.1</b>	<b>16.5</b>	
High-T fluid discharge	$882 \pm 662$	<b>7.1</b>	$8.5 \pm 2.7$	1, 2, 3, 4, 5, 6, 7, 8, 9
continental runoff (total)		<b>26.0</b>	<b>18.7</b>	
river water discharge	$0.46 \pm 0.94$	20.4	$20.3 \pm 8.0$	10, 11, 12, 13, 14, 15, 16, 17, 18, 19, 20, 21, 22, 23
groundwater discharge	$2.35 \pm 3.94$	5.6	$12.7 \pm 5.5$	14, 15, 24, 25, 26
fluid expulsion in subduction zones	$\sim 500$	<b>1.0</b>	<b>17.0</b>	27, 28, 29, 30, 31, 32, 33, 34
<i>Modern seawater</i>	$27 \pm 7$		$31.1 \pm 0.2$	35
		net volume: $1.335 \times 10^9 \text{ km}^3$		36

*References: (1) Coogan & Dosso (2012), (2) Edmond et al. (1979), (3) Edmond et al. (1982), (4) Von Damm et al. (1985), (5) Chan & Edmond (1988), (6) Von Damm (1990), (7) Chan et al. (1993), (8) Bray A.M. et al. , (9) Foustoukos et al. (2004), (11) Huh et al. (1998), (12) Huh et al. (2001), (13) Millot et al. (2010a), (14) Meredith et al. (2013), (15) Bagard et al. (2015), (16) Dellinger et al. (2015), (17) Pogge Von Strandmann & Henderson (2015), (18) Wang et al. (2015), (19) Henchiri et al. (2016), (20) Manaka et al. (2017), (21) Pogge Von Strandmann et al. (2017), (22) Gou et al. (2019), (23) Murphy et al. (2019), (24) Pogge Von Strandmann et al. (2014), (25) Liu et al. (2015), (26) Négrel et al. (2012), (27) Kastner et al. (1991), (28) Martin et al. (1991), (29) You et al. (1995), (30) Chan & Kastner (2000), (31) Solomon et al. (2009), (32) Hulme et al. (2010), (33) Scholz et al. (2010), (34) Tryon et al. (2010), (35) Jeffcoate et al. (2004), (36) Eakins & Sharman (2010).*

Lithium, Sr, and B are three elements whose ocean input fluxes (riverine and high temperature hydrothermal systems) were already studied in a larger number of publications (for Li see **Table 4.1-1** and references therein), but the removal fluxes are less certain and may be controlled in part by RFHS. For Li, steady state in the ocean is assumed, given a Li residence time in the oceans of  $10^6$  years compared to ocean mixing time of  $10^3$  years (Penniston-Dorland *et al.*, 2017). The two main removal mechanisms for Li from seawater that should balance the input fluxes in steady-state are the formation of secondary minerals from low-temperature ( $< 150$  °C) alteration of basaltic crust and marine sediment diagenesis. Both processes are also accompanied by distinct  $\delta^7\text{Li}$  shifts in the interacting fluids and solids (Chan *et al.*, 1992; Chan *et al.*, 1994) and thus were suggested to explain the discrepancy between the heavy  $\delta^7\text{Li}$  composition of modern seawater of +31 ‰ (Jeffcoate *et al.*, 2004), compared to cumulative source fluxes of approximately only +16.5 ‰ (see **Table 4.1-1** and **Chapter 4.4** for further details). Due to the high  $\delta^7\text{Li}$  value of seawater,  $\delta^7\text{Li}$  compositions of low-temperature altered basalts increase to typical values of +14 ‰, compared to fresh mid-ocean ridge (MOR) basalts of approximately +4 ‰ (Chan *et al.*, 1992). The proportions between low-temperature basalt alteration and authigenic marine sediment formation required to explain the Li sink and shift in seawater  $\delta^7\text{Li}$  composition are still unconstrained.

Like Li, Sr in modern seawater has a uniform isotopic composition of  $0.709175 \pm 0.000015$  (Scher *et al.*, 2014), consistent with a steady-state residence time of  $10^6$  years (McArthur, 1994). Primary sources that control the  $^{87}\text{Sr}/^{86}\text{Sr}$  seawater composition are riverine input, estimated between 0.7119 (Palmer & Edmond, 1989) and 0.7136 (Allègre *et al.*, 2010), and high-temperature hydrothermal input of approximately 0.7037 (Bach & Humphris, 1999; Davis *et al.*, 2003). Strontium is also delivered to the oceans by the dissolution of carbonates with a composition that closely matches that of modern seawater (Hodell *et al.*, 1989; Palmer & Edmond, 1989; Veizer, 1989). Based on Sr isotope composition of fluids from the Baby Bare outcrop on the eastern flank of the Juan de Fuca Ridge (JFR), Butterfield *et al.* (2001) suggested RFHS could also have an impact on the Sr isotopic budget of seawater. However, other authors (Palmer & Edmond, 1989; Davis *et al.*, 2003) proposed that the Sr isotopic composition of altered upper oceanic crust is inconsistent with a significant Sr source from RFHS and suggested that perhaps the global riverine flux is less radiogenic than estimated.

Finally, B is also in steady-state in ocean seawater consistent with an ocean residence time of  $10^7$  years (Lemarchand *et al.*, 2002) and a B isotopic composition of +39.6 ‰ (Foster *et al.*, 2010). Primary sources of B to the oceans are (i) riverine input with a  $\delta^{11}\text{B}$  composition of approximately +10 ‰ (Lemarchand *et al.*, 2002), (ii) high-temperature hydrothermal input in a range of +24.3 to +36.8 ‰ for MOR sediment-starved environments and -2.2 to +23.2 ‰ for MOR sediment-hosted systems (compiled by Marschall, 2018, and references therein), and (iii) fluid expulsion at subduction zones of +20 to +25 ‰ (You *et al.*, 1995). Similar to Li, reverse weathering leads to the

removal of B from seawater by low-temperature basalt alteration and sediment diagenesis. Additional B is removed through the formation of carbonates. Associated B isotope fractionation depends on the type of secondary mineralogy, temperature and coordination state of B. Clay minerals are the most significant secondary host minerals for B in altered basalts, incorporating B in a tetrahedral coordination, in contrast to modern ocean-pH (pH ~ 8) seawater that mainly hosts B in trigonal coordination (~80 %; Spivack & Edmond, 1987). This difference in B coordination between fluids and rocks and the exchange during alteration leads to major B isotopic fraction due to the difference in  $\delta^{11}\text{B}$  compositions of trigonal (prefers  $^{11}\text{B}$ ) and tetrahedral (passive enrichment of  $^{10}\text{B}$ ) coordinated species. The fresh MOR basalt  $\delta^{11}\text{B}$  composition of approximately -7 ‰ increases by low-temperature alteration to values of typically +5 to +10 ‰ (Marschall, 2018). The warmer (64 °C) fluids from Baby Bare outcrop, as part of a RFHS at the eastern flank of the JFR, are a clear source of B to the oceans (Wheat & Mottl, 2000). Indeed, more typical lower temperature fluids (~12.3 °C) from Dorado Outcrop are statistically indistinguishable from seawater, but potentially the removal flux of B from seawater was just so small that it was metrological not resolvable (Wheat *et al.*, 2017). Even a very small change in B and  $\delta^{11}\text{B}$  compositions of discharging fluids in RFHS compared to seawater (sink or source flux) potentially affects the oceanic B budget significantly due to the large water fluxes circulating through RFHS.

To better resolve the Li, Sr, and B removal and input fluxes from RFHS we determined Li and Sr isotopic compositions of low-temperature hydrothermal fluids and concentrations and isotopic compositions of Li, Sr, and B in fresh glass, altered whole rocks, and a vein separate (phillipsite + smectite + Fe-Mn-oxides) from Dorado Outcrop, which formed >18.5 Ma (Wheat *et al.*, 2019). It has been suggested that the Dorado Outcrop hydrothermal system represents a typical cool RFHS, given its low ( $\leq 15$  °C) temperature in upper basaltic basement and a fluid residence time of years (e.g. Wheat *et al.*, 2004). With this new study, we provide the first appraisal of the impact of RFHS on the  $\delta^7\text{Li}$  budget of seawater, present additional data to better define the effect of RFHS on the Sr isotope budget of the oceans, and define secondary host minerals of Li and B in low-temperature altered oceanic crust. Lastly, we make basic assumptions how fluctuations in seawater isotopic composition in the Cenozoic (Hathorne & James, 2006; Misra & Froelich, 2012; Li & West, 2014; Gaillardet & Lemarchand, 2018; Roberts *et al.*, 2018) could affect the isotopic signature of ocean reverse weathering products.

#### **4.2. Sample locations**

Dorado Outcrop is a basaltic edifice that is located on the Cocos Plate, east of the East Pacific Rise (**Figure 4.2-1**; Wheat *et al.*, 2017; 2019) and situated in a region where the conductive heat flow is only 60 to 90 % of the value predicted from lithospheric thickening, indicative of vigorous fluid flow within the upper oceanic crust (Hutnak *et al.*, 2008). Hydrothermal vent fluids, fresh glass, altered rocks and a vein separate were collected during two consecutive expeditions; one in 2013

(R/V Atlantis Expedition AT-26-09, equipped with the AUV *Sentry* and the ROV *Jason II*) and the other in 2014 (AT-26-24, equipped with the HOV *ALVIN*, Wheat *et al.*, 2017). Active fluid discharge was observed at three locations; (1) at an elevated location on the northern part of the outcrop, (2) on the southwest side of the southern topographical height and, (3) near the base of the southern slope (close to sampling locations R5, R8, R9; **Figure 4.2-1**).

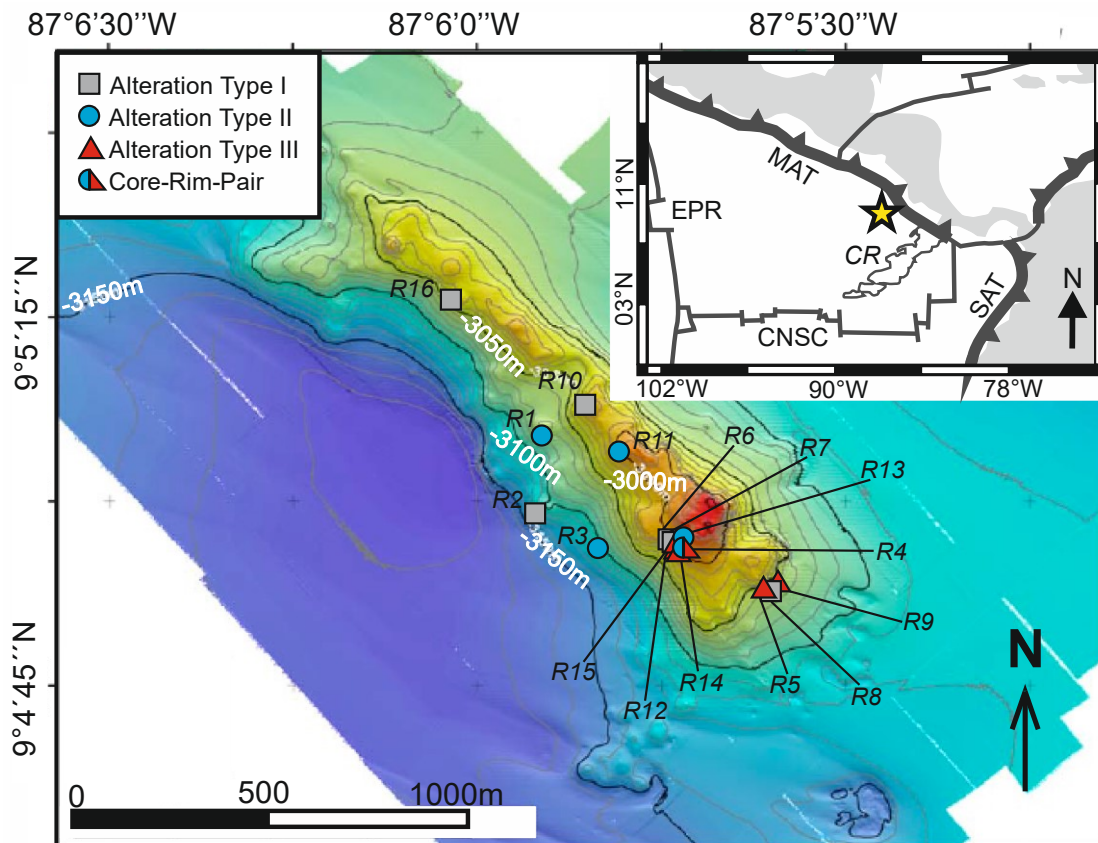


**Figure 4.2-1:** Topographic map of Dorado Outcrop (modified after Wheat *et al.*, 2017) and sampling positions labeled with R1 to R16 (see **Table 4.5-2**) of altered rock samples divided in three Alteration Types. Upper right corner: location of Dorado Outcrop (yellow star) on 18.5 to 23 Myr old crust of the Cocos Plate, west of Costa Rica. CNSC – Cocos-Nazca Spreading Center, CR – Cocos Ridge, EPR – East Pacific Rise, MAT – Middle America Trench, SAT – South America Trench.

### 4.3. Methods

#### 4.3.1. Sampling and sample preparation

Discrete fluid samples from Dorado Outcrop were taken with the submersible *ALVIN* using a novel sampler during Expedition AT26-24 in 2014 and the chemical composition (i.a. Li, Sr, B) was analyzed with standard protocols (details are described in Wheat *et al.*, 2017). Rock samples were collected by *Jason II* (AT-26-09) and *ALVIN* (AT-26-24) from the surface of the outcrop.

For preparation, rock slabs cut by a diamond saw were sandblasted, rinsed with Milli-Q water, and dried at 70 °C overnight. In addition, two fresh glass rims and one 2 mm thick vein (phillipste + smectite + Fe-oxyhydroxides) were handpicked under the binocular. Solid samples were powdered using an agate ball bearing mill (details of the procedures are given in the Supplemental Material in Wheat *et al.*, 2019). Powdered rock samples were washed with Milli-Q and dried at 100 °C overnight to avoid contamination by seawater prior to analysis. Thin sections were prepared by Dettmar Dissection Technology, Bochum, Germany.

#### 4.3.2. Scanning electron microscopy (SEM)

Micro images of vein samples were generated in backscatter electron mode by a Zeiss Supra 40 scanning electron microscope in the Historic Geology/ Palaeontology research group at the University of Bremen, Germany. Sample material was mounted on a graphite stamp and sputter coated with graphite. Semi-quantitative chemical compositions were determined using energy dispersive X-ray (EDX) spectra in conjunction with a Bruker X-Flash 6/30. An acceleration voltage of 15 kV was used. Single spot measurements are documented in the Appendix, **Table A. 3-3**.

#### 4.3.3. Electron microprobe analyses (EMPA)

Major element concentrations of alteration phases were determined using a Cameca SX100 electron microprobe at the Faculty of Geosciences, University of Bremen, Germany. Thin sections were sputter coated with graphite prior to measurement. An acceleration voltage of 15 kV, a probe current of 15 nA and a defocused electron beam of 5 µm in diameter were used, except for zeolites. Zeolites were analyzed using 1 nA probe current and a defocused electron beam of 10 µm in diameter. Reference materials were provided by the Smithsonian Institution, Washington D.C., USA (NMNH 133868, NMNH 111312-44, USNM 115900) and were repeatedly determined between sample spot measurements. Accuracy of elements with a higher abundance than 3 wt% was better than 6 % (1 relative standard deviation). Single spot measurements and measured values of reference materials are documented in the Appendix, **Table A. 3-4** and **Table A. 3-5**.

#### 4.3.4. Laser ablation inductively coupled plasma mass spectrometry (LA-ICP-MS)

Trace element concentrations of alteration phases were analyzed using a Thermo-Scientific Element 2 inductively coupled plasma mass spectrometer coupled to a NewWave UP193ss laser ablation system at the Faculty of Geosciences, University of Bremen. Irradiance for ablation was set to 1 GW cm<sup>-2</sup> and the beam diameter to 75 µm. The pulse rate for standards was 10 Hz, and 5 Hz for mineral phases from thin section. Helium (0.80 l min<sup>-1</sup>) was used for the carrier gas and argon (0.82 l min<sup>-1</sup>) used for the make-up gas. NIST SRM 612 and an internal Si standard were used for calibration. The Si concentrations were determined using the microprobe measurements. The computation of the trace element concentrations was performed using Cetac GeoPro<sup>TM</sup> software. The USGS basaltic glass reference material BCR-2G and BHVO-2G and the standard reference

material NIST SRM 612 were measured at least after every 20 sample spot measurements. Based on the index values provided by the GeoReM data base (Jochum *et al.*, 2005), the precision of BCR-2G (n=4) for elements with an average concentration < 300 µg/g was better than ± 2 µg/g (2sd) and for elements > 300 µg/g (Sr, Ba) was better than ± 30 µg/g (2sd). The accuracy of BCR-2G was better than 5 %, better than 10 % for Tm, and better than 15 % for B. The accuracy of BHVO-2G (n=2) was better than 5 % and better than 10 % for Y, Cs, Gd, Tm, Yb and U. Trace element compositions of secondary mineral phases and reference materials used for LA-ICP-MS measurements are given in the Appendix, **Table A. 3-6** and **Table A. 3-7**.

#### 4.3.5. Concentration and isotope analyses

Isotope analyses (Sr, B, Li) and B and Li concentrations of fluids, fresh glass, rocks and a vein (zeolites + smectites + Fe-oxyhydroxides) separate were determined in the Isotope Geochemistry Laboratory at the MARUM - Center for Marine Environmental Sciences, University of Bremen, Germany. For analyzing Sr and Li isotopic compositions of the silicates, 20-40 mg of the powdered sample material were digested in 2 ml of a mixture of concentrated HF/HNO<sub>3</sub> (5:1) for 72 h at 140 °C, dried at 80 °C, and re-dissolved in 4 ml 2 M HNO<sub>3</sub>. This procedure was conducted in triplicate to ensure complete sample digestion.

##### 4.3.5.1. Lithium concentrations and isotope analyses

Isolation and purification techniques of Li (detailed in Hansen *et al.*, 2017 and modified after Moriguti & Nakamura, 1998a, **Appendix A.2.1**) are based on two consecutive cleaning steps using Bio-Rad® Poly-Prep and Bio-Spin columns prepared with 1.4 ml and 1 ml of cation exchange resin AG 50W-X8, respectively. The first cleaning step consisted of Li elution with 0.15 M HCl. In the second step, the samples were transferred to the columns digested in 1 ml 0.15 M HCl, while for elution 0.5 M HCl with 50 % ethanol was used. During both steps, elute was collected before and after the main fraction to monitor Li loss by separation; the total Li loss was always < 0.5 % of the collected Li. The total procedural blank was less than 16 pg Li.

Lithium isotope analyses (and Li concentration determination for the altered rock samples and the vein separate) were performed on a Thermo-Fisher Scientific Neptune Plus multicollector – inductive coupled plasma – mass spectrometer (MC-ICP-MS) using the SIS (stable introduction system: low flow PFA nebulizer (50 µl) and a double pass quartz spray chamber) together with a high- efficiency x-cone. Processed samples and reference materials were dissolved in 2% HNO<sub>3</sub>, closely matched to 25 ppb Li, and repeatedly analyzed in the standard - sample bracketing mode using NIST RM 8545 (LSVEC, Li carbonate standard, Flesch *et al.*, 1973). For determination of the baseline, 2 % HNO<sub>3</sub> was measured before and after each sample and standard. Li isotope ratios are given relative to NIST RM 8545 in the conventional  $\delta^7\text{Li}$  (‰) notation: [ $\delta^7\text{Li} = \{[(^7\text{Li}/^6\text{Li})_{\text{sample}} / (^7\text{Li}/^6\text{Li})_{\text{NIST RM 8545}}] - 1\} \times 1000$ ]. The uncertainty of the  $\delta^7\text{Li}$  value is given as 2sd, based on multiple mass-spectrometer analyses. Reference and standard materials were processed and analyzed

together with the samples in order to control the analytical procedure. NIST RM 8545 showed a  $\delta^7\text{Li}$  of  $-0.1 \pm 0.2\text{‰}$  (n=2), indicating no significant isotope fractionation during the analytical procedure. The internal laboratory bottom seawater standard (BSW-SuSu Knolls) gave a  $\delta^7\text{Li}$  value of  $+31.2 \pm 0.2 \text{‰}$  (n=1) and was in good agreement with the laboratory internal long-term  $\delta^7\text{Li}$  composition for BSW-SuSu Knolls seawater of  $+30.9 \pm 0.5 \text{‰}$  (n=25). In addition, the standard agrees within uncertainty with the average seawater  $\delta^7\text{Li}$  values of  $+31.1 \pm 0.2 \text{‰}$  (n=31, Jeffcoate *et al.*, 2004) and  $+30.77 \pm 0.43 \text{‰}$  ( $2\sigma$ , n=17, Rosner *et al.*, 2007). The internal precision of the Li concentration measurements was always better than  $\pm 0.3 \mu\text{g/g}$  (2sd), based on the reproducibility of at least three measurements on the same solutions (samples and reference materials BHVO-2 and IAEA-B-5) relative to NIST RM 8545 of known concentration.

The basaltic reference material BHVO-2 showed a Li concentration of  $4.4 \pm 0.0 \mu\text{g/g}$  that is within the range of published concentrations of the GEOREM database (access 15. July 2019) of  $4.6 \pm 1.1 \mu\text{g/g}$  (2sd, n=158) and a  $\delta^7\text{Li}$  value of  $+4.4 \pm 0.3 \text{‰}$ , in good agreement with the average BHVO-2 value of the GEOREM database (access 15. July 2019) of  $+4.5 \pm 0.4 \text{‰}$  (2sd, n = 50 including all data measured relative to NIST RM 8545) and the value of  $+4.3 \pm 0.5 \text{‰}$  (2sd, n=3) published by Hansen *et al.* (2017). The basaltic reference material IAEA-B-5 showed a Li concentration of  $8.2 \pm 0.1 \mu\text{g/g}$  and a  $\delta^7\text{Li}$  value of  $+4.7 \pm 0.3 \text{‰}$ .

The Li concentrations of the discrete fluid samples from Dorado outcrop were taken from Wheat *et al.* (2017), determined by inductively coupled plasma optical emission spectrometry (ICP-AES). In some cases, the Li concentrations of altered whole rocks measured by MC-ICP-MS (this study) are lower (outside analytical uncertainty) than the reported ICP-MS (Wheat *et al.*, 2019) values (**Figure 4.5-2d**). This difference could be caused by different measuring procedures. Indeed, the much larger differences in Li concentrations for samples with high absolute Li concentrations (up to 22 % lower Li contents measured by MC-ICP-MS versus ICP-MS) compared to samples with lower absolute concentrations (maximum 8 % difference) pointed to loss of seawater Li due to the additional cleaning step with Milli-Q performed for MC-ICP-MS analyses.

#### 4.3.5.2. Boron concentrations and isotope analyses

Isolation and purification of B in silicates is based on the method described in Wilckens *et al.* (2018) and described in the **Appendix A.2.1**. A mixture of sample powder (100 – 250 mg)/  $\text{K}_2\text{CO}_3$  (1:4) was fused in Pt crucibles, followed by dissolution in ultrapure water, and repeated centrifugation and decantation. Boron was purified from solution by a two-step column separation and the input of pre-conditioned (2N  $\text{NH}_4\text{OH}$ ) Amberlit IRA 743 and an appropriate amount of mannitol (1  $\mu\text{g}$  B : 20  $\mu\text{g}$  mannitol) to keep B in solution. The total B loss was  $< 10 \text{ ng}$ , negligible in comparison to B concentrations in the sample materials.

For B isotope and concentration analyses, the same instrument (MC-ICP-MS) used for Li isotopic measurements was used. Samples were dissolved in 2% HNO<sub>3</sub>, closely matched to 100ppb B, and repeatedly analyzed in the standard - sample bracketing mode using NIST SRM 951, supplemented by baseline determination. Boron isotope values are given in the conventional  $\delta^{11}\text{B}$  (‰) notation:  $[\delta^{11}\text{B} = \{[(^{11}\text{B}/^{10}\text{B})_{\text{sample}} / (^{11}\text{B}/^{10}\text{B})_{\text{NIST SRM 951}}] - 1\} \times 1000]$ . The B isotopic values in the following are given as 2 sd. The standard NIST SRM 951 that were running within the sequence had a  $\delta^{11}\text{B}$  value of  $0.0 \pm 0.0$  ‰ and point to no isotopic fractionation during procedure. The basaltic reference material BHVO-2 showed a B concentration of  $2.3 \pm 0.0$   $\mu\text{g/g}$  within the range of published B values of 2.1 to 6.8  $\mu\text{g/g}$  (GEOREM database, 15. July 2019) and a  $\delta^{11}\text{B}$  value of  $-2.8 \pm 0.3$  ‰. The basaltic reference material IAEA-B-5 showed a B concentration of  $6.5 \pm 0.0$   $\mu\text{g/g}$  that is significantly lower than the B concentrations usually measured for IAEA-B-5 in the laboratory of around 9  $\mu\text{g/g}$ . The internal precision of B concentration measurements based on the reproducibility of the same solutions of samples and reference materials (BHVO-2 and IAEA-B-5) relative to NIST SRM 951 of known concentration was always better than  $\pm 0.3$   $\mu\text{g/g}$  (2 sd). However, regarding the large discrepancy between usual measured and this run measured B concentrations of IAEA-B-5, a deviation of the accuracy of around  $\pm 2.5$   $\mu\text{g/g}$  has to be assumed. However, the  $\delta^{11}\text{B}$  value of IAEA-B-5 was  $-3.9 \pm 0.1$  ‰, matching the average B5 value of the GEOREM database of  $-3.9 \pm 0.7$  ‰ (2sd, n = 10, two outliers excluded, (GEOREM, 15. July 2019), the value of  $-4.3 \pm 0.2$  ‰ (n=3) measured by Hansen *et al.* (2017) and of  $-4.2 \pm 0.2$  ‰ (n=4) published by (Wilckens *et al.*, 2018). The B loss was therefore apparently not accompanied by significant B isotopic fractionation.

#### 4.3.5.3. *Strontium isotope analyses*

Strontium separation and purification procedures were adapted from Deniel & Pin (2001) using 70  $\mu\text{l}$  Sr.spec™ resin in miniaturized columns (**Appendix A.2.1**). For separation, samples were digested in 1 ml 2 M HNO<sub>3</sub> and loaded onto the columns. Next, 1.2 ml of 2 M HNO<sub>3</sub> was added to remove unwanted elements, followed by 1 ml 0.05 M HNO<sub>3</sub> to extract strontium. After extraction, 30  $\mu\text{l}$  0.1 M H<sub>3</sub>PO<sub>4</sub> was added and the sample were dried. To remove organic material 40  $\mu\text{l}$  of concentrated HNO<sub>3</sub> was added and dried. Then, 40  $\mu\text{l}$  H<sub>2</sub>O<sub>2</sub> was added and dried. For analyses, 1.5  $\mu\text{l}$  Ta-emitter was loaded on a rhenium filament, followed by loading of the samples digested in 2  $\mu\text{l}$  0.1 M H<sub>3</sub>PO<sub>4</sub>. Afterwards, the filaments were conditioned by heating until red heat was reached. The determination of the <sup>87</sup>Sr/<sup>86</sup>Sr ratios was performed using a Thermo Scientific TRITON Plus thermal ionization mass spectrometer (TIMS) in the dynamic mode. The <sup>87</sup>Sr/<sup>86</sup>Sr ratio was based on the average of at least 75 cycles, each with three different masses focused to the central detector of the detector-arrangement and the equivalent masses in the mobile detectors related to the high and low masses of the multi-collector-arrangement. The instrumental fractionation was corrected to the natural <sup>87</sup>Sr/<sup>86</sup>Sr ratio of 0.1194. The blank contamination was < 50 pg and had no significant impact on measurements due to the much higher Sr contents of the samples (> 200 ng). The accuracy of the results was assessed based on measurements of the

strontium reference material NIST SRM 987 of  $0.710247 \pm 0.000006$  (2sd, n=2). The laboratory internal long-term reproducibility of NIST SRM 987 (from December 2011 to February 2017) was  $0.710249 \pm 0.000024$  (2sd, n=231). The average NIST SRM 987 value of the GEOREM database (18. Oct. 2018) was  $0.710250 \pm 0.000019$  (2sd, n = 1832, 7 outliers and 72 values without 2sd displayed in the database excluded).

#### **4.4. Estimates on the oceanic lithium and lithium isotopic budget**

The Li and  $\delta^7\text{Li}$  composition of seawater is controlled by input fluxes from (1) rivers, (2) high-temperature hydrothermal systems and (3) fluid expulsions at subduction zones that are in balance with output fluxes due to basalt weathering and sediment diagenesis in steady state. To resolve the potential impact of Li output fluxes on the composition of seawater and the consequences for  $\delta^7\text{Li}$ , we first constrained the input fluxes based on published data (**Table 4.1-1**). The input fluxes were constrained as follows:

- (1) The river input is calculated based on the average of global runoff of  $44,240 \pm 2660 \text{ km}^3/\text{yr}$  (Clark *et al.*, 2015). The weighted mean Li concentration ( $\pm 2\text{sd}$ ) and isotopic composition of river discharge is calculated based on data from Huh *et al.* (1998) and refined using recent published data that were taken closest to the mouth of larger rivers, like the Congo (Henchiri *et al.*, 2016), the Huanghe (Gou *et al.*, 2019) and integrating updated values for the Amazon (Dellinger *et al.*, 2015), Yangtze (Wang *et al.*, 2015), Brahmaputra (Manaka *et al.*, 2017), Lena river (Murphy *et al.*, 2019), Mackenzie river (Millot *et al.*, 2010b), and Ganges (Bagard *et al.*, 2015; Manaka *et al.*, 2017; Pogge Von Strandmann *et al.*, 2017). In addition, some smaller rivers ( $\leq 12 \text{ km}^3/\text{yr}$ ) are considered (Meredith *et al.*, 2013, Pogge Von Strandmann & Henderson, 2015). Overall, the global Li river flux is inferred from a dataset that comprises 28 % of global river water discharge. Discharge rates of single rivers are taken from Milliman & Farnsworth (2011). Beside rivers, we also consider the discharge of groundwater to the oceans with a water flux of  $2400 \text{ km}^3/\text{yr}$  (Pogge Von Strandmann *et al.*, 2014). The average Li concentration and isotopic composition of groundwater discharge is based on values published for several aquifers worldwide (Négre *et al.*, 2012; Meredith *et al.*, 2013; Pogge Von Strandmann *et al.*, 2014; Bagard *et al.*, 2015; Liu *et al.*, 2015).
- (2) The high-temperature hydrothermal Li flux is estimated by averaging the Li concentrations ( $\pm 2\text{sd}$ ) of fluids from the ridge axis (Edmond *et al.*, 1979; Edmond *et al.*, 1982; Damm *et al.*, 1985; Chan & Edmond, 1988; Damm, 1990; Chan *et al.*, 1993; Bray A.M. *et al.*; Foustoukos *et al.*, 2004) and using a water flux of  $8.0 \pm 2.1 \times 10^{12} \text{ kg/yr}$  (Coogan & Dosso, 2012). Fluid samples from the Guaymas Basin are not considered for calculations, due to their unusual low Li isotopic composition around +5 ‰ (Chan & Edmond, 1988). Our estimate matches constraints of ridge axis Li flux of  $8 \times 10^9 \text{ mol/yr}$ , based on ODP Hole

504B rock compositions that show a typical Li enrichment in the upper volcanics and a decreasing trend in Li concentration with depth due to higher temperature fluids (Chan *et al.*, 2002). In contrast, the low Li concentrations of the rocks recovered at ODP Site 1256 point to significant higher alteration temperatures that are probably less representative for global oceanic crust, interpreted to be caused by early sealing of the crust (Gao *et al.*, 2012).

(3) The least well-constrained input flux is the expulsion of fluids by porosity reduction and dehydration of hydrous minerals of the down going slab by early subduction processes at convergent plate boundaries. The water and mass fluxes accompanied with those settings are debatable with global estimates ranging from  $< 0.6 \times 10^9$  mol Li/yr (Hathorne & James, 2006) to  $6 \times 10^9$  mol Li/yr (Misra & Froelich, 2012). Fundamental to these estimates is the global fluid discharge flux assigned to subduction-related processes. Observations of fluid flow rates from COSOD II (1987) led to flux estimates as high as  $100 \text{ km}^3/\text{yr}$  at convergent plate boundaries. Calculations of potential available fluids by subduction and flow meter measurements showed that those fluxes are about one order of magnitude too high and probably influenced by external water sources, like entrainment of seawater and meteoric waters (Carson *et al.*, 1990; Kastner *et al.*, 1991; Le Pichon *et al.*, 1991). Kastner *et al.* (1991) estimated a possible fluid flux ranging from 1 to  $3 \times 10^{12}$  kg/yr, which is used for budget calculations in this study. Lithium concentrations of pore fluids from fore arc mud volcanoes, faults in sediment-rich subduction prisms, and serpentinite seamounts range from values that are lower than seawater up to  $1155 \text{ }\mu\text{M}$  (Martin *et al.*, 1991). Most published Li contents plot between 100 to  $500 \text{ }\mu\text{M}$  (Martin *et al.*, 1991; You *et al.*, 1995; Chan & Kastner, 2000; Solomon *et al.*, 2009; Hulme *et al.*, 2010; Scholz *et al.*, 2010; Tryon *et al.*, 2010). It can be estimated that collected pore fluids are diluted by external fluid sources to a certain degree; therefore, we use an elevated estimate of  $500 \text{ }\mu\text{M}$  for our calculations. The average of Li isotopic composition of pore fluids is  $+24 \text{ ‰}$  (Chan & Kastner, 2000; Solomon *et al.*, 2009; Scholz *et al.*, 2010). We assume an average dilution of 50 % by seawater ( $\delta^7\text{Li} +31\text{‰}$ ) and use a Li isotopic composition of  $+17 \text{ ‰}$  as end-member fluid. For comparison, Misra & Froelich (2012) assumed the  $\delta^7\text{Li}$  composition of discharging slab fluids to match the signature of the marine sediments they were liberating from of approximately  $+15 \text{ ‰}$ , similar to our estimate. Overall, the impact on the Li budget of seawater from subduction-related processes is only minor compared to the other two sources, but requires further refinement.

We calculated a total Li mass flux to the oceans of  $34.1 \times 10^9$  mol/yr that has a weighted average  $\delta^7\text{Li}$  composition of  $+16.5 \text{ ‰}$ , considering all three source fluxes accumulated (*Table 4.1-1*).

## 4.5. Results

### 4.5.1. Lithium concentrations and Li and Sr isotopes of hydrothermal fluid samples

Fluid samples from Dorado Outcrop show Li concentrations between 25.0 and 26.3  $\mu\text{mol Li/kg}$ , in comparison to bottom seawater with  $26.2 \pm 0.3 \mu\text{mol Li/kg}$  (1sd, Wheat *et al.*, 2017; **Table 4.5-1**; **Figure 4.5-1a**). The range in Li concentrations results from mixing of the end-member fluid with varying amounts of bottom seawater entrained during collection. In high-temperature hydrothermal systems, the end-member fluid composition is often determined by extrapolating to zero Mg concentrations. For low-temperature systems like Dorado Outcrop, this method is inappropriate because the fluids lose only a small fraction of Mg. Wheat *et al.* (2017) used the average concentrations from the time-series OsmoSampler fluids to determine the end-member composition for most elements, also for the contents of Li ( $25.1 \pm 0.1 \mu\text{mol Li/kg}$ , 1sd) and Mo ( $126 \pm 2 \text{ nmol Mo/kg}$ , 1sd). In this study, we estimate the Li content of the discrete fluid sample that is the most different from the seawater end-member to be most representative for the hydrothermal fluid end-member ( $25.0 \mu\text{mol Li/kg}$  and  $128 \text{ nmol Mo/kg}$ ). The discrete samples are chosen because the OsmoSampler fluids are potentially diluted with seawater, thus the “true” end-member would be more altered. Molybdenum concentration is used as reference for end-member calculation, as it shows a discrete trend pointing to mixing between an end-member fluid and seawater when plotted against other elements such as Li and the change in Mo concentrations is relatively large compared to analytical capabilities and the concentration in bottom seawater. The difference between seawater and discrete fluid is  $1.2 \pm 0.6 \mu\text{mol Li/kg}$  (1sd, same uncertainty for EM and seawater estimated).

**Table 4.5-1:** Mo, Li, Li isotopic and Sr isotopic compositions of seawater and discharging fluids that were collected at Dorado Outcrop and calculated end-member composition of the hydrothermal fluids.

Sample number	Latitude (N)	Longitude (W)	Mo* (nmol/kg)	$\pm$ 1sd (nmol/kg)	Li* ( $\mu\text{mol/kg}$ )	$\pm$ 1sd ( $\mu\text{mol/kg}$ )	$\delta^7\text{Li}$ (‰)	$\pm$ 2sd (‰)	$^{87}\text{Sr}/^{86}\text{Sr}$	$\pm$ 2 $\sigma$ $\times 10^{-6}$
bottom SW			115	$\pm$ 2	26.2	$\pm$ 0.3	31.2**	$\pm$ 0.2	0.709175 <sup>†</sup>	$\pm$ 15
end-member <sup>††</sup>			128		25.0		31.9			
4775-sq3	9.08249	87.09547	128		25.0		31.8	$\pm$ 0.1	0.709164	$\pm$ 8
4775-sq6	9.08249	87.09547	113		26.3		31.2	$\pm$ 0.2		
4775-sq9	9.08249	87.09545	126		25.1		31.7	$\pm$ 0.1	0.709176	$\pm$ 6
4776-sq10	9.08237	87.09535	126		25.3		31.7	$\pm$ 0.1	0.709211	$\pm$ 6
4777-sq6	9.08247	87.09546	125		25.2		32.0	$\pm$ 0.1		
4778-sq9	9.08255	87.09535	119		25.6				0.709166	$\pm$ 6
4780-sq1	9.08249	87.09537	122		25.4				0.709162	$\pm$ 5
4784-sq10	9.08238	87.09544	125		25.4		31.7	$\pm$ 0.2		

\*Wheat *et al.* (2017)

\*\*Laboratory internal seawater standard (BSW SuSu-Knolls)

<sup>†</sup>Scher *et al.* (2014)

<sup>††</sup> equals to lowest measured Mo and Li concentrations. The  $\delta^7\text{Li}$  value is calculated (see **Chapter 4.5.1** for details).

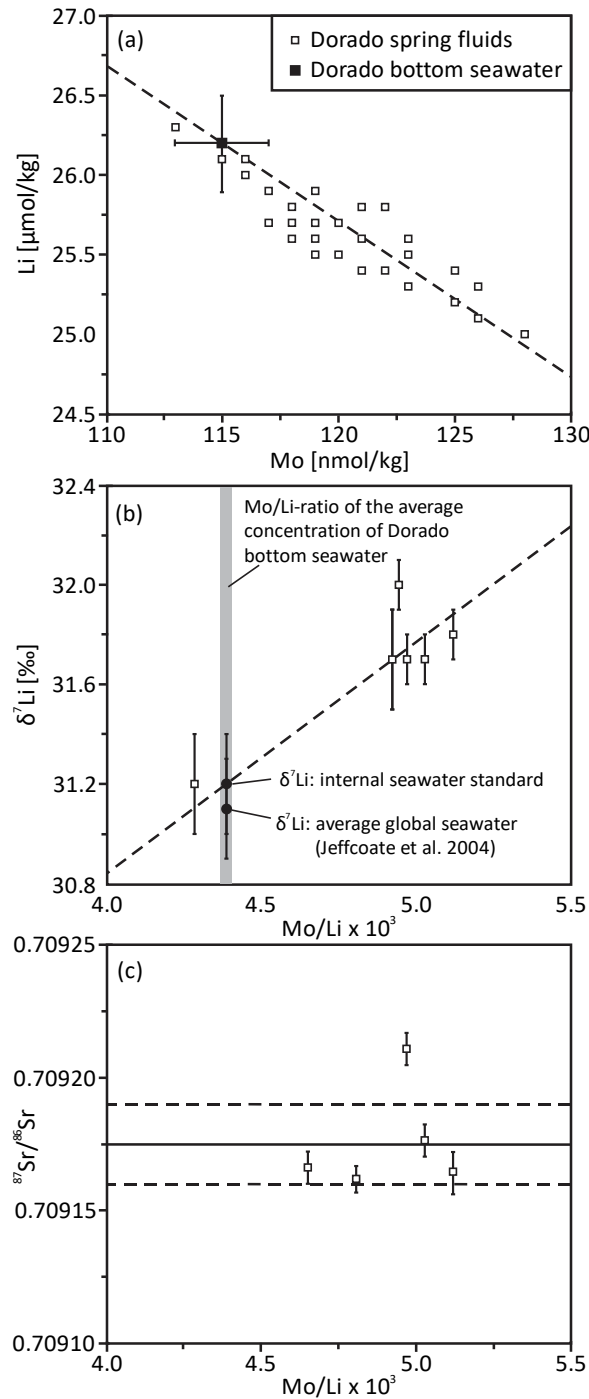


**Figure 4.5-1:** Compositions of hydrothermal fluids of Dorado Outcrop and seawater. (a) Mo vs. Li concentrations (Wheat et al., 2017). Uncertainties are 1sd like in the source publication. (b) Mo/Li  $\times 10^3$  ratios vs.  $\delta^7\text{Li}$  values. Uncertainties are 2sd. The seawater compositions with filled symbols in (b) represent hypothetical data points that derived from two sources. The Mo/Li ratios for both points derived from the bottom seawater composition measured in ambient seawater of Dorado Outcrop ( $\sim 4.4 \times 10^3$ ). The  $\delta^7\text{Li}$  value derived from BSW SuSu-Knolls ( $+31.2 \pm 0.2$  ‰, filled circle) or rather from the average global  $\delta^7\text{Li}$  seawater composition ( $+31.1 \pm 0.2$  ‰, Jeffcoate et al., 2004, filled diamond). Dashed lines show linear regression lines forced through seawater composition ((a)  $R^2 = 0.68$ ,  $p < 0.01$ , (b)  $R^2 = 0.85$ ,  $p < 0.01$ ). (c) Mo/Li versus  $^{87}\text{Sr}/^{86}\text{Sr}$  ratios of Dorado hydrothermal fluids. The solid line represents the average  $^{87}\text{Sr}/^{86}\text{Sr}$  composition of seawater after Scher et al. (2014). The dashed lines represent 2sd.

The six measured fluid samples have  $\delta^7\text{Li}$  values between +31.2 and +32.0 ‰ (**Table 4.5-1**). In comparison, the laboratory internal seawater standard (BSW-SuSu Knolls) has a  $\delta^7\text{Li}$  composition of  $+31.2 \pm 0.2$  ‰ and matches the global seawater  $\delta^7\text{Li}$  value of  $+31.1 \pm 0.2$  ‰ (Jeffcoate *et al.*, 2004). The Mo/Li molar ratios and  $\delta^7\text{Li}$  values of the fluids show a significant linear relationship ( $R^2 = 0.85$ ,  $p < 0.01$ , **Figure 4.5-1b**). The best estimate for the  $\delta^7\text{Li}$  end-member composition for the crustal fluid that discharges from Dorado Outcrop is deduced by determining the  $\delta^7\text{Li}$  value of the linear regression line at a Mo/Li ratio of  $5.1 \times 10^3$ . The corresponding  $\delta^7\text{Li}$  value is +31.9 ‰. In comparison, the best estimate for the  $\delta^7\text{Li}$  composition of seawater correlates to the point on the regression line matching to a Mo/Li ratio of  $4.4 \times 10^3$  and points towards a  $\delta^7\text{Li}$  value of +31.2 ‰. For the  $\delta^7\text{Li}$  composition of both seawater and crustal fluid, an uncertainty similar to the average of BSW-SuSu Knolls of  $\pm 0.2$  ‰ (2sd) is estimated. From this data treatment, the difference in  $\delta^7\text{Li}$  composition between seawater and the discharging fluid is  $0.7 \pm 0.4$  ‰ (2sd).

The  $^{87}\text{Sr}/^{86}\text{Sr}$  value of the spring fluids lie in the same range as the seawater value ( $0.709175 \pm 0.000015$ ; Scher *et al.*, 2014), with the exception of one sample that shows a slightly more radiogenic composition ( $0.709211 \pm 0.000006$ ; **Figure 4.5-1c**).

#### 4.5.2. Rock samples

##### 4.5.2.1. Petrographic characteristics and alteration types

Rocks sampled at Dorado Outcrop represent fragments of submarine basaltic pillow flows. Wheat *et al.* (2019) summarized the geological setting and basement compositional characteristics of Dorado Outcrop. The most important geochemical and petrographic features are reiterated here. Some samples show glassy rims, partly fresh and partly replaced by low-temperature alteration products (palagonite), especially along cracks. Based on the rare earth element (REE) patterns and Zr/Nb ratios, rocks are classified as interstage between N- and T-MORB (transitional MORB, Wheat *et al.*, 2019). The groundmass is cryptocrystalline with glomerocrysts, consisting of mostly fresh plagioclase and slightly to heavily altered olivine crystals; sparsely, clinopyroxene phenocrysts occur. The extent of whole-rock alteration varies between 5 and 40 %. This estimate is based on the relative occurrence of secondary mineral phases, replacing primary phases, predominantly olivine and pyroxene (**Table 4.5-2**). Rising extents of rock alteration result in typical increases in the contents of  $\text{H}_2\text{O}$  and U and losses of MgO and  $\text{SiO}_2$  (Wheat *et al.*, 2019). This study shows, that increasing extents of alteration (deduced from i.a. a rise in  $\text{H}_2\text{O}$ , MgO, and  $\text{K}_2\text{O}$  contents) are in good agreement with rising  $^{87}\text{Sr}/^{86}\text{Sr}$  values of whole rocks (**Figure 4.5-2a,b**).

Alteration types of whole rocks are divided into three categories based on alteration extents, petrographic appearance and chemical compositions (cf. Wheat *et al.*, 2019):

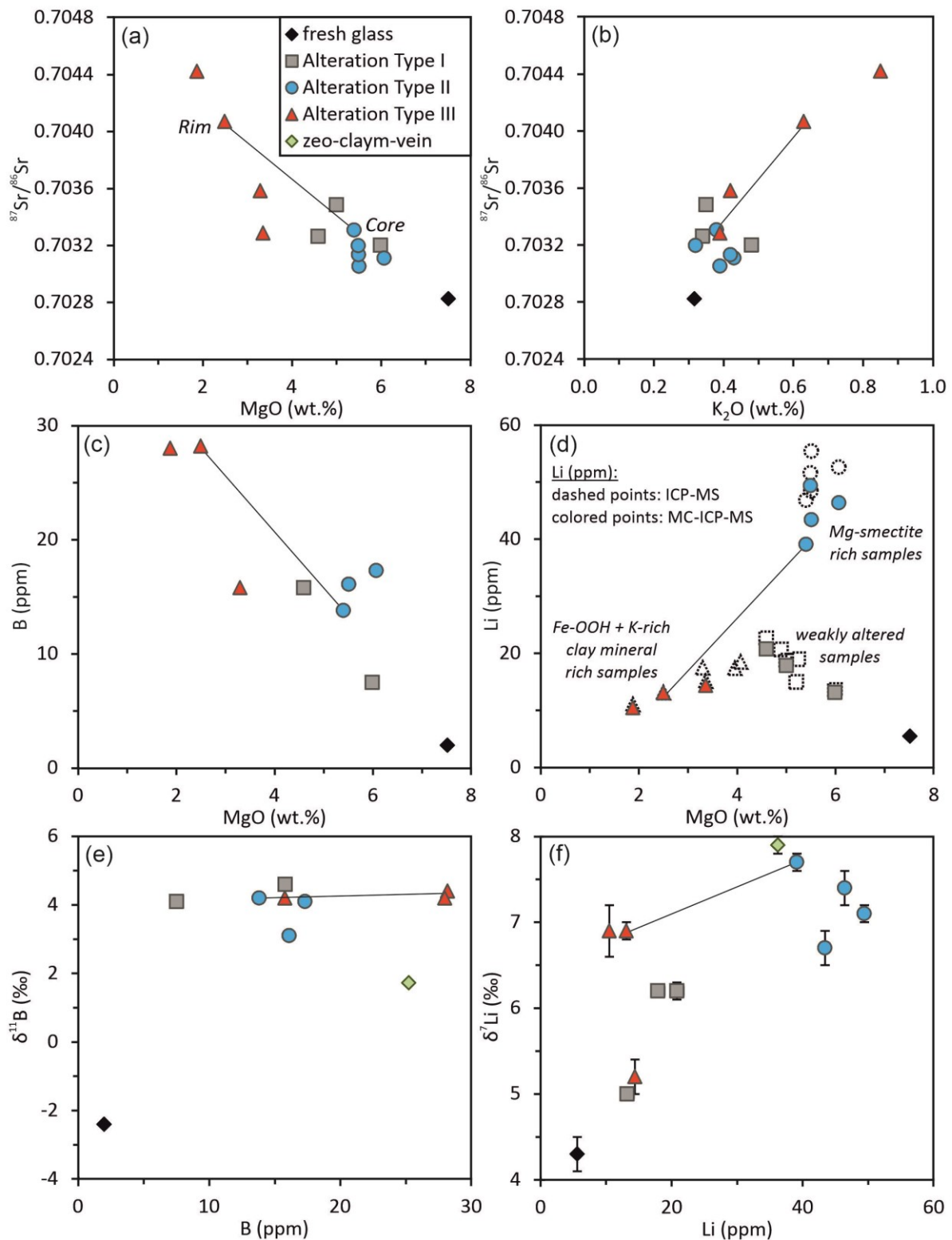


**Figure 4.5-2:** Geochemical composition of fresh glass, altered whole rocks and a zeolite-clay mineral (zeo-claym) vein of Dorado Outcrop. A solid line connects the core-rim pair. (d) Comparison of Li concentrations of whole rocks measured by ICP-MS (data derived from Wheat et al., 2019) and MC-ICP-MS (this study). (e,f) Error bars are 2sd, but too small for  $\delta^{11}\text{B}$  values to be displayed.

**Alteration Type I:** The altered matrix is grayish in color and interspersed with olivine phenocrysts, partly replaced by iddingsite. Relicts of olivine are preserved. The extent of alteration is 5 - 15 %, coupled with relatively low H<sub>2</sub>O contents (1.38 – 2.44 wt.%).

**Alteration Type II:** The matrix is grayish in color and olivine phenocrysts are completely pseudomorphed by saponite. The extents of alteration are intermediate (20 – 25 %) and H<sub>2</sub>O contents are relatively high (2.90 – 3.40 wt.%). Alteration Type II occurs at the inner parts of rock fragments that were altered under more reducing conditions than Alteration Type I.

**Alteration Type III:** The matrix is brownish-reddish in color and olivine is completely pseudomorphed by iddingsite. The extent of alteration is 20 – 40 % and the H<sub>2</sub>O contents are relatively high (2.03 – 3.38 wt.%). Alteration Type III occurs at the outer rims of rock fragments and is characterized by alteration under oxidizing conditions.

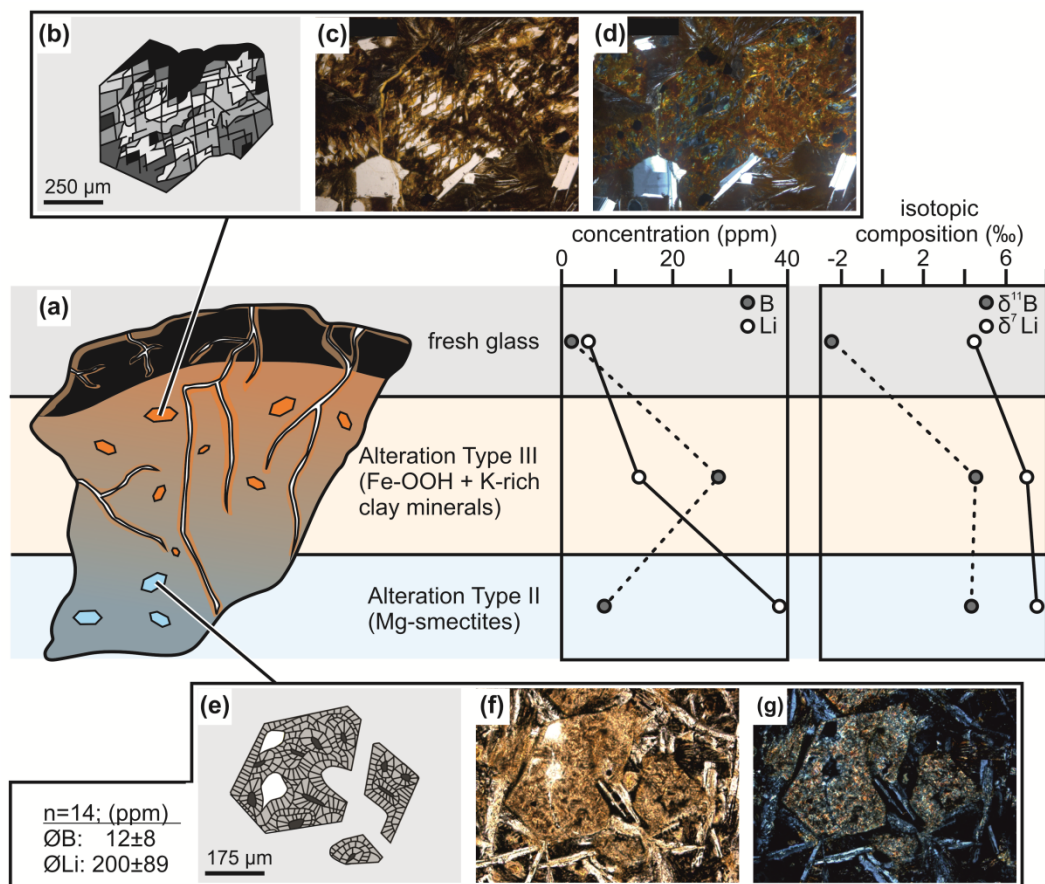


**Figure 4.5-3:** Distribution of olivine replacement types, B and Li concentrations in altered rim and core exemplified for sample AT-26-24-4776-RS-7, combined with the fresh glass sample AT-26-24-4779-RS-2. Upper row: Olivine replacement type (1) that occurs in Alteration Type I and III is dominated by an intergrowth of K-rich clay minerals and Fe-oxyhydroxides, referred to as iddingsite (AT-26-24-4776-RS-7). Lower row: Olivine replacement type (2) that occurs in Alteration Type II consists of saponite (AT-26-24-4776-RS-4). (b,e) schematic, (c,f) PPL - plane polarized light, (d,g) XPL - crossed polarized light. Boron and Li concentrations of saponite are based on LA-ICP-MS.

**Table 4.5-2:** Major element compositions and Sr, B and Li concentrations and isotopic compositions of altered rocks, fresh glass and a vein separate recovered during AT26-09 and AT26-24 from Dorado Outcrop. Sample labels are shown in **Figure 4.2-1**.

Label Figure 4.2-1	Sample location		Alteration		Compositions											
	Latitude N	Longitude W	Type*	Extent** %	MgO wt.% XRF†	K <sub>2</sub> O wt.% XRF†	H <sub>2</sub> O wt.% GFZ†	<sup>87</sup> Sr/ <sup>86</sup> Sr(2sd) TIMS	B μg/g MC-ICP-MS	δ <sup>11</sup> B ‰	2sd ‰	Li μg/g ICP-MS†	Li μg/g MC-ICP-MS	δ <sup>7</sup> Li ‰	2sd ‰	
<i>AT-26-24-</i>																
4776-RS-1	R1	9.084855812	-87.09841176	II	20	5.51	0.39	2.90	0.703054(10)	16.1	3.1	0.1	55.4	43.4	6.7	0.2
4776-RS-3	R2	9.083110127	-87.09859385	I	10	5.24	0.33	1.71					19.0			
4776-RS-4	R3	9.082386447	-87.09711057	II	25	6.07	0.43	3.40	0.703111(6)	17.3	4.1	0.1	52.6	46.4	7.4	0.2
4776-RS-7-CORE	R4	9.082341122	-87.09533606	II		5.40	0.38	3.13	0.703308(9)	13.8	4.2	0.1	46.9	39.1	7.7	0.1
4776-RS-7-RIM	R4	9.082341122	-87.09533606	III	35	2.50	0.63	3.22	0.704069(4)	28.2	4.4	0.1	13.1	13.1	6.9	0.1
4777-RS-1	R5	9.081391389	-87.09341611	III	25	3.36	0.39	2.40	0.703285(4)				15.2	14.4	5.2	0.2
4777-RS-3	R6	9.082467778	-87.09546333	I	15	5.20	0.42	2.05					15.0			
4778-RS-1	R7	9.0824416	-87.09541747	I	10	5.00	0.35	2.13	0.703486(6)				18.7	17.9	6.2	0.1
4779-RS-1	R8	9.081364133	-87.0933159	I	10	4.59	0.34	2.44	0.703265(5)	15.8	4.6	0.1	22.7	20.8	6.2	0.2
4779-RS-2	R9	9.081463619	-87.09316119	III	40	1.88	0.85	3.38	0.704422(5)	28	4.2	0.1	11.1	10.5	6.9	0.3
4782-RS-4	R10	9.085488916	-87.09743801	I	8	4.89	0.48	2.02					20.7			
4782-RS-5	R11	9.084457741	-87.09670095	II	25	5.50	0.42	3.20	0.703135(6)				48.4			
<i>AT-26-09-J2-757-</i>																
RO-08	R12	9.08217197	-87.09540376	III	20	4.07	0.33	2.19					18.5			
RO-09	R13	9.08252511	-87.09525696	II	20	5.49	0.32	3.30	0.703200(6)				51.6	49.4	7.1	0.1
RO-10	R14	9.08216896	-87.09536849	III	20	3.95	0.31	2.03					17.4			
RO-11	R15	9.0823913	-87.0953842	III	30	3.30	0.42	2.73	0.703583(6)	15.8	4.2	0.1	17.5			
RO-12	R16	9.08782868	-87.10047736	I	5	5.99	0.48	1.38	0.703202(5)	7.5	4.1	0.1	13.6	13.2	5	0.1
<i>AT-26-24-</i>																
						EMPA†	EMPA†									
4776-RS-7-GLASS	R4	9.082341122	-87.09533606			7.56	0.31									
4779-RS-2-GLASS	R9	9.081463619	-87.09316119			7.52	0.32	0.46	0.702825(5)	2	-2.4	0.1		5.6	4.3	0.2
4779-RS-2-VEIN	R9	9.081463619	-87.09316119						0.707459(8)	25.2	1.7	0.1		36.2	7.9	0.1

\*Alteration Types are split in three groups, for details see **Chapter 4.5.2.1**. \*\*Alteration extents are based the occurrence of secondary relative to primary minerals identified in thin sections. Measurements marked with a † were taken from Wheat et al. (2019), performed on the same rock material. XRF=X-ray fluorescence analysis, GFZ=VARIO EL III analyzer, TIMS=Thermal ionization mass spectrometry, MC-ICP-MS=Multi collector inductively coupled plasma mass spectrometry.

Two replacement types of olivine are identified: (1) an intergrowth of reddish-brownish clay minerals and Fe-oxyhydroxides (“iddingsite”) that primarily appears in Alteration Type I and III. The high K concentrations of the whole rocks dominated by this olivine replacement type (*Table 4.5-2*) point to a K-rich clay mineral component (e.g. celadonite, *Figure 4.5-3b-d*); and (2) a replacement by saponite, primarily appearing in Alteration Type II (*Figure 4.5-3e-g, Table 4.5-3*).

In summary, two main alteration styles can be related to differences in the redox conditions during alteration of basalt collected from Dorado Outcrop. A secondary mineral assemblage dominated by Fe-oxyhydroxides and K-rich clay mineral in the outer part of rock fragments (Alteration Type I), and in particular in the formerly glassy rims of lava flows (Alteration Type III, *Figure 4.5-3*) indicates highly oxic conditions. By contrast, alteration to Mg-smectites indicates more reducing, suboxic conditions (Marescotti *et al.*, 2000) in the center of fragments (Alteration Type II).

In addition, several rocks are cut by 0.05-2 mm thick veins, consisting of well-crystallized phillipsite, partly intergrown with Fe-Mn-oxides and clay minerals (*Figure 4.5-4, Table 4.5-3*). The clay minerals are part of the smectite-group, most likely an intergrowth of beidellite-montmorillonite (*Table 4.5-3*). One vein shows a zonation of a calcite-infill towards the rim, overgrown by phillipsite after further widening (*Figure 4.5-4b*).

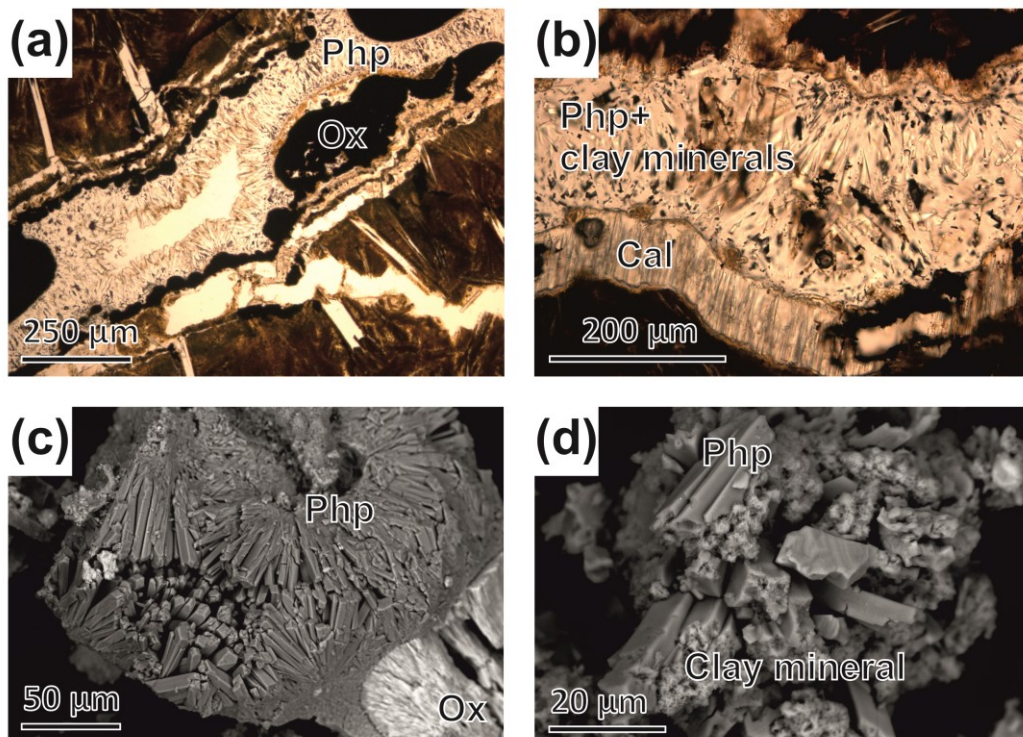


**Figure 4.5-4:** Examples of vein fillings. (a) vein filled by Fe-Mn-oxides (Ox), superimposed by freely grown phillipsite (Php, PPL, AT-26-24-4776-RS-7), (b) vein lined by fibrous calcite (Cal) and overgrown by (Php), partly interspersed with clay minerals (PPL, AT-26-24-4779-RS-2), (c) vein filled with (Ox) and (Php) (SEM, AT-26-24-4776-RS-7), (d) vein with intergrowth of (Php) and clay minerals (SEM, AT-26-24-4779-RS-2).

#### 4.5.2.2. Lithium and boron concentrations and isotopic compositions of rock samples

The fresh basaltic glass sample from Dorado Outcrop has Li and B concentrations of 5.6  $\mu\text{g/g}$  and 2.0  $\mu\text{g/g}$ , respectively (**Table 4.5-2**). The altered whole rocks are enriched in Li and B contents relative to the fresh glass. Whole rock analyses with the highest Li contents belong to Alteration Type II (maximum 49.4  $\mu\text{g/g}$ ), which is most abundant in the center of rock fragments and is characterized by the occurrence of saponite, which formed under more reducing conditions (**Figure 4.5-2d**, **Figure 4.5-3a**). Samples with the highest B concentrations (up to 28.2  $\mu\text{g/g}$ ) belong to Alteration Type III that is dominated by iddingsite as secondary phase formed under oxic conditions and show comparatively lower Li concentrations. Increased B concentrations are linked to other indicators for low-temperature seafloor alteration, like elevated  $^{87}\text{Sr}/^{86}\text{Sr}$  as well as  $\text{K}_2\text{O}$  values and low MgO contents (**Figure 4.5-2a-c**).

In-situ analyses of saponite by LA-ICP-MS show average Li and B concentrations of  $200 \pm 89$  and  $12 \pm 8$   $\mu\text{g/g}$  (2sd, n=14). The vein separate (zeolites + smectites + Fe-Mn-oxides) shows Li and B concentrations of 36.2 and 25.2  $\mu\text{g/g}$  (**Figure 4.5-2e,f**).

**Table 4.5-3:** Average compositions of mineral phases that are based on EMPA and SEM. All data points are given in the Appendix, **Table A. 3-3** and **Table A. 3-4**.

AVERAGES	n=18		n=5		n=21	
	Mg-smc	2sd	bei-mnt	2sd	zeo	2sd
SiO <sub>2</sub>	45.23	3.89	46.37	3.54	62.03	6.53
Al <sub>2</sub> O <sub>3</sub>	5.02	2.60	9.11	3.10	20.65	4.00
TiO <sub>2</sub>	0.04	0.05	0.22		0.13	0.46
MgO	20.47	2.56	7.04	3.91	0.39	1.08
FeO <sup>T</sup>	6.89	3.20	10.27	1.88	1.05	3.30
MnO	0.04	0.10	0.67	1.33	0.49	1.90
CaO	0.10	0.08	1.24	2.50	0.09	0.22
Na <sub>2</sub> O	2.13	0.59	0.65	0.64	4.41	3.50
K <sub>2</sub> O	1.19	0.97	2.67	1.80	5.73	1.24
ZnO	0.03	0.07			0.06	0.25
Cr <sub>2</sub> O <sub>3</sub>	0.06	0.06	0.01		0.02	0.06
<b>Total</b>	<b>81.19</b>		<b>79.58</b>		<b>95.06</b>	
tetrahedral			cations			
Si <sup>4+</sup>	3.59		3.85		Si <sup>4+</sup>	11.63
Al <sup>3+IV</sup>	0.41		0.15		Al <sup>3+</sup>	4.56
<b>total</b>	<b>4.00</b>		<b>4.00</b>		<b>total</b>	<b>16.19</b>
octahedral						
Al <sup>3+VI</sup>	0.06		0.74			
Ti <sup>4+</sup>	0.00		0.01		Ti <sup>4+</sup>	0.02
Mg <sup>2+</sup>	2.42		0.87		Mg <sup>2+</sup>	0.11
Fe <sup>2+</sup>	0.46		0.71		Fe <sup>2+</sup>	0.17
Mn <sup>2+</sup>	0.00		0.05		Mn <sup>2+</sup>	0.08
Zn <sup>2+</sup>	0.00		0.00		Zn <sup>2+</sup>	0.01
Cr <sup>3+</sup>	0.00		0.00		Cr <sup>3+</sup>	0.00
<b>total</b>	<b>2.94</b>		<b>2.39</b>		<b>total</b>	<b>0.38</b>
interlayer						
Ca <sup>2+</sup>	0.01		0.11		Ca <sup>2+</sup>	0.02
Na <sup>+</sup>	0.33		0.10		Na <sup>+</sup>	1.60
K <sup>+</sup>	0.12		0.28		K <sup>+</sup>	1.37
<b>total</b>	<b>0.46</b>		<b>0.50</b>		<b>total</b>	<b>2.99</b>

Mg-smc=Mg-smectite, bei-mnt=beidellite-montmorillonite, zeo=zeolite (phillipsite).

The  $\delta^7\text{Li}$  values of the altered rocks show compositions between +5.0 to +7.7 ‰, and a general increase in  $\delta^7\text{Li}$  value with increasing extents of alteration (**Figure 4.5-2f**). The  $\delta^{11}\text{B}$  values of the altered rocks are higher relative to those of the fresh glass and lie in a narrow range of +3.1 to

+4.6 ‰ (**Figure 4.5-2e**). The vein separate has a  $\delta^7\text{Li}$  value of  $+7.9 \pm 0.1$  ‰, and a  $\delta^{11}\text{B}$  value of  $+1.7 \pm 0.1$  ‰. The fresh glass has a  $\delta^7\text{Li}$  value of  $+4.3 \pm 0.2$  ‰ and a  $\delta^{11}\text{B}$  value of  $-2.4 \pm 0.1$  ‰, typical for unaltered MORB (Penniston-Dorland *et al.*, 2017; Marschall *et al.*, 2017).

## 4.6. Discussion

### 4.6.1. Impact of reverse weathering in ridge flanks on ocean geochemical budgets

#### 4.6.1.1. Lithium

Concentration and isotopic composition of Li in seawater are controlled by three main sources: (1) runoff from the continents by rivers and groundwater discharge, (2) venting of high-temperature hydrothermal fluids at the ridge axis, and by (3) expulsion of fluids in subduction zones. Misra & Froelich (2012) recently computed a weighted mean of these three sources at steady state and proposed that  $\delta^7\text{Li}$  seawater composition should be +16 ‰. From the difference between this hypothetical and the observed value of seawater (+31 ‰), they conclude that reverse weathering constitutes an important sink for Li and leads to a preferential uptake of  $^6\text{Li}$  by low-temperature basalt alteration (< 150 °C) and the diagenesis of marine sediments (see also Chan *et al.*, 2006). We have re-calculated the global budget of the modern ocean, using more recent estimates (**Table 4.1-1, Chapter 4.4**) and show that the weighted  $\delta^7\text{Li}$  source flux of seawater is approximately +16.5 ‰. This assigns a  $\Delta^7\text{Li}$  of +14.5 ‰ to Li uptake during reverse weathering. Despite the great impact of these removal processes to explain the discrepancy between the Li isotopic composition of seawater and that of the combined source fluxes, the relative roles of crustal alteration (e.g., in RFHS) versus sedimentary Li sink fluxes are poorly constrained. Additionally, it is uncertain if the two types of reverse weathering come with different isotope effects (cf. Li & West, 2014). Discharging fluids from Dorado Outcrop offer the unique opportunity to examine the role of RFHS as a Li sink in the oceans and determine the  $\delta^7\text{Li}$  value of the Li taken up by crustal alteration. Based on this estimate, we can make a first attempt to discern between removal of  $^6\text{Li}$  from seawater by crustal alteration and other removal mechanisms.

Existing estimates of Li uptake flux by reverse weathering are derived from rock alteration studies of modern ocean crust and ophiolites and show a large scatter (< 2 to > 20 × 10<sup>9</sup> mol Li/yr ; Penniston-Dorland *et al.*, 2017 and references therein). This large range is due to variable Li uptake preferences depending on the type of secondary minerals, overprinting relationships by low- and high-temperature alteration or because of differences in ocean composition and the intensity of seawater circulation (e.g. Chan *et al.*, 2002; Coogan *et al.*, 2017). The range equates to < 6 % to > 58 % of the total oceanic sink related to reverse silicate weathering (**Table 4.1-1**). This range indicates that the removal flux of Li in RFHS could play a trivial or dominant role in the oceanic Li budget.

Flux estimates based on fluid compositions were limited to data from warm spring fluids (64 °C) collected from the ridge flank of the JFR and gave an upper-limit for the Li flux into the crust of

$1.8 \times 10^9$  mol Li/yr (Wheat & Mottl, 2000). However, the crust at JFR is anomalous warm compared to average crustal temperature in ridge flanks, leading to a potential underestimate of Li removal flux. Hydrothermal fluid compositions from the more typical example of a RFHS at Dorado Outcrop (fluid discharge temperatures  $\sim 12.3$  °C) point to a higher Li removal flux than at the JFR (Wheat *et al.*, 2017). We calculate a global Li flux into the crust from RFHS of  $5.8 \times 10^9$  mol Li/yr, based on a temperature difference between bottom seawater and formation fluid of  $13.2$  °C at Dorado Outcrop (Wheat *et al.*, 2017), a global heat flux of  $8.1$  TW (Mottl, 2003), a heat capacity of  $3986$  J/(kg  $\times$  K) (Millero *et al.*, 1973) and the Li loss measured in the Dorado Outcrop end-member fluid relative to bottom seawater ( $-1.2$   $\mu$ mol Li/kg). This Li sink compensates around 28 % of the estimated riverine flux. To balance the calculated total Li source flux of  $34.1 \times 10^9$  mol Li/yr (**Table 4.1-1**) with removal only from RFHS, typical RFHS would need a similar Li anomaly and a formation fluid thermal anomaly that was  $<4$  °C. Assuming the observed Li anomaly is globally consistent, this simple calculation demonstrates that either low-temperature basalt alteration in RFHS primarily occurs at temperatures  $< 4$ °C above ambient or has to be accompanied by additional Li removal mechanisms, like marine sediment diagenesis.

Fluid samples from Dorado Outcrop also allow us to make a first quantitative estimate of the impact of RFHS processes on Li isotope fractionation and hence the  $\delta^7\text{Li}$  composition of seawater. The end-member fluid of Dorado Outcrop has a  $\delta^7\text{Li}$  composition of  $+31.9 \pm 0.2$  ‰ and is isotopically heavier than ambient seawater of  $+31.2 \pm 0.2$  ‰ due to the preferential removal of the lighter  $^6\text{Li}$  isotope by altered crust at low-temperatures. We constrain the impact of this preferential removal flux in RFHS on global seawater Li isotopic based on several assumptions. We presume that the total influx of Li to the oceans of  $34.1 \times 10^9$  mol Li/yr is matched by an equivalent removal flux at steady state. Using the Dorado constraints ( $\Delta T = 13.2$ °C; output flux =  $25.0$   $\mu$ mol Li/kg) and summing  $8.1$  TW convective heat loss, the annual amount of Li that passes through RFHS and flows back to the oceans, is  $121 \times 10^9$  mol Li/yr. The Li re-flux of RFHS is hence 3.6 times higher than the input flux of Li to the oceans. Our data show that fluids exiting the RFHS have a  $\delta^7\text{Li}$  that is  $0.7 \pm 0.4$  ‰ heavier than that of seawater. Therefore, using observation from Dorado Outcrop on a global scale, we can account for an elevation in seawater  $\delta^7\text{Li}$  composition of  $2.5 \pm 1.4$  ‰. Thus, the preferential uptake of  $^6\text{Li}$  by exchange in RFHS is capable of explaining between 7 and 27 % of the necessary shift  $\Delta^7\text{Li}$  of  $+14.5$  ‰. The remaining isotopic shift must be due to additional preferential uptake mechanisms of  $^6\text{Li}$ , most likely driven by diagenesis within marine sediments. However, the calculation is very sensitive for differences in temperature between formation fluid and bottom seawater. Hence, the role of low-temperature alteration in RFHS could be significantly larger in the case where temperature differences measured at Dorado Outcrop ( $\Delta T = 13.2$  °C) are higher than globally representative for RFHS. The end-member fluid composition from Dorado Outcrop gives a first estimate of the impact of RFHS on the Li isotope budget of modern seawater. Nevertheless, the calculation is based on observation of one RFHS only. To test the reliability of the

flux estimate, high quality samples from similar settings and with a range of reaction temperatures is needed to constraint the Li fluxes.

#### 4.6.1.2. *Strontium*

The  $^{87}\text{Sr}/^{86}\text{Sr}$  composition of modern seawater (0.7091) is mainly controlled by continental runoff and hot (>300 °C) hydrothermal discharge. However, a greater portion of unradiogenic Sr is necessary to balance the global seawater composition than can be solely explained by axial hydrothermal fluxes, e.g. by Elderfield & Schultz (1996). Butterfield *et al.* (2001) suggested that fluids reacting with basaltic crust at low temperatures may constitute an additional source of unradiogenic Sr to seawater, based on  $^{87}\text{Sr}/^{86}\text{Sr}$  compositions of warm (~ 64 °C) spring fluids from the eastern flank of the JFR. Davis *et al.* (2003) found that the Sr isotopic composition of altered upper oceanic crust is inconsistent with a large role for RFHS in the Sr budget and suggested that perhaps the global riverine flux is less radiogenic than proposed. Pore fluid data from the IODP Site U1301 (JFR) showed that the major portion of Sr is derived from the base of the sediment column and is significantly less radiogenic (lowest sample 0.707609) compared to seawater (0.7091), closely matching the  $^{87}\text{Sr}/^{86}\text{Sr}$  composition of Baby Bare spring fluids (0.70745, Butterfield *et al.*, 2001). Strontium concentrations in discharging fluids from Dorado Outcrop are more representative of typical RFHS (~12.3 °C). However, strontium concentrations in discrete and continuous fluid samples do not display a statistically different concentration relative to ambient seawater (Wheat *et al.*, 2017). In this study, we investigated the Sr isotopic composition of discharging fluids from Dorado Outcrop. Similar to the Sr concentrations, the Sr isotopic compositions do not show a statistically relevant difference compared to bottom seawater (**Figure 4.5-1c**). One sample shows even a slightly elevated  $^{87}\text{Sr}/^{86}\text{Sr}$  composition relative to seawater. Thus, the impact of low-temperature RFHS on the  $^{87}\text{Sr}/^{86}\text{Sr}$  composition of seawater cannot be confirmed based on these findings. However, many factors such as the age of the crust and the residence time of the fluids within the crust may affect the extent of isotopic exchange of Sr. Therefore, sampling of additional highly representative RFHS fluids is necessary for a more robust assessment.

#### 4.6.2. *Low-temperature basalt alteration and uptake of lithium and boron*

The altered basalts investigated in this study were collected from the seawater exposed surface of Dorado Outcrop and are, hence, not suitable to make quantitative assumptions of uptake fluxes within RFHS. However, rock samples from Dorado Outcrop provide a measure of low-temperature altered crust that was exposed to seawater for an exceptionally long time (> 18.5 Ma). Additional, hydrothermal discharge at the current sites is a “recent” phenomenon and hydrothermal fluid composition is similar to seawater composition (Wheat *et al.*, 2019, Wheat *et al.*, 2017). Alteration characteristics at the surface of Dorado Outcrop can therefore represent advanced seafloor alteration and help to constrain the principal Li and B uptake mechanisms, their secondary host minerals and potentially also to make qualitative assumptions on fluid-rock interactions within RFHS.

Altered basalts exposed at Dorado Outcrop are generally enriched in Li and B and in the heavy isotopes compared to the precursor as a result of alteration of the rocks by seawater at low-temperatures (**Figure 4.5-2c,d**). Other low-temperature alteration indicators, like MgO losses, K<sub>2</sub>O gains, and <sup>87</sup>Sr/<sup>86</sup>Sr ratio increases (**Figure 4.5-2a,b**) corroborate the idea of pronounced low-temperature alteration of the basalts. Interestingly, the Li and B concentrations of altered basalts strongly differ between the oxic altered outer surfaces and the inner parts of rock fragments that were altered under more reducing conditions (**Figure 4.5-3**).

We suggest that Li enrichment of the whole rocks by alteration reflects Li substitution for Mg (and minor Fe) that occurs in the octahedral layers of Mg-rich smectites (e.g. Berger *et al.*, 1988, Chan *et al.*, 1992, Chan *et al.*, 2002), typical for more reducing alteration conditions (Marescotti *et al.*, 2000). Accordingly, the whole rocks at Dorado Outcrop show the highest Li contents (up to 49.4 µg/g) at the Mg-smectite- (saponite) rich inner parts of rock pieces that are not directly exposed to seawater (Alteration Type II), and also the LA-ICP-MS data identify saponite (on average 200 ± 89 µg/g Li) as principal host of Li (**Figure 4.5-3**). If we assume that the Li contents of the Mg-smectite-rich whole rocks (~ 50 µg/g) are solely produced by adding Li from newly formed saponite (200 ± 89 µg/g) to the precursor (5.6 µg/g), roughly 23 % replacement by saponite is necessary to explain the whole rock Li contents at Dorado Outcrop. This degree of replacement is similar to the extent of alteration (20 – 25 %) identified by petrographic observations (**Table 4.5-2**). In contrast, the iddingsite-rich rims that were altered under oxic conditions (Alteration Type III), show only minor Li enrichment compared to the precursor and the rock interiors (**Figure 4.5-3**), reinforcing the major role of Mg-rich secondary phases for Li fixation. Indeed, in contrast to the Dorado Outcrop rocks, the low-temperature altered basalts from a transect along the Mid-Atlantic Ridge (MAR) described by Chan *et al.* (1992) display the highest Li enrichment (75.3 µg/g) in the oxic altered rims, while the rock interiors show similar Li contents (56 µg/g) like the Dorado Outcrop rocks. This mismatch between our findings and those of Chan *et al.* (1992) may indicate that either Mg-rich smectites can also form under more oxidizing conditions or that the altered rims from the MAR contain another major secondary host mineral for Li (e.g. zeolites), which is not present in noticeable amount in the oxic altered rims at Dorado Outcrop. The zeolite- and smectite-rich vein separate from Dorado Outcrop shows Li concentrations of 36.2 µg/g, higher than fresh glass (5.6 µg/g) but also not capable to explain the high Li concentrations of up to 75.3 µg/g at the rims of the MAR samples. Nevertheless, the composition of the interlayer in zeolites can vary greatly, in strong dependence on exchange reactions with compensating cations (Berger *et al.*, 1988; Berger, 1992) and therefore zeolites at the MAR may reached such high Li concentrations.

The greatest level of B enrichment is in the oxidized rims (Alteration Type III), and is either incorporated in the K-rich clay mineral component or sorbed onto surfaces of Fe-oxyhydroxides in iddingsite (Goldberg *et al.*, 1993; Demetriou & Pashalidis, 2012). The saponite-rich interiors

(Alteration Type II) are enriched in B relative to the precursor, but show lesser B enrichment than the rims (**Figure 4.5-2c; Figure 4.5-3**), matching the comparable low B concentrations of the interior dominating alteration phase saponite (on average  $12 \pm 8 \mu\text{g/g}$ ). When comparing our data to published B data for low-temperature altered oceanic crust from other locations, the B enrichment at Dorado Outcrop is relatively moderate in particular given the long exposure time of the crust to seawater and the low alteration temperatures (**Figure 4.6-1a**, Spivack & Edmond, 1987, Smith *et al.*, 1995, Yamaoka *et al.*, 2015). Still, our data show that oxidative seawater alteration constitutes a sink of B in the oceans.

If we assume that the general alteration characteristics within the RFHS are comparable to the directly seawater exposed surface of Dorado Outcrop, we can use the hydrothermal fluid compositions to make assumptions about the alteration conditions in deeper portions of the crust. The discharging fluids of Dorado Outcrop show a decrease in Li and a tendency to higher B concentrations than ambient seawater (Wheat *et al.*, 2017), similar in flux direction to the warmer (64 °C) RFHS at the JFR but with smaller absolute concentrations (Wheat & Mottl, 2000). The uptake of Li by the crust, while B is only minor affected or behaves as a source, points to a Mg-rich smectite as major alteration phase in deeper portions of the RFHS, according to the high Li concentrations of the Mg-smectite-rich rocks at the surface (**Figure 4.5-2d**). The occurrence of Mg-smectites in turn is associated with more reducing alteration conditions (Marescotti *et al.*, 2000). However, fluid flow at Dorado Outcrop is quick (< 10 years) and the chemical composition of discharging fluids shows only minor evolution compared to ambient seawater (Wheat *et al.*, 2017), for that reason we would presume that oxic alteration should also play a significant role within RFHS. Indeed, based on surface alteration patterns we would expect a decrease in discharging fluid B concentrations by oxic alteration that is not displayed in the data. This points to the high complexity of B partitioning between low-temperature hydrothermal fluids and oceanic crust and demonstrate that more work on marine B output fluxes is necessary to elucidate the role of RFHS on global B budgets.

#### 4.6.3. *Impact of variations in past isotopic seawater composition on altered basalts*

In this section, we examine if variations in seawater  $\delta^7\text{Li}$  and  $\delta^{11}\text{B}$  values in the past may had an influence on the crustal composition of Dorado Outcrop that formed 18.5 to 23 Ma. Similar to Sr isotope that have been used to determine relative changes in continental and hydrothermal sources of Sr to the oceans over time (e.g. McArthur, 1994; Coggon *et al.*, 2010), Li and B isotopes are likely also subjected to variations in reservoir fluxes. Planktonic foraminifera data indicate a significant shift towards higher  $\delta^7\text{Li}$  seawater values in the Cenozoic (Hathorne & James, 2006; Misra & Froelich, 2012; Li & West, 2014; Vigier & Godd ris, 2015; Roberts *et al.*, 2018). Li & West (2014) suggested a drastic increase in  $\delta^7\text{Li}$  seawater composition by approximately +9 ‰ over the last 60 Myr. The reconstruction of past  $\delta^{11}\text{B}$  seawater values is less straightforward due to the

pH dependence of B speciation in aqueous solution, which impacts the  $\delta^{11}\text{B}$  composition of carbonate precipitates. Also, the uncertainties associated with vital effects in biogenic carbonates are large for B (see Gaillardet & Lemarchand, 2018 for a recent review). Foraminifera data (Pearson & Palmer, 2000, Raitzsch & Hönisch, 2013, Greenop *et al.*, 2017) point to a uniform  $\delta^{11}\text{B}$  seawater composition over the past 20 Myr between +38 ‰ and +39.6 ‰, in good agreement with calculated  $\delta^{11}\text{B}$  seawater values by Lemarchand *et al.* (2000). In contrast, data deduced from fluid inclusions in halites indicate that seawater  $\delta^{11}\text{B}$  values may have been as low as +32 ‰ in the last 40 Myr (Paris *et al.*, 2010).

In the following, we first discuss the impact that parameters like temperature, mineralogy, and host rock composition may have on the  $\delta^7\text{Li}$  composition of basalt alteration products and then continue with possible effects caused by paleo-seawater variations. The  $\delta^7\text{Li}$  data of Dorado Outcrop altered basalts and a vein separate (phillipste + smectite + Fe-Mn-oxides) fall on a common trend, pointing to a  $\delta^7\text{Li}$  alteration end-member (EM) composition of approximately +8 ‰ (**Figure 4.6-1b**). This trend holds regardless of the Alteration Types and associated variations in secondary mineralogy. In comparison to literature data, the  $\delta^7\text{Li}$  end-member composition of the Dorado Outcrop rocks is relatively low (**Figure 4.6-1b**). The high  $\delta^7\text{Li}$  values of altered rocks from ODP Hole 504B and 896A can be explained by interaction with fluids at elevated temperatures (Chan *et al.*, 2002). But the altered basalts dredged from a transect at the Mid-Atlantic Ridge at 23°N (1 to 46 Myr old crust; Chan *et al.*, 1992) also point to a  $\delta^7\text{Li}$  EM of +14 ‰; about +6 ‰ higher than the Dorado Outcrop EM. The altered basalts and celadonite separates from the Cretaceous Troodos Ophiolite (Coogan *et al.*, 2017) show mostly lower  $\delta^7\text{Li}$  compositions than dredged samples published by Chan *et al.* (1992), similar to Dorado Outcrop. All three data sets (Dorado Outcrop, MAR, and Troodos Ophiolite) are derived from oceanic crust that was altered by seawater at low temperatures (2-15 °C) and show similar secondary Li host phases (smectites, celadonite, and zeolites). The  $\delta^7\text{Li}$  compositions of global fresh basalts and basaltic glasses plot in a narrow range of +3 to +5 ‰, and all three data sets form a mixture line between EM and the precursor that point to a fresh basalt  $\delta^7\text{Li}$  composition that is close to the fresh glass of Dorado Outcrop (+4.3 ± 0.2 ‰, **Figure 4.6-1b**). Therefore, variations in host rock composition have not caused the differences in  $\delta^7\text{Li}$  EM values of altered basalts from the three locations.

To elucidate the possible impacts of changing seawater (SW) composition on the  $\delta^7\text{Li}$  value of seafloor weathering products, we ran a simple calculation (pink box in **Figure 4.6-1b**). We kept the fractionation factor  $\alpha_{\text{EM-SW}}$  constant at 0.98067, based on a linear extrapolation of experimental data to an alteration temperature of 2 °C (**Figure 4.6-2**). Seawater  $\delta^7\text{Li}$  compositions for the discrete time intervals in **Figure 4.6-1b** were deduced from the smoothed fit by a Gaussian filter with 0.5 Myr total width that was published by Li & West (2014), based on the  $\delta^7\text{Li}$  foraminifera data and standard deviation of all  $\delta^7\text{Li}$  values of ± 1.1 ‰ ( $2\text{sd}_{\text{mean}}$ ) measured by Misra & Froelich (2012).

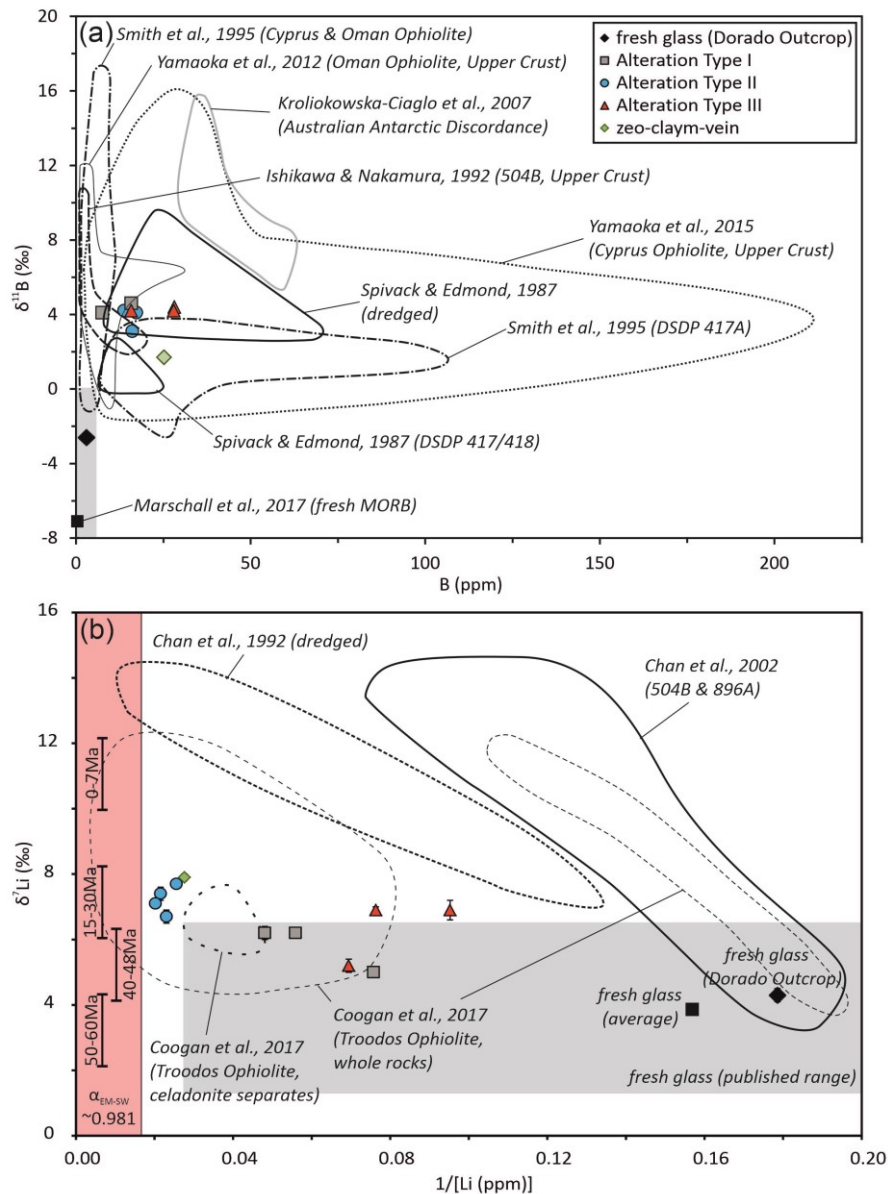


**Figure 4.6-1:** Isotopic compositions of Dorado outcrop glass, altered rock and vein samples merged with published data of low-temperature altered oceanic crust from different locations. (a) Boron concentrations versus B isotopes. For (Yamaoka et al., 2015) only pillow basalts are shown. The grey box shows the range of fresh basaltic glass values without predicted assimilation of altered crust in the magma source in literature (see Marschall, 2018 and references therein). (b) Lithium concentrations ( $1/\text{Li}$   $\mu\text{g/g}$ ) versus Li isotopes. For Coogan et al. (2017) three stronger deviating data points are excluded, for Chan et al. (2002) the upper crust down to 595 mbsf is shown, breccias excluded. The grey box represents the range of published fresh glass values (Chan et al., 1992, Moriguti & Nakamura, 1998b, Elliott et al., 2006, Nishio et al., 2007, Tomascak et al., 2008); the filled black square shows the average of all fresh glass values. The pink box shows calculated  $\delta^7\text{Li}$  rock altered end-member (EM) compositions with the assumption of changing  $\delta^7\text{Li}$  values of seawater (SW) over time (0-7 Ma: +31 ‰, 15-30 Ma: +27 ‰, 40-48 Ma: +25 ‰, 50-60 Ma: +23 ‰, Misra & Froelich, 2012, Li & West, 2014) and fixed uncertainties (2sd mean) of 1.1 ‰ based on the average standard deviation of all measured  $\delta^7\text{Li}$  compositions (Misra & Froelich, 2012). For calculations, a constant isotopic fractionation factor  $\alpha_{\text{EM-SW}} = 0.98067$  deduced from linear extrapolation of experimental data at 2 °C is used (see Figure 4.6-2).

Previous workers (Li & West, 2014; Misra & Froelich, 2012) suggested that the  $\delta^7\text{Li}$  seawater value was steady in four periods (0-7 Ma: +31 ‰, 15-30 Ma: +27 ‰, 40-48 Ma: +25 ‰, 50-60 Ma: +23 ‰). These periods are separated by three events of abrupt increases in seawater  $\delta^7\text{Li}$  values. Our calculations (**Figure 4.6-1b**) reveal that a  $\delta^7\text{Li}$  end-member composition of +8 ‰ is in good agreement with interaction between oceanic crust and a seawater composition of approximately +27 ‰, similar to the composition of seawater 15-30 Ma and consistent with the minimum age of Dorado Outcrop of 18.5 Myr (Wheat *et al.*, 2019). The Troodos Ophiolite crust has an age of 85-92 Ma but alteration and celadonite formation continued for up to 19 Myrs after crustal formation (Staudigel *et al.*, 1986). Because altered basalts from Dorado Outcrop and the Troodos Ophiolite lie in the same range (**Figure 4.6-1b**) seawater may have had a  $\delta^7\text{Li}$  value of +27 ‰ during Troodos crust alteration, which is roughly in line with the estimates by Misra & Froelich (2012).

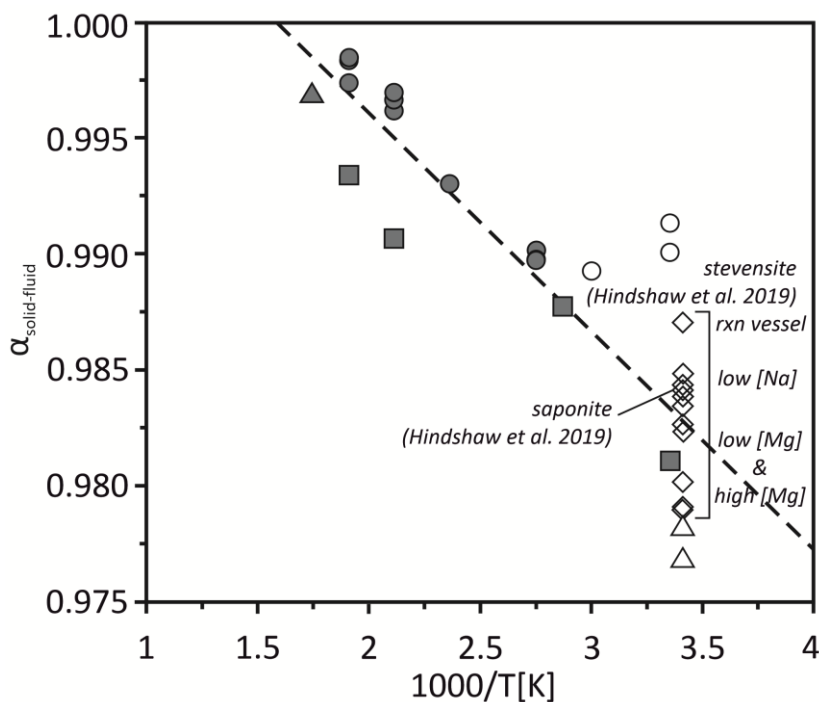


**Figure 4.6-2:** Correlation of temperature versus Li isotope fractionation factor ( $\alpha_{\text{solid-solution}}$ ), based on low-temperature experiments in literature, used to determine  $\alpha=0.98067$  at  $2^\circ\text{C}$  (modern bottom seawater temperature) by linear regression ( $\alpha_{\text{solid-solution}} = -0.00942 \times 1000/T[\text{K}] + 1.01491$ ,  $R^2 = 0.843$ ,  $p < 0.01$ ). Symbols (only measurements with filled symbols were used for calculations): filled triangle = illitization of smectite at  $300^\circ\text{C}$ , 100 MPa (Williams & Hervig, 2005); circles = synthesis of hectorite (smectite) at up to  $250^\circ\text{C}$ , equilibrium vapor pressure, experiments  $< 90^\circ\text{C}$  are excluded due to strongly deviating values interpreted to be caused by low crystallinity of the formed secondary phases (Vigier *et al.*, 2008); squares = basalt-seawater exchange at  $25 - 250^\circ\text{C}$  (Millot *et al.*, 2010a); diamonds = residual phases of saponite and stevensite, synthesized at  $20^\circ\text{C}$  using a reaction vessel or precipitated from solutions of low [Na], low [Mg] or high [Mg] (Hindshaw *et al.*, 2019); open triangles = leached secondary minerals, formed by reaction of basaltic-sand and river water in a closed system at  $20^\circ\text{C}$  (Pogge von Strandmann *et al.*, 2019). Data of high-pressure experiments (Wunder *et al.*, 2005; Wunder *et al.*, 2006; Wunder *et al.*, 2007) and model calculations (e.g. Dupuis *et al.*, 2017) were not considered.

We showed that the Dorado Outcrop and Troodos Ophiolite crust might have been influenced by interaction with seawater that was lower in  $\delta^7\text{Li}$  composition than modern seawater. It is unclear, why the dredged samples from the transect between 1 and 46 Myr old crust reported by Chan *et al.* (1992) imply a uniform and (relative to Dorado Outcrop and the Troodos Ophiolite) higher  $\delta^7\text{Li}$  end-member composition. One possible explanation is that Li uptake by the altered crust along the transect continued for a longer period, while alteration at the exposed Dorado Outcrop was completed shortly after crustal formation when  $\delta^7\text{Li}$  seawater composition still was low (around +27 ‰). More research of low-temperature altered crust of different ages in the context of the hydrological setting is necessary to confirm our assumptions.

In contrast to Li isotopes, the B isotope data of fossil foraminifera do not indicate major variations in  $\delta^{11}\text{B}$  seawater composition over the last 20 Myr (see explanations in the beginning of this chapter). Consistent with this notion, the altered rocks at Dorado Outcrop show a uniform  $\delta^{11}\text{B}$  composition of approximately +4 ‰ (**Figure 4.5-2e**; **Figure 4.6-1a**), irrespective of the different Alteration Type or B concentrations. All published  $\delta^{11}\text{B}$  compositions of modern low-temperature altered oceanic crust from younger crust fall in a similar range (**Figure 4.6-1a**). Higher  $\delta^{11}\text{B}$  values coupled with comparatively weak B enrichment documented for altered crust from ODP Hole 504B (Smith *et al.*, 1995) can be explained by interaction with higher-temperature fluids after sediment burial and conductive reheating, leading to a decrease in B isotope fractionation. A vein separate from Dorado Outcrop (smectite, phillipsite, Fe-Mn-oxides) shows a slightly lower B isotopic composition of  $+1.7 \pm 0.1$  ‰ than the altered whole rocks, most likely caused by a different isotope fractionation factor due to the fact that the vein mineralogy differs from that of the altered rock.

#### **4.7. Summary and conclusions**

Low-temperature alteration in RFHS is a significant removal process of isotopic light Li and B from seawater into secondary forming mineral phases, e.g. clay minerals. The fluid-discharge rate in global RFHS is similar to river input and has the potential to solve oceanic budgets. However, quantification of chemical fluxes from RFHS is poorly constrained compared to those estimated for riverine and hot hydrothermal processes. Rock samples of Dorado Outcrop give the opportunity to investigate crust in direct contact with seawater for at least 18.5 Myr and the fluid samples are the first ones from a typical RFHS, offering the unique opportunity to make first quantitative assumptions on fluxes based on low-temperature fluids. Nevertheless, only two RFHS discharge sites (Dorado Outcrop and JFR) have been sampled and refinement of findings will only come by sampling additional systems.

In summary, the data of Dorado Outcrop enable the following initial statements:

- (1) Lithium in discharging fluids from Dorado Outcrop was used to estimate the role of ridge flank seawater circulation on a global scale. We estimated a Li flux of  $5.8 \times 10^9$  mol Li/kg

that corresponds to approximately 28 % of the predicted river flux. Following, a combination of crust alteration with additional Li removal processes (e.g. sediment diagenesis) or a globally representative lower reaction temperature than observed at Dorado Outcrop ( $\sim 12.3$  °C) are needed to solve the global Li budget at steady state.

- (2) The hydrothermal end-member fluid has a  $\delta^7\text{Li}$  composition of +31.9 ‰ and is hence isotopically shifted relative to seawater by  $0.7 \pm 0.4$  ‰. By combining this constraint with the Li elemental fluxes, we deduced that circulation in RFHS can account for 7 to 27 % of the difference between the  $\delta^7\text{Li}$  value of modern seawater and that of the weighted source fluxes. Calculations are, however, prone to temperature variations and the impact of RFHS on global Li budgets could be significantly higher, assuming lower fluid temperatures in typical RFHS than those measured at Dorado Outcrop.
- (3) The lack of a difference in  $^{87}\text{Sr}/^{86}\text{Sr}$  composition between hydrothermal fluids and bottom seawater implies that low temperature RFHS may not influence the Sr isotopic budget of modern seawater.
- (4) Altered whole rocks from Dorado Outcrop exhibit two main alteration characteristics at interiors and rims of rock fragments. The inner parts are dominated by Mg-smectites that typically form under reducing alteration conditions and are highly enriched in Li and weakly enriched in B compared to fresh glass. The oxidized altered rims show iddingsite as the major secondary phase (K-rich clay mineral component and Fe-oxyhydroxides) and are strongly enriched in B and intermediately enriched in Li relative to fresh glass. The spring fluids of Dorado Outcrop display a loss of Li and no clear difference in B relative to ambient seawater, and potentially indicate that Mg-smectites and more reducing alteration conditions are most representative for alteration in greater depth. Vein-fillings show phillipsite + smectite + Fe-Mn-oxides  $\pm$  calcite. Glassy rims are replaced by palagonite.
- (5) Lithium isotopic compositions of altered rocks and a vein separate show a common alteration end-member of approximately +8 ‰ versus fresh glass of  $+4.3 \pm 0.2$  ‰. The relatively low  $\delta^7\text{Li}$  end-member composition compared to altered end-members from the MAR (+14 ‰, Chan *et al.*, 1992) was potentially produced by interaction with isotopically lighter seawater (+27 ‰) when the outcrop was formed  $>18.5$  Ma compared to modern seawater composition (+31 ‰).
- (6) Boron isotopic compositions of altered rocks show a uniform value of approximately +4 ‰, relative to fresh glass of  $-2.4 \pm 0.1$  ‰, that is in good agreement with younger low-temperature altered oceanic crust formerly published and with assumptions of minor variations in  $\delta^{11}\text{B}$  seawater composition over the last 20 Myr. The slightly lower  $\delta^{11}\text{B}$  composition of a vein separate composed of phillipsite + smectites + Fe-oxyhydroxides ( $+1.7 \pm 0.1$  ‰) compared to the altered whole rocks, points to small variations of the fractionation factor due to varying secondary mineralogy.

## ***Acknowledgements***

The authors thank the shipboard participants of AT26-24, including the crews and pilots of *ALVIN*. This research was supported by National Science Foundation grants OCE-1130146 (CGW). We also acknowledge funding from the DFG Research Instrumentation Program grant INST 144/308-1.

## ***References***

- Allègre C. J., Louvat P., Gaillardet J., Meynadier L., Rad S. and Capmas F. (2010) The fundamental role of island arc weathering in the oceanic Sr isotope budget. *Earth Planet. Sci. Lett.* **292**, 51–56.
- Alt J. C., Teagle D. A. H., Laverne C., Vanko D. A., Bach W., Honnorez J., Becker K., Ayadi M. and Pezard P. A. (1996) Ridge-flank alteration of upper ocean crust in the eastern Pacific. In *Proc. Ocean Drill. Progr.* (eds J. C. Alt, H. Kinoshita, L. B. Stokking and P. J. Michael), pp. 435–452.
- Bach W. and Humphris S. E. (1999) Relationship between the Sr and O isotope compositions of hydrothermal fluids and the spreading and magma-supply rates at oceanic spreading centers. *Geol.* **27**, 1067.
- Bagard M.-L., West A. J., Newman K. and Basu A. R. (2015) Lithium isotope fractionation in the Ganges–Brahmaputra floodplain and implications for groundwater impact on seawater isotopic composition. *Earth Planet. Sci. Lett.* **432**, 404–414.
- Berger G. (1992) Distribution of trace elements between clays and zeolites and aqueous solutions similar to seawater. *Appl. Geochem.* **7**, 193–203.
- Berger G., Schott J. and Guy C. (1988) Behavior of Li, Rb and Cs during basalt glass and olivine dissolution and chlorite, smectite and zeolite precipitation from seawater. *Chem. Geol.* **71**, 297–312.
- Bray A.M., Chan L.-H. and Von Damm K.L. Constancy of the Li-Isotopic Signature in Mid-Ocean Ridge Hydrothermal Fluids: Evidence for Equilibrium Control. *AGU, Fall Meeting 2001*, abstract id. OS41A-0440.
- Butterfield D. A., Nelson B. K., Wheat C., Mottl M. J. and Roe K. K. (2001) Evidence for basaltic Sr in midocean ridge-flank hydrothermal systems and implications for the global oceanic Sr isotope balance. *Geochim. Cosmochim. Acta* **65**, 4141–4153.
- Carson B., Suess E. and Strasser J. C. (1990) Fluid flow and mass flux determinations at vent sites on the Cascadia Margin Accretionary Prism. *J. Geophys. Res.* **95**, 8891.
- Chan L. H. and Edmond J. M. (1988) Variation of lithium isotope composition in the marine environment. *Geochim. Cosmochim. Acta* **52**, 1711–1717.
- Chan L.-H., Alt J. C. and Teagle D. A. H. (2002) Lithium and lithium isotope profiles through the upper oceanic crust: a study of seawater-basalt exchange at ODP Sites 504B and 896A. *Earth Planet. Sci. Lett.* **201**, 187–201.
- Chan L.-H., Edmond J. M. and Thompson G. (1993) A lithium isotope study of hot springs and metabasalts from Mid-Ocean Ridge Hydrothermal Systems. *J. Geophys. Res.* **98**, 9653.
- Chan L.-H., Edmond J. M., Thompson G. and Gillis K. (1992) Lithium isotopic composition of submarine basalts. *Earth Planet. Sci. Lett.* **108**, 151–160.
- Chan L., Gieskes J. M., You C.-F. and Edmond J. M. (1994) Lithium isotope geochemistry of sediments and hydrothermal fluids of the Guaymas Basin, Gulf of California. *Geochim. Cosmochim. Acta* **58**, 4443–4454.
- Chan L.-H. and Kastner M. (2000) Lithium isotopic compositions of pore fluids and sediments in the Costa Rica subduction zone. *Earth Planet. Sci. Lett.* **183**, 275–290.
- Chan L.-H., Leeman W. P. and Plank T. (2006) Lithium isotopic composition of marine sediments. *Geochem. Geophys. Geosyst.* **7**, Q06005.
- Clark E. A., Sheffield J., van Vliet M. T. H., Nijssen B. and Lettenmaier D. P. (2015) Continental Runoff into the Oceans (1950–2008). *J. Hydrometeorol.* **16**, 1502–1520.
- Coggon R. M., Teagle D. A. H., Smith-Duque C. E., Alt J. C. and Cooper M. J. (2010) Reconstructing past seawater Mg/Ca and Sr/Ca from mid-ocean ridge flank calcium carbonate veins. *Science* **327**, 1114–1117.

- Coogan L. A. and Dosso S. (2012) An internally consistent, probabilistic, determination of ridge-axis hydrothermal fluxes from basalt-hosted systems. *Earth Planet. Sci. Lett.* **323-324**, 92–101.
- Coogan L. A., Gillis K. M., Pope M. and Spence J. (2017) The role of low-temperature (off-axis) alteration of the oceanic crust in the global Li-cycle. *Geochim. Cosmochim. Acta* **203**, 201–215.
- Damm K. L. von (1990) Seafloor Hydrothermal Activity. *Annu. Rev. Earth Planet. Sci.* **18**, 173–204.
- Damm K. von, Edmond J., Grant B., Measures C., Walden B. and Weiss R. (1985) Chemistry of submarine hydrothermal solutions at 21 °N, East Pacific Rise. *Geochim. Cosmochim. Acta* **49**, 2197–2220.
- Davis A. C., Bickle M. J. and Teagle D. A. (2003) Imbalance in the oceanic strontium budget. *Earth Planet. Sci. Lett.* **211**, 173–187.
- Dellinger M., Gaillardet J., Bouchez J., Calmels D., Louvat P., Dosseto A., Gorge C., Alanoca L. and Maurice L. (2015) Riverine Li isotope fractionation in the Amazon River basin controlled by the weathering regimes. *Geochim. Cosmochim. Acta* **164**, 71–93.
- Demetriou A. and Pashalidis I. (2012) Adsorption of boron on iron-oxide in aqueous solutions. *Desalin. Water Treat.* **37**, 315–320.
- Deniel C. and Pin C. (2001) Single-stage method for the simultaneous isolation of lead and strontium from silicate samples for isotopic measurements. *Anal. Chim. Acta* **426**, 95–103.
- Donnelly T. W., Pritchard R. A., Emmermann R. and Puchelt H. (1980) The Aging of Oceanic Crust. In *Initial Reports of the Deep Sea Drilling Project, 51/52/53* (eds. T. Donnelly, J. Francheteau, W. Bryan, P. Robinson, M. Flower and M. Salisbury). U.S. Government Printing Office.
- Dupuis R., Benoit M., Tuckerman M. E. and Méheut M. (2017) Importance of a Fully Anharmonic Treatment of Equilibrium Isotope Fractionation Properties of Dissolved Ionic Species As Evidenced by Li+(aq). *Acc. Chem. Res.* **50**, 1597–1605.
- Eakins B. W. and Sharman G. F. (2010) Volumes of the World's Oceans from ETOPO1. *NOAA National Geophysical Data Center, Boulder, CO*.
- Edmond J. M., Damm K. L. von, McDuff R. E. and Measures C. I. (1982) Chemistry of hot springs on the East Pacific Rise and their effluent dispersal. *Nature* **297**, 187–191.
- Edmond J. M., Measures C., McDuff R. E., Chan L. H., Collier R., Grant B., Gordon L. I. and Corliss J. B. (1979) Ridge crest hydrothermal activity and the balances of the major and minor elements in the ocean. *Earth Planet. Sci. Lett.* **46**, 1–18.
- Elderfield H. and Schultz A. (1996) Mid-Ocean Ridge Hydrothermal Fluxes and the Chemical Composition of the Ocean. *Annu. Rev. Earth Planet. Sci.* **24**, 191–224.
- Elliott T., Thomas A., Jeffcoate A. and Niu Y. (2006) Lithium isotope evidence for subduction-enriched mantle in the source of mid-ocean-ridge basalts. *Nature* **443**, 565–568.
- Flesch G. D., Anderson A. R. and Svec H. J. (1973) A secondary isotopic standard for  $6\text{Li}/7\text{Li}$  determinations. *Int. J. Mass Spectrom.* **12**, 265–272.
- Foster G. L., Pogge von Strandmann P. A. E. and Rae J. W. B. (2010) Boron and magnesium isotopic composition of seawater. *Geochem. Geophys. Geosyst.* **11**, Q08015.
- Foustoukos D. I., James R. H., Berndt M. E. and Seyfried W. E. (2004) Lithium isotopic systematics of hydrothermal vent fluids at the Main Endeavour Field, Northern Juan de Fuca Ridge. *Chem. Geol.* **212**, 17–26.
- Gaillardet J. and Lemarchand D. (2018) Boron in the weathering environment. In *Boron Isotopes* (eds. H. R. Marschall and G. Foster). Springer. Heidelberg, pp. 163–188.
- Gao Y., Vils F., Cooper K. M., Banerjee N., Harris M., Hoefs J., Teagle D. A. H., Casey J. F., Elliott T., Laverne C., Alt J. C. and Muehlenbachs K. (2012) Downhole variation of lithium and oxygen isotopic compositions of oceanic crust at East Pacific Rise, ODP Site 1256. *Geochem. Geophys. Geosyst.* **13**.
- Goldberg S., Forster H. S. and Heick E. L. (1993) Boron Adsorption Mechanisms on Oxides, Clay Minerals, and Soils Inferred from Ionic Strength Effects. *Soil Sci. Soc. Am. J.* **57**, 704.
- Gou L.-F., Jin Z., Pogge Von Strandmann P. A., Li G., Qu Y.-X., Xiao J., Deng L. and Galy A. (2019) Li isotopes in the middle Yellow River. *Geochim. Cosmochim. Acta* **248**, 88–108.

- Greenop R., Hain M. P., Sosdian S. M., Oliver K. I. C., Goodwin P., Chalk T. B., Lear C. H., Wilson P. A. and Foster G. L. (2017) A record of Neogene seawater  $\delta^{11}\text{B}$  reconstructed from paired  $\delta^{11}\text{B}$  analyses on benthic and planktic foraminifera. *Clim. Past* **13**, 149–170.
- Hansen C. T., Meixner A., Kasemann S. A. and Bach W. (2017) New insight on Li and B isotope fractionation during serpentinization derived from batch reaction investigations. *Geochim. Cosmochim. Acta* **217**, 51–79.
- Hathorne E. and James R. (2006) Temporal record of lithium in seawater. *Earth Planet. Sci. Lett.* **246**, 393–406.
- Henchiri S., Gaillardet J., Dellinger M., Bouchez J. and Spencer R. G. M. (2016) Riverine dissolved lithium isotopic signatures in low-relief central Africa and their link to weathering regimes. *Geophys. Res. Lett.* **43**, 4391–4399.
- Hindshaw R. S., Tosca R., Goût T. L., Farnan I., Tosca N. J. and Tipper E. T. (2019) Experimental constraints on Li isotope fractionation during clay formation. *Geochim. Cosmochim. Acta* **250**, 219–237.
- Hodell D. A., Mueller P. A., McKenzie J. A. and Mead G. A. (1989) Strontium isotope stratigraphy and geochemistry of the late Neogene ocean. *Earth Planet. Sci. Lett.* **92**, 165–178.
- Huh Y., Chan L.-H. and Edmond J. M. (2001) Lithium isotopes as a probe of weathering processes. *Earth Planet. Sci. Lett.* **194**, 189–199.
- Huh Y., Chan L.-H., Zhang L. and Edmond J. M. (1998) Lithium and its isotopes in major world rivers. *Geochim. Cosmochim. Acta* **62**, 2039–2051.
- Hulme S. M., Wheat C. G., Fryer P. and Mottl M. J. (2010) Pore water chemistry of the Mariana serpentinite mud volcanoes. *Geochem. Geophys. Geosyst.* **11**, Q01X09.
- Humphris S. E., Thompson R. N. and Marriner G. F. (1980) The mineralogy and geochemistry of basalt weathering, Holes 417A and 418A. *Init. Rep. DSDP* **51**, 1201.
- Hutnak M., Fisher A. T., Harris R., Stein C., Wang K., Spinelli G., Schindler M., Villinger H. and Silver E. (2008) Large heat and fluid fluxes driven through mid-plate outcrops on ocean crust. *Nature Geosci.* **1**, 611–614.
- Jeffcoate A. B., Elliott T., Thomas A. and Bouman C. (2004) Precise/ Small Sample Size Determinations of Lithium Isotopic Compositions of Geological Reference Materials and Modern Seawater by MC-ICP-MS. *Geostand. Geoanalyt. Res.* **28**, 161–172.
- Jochum K. P., Nohl U., Herwig K., Lammel E., Stoll B. and Hofmann A. W. (2005) GeoReM. *Geostand. Geoanalyt. Res.* **29**, 333–338.
- Kastner M., Elderfield H. and Martin J. B. (1991) Fluids in convergent margins. *Phil. Trans. R. Soc. Lond. A* **335**, 243–259.
- Le Pichon X., Henry P. and Kaiko-Nankai Scientific Crew (1991) Water budgets in accretionary wedges. *Phil. Trans. R. Soc. Lond. A* **335**, 315–330.
- Lemarchand D., Gaillardet J., Lewin E. and Allègre C. J. (2000) The influence of rivers on marine boron isotopes and implications for reconstructing past ocean pH. *Nature* **408**, 951–954.
- Lemarchand D., Gaillardet J., Lewin É. and Allègre C. (2002) Boron isotope systematics in large rivers. *Chem. Geol.* **190**, 123–140.
- Li G. and West A. J. (2014) Evolution of Cenozoic seawater lithium isotopes. *Earth Planet. Sci. Lett.* **401**, 284–293.
- Liu X.-M., Wanner C., Rudnick R. L. and McDonough W. F. (2015) Processes controlling  $\delta^7\text{Li}$  in rivers illuminated by study of streams and groundwaters draining basalts. *Earth Planet. Sci. Lett.* **409**, 212–224.
- Mackenzie F. T. and Garrels R. M. (1966) Chemical mass balance between rivers and oceans. *Am. J. Sci.* **264**, 507–525.
- Manaka T., Araoka D., Yoshimura T., Hossain H. M. Z., Nishio Y., Suzuki A. and Kawahata H. (2017) Downstream and seasonal changes of lithium isotope ratios in the Ganges-Brahmaputra river system. *Geochem. Geophys. Geosyst.* **18**, 3003–3015.

- Marescotti P., Vanko D. A. and Cabella R. (2000) From oxidizing to reducing alteration: Mineralogical variations in pillow basalts from the east flank, Juan de Fuca ridge. In *Proc. Ocean Drill. Progr.* (eds. A. Fisher, E. E. Davis and C. Escutia), pp. 119–136.
- Marschall H. R. (2018) Boron Isotopes in the Ocean Floor Realm and the Mantle. In *Boron Isotopes* (eds. H. R. Marschall and G. Foster). Springer. Heidelberg, pp. 189–215.
- Marschall H. R., Wanless V. D., Shimizu N., Pogge Von Strandmann P. A., Elliott T. and Monteleone B. D. (2017) The boron and lithium isotopic composition of mid-ocean ridge basalts and the mantle. *Geochim. Cosmochim. Acta* **207**, 102–138.
- Martin J. B., Kastner M. and Elderfield H. (1991) Lithium. *Mar. Geol.* **102**, 281–292.
- McArthur J. M. (1994) Recent trends in strontium isotope stratigraphy. *Terra Nova* **6**, 331–358.
- Meredith K., Moriguti T., Tomascak P., Hollins S. and Nakamura E. (2013) The lithium, boron and strontium isotopic systematics of groundwaters from an arid aquifer system. *Geochim. Cosmochim. Acta* **112**, 20–31.
- Millero F. J., Perron G. and Desnoyers J. E. (1973) Heat capacity of seawater solutions from 5° to 35°C and 0.5 to 22‰ chlorinity. *J. Geophys. Res.* **78**, 4499–4507.
- Milliman J. D. and Farnsworth K. L. (2011) *River discharge to the coastal ocean*. Cambridge University Press, Cambridge.
- Millot R., Vigier N. and Gaillardet J. (2010a) Behaviour of lithium and its isotopes during weathering in the Mackenzie Basin, Canada. *Geochim. Cosmochim. Acta* **74**, 3897–3912.
- Millot R., Scaillet B. and Sanjuan B. (2010b) Lithium isotopes in island arc geothermal systems. *Geochim. Cosmochim. Acta* **74**, 1852–1871.
- Misra S. and Froelich P. N. (2012) Lithium isotope history of Cenozoic seawater. *Science* **335**, 818–823.
- Moriguti T. and Nakamura E. (1998a) High-yield lithium separation and the precise isotopic analysis for natural rock and aqueous samples. *Chem. Geol.* **145**, 91–104.
- Moriguti T. and Nakamura E. (1998b) Across-arc variation of Li isotopes in lavas and implications for crust/mantle recycling at subduction zones. *Earth Planet. Sci. Lett.* **163**, 167–174.
- Mottl M. (2003) *Partitioning of energy and mass fluxes between mid-ocean ridge axes and flanks at high and low temperature, in Energy and mass transfer in submarine hydrothermal systems*. Dahlem University Press, Berlin, Germany.
- Mottl M. J. and Wheat C. (1994) Hydrothermal circulation through mid-ocean ridge flanks. *Geochim. Cosmochim. Acta* **58**, 2225–2237.
- Murphy M. J., Porcelli D., Pogge Von Strandmann P. A., Hirst C. A., Kutscher L., Katchinoff J. A., Mörth C.-M., Maximov T. and Andersson P. S. (2019) Tracing silicate weathering processes in the permafrost-dominated Lena River watershed using lithium isotopes. *Geochim. Cosmochim. Acta* **245**, 154–171.
- Négrel P., Millot R., Guerrot C., Petelet-Giraud E., Brenot A. and Malcuit E. (2012) Heterogeneities and interconnections in groundwaters. *Chem. Geol.* **296–297**, 83–95.
- Nishio Y., Nakai S., Ishii T. and Sano Y. (2007) Isotope systematics of Li, Sr, Nd, and volatiles in Indian Ocean MORBs of the Rodrigues Triple Junction. *Geochim. Cosmochim. Acta* **71**, 745–759.
- Palmer M. R. and Edmond J. M. (1989) The strontium isotope budget of the modern ocean. *Earth Planet. Sci. Lett.* **92**, 11–26.
- Paris G., Gaillardet J. and Louvat P. (2010) Geological evolution of seawater boron isotopic composition recorded in evaporites. *Geol.* **38**, 1035–1038.
- Pearson P. N. and Palmer M. R. (2000) Atmospheric carbon dioxide concentrations over the past 60 million years. *Nature* **406**, 695–699.
- Penniston-Dorland S., Liu X.-M. and Rudnick R. L. (2017) Lithium Isotope Geochemistry. *Rev. Mineral. Geochem.* **82**, 165–217.
- Pogge von Strandmann P. A. E., Fraser W. T., Hammond S. J., Tarbuck G., Wood I. G., Oelkers E. H. and Murphy M. J. (2019) Experimental determination of Li isotope behaviour during basalt weathering. *Chem. Geol.* **517**, 34–43.

- Pogge Von Strandmann P. A., Frings P. J. and Murphy M. J. (2017) Lithium isotope behaviour during weathering in the Ganges Alluvial Plain. *Geochim. Cosmochim. Acta* **198**, 17–31.
- Pogge Von Strandmann P. A. and Henderson G. M. (2015) The Li isotope response to mountain uplift. *Geol.* **43**, 67–70.
- Pogge Von Strandmann P. A., Porcelli D., James R. H., van Calsteren P., Schaefer B., Cartwright I., Reynolds B. C. and Burton K. W. (2014) Chemical weathering processes in the Great Artesian Basin. *Earth Planet. Sci. Lett.* **406**, 24–36.
- Raitzsch M. and Hönisch B. (2013) Cenozoic boron isotope variations in benthic foraminifers. *Geol.* **41**, 591–594.
- Roberts J., Kaczmarek K., Langer G., Skinner L. C., Bijma J., Bradbury H., Turchyn A. V., Lamy F. and Misra S. (2018) Lithium isotopic composition of benthic foraminifera. *Geochim. Cosmochim. Acta* **236**, 336–350.
- Rosner M., Ball L., Peucker-Ehrenbrink B., Blusztajn J., Bach W. and Erzinger J. (2007) A Simplified, Accurate and Fast Method for Lithium Isotope Analysis of Rocks and Fluids, and  $\delta^7\text{Li}$  Values of Seawater and Rock Reference Materials. *Geostand. Geoanalyt. Res.* **31**, 77–88.
- Scher H. D., Griffith E. M. and Buckley W. P. (2014) Accuracy and precision of  $^{88}\text{Sr}/^{86}\text{Sr}$  and  $^{87}\text{Sr}/^{86}\text{Sr}$  measurements by MC-ICPMS compromised by high barium concentrations. *Geochem. Geophys. Geosyst.* **15**, 499–508.
- Scholz F., Hensen C., Lange G. J. de, Haeckel M., Liebetrau V., Meixner A., Reitz A. and Romer R. L. (2010) Lithium isotope geochemistry of marine pore waters – Insights from cold seep fluids. *Geochim. Cosmochim. Acta* **74**, 3459–3475.
- Seyfried W. E., Janecky D. R. and Mottl M. J. (1984) Alteration of the oceanic crust. *Geochim. Cosmochim. Acta* **48**, 557–569.
- Smith H., Spivack A. J., Staudigel H. and Hart S. R. (1995) The boron isotopic composition of altered oceanic crust. *Chem. Geol.* **126**, 119–135.
- Solomon E. A., Kastner M., Wheat C. G., Jannasch H., Robertson G., Davis E. E. and Morris J. D. (2009) Long-term hydrogeochemical records in the oceanic basement and forearc prism at the Costa Rica subduction zone. *Earth Planet. Sci. Lett.* **282**, 240–251.
- Spivack A. and Edmond J. (1987) Boron isotope exchange between seawater and the oceanic crust. *Geochim. Cosmochim. Acta* **51**, 1033–1043.
- Staudigel H., Gillis K. and Duncan R. (1986) K/Ar and Rb/Sr ages of celadonites from the Troodos ophiolite, Cyprus. *Geol.* **14**, 72–75.
- Stein C. A. and Stein S. (1994) Constraints on hydrothermal heat flux through the oceanic lithosphere from global heat flow. *J. Geophys. Res.* **99**, 3081–3095.
- Tomascak P. B., Langmuir C. H., Le Roux P. J. and Shirey S. B. (2008) Lithium isotopes in global mid-ocean ridge basalts. *Geochim. Cosmochim. Acta* **72**, 1626–1637.
- Tryon M. D., Wheat C. G. and Hilton D. R. (2010) Fluid sources and pathways of the Costa Rica erosional convergent margin. *Geochem. Geophys. Geosyst.* **11**, Q04S22.
- Veizer J. (1989) Strontium Isotopes In Seawater Through Time. *Annu. Rev. Earth Planet. Sci.* **17**, 141–167.
- Vigier N., Decarreau A., Millot R., Carignan J., Petit S. and France-Lanord C. (2008) Quantifying Li isotope fractionation during smectite formation and implications for the Li cycle. *Geochim. Cosmochim. Acta* **72**, 780–792.
- Vigier N. and Godd eris Y. (2015) A new approach for modeling Cenozoic oceanic lithium isotope paleo-variations. *Clim. Past* **11**, 635–645.
- Wang Q.-L., Chetelat B., Zhao Z.-Q., Ding H., Li S.-L., Wang B.-L., Li J. and Liu X.-L. (2015) Behavior of lithium isotopes in the Changjiang River system. *Geochim. Cosmochim. Acta* **151**, 117–132.
- Wheat C. and Mottl M. J. (2000) Composition of pore and spring waters from Baby Bare. *Geochim. Cosmochim. Acta* **64**, 629–642.
- Wheat C. G., Fisher A. T., McManus J., Hulme S. M. and Orcutt B. N. (2017) Cool Seafloor Hydrothermal Springs Reveal Global Geochemical Fluxes. *Earth Planet. Sci. Lett.* **476**, 1–10.

- Wheat C. G., Hartwell A. M., McManus J., Fisher A. T., Orcutt B. N., Schlicht L. E. M., Niedenzu S. and Bach W. (2019) Geology and Fluid Discharge at Dorado Outcrop, a Low Temperature Ridge-Flank Hydrothermal System. *Geochem. Geophys. Geosyst.* **20**, 487–504.
- Wheat C. G., Mottl M. J., Fisher A. T., Kadko D., Davis E. E. and Baker E. (2004) Heat flow through a basaltic outcrop on a sedimented young ridge flank. *Geochem. Geophys. Geosyst.* **5**, Q12006.
- Wilckens F. K., Reeves E. P., Bach W., Meixner A., Seewald J. S., Koschinsky A. and Kasemann S. A. (2018) The influence of magmatic fluids and phase separation on B systematics in submarine hydrothermal vent fluids from back-arc basins. *Geochim. Cosmochim. Acta* **232**, 140–162.
- Williams L. B. and Hervig R. L. (2005) Lithium and boron isotopes in illite-smectite. *Geochim. Cosmochim. Acta* **69**, 5705–5716.
- Wunder B., Meixner A., Romer R. L., Feenstra A., Schettler G. and Heinrich W. (2007) Lithium isotope fractionation between Li-bearing staurolite, Li-mica and aqueous fluids. *Chem. Geol.* **238**, 277–290.
- Wunder B., Meixner A., Romer R. L. and Heinrich W. (2006) Temperature-dependent isotopic fractionation of lithium between clinopyroxene and high-pressure hydrous fluids. *Contrib. Mineral. Petrol.* **151**, 112–120.
- Wunder B., Meixner A., Romer R. L., Wirth R. and Heinrich W. (2005) The geochemical cycle of boron. *Lithos* **84**, 206–216.
- Yamaoka K., Matsukura S., Ishikawa T. and Kawahata H. (2015) Boron isotope systematics of a fossil hydrothermal system from the Troodos ophiolite, Cyprus. *Chem. Geol.* **396**, 61–73.
- You C.-F., Chan L. H., Spivack A. J. and Gieskes J. M. (1995) Lithium, boron, and their isotopes in sediments and pore waters of Ocean Drilling Program Site 808, Nankai Trough. *Geol.* **23**, 37.

**CHAPTER 5:**  
**BORON, LITHIUM, STRONTIUM AND OXYGEN ISOTOPE**  
**SYSTEMATICS OF TWO HYDROTHERMAL SYSTEMS IN**  
**MODERN BACK-ARC AND ARC CRUST**  
**(PACMANUS AND BROTHERS VOLCANO, W-PACIFIC)**

Lucy E.M. Schlicht<sup>1\*</sup>, Olivier Rouxel<sup>2</sup>, Jeremy Deans<sup>3</sup>, Stephen Fox<sup>4</sup>, Yaron Katzir<sup>4</sup>,  
Simone A. Kasemann<sup>1</sup>, Anette Meixner<sup>1</sup>, Wolfgang Bach<sup>1</sup>

<sup>1</sup>Faculty of Geosciences and MARUM-Center for Marine Environmental Sciences, University of Bremen,  
Leobener Str. 8, 28359 Bremen, Germany

<sup>2</sup>IFREMER, Unité de Géosciences Marines, Plouzané, France

<sup>3</sup>School of Biological, Environmental, and Earth Sciences, the University of Southern Mississippi, Walker  
Science Building, 117601-266-5381, USA

<sup>4</sup>Department of Geological and Environmental Sciences, Marcus Family Campus, Ben Gurion University of  
the Negev, Be'er Sheva 84105, Israel

---

Manuscript in preparation for a special issue in *Economic Geology*

***Abstract***

A better characterization of subsurface processes in seafloor hydrothermal systems is key to a deeper understanding of fluid-rock interaction and ore forming mechanisms. Vent systems that are hosted in oceanic crust close to subduction zones, like at Brothers volcano and in the Eastern Manus Basin, are known to be especially ore- and Au-rich. We investigated the B, Li and Sr concentrations and isotopic compositions of fresh and altered lava and O isotopes of quartz separates that were recovered from drill-sites at Brothers volcano and Snowcap (Eastern Manus Basin) to test their sensitivity for different alteration parameters and to constrain changing alteration conditions with depth. All altered rocks are depleted in B and Li compared to the fresh rocks and point to interaction with a high-temperature (> 150 °C) hydrothermal fluid. The B and Li isotopic compositions of the altered rocks are variable and show values slightly lower as well as significantly higher than the fresh rocks. We show that the combination of Sr, B and O isotopic systematics is a useful approach to determine changing water-to-rock-ratios and temperatures in seafloor hydrothermal systems. At the rim of the NW Caldera as well as the Upper Cone site of Brothers volcano we suggest an evolution from a fluid-dominated to a more rock-dominated alteration regime from shallower to

deeper crustal levels. A deformed zone at greater depth of the NW Caldera rim site indicates alteration at higher temperatures. The basement of the NW Caldera wall experienced a varied alteration history that was affected by changing water-to-rock-ratios due to permeability contrasts between different lithology and alteration type boundaries as well as contrasting alteration temperatures. At Snowcap, a magnetite- and corrensite-rich zone appears in intermediate depth and spatial association with a volcanic facies boundary of contrasting permeability and gives evidence for alteration under increased water-to-rock-ratios. These findings highlight the importance of permeability differences between adjacent lithologies for the fluid flow regime and alteration temperatures in the seafloor hydrothermal systems. The  $\delta^7\text{Li}$  compositions of altered rocks show no distinct correlation with secondary mineralogy, water-to-rock-ratios or temperatures, and most likely results from a not resolvable combination of all three factors.

## 5.1. Introduction

Water-rock (w/r) interactions in seafloor hydrothermal systems cause intense mass exchange between oceanic crust and the ocean, and form seafloor massive sulfide deposits of economical important base metals. Hydrothermal activity in back-arc basin (BAB) and arc settings is of particular interest because of the commonly observed formation of high-grade and Au-rich ore bodies (e.g., Yang & Scott, 1996) and the high similarity to porphyry-type and epithermal ore deposits on-land (e.g. Whitney, 1975; Audétat, 2019). Experiments (Williams-Jones & Heinrich, 2005), melt inclusion studies (Yang & Scott, 1996) and similarities to subaerial geothermal systems (Stoiber & Rose, 1974; Taran *et al.*, 1995) suggest that magma degassing is a major metal source in hydrothermal systems in supra-subduction zones. However, mass exchange processes and the impact of magmatic fluids in contrast to other parameters (e.g. temperature) that influence submarine hydrothermal circulation are poorly constrained.

Boron and Li are highly fluid-mobile elements and B can show a moderately volatile character as well, depending on the salinity of solutions (Foustoukos & Seyfried, 2007). Both are leached from the crust by interaction of fluids with felsic or mafic crust at high temperatures ( $> 150$  °C) but become enriched in the rocks at low temperatures ( $< 150$  °C, e.g. James *et al.*, 2003). The B and Li concentrations of rocks from immature BAB and arc crust are usually elevated (up to 37  $\mu\text{g/g}$  B and up to 23  $\mu\text{g/g}$  Li) compared to mid-ocean ridge basalts (MORB  $< 1$   $\mu\text{g/g}$  B and  $\sim 5$   $\mu\text{g/g}$  Li) due to reflux of recycled altered crust and sediments of higher B and Li concentrations (Tomascak *et al.*, 2002; Hoog & Savov, 2018). Both elements have two isotopes;  $^{10}\text{B}$  and  $^{11}\text{B}$ , and  $^6\text{Li}$  and  $^7\text{Li}$ . The  $\delta^{11}\text{B}$  and  $\delta^7\text{Li}$  compositions of different reservoirs in BAB and arc hydrothermal environments strongly deviate: while seawater shows high isotopic values ( $\delta^{11}\text{B} \approx +40$  ‰;  $\delta^7\text{Li} \approx +31$  ‰), fresh crust in BAB and arc settings shows highly variable but generally lower isotopic values than seawater ( $\delta^{11}\text{B} \approx -9$  to  $+16$  ‰;  $\delta^7\text{Li} \approx +3.6 \pm 1.2$  ‰; Penniston-Dorland *et al.*, 2017; Hoog & Savov, 2018; Marschall, 2018 and references therein). The  $\delta^{11}\text{B}$  values of unaltered volcanic rocks in supra-subduction zones are often higher than MORB with a  $\delta^{11}\text{B}$  value of  $-7.1 \pm 0.9$  ‰ (Marschall *et al.*, 2017) due to recycling of B from the subducting slab. In contrast,  $\delta^7\text{Li}$  values of MORB ( $+3.4 \pm 0.7$  ‰ Penniston-Dorland *et al.*, 2017) are similar to ocean island volcanic rocks (on average  $+3.8$  ‰ in a range from  $+2.4$  to  $+7.9$  ‰, Penniston-Dorland *et al.*, 2017 and references therein). Based on the different geochemical behaviors and variable isotopic composition of potential sources, the concentrations and isotope systematics of B and Li are useful tracers for hydrothermal w/r interaction processes. In addition, the release of magmatic fluids may affect the B compositions of discharging fluids from BAB environments as suggested in a recent study (Wilckens *et al.*, 2018). Strontium isotopic composition of hydrothermal fluids and altered rocks is a well-established tracer for submarine w/r interaction (Albarède *et al.*, 1981; Kawahata *et al.*, 2001) and can be used as benchmark for the behavior of the lesser known Li and B systems. Further, O isotopes in specific

mineral phases can be used as paleo-thermometer to reconstruct the equilibrating fluid temperatures (e.g. Sharp & Kirschner 1994).

This study was focused on the B, Li and Sr concentrations and isotopic compositions of fresh and variably altered rocks from two drill sites that sampled the deeper sections of active seafloor hydrothermal systems in supra-subduction zones. One site is located in the Manus back-arc basin of Papua New Guinea (ODP Leg 193) and the other site is Brothers volcano within the Southern Kermadec arc, New Zealand (IODP Expedition 376). For the Brothers volcano, we also performed oxygen isotope measurements on quartz separates to make temperature constraints. At both sites, the compositions of discharging fluids (Reeves *et al.*, 2011; de Ronde *et al.*, 2011de) and secondary mineralogy (de Ronde *et al.*, 2005; Seewald *et al.*, 2019) indicated that hydrothermal fluid-rock interactions are controlled by reactions between basement rocks and seawater-derived fluid, as well as by the influx and mixing of magmatic fluids into the hydrothermal systems. Our goal is to obtain a deeper understanding of B and Li isotopic fractionation processes and the overall variations in Li and B isotopic composition in seafloor hydrothermal systems. Furthermore, we want to investigate the impact of changing parameters of w/r interactions like temperature, secondary mineralogy, initial rock composition, w/r-ratios and fluid sources (seawater- versus magma degassing-derived fluids) on the B, Li and Sr isotopic alteration patterns.

## **5.2. Geological setting**

### *5.2.1. Snowcap, Manus Basin*

Snowcap (ODP Leg 193, Site 1188) is a hydrothermal vent site in a water depth of 1640 mbsl (meters below sea-level) of diffusive, low-temperature fluid discharge within the PACManus (Papua New Guinea-Australia-Canada-Manus) hydrothermal vent field in the Manus back-arc basin (Western Pacific, **Figure 5.2-1**). The sub-seafloor of Snowcap consists of dacitic coherent lava flows (Paulick *et al.*, 2004; Thal *et al.*, 2014) that range from fresh to extensively altered and are part of the crest of the neovolcanic edifice Pual Ridge that is located at the Southeast Ridges (SER) of the Manus Basin between the Djaul and Weitin Transforms. The Manus basin opens along the Manus Spreading Center and is delimited to the north by the now inactive Manus Trench and to the south by the actively subducting New Britain Trench (Martinez & Taylor, 1996). Temperatures of the discharging fluids are 6 °C but a maximum measured temperature of 313 °C at 360 mbsf (meters below seafloor) of the borehole eight days after drilling points to a steep geothermal gradient at Snowcap (Shipboard Scientific Party, 2002). The northwestern corner of the Snowcap area hosts a small cluster of sulfide chimneys that vent fluids at 150-180°C; these fluids show evidence for subseafloor entrainment of seawater and precipitation of anhydrite (Reeves *et al.*, 2011). The presence of abundant native sulfur (Thal *et al.*, 2014) is indicative of prior venting of acid-sulfate fluids involved in advanced argillic alteration.

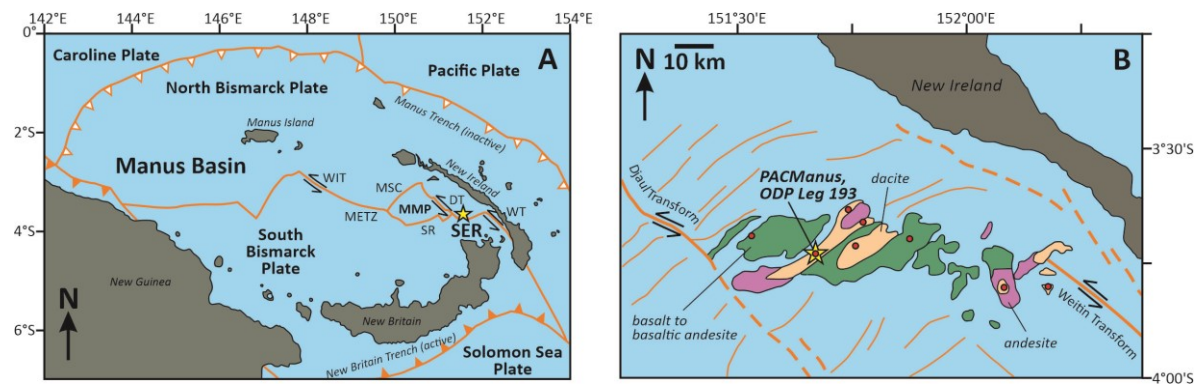


**Figure 5.2-1:** Geological setting of the Manus Basin. (A) Location of ODP Leg 193, PACManus in the Manus Basin (yellow star) modified after Thal et al. (2014). (B) Rock types at Pual Ridge, sites of hydrothermal activity (red dots) and location of PACManus, modified after Shipboard Scientific Party (2002). The thick orange lines represent plate boundaries. Lines complemented by open triangles symbolize inactive subduction, while closed triangles stand for active subduction. Thin orange lines in (B) show extensional faults. The parallel arrows represent the movement at transform faults (WIT=Willaumez Transform; METZ=Manus Extensional Transform Zone; DT=Djaul Transform; WT=Weit Transform). MMP=Manus Microplate; MSC=Manus Spreading Center; SER=Southeast Ridges.

### 5.2.2. Brothers volcano, Kermadec arc

Brothers volcano is located in the southern part of the Kermadec arc and represents an active, submarine caldera volcano of 3 to 3.5 km in diameter and is seated in water depth of approximately 2200 mbsl at the base, 1850 mbsl at the caldera floor and up to a range of 1320 to 1540 mbsl at the caldera rim (de Ronde et al., 2019a; **Figure 5.2-2**). In the center of the caldera two neovolcanic cones arise. The larger Upper Cone reaches water depth of 1220 mbsl and is partly conjoined with the smaller Lower Cone to the NE.

Brothers volcano is the most hydrothermally active volcano along the Kermadec arc and hosts two contrasting types of hydrothermal systems in a short distance, regarding fluid chemistry and rock alteration characteristics (de Ronde et al., 2005; de Ronde et al., 2011; de Ronde et al., 2019d). The first hydrothermal system type shows high-temperature ( $\leq 320$  °C) discharge of fluids that are moderately acidic and originate from heating of infiltrating seawater. The first type was found at the W, NW, and Upper Caldera sites and is commonly featured by Cu-Au-rich sulfide chimneys (Sites U1527 and U1530; **Figure 5.2-2B**). The primary dacitic rocks are typically altered to a secondary mineral assemblage that comprises chlorite, illite and quartz replacing the matrix and pyrite as vesicle infill. The second hydrothermal system type is defined by the venting of lower temperature ( $\leq 120$  °C) fluids that are very rich in volatiles and highly acidic, often observed together with native sulfur chimneys, pointing to the influence of magmatic fluids. Typical alteration minerals for the second type are pyrophyllite, natroalunite and native sulfur, associated with cristobalite and/or quartz. This assemblage of advanced argillic alteration is related to the upwelling of acid-sulfate fluids, which actively vent at the crests of the neovolcanic Cone sites (Site U1528). However, a

similar alteration mineral assemblage was also found in the deeper section of drill core at the NW Caldera (Hole U1530A of IODP Expedition 376; de Ronde *et al.*, 2019c; de Ronde *et al.*, 2019d), indicating the ingress of magmatic fluids also to the NW Caldera site at an earlier stage of hydrothermal and magmatic activity (de Ronde *et al.*, 2019d). Seewald *et al.* (2019) suggested that assemblages of advanced argillic alteration may affect the composition of vent fluids in the Manus Basin systems as well. These studies point to that the advanced argillic alteration type may be more abundant than would be expected based on the occurrence of active venting of acid-sulfate fluids.

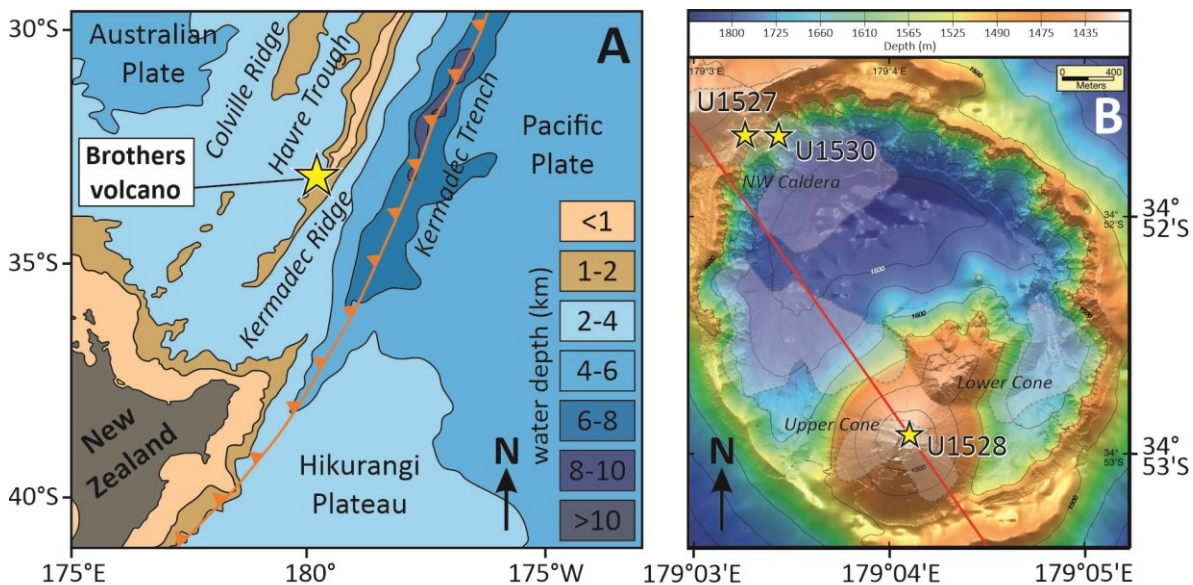


**Figure 5.2-2:** Geological setting of the Southern Kermadec Arc. (A) Location of Brothers volcano within the Southern Kermadec Arc, modified after Ballance *et al.* (1999). (B) Map of Brothers volcano taken from Embley *et al.* (2012) based on high-resolution (2m) autonomous underwater vehicle (AUV) data and a ship-derived bathymetry (25m resolution). The map is complemented by zones of low magnetization intensity (Caratori Tontini *et al.*, 2012) shown in light gray that are suggested to represent high-temperature fluid up flow zones. The three yellow stars mark the drilling locations (IODP Leg 376) from which the sample material used in this study is coming from. The red line refers to the cross-section that is shown in **Figure 5.5-2**.

### 5.3. Sample material

#### 5.3.1. Snowcap, Manus Basin

We investigated one unaltered plagioclase-phyric dacitic rock that was collected at Snowcap by the ROV (remotely operating vehicle) *MARUM-QUEST* during the *RV SONNE* Expedition SO-216 in 2011 (**Table 5.3-1**). The nine altered rock samples from Snowcap we used in this study were drilled during ODP Expedition 193 (Site 1188) and show variable extents of alteration and types of secondary mineral assemblages. Two main alteration types can be distinguished based on the secondary mineralogy: a first type that typically contains chlorite, illite, and magnetite and a second type of argillic alteration with rocks of bleached appearance and abundant pyrophyllite as replacing phase (**Figure 5.3-1M**). The presence of pyrophyllite suggests alteration by somewhat acidic fluids

at moderate temperatures. The low pH may be related to the ingress of magmatic fluids to shallower depth known from terrestrial and marine magma-hydrothermal systems (Gamo *et al.*, 1997; Yeats *et al.*, 2001; Paulick & Bach, 2006; Seewald *et al.*, 2019). These two main alteration types can be further subdivided in five alteration subtypes, using a simplified classification scheme that is based on formerly published studies (Shipboard Scientific Party, 2002; Lackschewitz *et al.*, 2004; Paulick *et al.*; Lackschewitz *et al.*; Paulick & Bach, 2006). In the following, the alteration types are described in order of their first occurrence with depth (in brackets the dedicated colors in **Figure 5.5-1** are given):

- (1) fresh dacite (dark gray): seafloor down to ~33.80 mbsf, the recovered dacitic to rhyodacitic rocks are fresh to weakly altered lava flows that are aphyric to plagioclase-clinopyroxene aphyric and moderately vesicular. The groundmass is glassy to microlitic and locally shows a perlitic texture. The unaltered rock from the surface of Snowcap used in this study is part of this unit.
- (2) Pyrophyllite (prl)-rich alteration (light pink): is manifest in pervasive bleaching and replacement of primary phases by pyrophyllite, accompanied by varying proportions of illite, chlorite, cristobalite, smectite, anhydrite, gypsum, barite, mixed-layer clays and pyrite down to 116.86 mbsf, with some gaps where pyrophyllite is absent. The top two samples investigated in this study from Site 1188 are part of this alteration type (**Table 5.3-1**). A second bleached and pyrophyllite-rich zone appears at deeper levels of Site 1188 (236.40 to 255.80 mbsf); it has quartz instead of cristobalite. Interaction with an upwelling magmatic fluid was suggested based on the observed alteration patterns (Lackschewitz *et al.*, 2004).
- (3) Illite (ill)-rich alteration (blue): illite is present in most of the recovered altered rocks, typical for hydrothermal alteration by seawater-derived fluids (K-rich) at elevated temperatures. The alteration type is defined by the absence of other secondary minerals indicative for one of the other alteration types. Besides illite, only quartz or cristobalite, anhydrite and pyrite were detected. One sample of this alteration type collected at 256.29 mbsf was investigated in our study (**Table 5.3-1**).
- (4) Chlorite (chl)-rich alteration (green): several zones show significant amounts of chlorite, along with illite, quartz or cristobalite, mixed-layer clays, magnetite, anhydrite and pyrite. Especially below around 275 mbsf, chlorite becomes a prominent secondary phase. The appearance of chlorite points to hydrothermal alteration by entrained seawater (Mg-rich) at elevated temperatures. The sample collected at 300.03 mbsf top depth at Hole 1188F is part of this alteration type (**Table 5.3-1**).
- (5) Magnetite (mgt)-rich alteration (brown): two depth intervals stand out by the abundance of magnetite, beside illite and/or chlorite, quartz, anhydrite and pyrite as other common secondary phases (154.98 to 183.87 mbsf and 318.23 mbsf to down to the bottom of the Hole 1188F at 386.7 mbsf). Magnetite appears in vesicles, as halo around anhydrite-pyrite

veins, and disseminated in the groundmass. The lower part of the first magnetite-rich section also contains noticeable amounts of corrensite. Five of the investigated rocks contain significant portions of hydrothermal magnetite; two, also corrensite (**Table 5.3-1**).

**Table 5.3-1:** Alteration types, secondary mineral assemblages, B concentrations and isotopic compositions of fresh and altered rocks from Snowcap, Manus Basin.

sample name	alteration type*	depth (mbsf)		secondary mineral assemblage**	B	$\delta^{11}\text{B}$	2sd
		top	bottom		$\mu\text{g/g}$	$\text{‰}$	$\text{‰}$
193-U1188A-7R-1W, 145-147	prl-rich	49.65	49.67	anh (crs, py, prl, qtz)	7.8	10.0	0.1
193-U1188A-10R-1W, 35-37	prl-rich	77.65	77.67	qtz, crs (prl, ba, py)	4.8	9.0	0.1
193-U1188A-20R-1W, 46-47	mgt-ill-rich	174.36	174.37	qtz (plg, anh, crr, mgt, ill, py)	2.0	23.2	0.1
193-U1188A-21R-1W, 20-21	mgt-rich	183.30	183.31	qtz (plg, mgt, crr, py)	1.9	17.5	0.1
193-U1188F-16Z-1W, 139-141	ill-rich	256.29	256.31	qtz (py, ill, brittle mica, anh)	3.3	5.0	0.1
193-U1188F-26Z-1W, 20-23	chl-rich	300.03	300.06	qtz (anh, py, ill, chl, chl-mixed-layer, smc)	3.1	8.0	0.1
193-U1188F-31Z-1W, 1-3	mgt-chl-rich	322.61	322.63	qtz, plg (chl, mgt, py, anh)	1.2	11.4	0.1
193-U1188F-34Z-1W, 40-41	mgt-chl-rich	336.80	336.81	plg, qtz (ill, chl, py, mgt, ill-mixed-layer)	3.9	7.2	0.1
193-U1188F-43Z-1W, 90-91	mgt-chl-rich	372.40	372.41	qtz, plg (chl, anh, py, mgt)	2.8	5.8	0.1
SO-216-043-ROV10				fresh dacitic cap rock	21.7	6.8	0.1

\* alteration types are described in **Chapter 5.3.1**.

\*\*secondary mineral assemblages were identified by XRD (Lackschewitz *et al.*, 2006)

Mineral abbreviations: anh=anhydrite; ba=barite; chl=chlorite; crr=corrensite; crs=cristobalite; ill=illite; mgt=magnetite; plg=plagioclase; prl=pyrophyllite; py=pyrite; qtz=quartz; smc=smectite

### 5.3.2. Brothers volcano, Kermadec arc

Brothers volcano consists of dacitic to rhyolitic lavas that are often plagioclase-clinopyroxene phyric and show a glassy to microlitic groundmass, as well as volcanoclastics, mono- or polymict lapillistones and pyroclastic material (de Ronde *et al.*, 2019a; Haase *et al.*, 2006). At the drilling Site U1530 of IODP Expedition 376, a sedimentary unit is also present from 30.70 to 59.62 mbsf, which is comprised of mud-, silt-, and sandstone (de Ronde *et al.*, 2019c). In this study, we investigated four rocks from Brothers volcano that were classified as unaltered, plagioclase-clinopyroxene phyric, dacitic lavas; two were collected by ROV *MARUM-QUEST* during *RV Sonne* Expedition SO-253 (one at the NW Caldera and one at the Upper Cone site) and two were recovered during IODP drilling Expedition 376, one from Site U1527 at the NW Caldera and one from Site U1528 at the Upper Cone (**Table 5.3-2**). We also investigated 76 altered rock samples from Brothers volcano that were all recovered during IODP Expedition 376: 24 samples from Site U1527, 28 samples from Site U1528, and 24 samples from Site U1530 (**Table 5.3-2**). In eleven cases, one rock piece was split in two separate sub-samples (e.g. center and halo or clast and matrix) to analyze specific alteration zones and small-scale chemical variations.

The alteration type classification of Brothers volcano used in this study is based on the secondary mineralogy, inferred from observations of the IODP Expedition 376 shipboard scientists and XRD

data of five drill cores (de Ronde *et al.*, 2019e; de Ronde *et al.*, 2019d). Two of the cores studied are located at the NW Caldera, approximately 400 m horizontal distance from each other; Site U1527 is located on the rim of the caldera wall in a water depth of 1464 m and reaches a depth of 238 mbsf, whereas Hole U1530A was drilled to 453.1 mbsf on a narrow terrace along the caldera wall at 1595 mbsl (**Figure 5.2-2B**). Five alteration types for the NW Caldera were distinguished in this study (in brackets the dedicated colors in **Figure 5.5-2** are given):

- (1) stockwork zone (red): At the very top of Hole U1530A (0 to 31.28 mbsf), rocks of a stockwork zone consisting of bluish altered lava fragments replaced by opal-CT, smectite, chlorite and pyrite were cored. These clasts are surrounded by a network of up to cm-thick veins of anhydrite, barite, pyrite, sphalerite and minor chalcopryrite (**Figure 5.3-1D**).
- (2) chlorite (chl)-rich alteration (green): this alteration type underlies the stockwork zone in Hole U1530A and is the only alteration type at Site U1527 underneath the fresh dacitic cap. The protoliths are lava flows, volcanoclastics, pyroclastics and also sedimentary units (**Figure 5.3-1A,B,C**). The main alteration color is green but at Site U1527 some parts are brownish in color (**Figure 5.3-1A**). The secondary mineral assemblage comprises chlorite, quartz, illite and pyrite. In Hole U1527 chalcopryrite and mordenite were detected. In core from Hole U1530A, plagioclase is pseudomorphed by chlorite, anhydrite, quartz and smectite (**Figure 5.3-1C**) and vugs are often lined by quartz and anhydrite. In deeper levels of Hole U1530A, chlorite-rich alteration of massive lava flows reappears several times (**Figure 5.5-2D**), alternating with the pyrophyllite-rich (4) and pyrophyllite-diaspora-rich (5) alteration types.
- (3) Illite (ill)-rich alteration (blue): In Hole U1530A between 65.65 and 185.16 mbsf, an illite-rich secondary mineral assemblage occurs, accompanied by quartz, pyrite and chlorite and mainly hosted in lapillistones and other volcanoclastics (**Figure 5.3-1E**). The degree of silicification varies with depth.
- (4) Pyrophyllite (prl)-rich alteration (light orange): following the illite-rich alteration and starting at 189.1 mbsf, a pyrophyllite alteration together with quartz, illite, pyrite and rutile occurs that has a strongly bleached appearance; affecting the whole rock or occurs as halos around veins and fractures.
- (5) Pyrophyllite (prl)-diaspora(dsp)-rich alteration (dark orange): starting at 227.50 mbsf, the pyrophyllite-rich mineral assemblage already present in the overlying alteration type is accompanied by diaspora, as well as quartz, illite, pyrite, rutile and in the upper part of this alteration type also zunyite (**Figure 5.3-1F**). The rocks have a buff to white color and fresh cut faces rapidly develop a yellowish to orange staining when exposed to air.

The upper three alteration types of the stockwork zone (1), as well as the chlorite-rich (2) and illite-rich (3) alteration at the NW Caldera are typical for a seawater dominated w/r interaction at elevated

temperatures, similar to alteration patterns observed for MOR hydrothermal systems and matching the composition of the actively venting fluids at the NW Caldera (de Ronde *et al.*, 2019e; Honnorez *et al.*, 1998). Deep in Hole U1527C (220.98 to 226.49 mbsf), there is a zone of plastic deformation in which the rocks have elevated chlorite and illite contents (**Figure 5.3-1B**, **Figure 5.5-2B**). The pyrophyllite-rich (4) and pyrophyllite-diaspore-rich (5) alteration types in the lower part of Hole U1530A are indicative of interactions between basement and an acidic fluid at moderate temperatures. These fluid types are typically associated with magmatic fluid contributions (e.g. Seewald *et al.*, 2015).

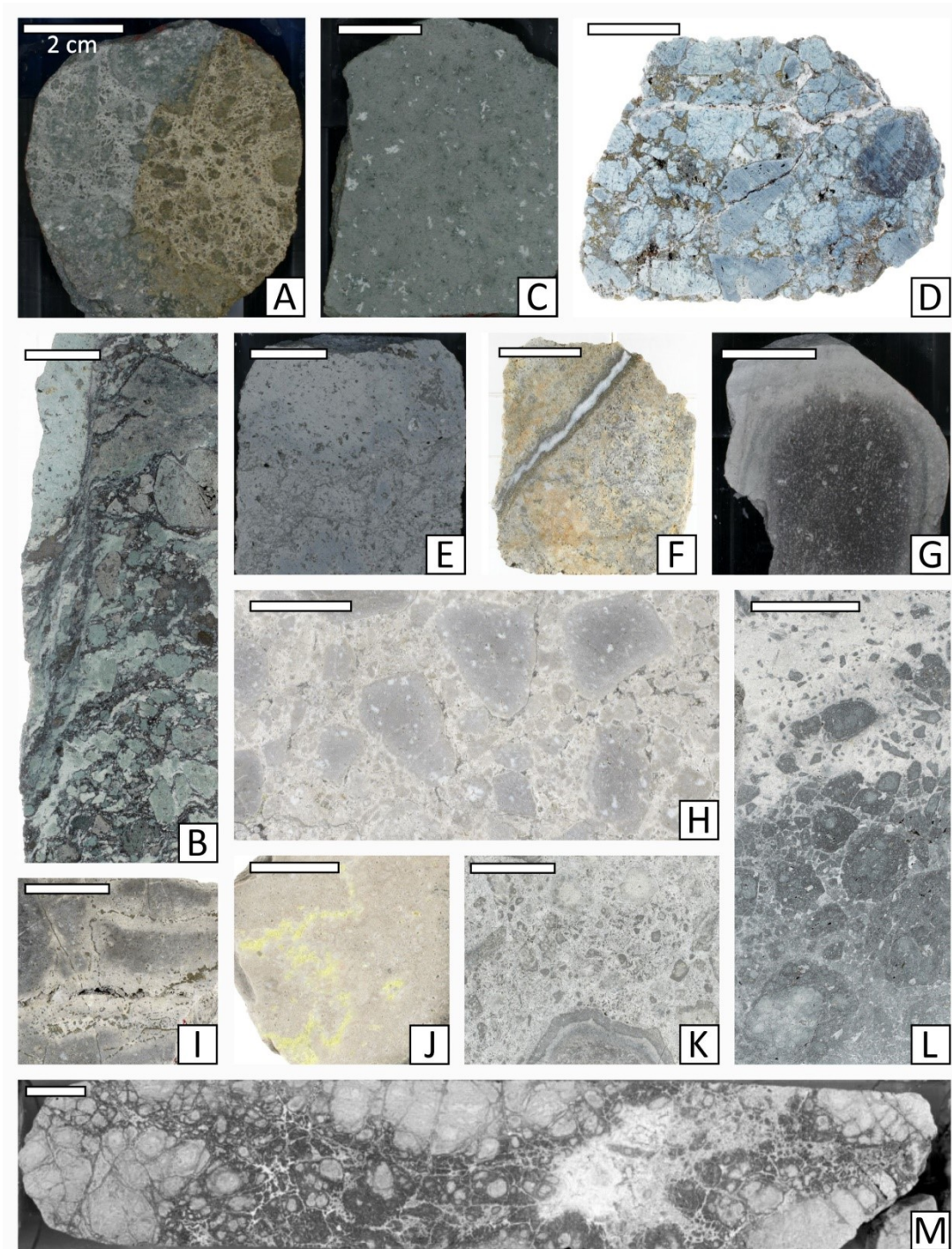


**Figure 5.3-1 (previous page):** Core images of altered rocks that were sampled at Brothers volcano (A-L, line-scan digital images and core close-up photos were taken from the LIMS database, <https://iodp.tamu.edu/database/coreimages.html>) and Snowcap, Manus Basin (M, photo was taken from Shipboard Scientific Party, 2002). The scale bar for all images is 2 cm. IODP Site U1527 (NW Caldera): chlorite-rich rocks that exhibits two colors in hand specimen, a more greenish and a brownish alteration, separated by a sharp boundary (A, 376-U1527C-11R-3W,1-7cm); chlorite-rich alteration that shows deformation structures (376-U1527C-18R-1A,51-78cm). IODP Site U1530 (slope at NW Caldera): massive lava flow that shows replacement by a chlorite-rich mineral assemblage of the groundmass and plagioclase is pseudomorphed by chlorite, smectite and quartz (C, 376-U1530A-83R-1W,48-55cm); rock from the stockwork zone of bluish altered fragments, surrounded by a network of anhydrite-barite-pyrite-sphalerite veins (D, 376-U1530A-4R-1A,47-56cm); rock is altered by a illite-rich secondary mineral assemblage and grayish- bluish in color (E, 376-U1530A-26R-1W,40-46cm); alteration by a pyrophyllite-diaspora rich mineral assemblage that is crossed by vein consisting of anhydrite and quartz with a pyrite-rich halo (F, 376-U1530A-55R-1A,80-86cm). IODP Site U1528 (Upper Cone): a weakly altered plagioclase-clinopyroxene phytic dacitic core with a pyrophyllite-natroalunite rich halo (G, 376-U1528D-57R-1W,15-19cm); a polymict lappilistone that is altered by a pyrophyllite-natroalunite secondary mineral assemblage (H, 376-U1528A-9R-2A,80-94cm); vuggy vein of anhydrite, quartz and pyrite (I, 376-U1528D-39R-1A,61-66cm); pyrophyllite-natroalunite-rich rock with vuggy veins filled with native sulfur (J, 376-U1528D-49R-1A-134-138cm); a polymict lappilistone that is altered by a pyrophyllite-natroalunite secondary mineral assemblage (K, 376-U1528A-7R-1A,18-30cm); transition from an illite-rich alteration of dark color to a highly bleached secondary mineral assemblage that is dominated by pyrophyllite and natroalunite (L, 376-U1528D-21R-2A,58-67cm). ODP Site 1188: rock that is altered by green silica-clay and shows strongly bleached patches, traversed by anhydrite-silica-pyrite veins (M, 193-1188A-8R-1,108-140cm).

---

In addition to the fresh and altered rock samples, we also investigated quartz separates from the NW Caldera (Hole U1530A) that formed due to hydrothermal circulation in vugs, veins or replaced the matrix.

The third studied drill core was from Hole U1528D (359-m deep) at the Upper Cone in a water depth of 1228 mbsl. The uppermost basement of Upper Cone comprises unconsolidated dacitic lava fragments (purple cap in **Figure 5.5-2A**) that contain aggregates of native sulfur. Below around 40 mbsf two alteration types were identified with diffuse boundaries against each other that are strongly intercalated (L) and mixed with each other (in brackets the dedicated colors in **Figure 5.5-2** are given):

- (1) Pyrophyllite (prl)-natroalunite(natro)-rich altered effusive and volcanoclastic rocks show white to light gray color due to strong bleaching. Pyrophyllite, natroalunite, anhydrite and pyrite are the main secondary phases (**Figure 5.3-1H,I,J,K,L**). Veins and vugs are commonly filled with native sulfur, quartz, anhydrite and pyrite.
- (2) Illite-rich alteration of lavas and volcanoclastics, show dark to grayish-blue alteration colors and a mineral assemblage of illite, opal-CT, quartz, anhydrite and pyrite (**Figure 5.3-1L**).

**Table 5.3-2:** Alteration types, and B, Li and Sr concentrations and isotopic compositions of altered and unaltered classified rocks based on petrographic characteristics from Brothers volcano, Kermadec arc.

sample name	alteration type*	depth (mbsf)		B <sup>†</sup> μg/g	Li <sup>†</sup> μg/g	Sr <sup>†</sup> μg/g	δ <sup>11</sup> B ‰	2sd ‰	δ <sup>7</sup> Li ‰	2sd ‰	<sup>87</sup> Sr/ <sup>86</sup> Sr (2sd)
		top	bottom								
<i>altered rock samples</i>											
376-U1527C-											
11R-1W, 17-18	chl-rich	185.37	185.38	15.6	4.7	191	2.1	0.1			0.704621(9) <sup>†</sup>
11R-1W, 143-145	chl-rich	186.63	186.65	4.9	5.3	179					
11R-2W, 108-110	chl-rich	187.74	187.76	2.2	1.4	187					
11R-3W, 8-12	chl-rich	188.06	188.10	4.9	5.4	204	2.3	0.1	6.7	0.1	0.704336(4)
12R-1W, 142-144	chl-rich	196.22	196.24	2.4	6.2	222			10.1	0.2	0.704286(15) <sup>†</sup>
13R-1W, 65-68	chl-rich	200.25	200.28	2.2	5.4	205					
13R-3W, 50-52 GREEN	chl-rich	202.87	202.89	2.4	4.9	254	2.6	0.0	8.0	0.1	0.704208(4)
13R-3W, 50-52 YELLOW	chl-rich	202.87	202.89	3.5	6.1	216			8.0	0.1	0.704202(6)
14R-1W, 32-34	chl-rich	204.72	204.74	1.8	3.0	241					
14R-1W, 55-58	chl-rich	204.95	204.98	1.8	2.9	234					
14R-2W, 47-50	chl-rich	205.64	205.67	2.1	3.7	247					
14R-3W, 45-49 CLAST	chl-rich	207.01	207.05	1.6	3.5	242					
14R-3W, 45-49 MATRIX	chl-rich	207.01	207.05	2.0	3.4	223					
15R-2W, 43-50 MIX	chl-rich	211.02	211.09	2.2	3.1	222					
15R-2W, 43-50 CLAST	chl-rich	211.02	211.09	2.3	2.7	249					
15R-3W, 3-6	chl-rich	212.12	212.15	1.9	3.7	240					
17R-2W, 45-49	chl-rich	220.60	220.64	1.5	3.9	213					
18R-1W,60-63	chl-rich	224.20	224.23	1.4			8.7	0.1			
18R-2W, 52-56	chl-rich	225.51	225.55	1.5	2.9	200	7.1	0.0	9.2	1.1	0.704190(5)
18R-2W, 97-99	chl-rich	225.96	225.98	1.7	3.0	188					
19R-1W, 71-75	chl-rich	229.11	229.15	1.4	2.7	72			7.7	0.4	0.704536(13) <sup>†</sup>
19R-1W, 117-120 CLAST	chl-rich	229.57	229.60	2.3	2.9	209					
19R-1W, 117-120 MATRIX	chl-rich	229.57	229.60	1.5	2.5	121					
20R-1W, 40-43	chl-rich	233.60	233.63	1.4	3.5	210					
376-U1528A-											
7R-1W, 21-23 CLAST	prl-rich	45.21	45.23	3.5	0.3	127	8.8	0.1			0.704688(9) <sup>†</sup>
7R-1W, 21-23 MATRIX	prl-rich	45.21	45.23	1.5	0.3	189	7.1	0.1			0.704935(18) <sup>†</sup>
9R-2W, 97-99 CORE	ill-rich	57.07	57.09	1.3	0.1	147	13.0	0.1			0.704555(9) <sup>†</sup>
9R-2W, 97-99 HALO	prl-rich	57.07	57.09	0.9	0.0	430	11.0	0.1			0.705622(11) <sup>†</sup>
13R-1W, 57-59	prl-rich	74.37	74.39	1.9	0.1	138	10.7	0.1	10.1	0.2	0.704898(5)
14R-1W, 53-56 CORE	ill-rich	79.13	79.16	1.3	0.1	169					
376-U1528D-											
3R-1W, 75-77	prl-rich	66.85	66.87	1.0	0.0	215	8.7	0.1	13.2	1.0	0.706188(6)
4R-2W, 28-31 CLAST	prl-rich	72.64	72.75	0.8	0.0	222					
4R-2W, 28-31 MATRIX	ill-rich	72.64	72.75	1.4	0.0	213					
10R-2W, 16-18 HALO	prl-rich	101.72	101.74	0.9	0.0	424					
11R-1W, 100-102	ill-rich	105.90	105.92	1.3	0.2	220	3.6	0.0	13.6	0.1	0.704721(5)
11R-3W, 44-46 CORE	ill-rich	108.33	108.35	1.8	0.3	340					
11R-3W, 44-46 HALO	prl-rich	108.33	108.35	1.3	0.2	206					
14R-1W, 80-82	ill-rich	120.10	120.12	1.0	0.2	226					
16R-1W, 48-50 MATRIX	ill-rich	129.38	129.40	1.1	0.2	196					
16R-1W, 48-50 CLAST	prl-rich	129.38	129.40	0.8	0.0	235					
21R-1W, 16-18	ill-rich	153.06	153.08	1.8	0.3	148	4.4	0.1	8.1	0.1	0.705048(5)
23R-1W, 61-63	prl-rich	163.11	163.13	0.8	0.0	232					
29R-1W, 65-67	prl-rich	191.95	191.97	2.0	0.6	150					
45R-1W, 52-54	prl-rich	268.62	268.64	0.9	0.0	271					
46R-1W, 32-34 CORE	weakly altered	273.22	273.24	4.8	0.5	189	3.7	0.1			0.704191(19) <sup>†</sup>
46R-1W, 32-34 HALO	prl-rich	273.22	273.24	3.9	0.4	190					
49R-1W, 19-21	prl-rich	287.49	287.51	1.5	0.0	174					
51R-1W, 60-62	prl-rich	297.50	297.52	1.0	0.0	213					
51R-1W, 60-62 (replicate)	prl-rich	297.50	297.52	1.8	0.5	194					
55R-1W, 51-53	prl-rich	316.61	316.63	0.8	0.0	169					
57R-1W, 15-18 CORE	weakly altered	325.85	325.88	3.3	0.7	192	3.5	0.1	19.3	0.1	0.704227(14) <sup>†</sup>
57R-1W, 15-18 HALO	prl-rich	325.85	325.88	2.1	0.2	203	4.5	0.1	19.1	0.1	0.704383(6)
376-U1530A-											
3R-1W, 60-62	stockwork	17.50	17.52	1.6	1.3	297					
4R-1W, 67-69	stockwork	22.07	22.09	1.6	0.5	766			5.7	0.1	0.706376(5)
8R-1W, 19-21	chl-rich (sandstone)	40.49	40.51	4.4	4.6	15			6.3	0.2	0.705059(7)
12R-2W, 8-11	chl-rich (lava flow)	61.08	61.11	2.7	4.9	87	11.1	0.1	4.6	0.3	0.706809(7)
13R-1W, 100-102	ill-rich	65.30	65.32	4.1	5.9	84	16.7	0.1			0.706982(13) <sup>†</sup>
15R-2W, 43-45	ill-rich	75.78	75.85	5.2	3.3	124					
20R-1W, 24-26	ill-rich	98.14	98.16	1.2	0.1	29	10.5	0.1	9.4	0.1	0.706354(8)
25R-1W, 43-45	ill-rich	122.33	122.35	2.5	1.0	21					
26R-1W, 41-43 CLAST	ill-rich	127.11	127.13	3.1	0.7	39	1.3	0.1			0.706436(14) <sup>†</sup>
26R-1W, 41-43 MATRIX	ill-rich	127.11	127.13	1.7	1.0	19	6.3	0.1			0.705929(17) <sup>†</sup>
29R-1W, 22-24	ill-rich	141.32	141.34	1.9	1.2	42					
39R-1W, 6-8	prl-rich	189.16	189.18	2.0	0.4	58					



the rock samples were wrapped in plastic foil and crushed in approximately 2 mm pieces by a hammer. The rock pieces were flushed repeatedly with deionized water and then dried, followed by powdering with an agate mortar and agate mill.

For the altered material from the drilling cores of Snowcap (ODP Leg 193), the shipboard rock powders from the core depository were used.

#### 5.4.2. Boron, lithium and strontium concentrations

The B concentrations of the unaltered and altered rock samples from Snowcap (Manus Basin), as well as the B and Li concentrations of the unaltered rocks recovered from Brothers volcano were measured at the Isotope Geochemistry Laboratory at the Center for Marine Environmental Sciences (MARUM), University of Bremen, Germany by a Thermo-Fisher Scientific Neptune Plus multicollector – inductive coupled plasma – mass spectrometer (MC-ICP-MS) using the SIS (stable introduction system: low flow PFA nebulizer (50  $\mu$ l) and a double pass quartz spray chamber) and a high- efficiency x-cone. For B concentrations, the reproducibility of values for the same sample solution was always better than  $\pm 0.9$   $\mu$ g/g (2sd). The B concentration measurements of four independent sample solutions of the basaltic reference material IAEA-B-5 was  $9.2 \pm 1.2$   $\mu$ g/g (2sd, n=4) or rather  $9.2 \pm 0.6$   $\mu$ g/g (2sd<sub>mean</sub>, n=4), in good agreement with the range that is stated by the GEOREM database of 8.4 to 11.9  $\mu$ g/g for IAEA-B-5 (10 values, 20<sup>th</sup> of January 2020); the granitic reference material IAEA-GM showed a B concentration of  $4.8 \pm 0.7$   $\mu$ g/g (2sd, n=4) or rather  $4.8 \pm 0.3$   $\mu$ g/g (2sd<sub>mean</sub>, n=4). The maximum measured uncertainty of  $\pm 1.2$   $\mu$ g/g (2sd) that was determined for reference material IAEA-B-5 was assumed as standard error for all sample solutions. For Li concentrations, the reproducibility of values for the same solution (samples and reference materials) was always better than  $\pm 0.9$   $\mu$ g/g (2sd). Measurements of two independent sample solutions of the reference material IAEA-B-5 showed Li concentrations of  $8.1 \pm 0.1$   $\mu$ g/g (2sd, n=2). Repeated measurements of the same solutions showed Li concentrations of  $4.4 \pm 0.0$   $\mu$ g/g (2sd) for IAEA-BHVO-2, and  $45.6 \pm 0.8$   $\mu$ g/g (2sd) for IAEA-GM, in good agreement with published values by the GEOREM database (20th January, 2020) of  $4.5 \pm 1.0$  (2sd, n=169) for IAEA-BHVO-2 and close to the compiled value of 50  $\mu$ g/g that is given for IAEA-GM. The maximum measured uncertainty of  $\pm 0.9$   $\mu$ g/g (2sd) was assumed as standard error for all sample solutions.

The B, Li and Sr concentrations of altered rock samples from Brothers drill-core samples were measured by ICP-MS at the at the PSO (Pôle Spectrométrie Océan), Brest, France. The detection limits and blank concentrations were 0.01  $\mu$ g/g and 0.01  $\mu$ g/g (Li concentrations), 0.64  $\mu$ g/g and 0.31  $\mu$ g/g (B concentrations), and 0.05  $\mu$ g/g and 0.01  $\mu$ g/g (Sr concentrations).

The Sr concentrations of the unaltered rock samples from Brothers drill-cores were determined by a SPECTRO Xepos Plus X-Ray fluorescence (XRF) analyzer at the GeoZentrum Nordbayern, FAU Erlangen-Nürnberg. Analyses were performed from fused discs created from the powdered sample

materials. The uncertainties of measured compared to expected Sr concentrations of reference materials measured along the sample material showed <2% RSD for high concentrations (basaltic reference materials BE-N of 1370 µg/g and BR of 1320 µg/g), <4% for intermediate concentrations (granitic reference material GA of 310 µg/g), and <11% for low concentrations (granitic reference material AC-E of 3 µg/g). Reference Sr values were taken from the GeoREM data base.

#### 5.4.3. Boron isotopes

Preparation and determination of B isotopic compositions of three unaltered and 36 altered rock samples from Snowcap and Brothers volcano were performed in the Isotope Geochemistry Laboratory at the MARUM by using the same instrument as for the B concentration determination (*Chapter 5.4.2*). Isolation and purification of B were adapted from Romer *et al.* (2014) and are described in further detail in Hansen *et al.* (2017). The procedure was based on alkaline fusion of rock powders (44.5 to 454.9 mg) with K<sub>2</sub>CO<sub>3</sub> as fluxing agent (1:4), followed by a two-step column separation; first step by Amberlit IRA 743 and second step by AG 50W-X8 (mesh 200-400). An appropriate amount of mannitol (1 µg B : 20 µg mannitol) were used to keep B stable in solution. The total B losses during preparation were usually < 0.1 % and always < 0.2 % of the total amount of B in sample solution (range from 221 to 3514 ng). Purified sample solutions were dissolved in 2% HNO<sub>3</sub>, closely matched to 50ppb B, repeatedly analyzed in the standard – sample - standard bracketing mode using NIST SRM 951, and supplemented by baseline determination. Boron isotopic values are given in the δ<sup>11</sup>B (‰) notation: [δ<sup>11</sup>B = {(<sup>11</sup>B/<sup>10</sup>B)<sub>sample</sub> / (<sup>11</sup>B/<sup>10</sup>B)<sub>NIST SRM 951</sub>} - 1} × 1000]. Four measured blanks contained between 8 to 23 ng B and showed a B isotopic composition between +0.3 ± 0.3 ‰ (2sd) to -5.1 ± 0.3 ‰ (2sd). The blank corrected internal reference material NIST SRM 951 showed a δ<sup>11</sup>B composition of -0.1 ± 0.1 ‰ (2sd the same as 2sd<sub>mean</sub>, n=4) that indicate an insignificant isotopic fractionation during procedure. The basaltic reference material IAEA-B-5 showed a blank and NIST SRM 951 corrected δ<sup>11</sup>B value of -4.1 ± 0.1 ‰ (2sd, n=4), in good agreement with the GEOREM database that reported on average -3.9 ± 0.7 ‰ (n = 10, two outliers excluded, 20th January 2020), and values of -4.3 ± 0.2 ‰ (n=3, Hansen *et al.*, 2017), and -4.2 ± 0.2 ‰ (n=4, Wilckens *et al.*, 2018). The granitic reference material IAEA-GM displayed a blank and NIST SRM 951 corrected δ<sup>11</sup>B value of -0.1 ± 0.1 ‰ (2sd, n=4). In the following, the B isotopic composition of rock samples is always given in 2sd and is corrected for blank and NIST SRM 951 compositions.

#### 5.4.4. Lithium isotopes

The Li isotope preparation and determination of four unaltered and 22 altered rock samples from Brothers volcano were performed in the same laboratory and by using the same instrument as for Li concentration determination (*Chapter 5.4.2*). For preparation, rock powders (81.7 to 253.2 mg) were dissolved in at least five consecutive steps. First, a mixture of concentrated HF and HNO<sub>3</sub>

(5:1) was added to the rock powders and the closed beakers were placed on the hotplate for three days at 140 °C, followed by drying. The residuum was digested in a mixture of 2 ml concentrated HCl and 1 ml concentrated HNO<sub>3</sub> and placed on the hotplate for two days at 140 °C and then dried. After that, 300 µl of HNO<sub>3</sub> and 150 µl H<sub>2</sub>O<sub>2</sub> were carefully added and samples were dried at 65 °C. Following, 3 ml of 2.5 M HNO<sub>3</sub> were added and solutions were placed on the hotplate overnight at 140 °C and then dried. Lastly, samples were digested in 2 to 4 ml of 4 N HCl. It was always ensured that rock powders were completely in solution by centrifugation and for some samples the last two steps had to be repeated several more times before all sample material was in solution. For the barite-rich sample from the stockwork zone (376-U1530A-4R-1W, 67-69cm), an insoluble residuum remained that had to be removed by centrifugation before purification.

Purification of Li was processed by two consecutive column separation steps modified after Moriguti & Nakamura (1998) and detailed in Hansen *et al.* (2017), by using Bio-Rad® Poly-Prep and Bio-Spin columns prepared with 1.4 ml and 1 ml of cation exchange resin AG 50W-X8. In the first step, Li elution is accomplished with 0.15 M HCl and in the second step 0.5 M HCL with 50 % ethanol portion was used. The total Li loss was usually < 0.01 % of the Li amount in the sample aliquot. The total procedural blank was always < 18.5 pg Li (n=3) and negligible small compared to Li amounts in sample solutions (usually > 50 ng). However, two sample aliquots showed extremely low total Li amounts (< 20 ng) and following the procedural losses account for up to 0.75 % and the maximum measured blank could contribute up to 0.35 % of total Li in solution. The Li isotopic compositions of those two samples have to be considered with care, as indicated in **Table 5.3-2**.

Determination of the Li isotopic compositions by MC-ICP-MS of the purified sample solutions dissolved in 2% HNO<sub>3</sub> were performed in the standard - sample – standard bracketing mode using NIST RM 8545 (LSVEC), and supplemented by baseline determinations. The measuring concentration for Li isotope determination usually matched 25 ppb, but matched at least 8 ppb for very low concentrated samples. All samples were always accompanied by measurements of reference material NIST RM 8545 in the same concentration. The Li isotopic compositions are given in the conventional notation:  $[\delta^7\text{Li} = \{[(^7\text{Li}/^6\text{Li})_{\text{sample}} / (^7\text{Li}/^6\text{Li})_{\text{NIST RM 8545}}] - 1\} \times 1000]$ . The reference material NIST RM 8545 that was processed along the sample solutions showed a  $\delta^7\text{Li}$  composition of  $-0.2 \pm 0.1 \text{ ‰}$  (2sd, n=4) and  $-0.2 \pm 0.2 \text{ ‰}$  (2sd<sub>mean</sub>, n=4) and point to negligible isotopic fractionation during procedure. The Li isotopic compositions of rock reference materials and rock samples are corrected for the NIST RM 8545 composition. The basaltic reference material IAEA-BHVO-2 showed a  $\delta^7\text{Li}$  value of  $+4.3 \pm 0.2 \text{ ‰}$  (2sd, n=1), in agreement with the GEOREM database that displayed  $+4.5 \pm 0.7 \text{ ‰}$  (2sd, n=56, 20<sup>th</sup> January 2020). The granitic reference material IAEA-GM showed a  $\delta^7\text{Li}$  value of  $-0.7 \pm 0.1 \text{ ‰}$  (2sd, n=1) and IAEA-B5 had  $+4.4 \pm 1.5 \text{ ‰}$  (2sd and 2sd<sub>mean</sub>, n=2). The estimated Li isotopic standard error for all rock samples in this study is

oriented by the maximum determined uncertainty of  $\pm 1.5\%$  (2sd) that was measured for the two independent solutions of reference material IAEA-B5.

#### 5.4.5. *Strontium isotopes*

The Sr isotope preparation and measurements of one fresh and 18 altered rock samples from Brothers volcano were also performed at the Isotope Geochemistry Laboratory at the MARUM by using the same sample solutions as for the Li isotope measurements (see *Chapter 5.4.4*). Separation and purification of Sr were conducted by column separation prepared with 70  $\mu\text{l}$  Sr.spec<sup>TM</sup> resin, following the procedure described by Deniel & Pin (2001). Firstly, the sample material digested in 1 ml 2 M HNO<sub>3</sub> were loaded on the columns (in 100  $\mu\text{l}$  steps). Secondly, 1.2 ml of 2 M HNO<sub>3</sub>, 1 ml 7 M HNO<sub>3</sub> and 0.3 ml 2 M HNO<sub>3</sub> were added (in 100  $\mu\text{l}$ , 500  $\mu\text{l}$  and 100  $\mu\text{l}$  steps) to remove unwanted elements. Following, Sr was collected by adding 1 ml of 0.05 M HNO<sub>3</sub> (in 100  $\mu\text{l}$  steps), charged with 30  $\mu\text{l}$  0.1 M H<sub>3</sub>PO<sub>4</sub> and dried at 90 °C on a hotplate. Removal of organic material was ensured by adding 40  $\mu\text{l}$  of concentrated HNO<sub>3</sub>, drying at 90 °C and adding of 40  $\mu\text{l}$  H<sub>2</sub>O<sub>2</sub> and drying.

The determination of Sr isotopes was performed by a Thermo Scientific TRITON Plus thermal ionization mass spectrometer (TIMS) at the Isotope Geochemistry Laboratory at the MARUM. A rhenium filament was prepared by loading 1.5  $\mu\text{l}$  Ta-emitter, followed by loading of the sample material digested in 2  $\mu\text{l}$  0.1 M H<sub>3</sub>PO<sub>4</sub> and conditioning by heating up the filament until red heat was reached. The instrumental fractionation was corrected to the natural <sup>87</sup>Sr/<sup>86</sup>Sr ratio of 0.1194. The blank did not affect the Sr isotope measurements regarding the much lower Sr blank concentration (< 50 pg Sr) compared to sample solutions ( $\geq$  200 ng Sr). The reference material NIST SRM 987 showed a composition of  $0.710247 \pm 0.000004$  (2sd, n = 1), in line with the laboratory internal long-term reproducibility of NIST SRM 987 (from December 2011 to February 2017) that matches  $0.710249 \pm 0.000024$  (2sd, n=231).

In addition, Sr isotopic compositions of 16 altered rock samples from Brothers volcano drill-cores were measured by a Thermo Scientific Triton TIMS at the PSO, Brest, France. Prior to measurements, Sr was purified by a two stage chromatography procedure: by using (1) cationic Dowex AG50 X8 columns, and (2) Sr.spec<sup>TM</sup> resin. Strontium isotopic measurements replicated for one altered rock sample (376-U1530A-39R-2W,78-80) at the University of Bremen ( $0.705990 \pm 0.000006$ ) and at the PSO ( $0.706007 \pm 0.000014$ ) showed the same <sup>87</sup>Sr/<sup>86</sup>Sr composition within the uncertainties.

#### 5.4.6. *Quartz separate preparation and cathodoluminescence (CL) spectroscopy*

For Site U1530A at the NW Caldera of the Brothers volcano, we handpicked in total 13 quartz separates under the binocular from vein (7 separates) and vug fillings (4 separates) and also separated coarse quartz grains replacing the matrix (2 separates).

For investigations by CL spectroscopy, the quartz separates were embedded in epoxy resin followed by polishing and coating with a thin carbon layer of the epoxy mounts. The CL imaging was performed by using a JEOL Superprobe JXA-8230 at the Hebrew University, Institute of Earth Sciences, Israel (see *Appendix A.3*).

#### 5.4.7. *In-situ oxygen isotope measurements*

In-situ oxygen isotope measurements were performed on quartz separates (same samples that were used for CL imaging) by using the CAMECA ims-1280 secondary ion mass spectrometer (SIMS) at the Wisc-SIMS (Wisconsin Secondary Ion Mass Spectrometry) Laboratory, Department of Geoscience at the University of Wisconsin-Madison. Detailed descriptions of the oxygen isotope measuring procedure at the Wisc-SIMS are amongst others given in Kelly *et al.* (2007) and Heck *et al.* (2011). Following, the most important analyzing steps and parameters are summarized. Oxygen isotope measurements were performed by using a primary beam of 1.6 nA  $^{133}\text{Cs}^+$  ions focusing to a spot diameter of approximately 10  $\mu\text{m}$  (1 to 2  $\mu\text{m}$  pit depth), and using a sample current of around 2 nA. One spot analysis took around four minutes, including pre-sputtering through the gold layer, stabilizing of the sputtering, and centering as well as integrating of the secondary ions. The ions of  $^{16}\text{O}^-$  and  $^{18}\text{O}^-$  were simultaneously collected in two movable Faraday cup detectors, accompanied by collection of  $^{16}\text{OH}^-$  ions in the axial Faraday cup to identify potential water traces in the quartz. The average  $^{16}\text{O}^-$  intensity was  $3.0 \times 10^9$  counts per second (cps). A nuclear magnetic resonance (NMR) probe stabilized the magnetic field strength, readjusted every 12h. Analyses were performed in the standard-sample-standard bracketing mode, four UWQ-1 standard analyses – maximum 20 sample analyses – four UWQ-1 standard analyses, to evaluate the reproducibility of measurements and to ensure the measurements were not affected by instrumental bias or drifts. Raw  $^{18}\text{O}/^{16}\text{O}$  sample ratios were corrected for the VSMOW oxygen scale based on UWQ-1 standard measurements prior and after the sample measurements (UWQ-1:  $\delta^{18}\text{O} = +12.22$  ‰, Kelly *et al.*, 2007; Heck *et al.*, 2011). The oxygen isotopic compositions are given in the conventional notation:  $[\delta^{18}\text{O}_{\text{VSMOW}} (\text{‰}) = \{[(^{18}\text{O}/^{16}\text{O})_{\text{sample}} / (^{18}\text{O}/^{16}\text{O})_{\text{VSMOW}}] - 1\} \times 1000]$ . The external reproducibility of the  $\delta^{18}\text{O}$  bracketing standard measurements was on average  $\pm 0.2$  ‰ (2sd, n=27, see *Appendix A.3*).

## 5.5. *Results*

### 5.5.1. *Unaltered rocks*

The unaltered dacite that was collected at Snowcap shows a B concentration of 21.7  $\mu\text{g/g}$  and a  $\delta^{11}\text{B}$  value of  $+6.8 \pm 0.1$  ‰ and are similar to the two unaltered dacites that were collected at Brothers volcano (18.7 and 19.6  $\mu\text{g/g}$  B and  $\delta^{11}\text{B}$  values of  $+4.8 \pm 0.1$  and  $+5.8 \pm 0.1$  ‰). Unaltered rocks from Brothers volcano show a Sr isotopic composition of 0.703970(4) at the Lower Cone and 0.704109(6) at the NW Caldera Site. Unaltered rocks from Brothers show a small range in Sr contents of 202 and 232  $\mu\text{g/g}$ . The two unaltered rocks from Brothers volcano recovered by ROV

have Li concentrations of 11.9 and 11.2  $\mu\text{g/g}$  and  $\delta^7\text{Li}$  values of  $+3.6 \pm 0.1$  and  $+4.8 \pm 0.1$  ‰. In contrast, the two drill core samples from Brothers volcano that were classified as unaltered based on petrographic observations show lower Li concentration (6.2 and 0.2  $\mu\text{g/g}$ ) and higher  $\delta^7\text{Li}$  values ( $+6.3 \pm 0.6$  and  $+17.5 \pm 0.2$  ‰).

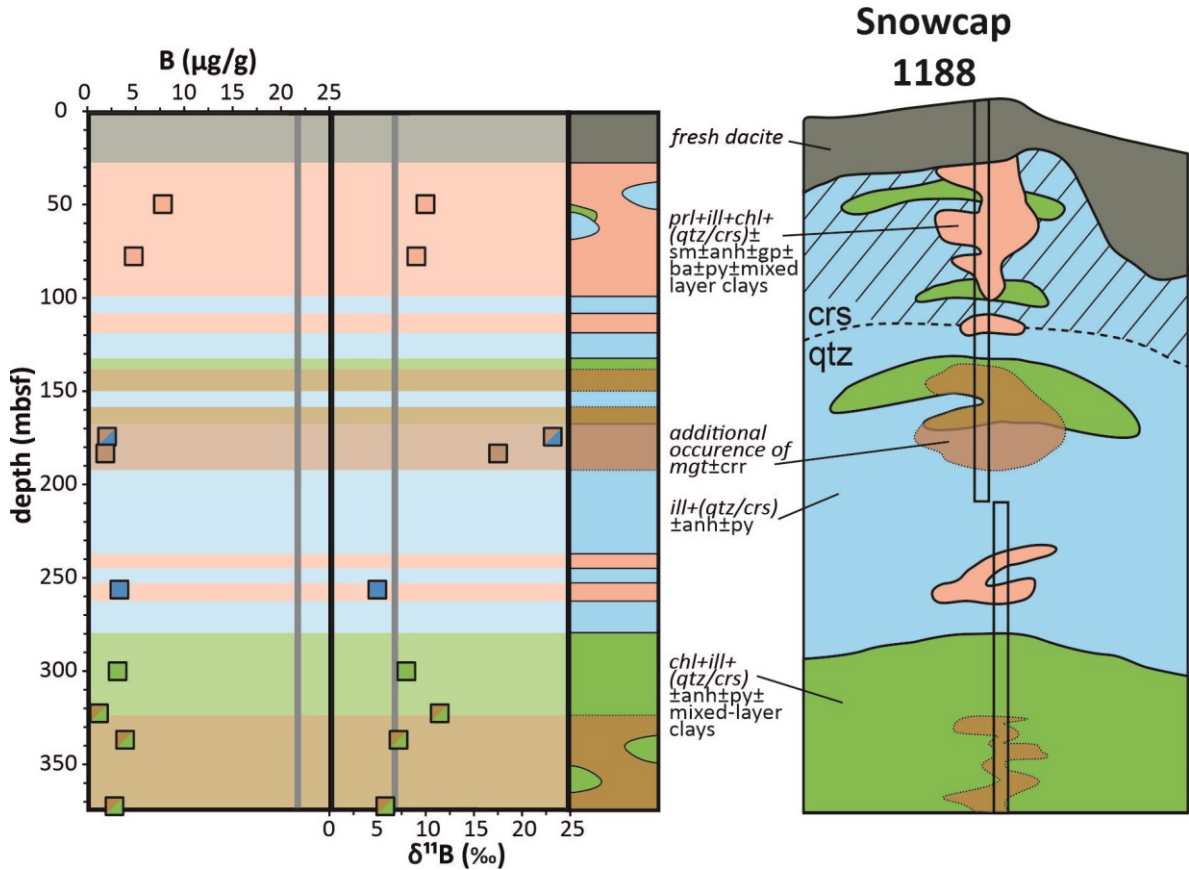


**Figure 5.5-1:** Boron concentrations and isotopic compositions of altered rocks and the alteration mineral assemblages with depth at Snowcap, ODP Site 1188, Manus Basin. The gray vertical line represents the precursor composition. Errors of 2sd are too small to be displayed. Mineral abbreviations: prl = pyrophyllite, ill = illite, chl=chlorite, qtz=quartz, crs=cristobalite, sm=smectite, anh=anhydrite, gp=gypsum, ba=barite, py=pyrite, mgt=magnetite, crr=corrensite.

### 5.5.2. Altered rocks

The B concentrations and  $\delta^{11}\text{B}$  values of altered rocks cored at the Snowcap site in the Manus Basin range from 1.2 to 7.8  $\mu\text{g/g}$  and  $+5.0 \pm 0.1$  to  $+23.2 \pm 0.1$  ‰ (Table 5.3-1; Figure 5.5-1; Figure 5.5-3A).

Altered rocks from the three drill sites at Brothers volcano range between 0.8 to 5.2  $\mu\text{g/g}$  B (with one exceptional high value of 15.6  $\mu\text{g/g}$ ) and from  $+1.3 \pm 0.1$  to  $+17.4 \pm 0.1$  ‰ in  $\delta^{11}\text{B}$  (Table 5.3-2; Figure 5.5-3A,B). Altered rocks at Brothers volcano have Sr concentrations between 15 and 766  $\mu\text{g/g}$ , and show the greatest variability at Site U1530. The  $^{87}\text{Sr}/^{86}\text{Sr}$  values lie between 0.704190(5) and 0.706982(13) (Figure 5.5-3B,D). The Li contents range from  $>0.1$  to 6.2  $\mu\text{g/g}$  and  $\delta^7\text{Li}$  compositions are between  $+4.1 \pm 0.4$  and  $+26.8 \pm 0.7$  ‰ (Figure 5.5-3C,D).

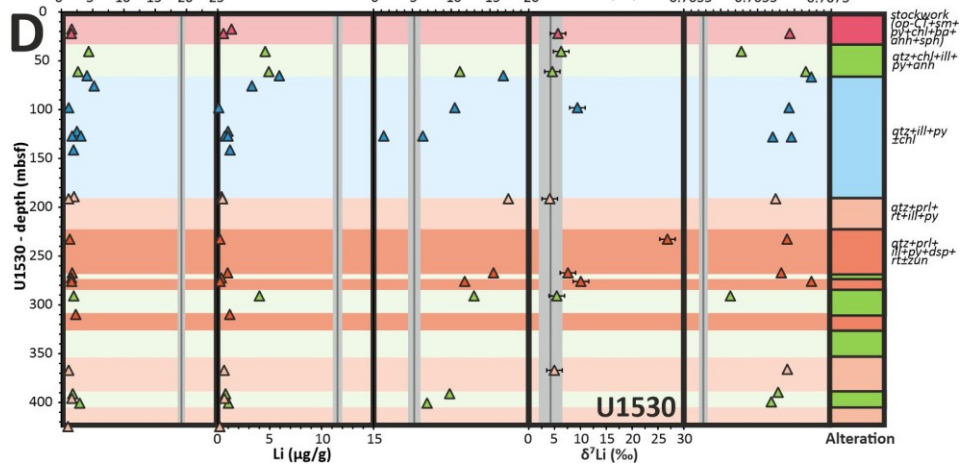
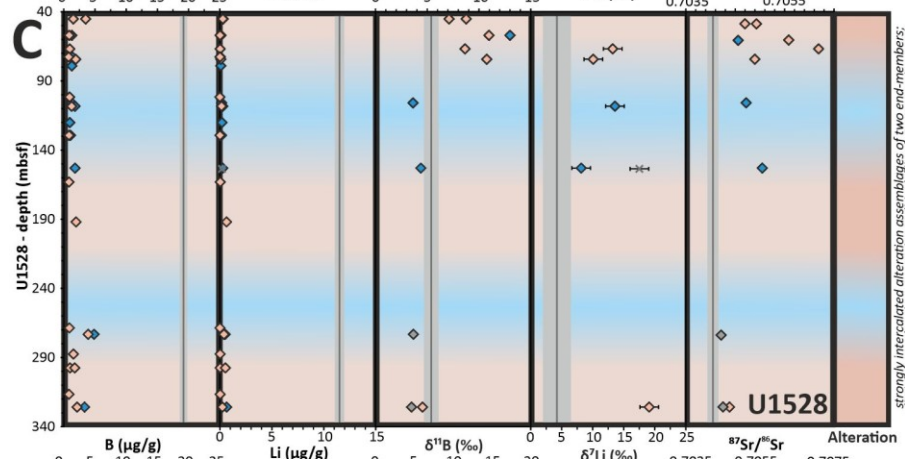
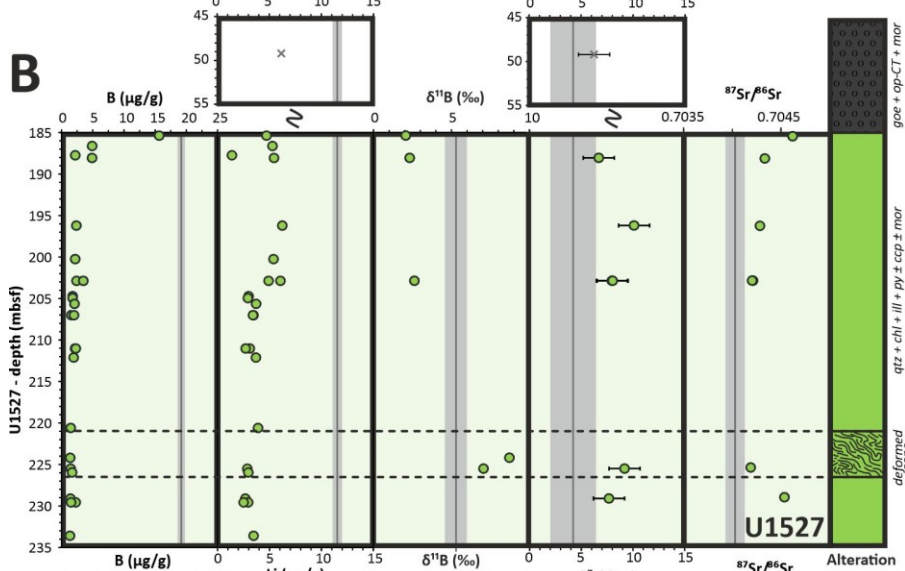
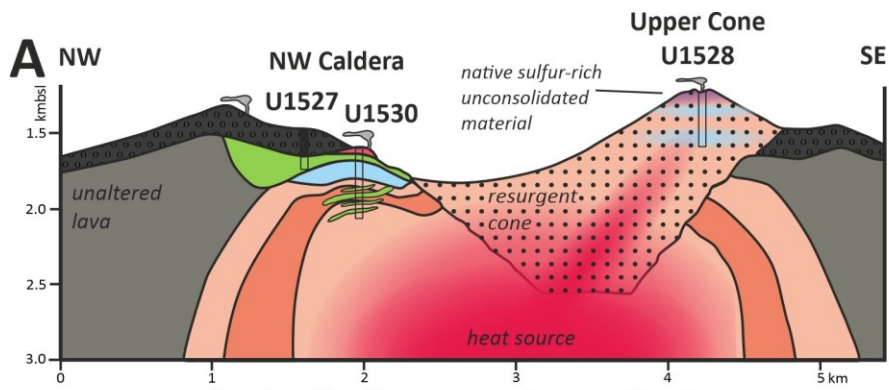


**Figure 5.5-2 (previous page):** Alteration patterns and geochemical variations with depth at Brothers volcano. (A) Cross-section (see **Figure 5.2-2B**) of Brothers volcano and distribution of alteration types based on shipboard observations and XRD analyses of IODP Expedition 376, modified after de Ronde et al. (2019d). The B and Li concentrations and B, Li and Sr isotopic compositions of altered rocks are shown at Site U1527 (B), Site U1528 (C), and Site U1530 (D). The symbols are the same as in **Figure 5.5-3**; symbol colors match the alteration type colors. The errors (2sd) of the B and Sr isotopic compositions are smaller than the symbol sizes. For Li isotopic composition, a general error of  $\pm 1.5$  ‰ (2sd) is estimated (see **Chapter 5.4.4**). The range of pristine compositions is illustrated as light gray vertical line, with the average of this range shown in dark gray. For Sr isotopes, the range of fresh rock compositions comprises of dacites that were measured in this study and data of Brothers volcano published in Diehl (2019).

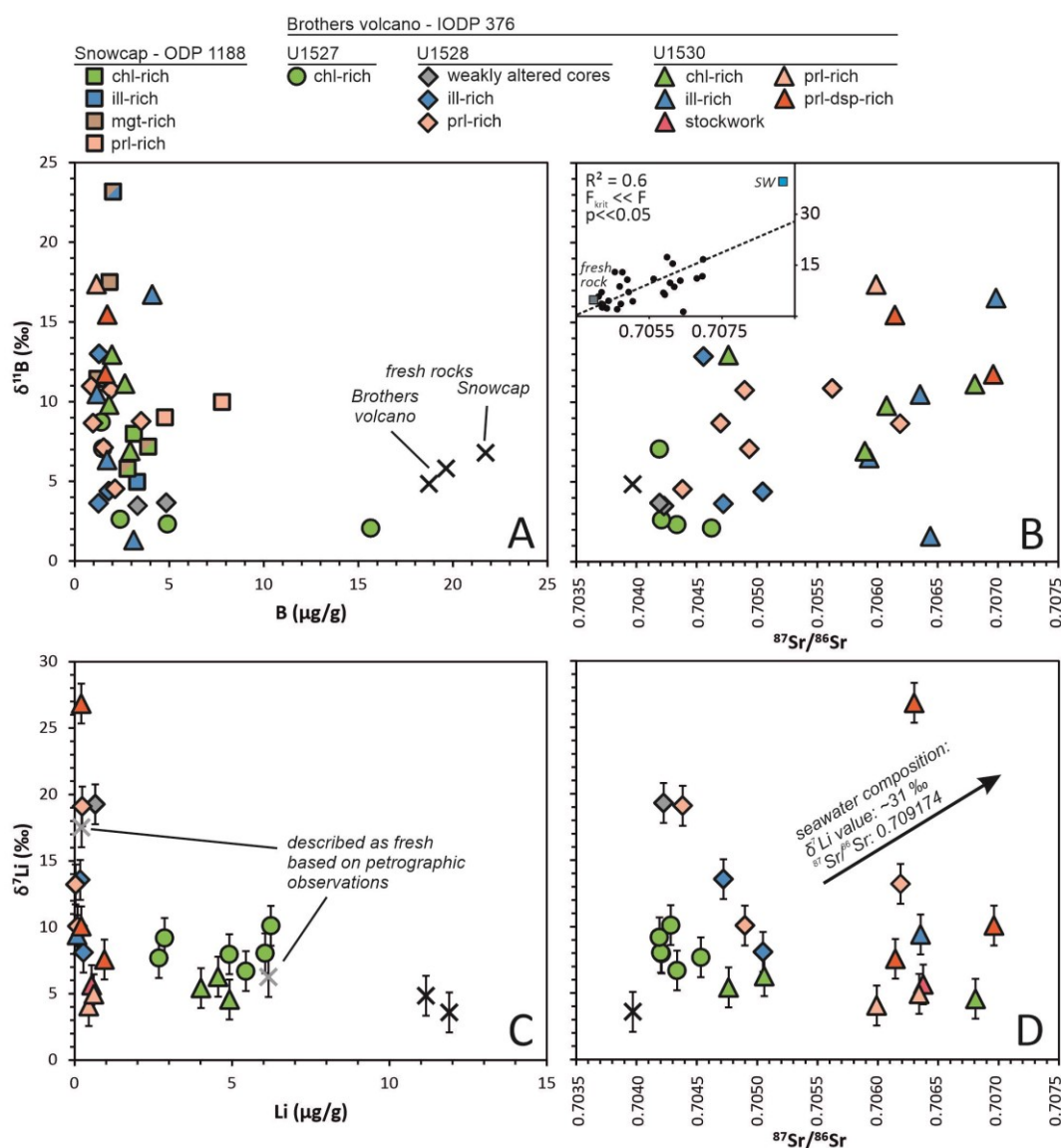


**Figure 5.5-3:** Elemental and isotopic compositions of fresh and altered rocks from Snowcap and Brothers volcano; errors (2sd). For  $\delta^7\text{Li}$  values, a general error of  $\pm 1.5$  ‰ (2sd) is estimated (see **Chapter 5.4.4**). (A) B contents versus  $\delta^{11}\text{B}$  values. (B) Sr versus B isotopic values. The inserted diagram shows the linear regression of the data ( $R^2=0.6$ ,  $F_{\text{krit}} \ll F$ ,  $p \ll 0.05$ ), with the fresh rock and seawater as end-members. (C) Li versus  $\delta^7\text{Li}$  values. (D) Sr versus Li isotopic values.

### 5.5.3. Quartz separates and temperature constraints

The in-situ  $\delta^{18}\text{O}$  values of the quartz separates from Hole U1530A at the NW Caldera of Brothers volcano (**Table 5.6-1; Figure 5.6-1; Table A. 3-8**) were used to calculate the quartz formation temperatures by using the equation given by Sharp & Kirschner (1994):  $1000 \ln \alpha_{(\text{qtz-fluid})} = -2.9 + (3.65 \times 10^6/T^2)$ . The exact  $\delta^{18}\text{O}$  of the interacting fluid is unknown, therefore we calculated a temperature range for the minimum ( $\delta^{18}\text{O}_{\text{fluid}} = 0 \text{ ‰}$ ) and maximum ( $\delta^{18}\text{O}_{\text{fluid}} = +1 \text{ ‰}$ ) measured fluid compositions at the NW Caldera (de Ronde *et al.*, 2011), resulting in an absolute temperature difference for individual measurements of on average  $31 \pm 10 \text{ °C}$  (2sd, **Table 5.6-1**).

Oxygen isotope values and temperature constraints were obtained from six depth intervals of Hole U1530A and 13 individual quartz separates (**Table 5.6-1; Figure 5.6-1**). The total range of formation temperatures ranges from 262 to 425 °C (for  $\delta^{18}\text{O}_{\text{fluid}}$  between 0 and +1 ‰). Two quartz separates from the stockwork zone at shallow levels (22.07 to 22.09 mbsf) of Hole U1530A indicated comparable low but uniform formation temperatures (278 to 315 °C). Two quartz separates handpicked from a lava flow altered to a chlorite-rich secondary mineral assemblage (61.08 to 61.11 mbsf) showed a high variability in formation temperatures but with a tendency towards relatively high calculated formation temperatures (269 to 425 °C). Similarly, a primarily chlorite-altered lava flow in greater depth of Hole U1530A (290.86 to 290.88 mbsf) also showed similarly high formation temperatures in the range of 334 to 400 °C, except for one measurement very close to a crack within the grain (289 to 315 °C). Quartz separates from host rocks dominated by a pyrophyllite and diaspora-rich secondary mineral assemblage from three depth intervals above and below the chlorite-rich altered lava flow (272.40 to 272.42, 276.07 to 276.09, and 309.83 to 309.85 mbsf) showed considerable variation in  $\delta^{18}\text{O}$ , but a tendency towards lower formation temperatures (262 to 353 °C). Quartz separates from the deepest interval (309.83 to 309.85 mbsf) displayed chemical zoning in the CL images (**Figure 5.6-1E**) and the in-situ  $\delta^{18}\text{O}$  measurements showed increased  $\delta^{18}\text{O}$  values in the center (i.e, formation temperatures as low as 262 °C) and decreased  $\delta^{18}\text{O}$  towards the rims (indicative of formation temperatures as high as 380 °C) for two of the three separates. Indeed, for one separate the low  $\delta^{18}\text{O}$  values were measured only for the two measuring points at the outer edges and therefore may represent secondary effects, like diffusion.

## 5.6. Discussion

Seafloor hydrothermal systems are controlled by various parameters like primary rock composition, temperature, phase separation, magma degassing and w/r-ratios. These parameters affect composition and pH of fluids, secondary mineralogy during rock alteration as well as element fluxes, and ore forming processes. The most useful approach for obtaining a comprehensive picture of the processes in the subsurface is to use multiple geochemical tracers with different sensitivities to the various alteration parameters. We merged Sr isotopic systematics that are insensitive for temperature and mineralogical variations but sensitive to the intensity of w/r interactions with B and

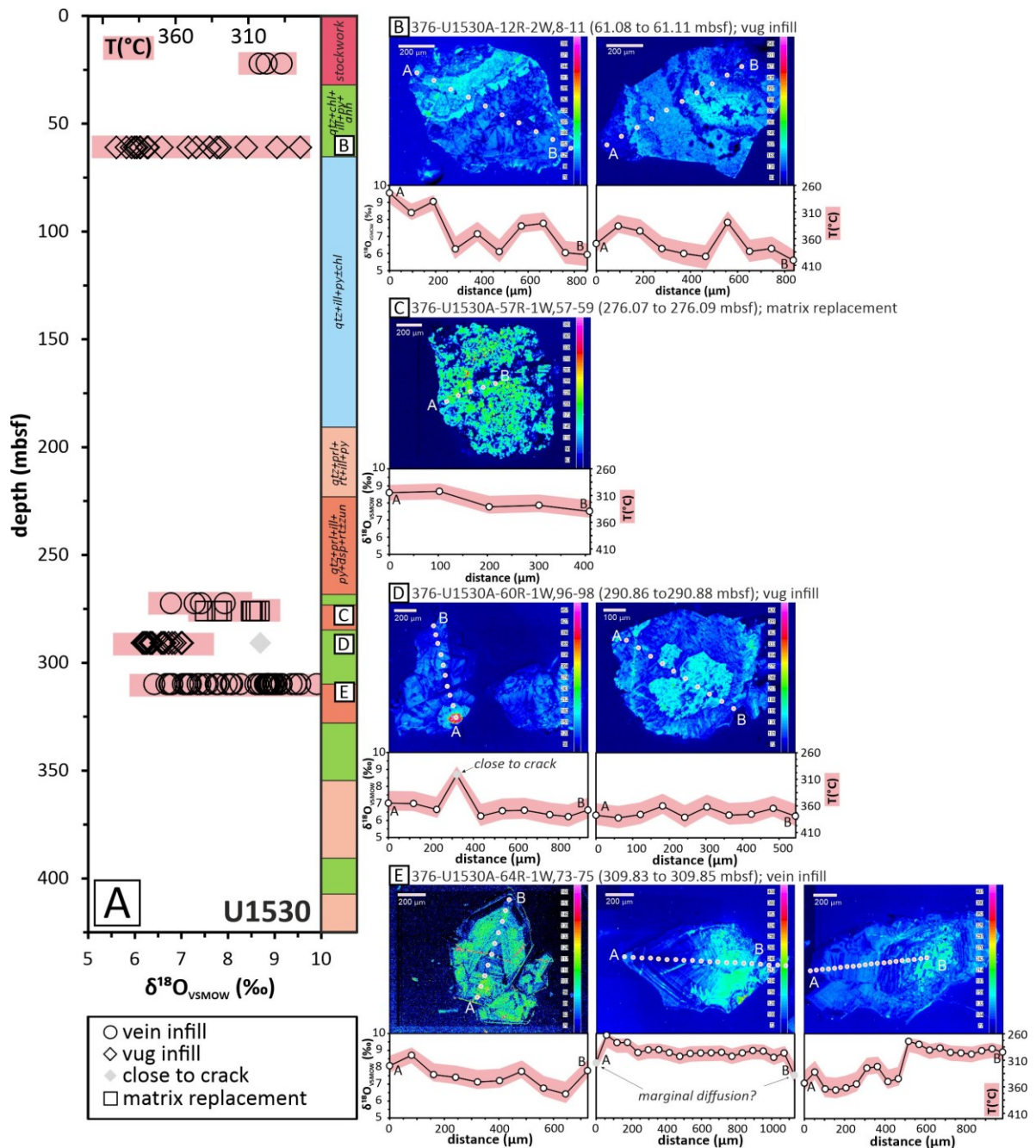


**Figure 5.6-1:** In-situ oxygen isotopic compositions ( $\delta^{18}O_{VSMOW}$ ) and calculated formation temperatures (pink shaded) of quartz separates, handpicked from different depth and alteration types of Hole U1530A, NW Caldera. Temperatures were calculated based on the equation published by Sharp & Kirschner (1994). Given are the minimum and maximum temperatures, calculated by using the hydrothermal fluid minimum ( $\delta^{18}O = 0\%$ ) and maximum ( $\delta^{18}O = +1\%$ ) values measured for the NW Caldera (de Ronde et al., 2011). (A)  $\delta^{18}O_{VSMOW}$  and temperatures versus depth, alteration types also included; (B), (C), (D), and (E) show the CL micrographs of single quartz separates, including the in-situ  $\delta^{18}O$  measuring points and the  $\delta^{18}O$  and temperature patterns, for quartz separates more than two  $\delta^{18}O$  measurements were performed on.

Li isotope systematics that are affected by shifts in temperature and secondary mineralogy and used O isotopes of quartz separates as a proxy for formation temperatures. B is additionally affected by magma degassing and may be a tracer of this process in fluid-rock interactions. In the following

three subchapters, we discuss the Li, B and Sr concentrations and isotopic signatures of fresh rocks and potential modifications of the primary signal by hydrothermal alteration (*Chapter 5.6.1.*), the signatures of altered rocks (*Chapter 5.6.2.*), and furthermore we estimate the implications of our results on the characteristics of subsurface processes (*Chapter 5.6.3.*) at Snowcap and Brothers volcano. For Brothers we also used temperature constraints based on  $\delta^{18}\text{O}$  of quartz to put constraints on the thermal regime during alteration.

**Table 5.6-1:** In-situ oxygen isotope measurements ( $\delta^{18}\text{O}_{\text{VSMOW}}$ ) for quartz separates of Hole U1530A, NW Caldera, Brothers volcano (point positions are given in the Appendix, *Table A. 3-8*).

Host rock sample name	alteration type*	depth (mbsf)		quartz separate			$\delta^{18}\text{O}_{\text{VSMOW}}$ (‰)	2sd (‰)	temperature (°C)† $\delta^{18}\text{O}_{\text{fluid}} = 0 \text{ ‰}$	$\delta^{18}\text{O}_{\text{fluid}} = 1 \text{ ‰}$
		top	bottom	grain No.	point No.	description				
<i>376-U1530A-</i>										
4R-1W, 67-69	stockwork	22.07	22.09	LSM1-17	1	vein infill	9.2	0.2	278	303
4R-1W, 67-69	stockwork	22.07	22.09	LSM1-17	2	vein infill	8.8	0.2	286	311
4R-1W, 67-69	stockwork	22.07	22.09	LSM1-18	1	vein infill	8.7	0.2	289	315
12R-2W, 8-11	chl-rich (lava flow)	61.08	61.11	LSM1-14	1	vug infill	9.6	0.2	269	292
12R-2W, 8-11	chl-rich (lava flow)	61.08	61.11	LSM1-14	2	vug infill	8.4	0.2	296	323
12R-2W, 8-11	chl-rich (lava flow)	61.08	61.11	LSM1-14	3	vug infill	9.1	0.2	280	305
12R-2W, 8-11	chl-rich (lava flow)	61.08	61.11	LSM1-14	4	vug infill	6.3	0.2	359	396
12R-2W, 8-11	chl-rich (lava flow)	61.08	61.11	LSM1-14	5	vug infill	7.1	0.2	330	363
12R-2W, 8-11	chl-rich (lava flow)	61.08	61.11	LSM1-14	6	vug infill	6.1	0.2	364	403
12R-2W, 8-11	chl-rich (lava flow)	61.08	61.11	LSM1-14	7	vug infill	7.6	0.2	317	347
12R-2W, 8-11	chl-rich (lava flow)	61.08	61.11	LSM1-14	8	vug infill	7.8	0.2	313	342
12R-2W, 8-11	chl-rich (lava flow)	61.08	61.11	LSM1-14	9	vug infill	6.0	0.2	366	405
12R-2W, 8-11	chl-rich (lava flow)	61.08	61.11	LSM1-14	10	vug infill	5.9	0.2	370	410
12R-2W, 8-11	chl-rich (lava flow)	61.08	61.11	LSM1-16	1	vug infill	5.6	0.1	383	425
12R-2W, 8-11	chl-rich (lava flow)	61.08	61.11	LSM1-16	2	vug infill	6.3	0.1	358	395
12R-2W, 8-11	chl-rich (lava flow)	61.08	61.11	LSM1-16	3	vug infill	6.1	0.1	363	402
12R-2W, 8-11	chl-rich (lava flow)	61.08	61.11	LSM1-16	4	vug infill	7.8	0.1	311	340
12R-2W, 8-11	chl-rich (lava flow)	61.08	61.11	LSM1-16	5	vug infill	5.8	0.1	374	415
12R-2W, 8-11	chl-rich (lava flow)	61.08	61.11	LSM1-16	6	vug infill	6.0	0.1	368	407
12R-2W, 8-11	chl-rich (lava flow)	61.08	61.11	LSM1-16	7	vug infill	6.3	0.1	358	395
12R-2W, 8-11	chl-rich (lava flow)	61.08	61.11	LSM1-16	8	vug infill	7.3	0.1	325	357
12R-2W, 8-11	chl-rich (lava flow)	61.08	61.11	LSM1-16	9	vug infill	7.6	0.1	317	347
12R-2W, 8-11	chl-rich (lava flow)	61.08	61.11	LSM1-16	10	vug infill	6.6	0.2	348	384
56R-2W, 40-42	prl-dsp-rich	272.40	272.42	LSM1-3	1	vein infill	7.4	0.1	322	354
56R-2W, 40-42	prl-dsp-rich	272.40	272.42	LSM1-3	2	vein infill	7.3	0.1	326	358
56R-2W, 40-42	prl-dsp-rich	272.40	272.42	LSM1-10	1	vein infill	6.8	0.1	342	376
56R-2W, 40-42	prl-dsp-rich	272.40	272.42	LSM1-10	2	vein infill	7.9	0.1	308	337
57R-1W, 57-59	prl-dsp-rich	276.07	276.09	LSM1-1	1	matrix replacement	8.5	0.1	294	320
57R-1W, 57-59	prl-dsp-rich	276.07	276.09	LSM1-1	2	matrix replacement	8.5	0.1	293	320
57R-1W, 57-59	prl-dsp-rich	276.07	276.09	LSM1-2	1	matrix replacement	7.5	0.1	320	351
57R-1W, 57-59	prl-dsp-rich	276.07	276.09	LSM1-2	2	matrix replacement	7.9	0.1	310	339
57R-1W, 57-59	prl-dsp-rich	276.07	276.09	LSM1-2	3	matrix replacement	7.8	0.1	313	342
57R-1W, 57-59	prl-dsp-rich	276.07	276.09	LSM1-2	4	matrix replacement	8.7	0.1	289	315
57R-1W, 57-59	prl-dsp-rich	276.07	276.09	LSM1-2	5	matrix replacement	8.6	0.1	291	317
60R-1W, 96-98	chl-rich (lava flow)	290.86	290.88	LSM1-4	1	vug infill	7.0	0.1	334	367
60R-1W, 96-98	chl-rich (lava flow)	290.86	290.88	LSM1-4	2	vug infill	7.0	0.1	335	368
60R-1W, 96-98	chl-rich (lava flow)	290.86	290.88	LSM1-4	3	vug infill	6.6	0.1	346	381
60R-1W, 96-98	chl-rich (lava flow)	290.86	290.88	LSM1-4	4	vug infill; crack?	8.7	0.1	289	315
60R-1W, 96-98	chl-rich (lava flow)	290.86	290.88	LSM1-4	5	vug infill	6.3	0.1	359	397
60R-1W, 96-98	chl-rich (lava flow)	290.86	290.88	LSM1-4	6	vug infill	6.6	0.1	348	384
60R-1W, 96-98	chl-rich (lava flow)	290.86	290.88	LSM1-4	7	vug infill	6.6	0.1	347	383
60R-1W, 96-98	chl-rich (lava flow)	290.86	290.88	LSM1-4	8	vug infill	6.3	0.1	356	393
60R-1W, 96-98	chl-rich (lava flow)	290.86	290.88	LSM1-4	9	vug infill	6.2	0.1	360	398
60R-1W, 96-98	chl-rich (lava flow)	290.86	290.88	LSM1-4	10	vug infill	6.6	0.1	347	383
60R-1W, 96-98	chl-rich (lava flow)	290.86	290.88	LSM1-5	1	vug infill	6.3	0.1	358	396
60R-1W, 96-98	chl-rich (lava flow)	290.86	290.88	LSM1-5	2	vug infill	6.7	0.1	343	378
60R-1W, 96-98	chl-rich (lava flow)	290.86	290.88	LSM1-5	3	vug infill	6.4	0.1	355	391
60R-1W, 96-98	chl-rich (lava flow)	290.86	290.88	LSM1-5	4	vug infill	6.3	0.1	356	394
60R-1W, 96-98	chl-rich (lava flow)	290.86	290.88	LSM1-5	5	vug infill	6.8	0.1	341	375
60R-1W, 96-98	chl-rich (lava flow)	290.86	290.88	LSM1-5	6	vug infill	6.2	0.1	361	399
60R-1W, 96-98	chl-rich (lava flow)	290.86	290.88	LSM1-5	7	vug infill	6.9	0.1	339	373
60R-1W, 96-98	chl-rich (lava flow)	290.86	290.88	LSM1-5	8	vug infill	6.4	0.1	355	392
60R-1W, 96-98	chl-rich (lava flow)	290.86	290.88	LSM1-5	9	vug infill	6.2	0.1	362	400
60R-1W, 96-98	chl-rich (lava flow)	290.86	290.88	LSM1-5	10	vug infill	6.3	0.1	357	394
64R-1W, 73-75	prl-dsp-rich	309.83	309.85	LSM1-11	1	vein infill	8.1	0.2	304	332
64R-1W, 73-75	prl-dsp-rich	309.83	309.85	LSM1-11	2	vein infill	8.7	0.2	288	314
64R-1W, 73-75	prl-dsp-rich	309.83	309.85	LSM1-11	3	vein infill	7.6	0.2	318	349
64R-1W, 73-75	prl-dsp-rich	309.83	309.85	LSM1-11	4	vein infill	7.4	0.2	323	354
64R-1W, 73-75	prl-dsp-rich	309.83	309.85	LSM1-11	5	vein infill	7.1	0.2	331	363

(continued from previous page)

64R-1W, 73-75	prl-dsp-rich	309.83	309.85	LSM1-11	6	vein infill	7.2	0.2	329	361
64R-1W, 73-75	prl-dsp-rich	309.83	309.85	LSM1-11	7	vein infill	7.8	0.2	313	343
64R-1W, 73-75	prl-dsp-rich	309.83	309.85	LSM1-11	8	vein infill	6.8	0.2	342	377
64R-1W, 73-75	prl-dsp-rich	309.83	309.85	LSM1-11	9	vein infill	6.4	0.2	353	390
64R-1W, 73-75	prl-dsp-rich	309.83	309.85	LSM1-11	10	vein infill	7.8	0.2	312	341
64R-1W, 73-75	prl-dsp-rich	309.83	309.85	LSM1-12	1	vein infill; diffusion?	7.5	0.2	319	350
64R-1W, 73-75	prl-dsp-rich	309.83	309.85	LSM1-12	2	vein infill	8.8	0.2	285	311
64R-1W, 73-75	prl-dsp-rich	309.83	309.85	LSM1-12	3	vein infill	8.6	0.2	291	318
64R-1W, 73-75	prl-dsp-rich	309.83	309.85	LSM1-12	4	vein infill	9.0	0.2	283	308
64R-1W, 73-75	prl-dsp-rich	309.83	309.85	LSM1-12	5	vein infill	9.0	0.2	282	307
64R-1W, 73-75	prl-dsp-rich	309.83	309.85	LSM1-12	6	vein infill	8.9	0.2	285	311
64R-1W, 73-75	prl-dsp-rich	309.83	309.85	LSM1-12	7	vein infill	8.6	0.2	290	316
64R-1W, 73-75	prl-dsp-rich	309.83	309.85	LSM1-12	8	vein infill	8.9	0.2	284	310
64R-1W, 73-75	prl-dsp-rich	309.83	309.85	LSM1-12	9	vein infill	8.9	0.2	285	310
64R-1W, 73-75	prl-dsp-rich	309.83	309.85	LSM1-12	10	vein infill	8.8	0.2	285	311
64R-1W, 73-75	prl-dsp-rich	309.83	309.85	LSM1-12	11	vein infill	8.8	0.2	286	312
64R-1W, 73-75	prl-dsp-rich	309.83	309.85	LSM1-12	12	vein infill	8.6	0.2	290	316
64R-1W, 73-75	prl-dsp-rich	309.83	309.85	LSM1-12	13	vein infill	8.9	0.2	285	310
64R-1W, 73-75	prl-dsp-rich	309.83	309.85	LSM1-12	14	vein infill	9.0	0.2	281	305
64R-1W, 73-75	prl-dsp-rich	309.83	309.85	LSM1-12	15	vein infill	9.0	0.2	281	306
64R-1W, 73-75	prl-dsp-rich	309.83	309.85	LSM1-12	16	vein infill	8.9	0.2	285	310
64R-1W, 73-75	prl-dsp-rich	309.83	309.85	LSM1-12	17	vein infill	9.5	0.2	271	295
64R-1W, 73-75	prl-dsp-rich	309.83	309.85	LSM1-12	18	vein infill	9.5	0.2	271	295
64R-1W, 73-75	prl-dsp-rich	309.83	309.85	LSM1-12	19	vein infill	9.9	0.2	262	284
64R-1W, 73-75	prl-dsp-rich	309.83	309.85	LSM1-12	20	vein infill; diffusion?	8.3	0.2	300	327
64R-1W, 73-75	prl-dsp-rich	309.83	309.85	LSM1-13	1	vein infill	8.9	0.2	284	309
64R-1W, 73-75	prl-dsp-rich	309.83	309.85	LSM1-13	2	vein infill	9.1	0.2	279	304
64R-1W, 73-75	prl-dsp-rich	309.83	309.85	LSM1-13	3	vein infill	9.0	0.2	282	307
64R-1W, 73-75	prl-dsp-rich	309.83	309.85	LSM1-13	4	vein infill	8.8	0.2	286	312
64R-1W, 73-75	prl-dsp-rich	309.83	309.85	LSM1-13	5	vein infill	8.9	0.2	285	310
64R-1W, 73-75	prl-dsp-rich	309.83	309.85	LSM1-13	6	vein infill	8.9	0.2	284	309
64R-1W, 73-75	prl-dsp-rich	309.83	309.85	LSM1-13	7	vein infill	9.2	0.2	278	303
64R-1W, 73-75	prl-dsp-rich	309.83	309.85	LSM1-13	8	vein infill	9.0	0.2	281	306
64R-1W, 73-75	prl-dsp-rich	309.83	309.85	LSM1-13	9	vein infill	9.4	0.2	273	297
64R-1W, 73-75	prl-dsp-rich	309.83	309.85	LSM1-13	10	vein infill	9.5	0.2	269	293
64R-1W, 73-75	prl-dsp-rich	309.83	309.85	LSM1-13	11	vein infill	7.3	0.2	325	356
64R-1W, 73-75	prl-dsp-rich	309.83	309.85	LSM1-13	12	vein infill	7.2	0.2	329	362
64R-1W, 73-75	prl-dsp-rich	309.83	309.85	LSM1-13	13	vein infill	8.1	0.2	305	333
64R-1W, 73-75	prl-dsp-rich	309.83	309.85	LSM1-13	14	vein infill	8.0	0.2	307	336
64R-1W, 73-75	prl-dsp-rich	309.83	309.85	LSM1-13	15	vein infill	7.0	0.2	334	367
64R-1W, 73-75	prl-dsp-rich	309.83	309.85	LSM1-13	16	vein infill	6.8	0.2	341	375
64R-1W, 73-75	prl-dsp-rich	309.83	309.85	LSM1-13	17	vein infill	6.7	0.2	345	380
64R-1W, 73-75	prl-dsp-rich	309.83	309.85	LSM1-13	18	vein infill	6.7	0.2	343	378
64R-1W, 73-75	prl-dsp-rich	309.83	309.85	LSM1-13	19	vein infill	7.7	0.2	313	343
64R-1W, 73-75	prl-dsp-rich	309.83	309.85	LSM1-13	20	vein infill	7.1	0.2	332	365

\*alteration types are described in **Chapter 5.3.2**.

†temperatures were calculated based on the equation given by Sharp & Kirschner (1994).

◇minimum and maximum measured  $\delta^{18}O$  hydrothermal fluid compositions at the NW Caldera of Brothers volcano after de Ronde *et al.* (2011).

### 5.6.1. Signatures of unaltered rocks and sample preservation

Arc lavas at divergent plate boundaries are typically enriched in LILE (large-ion-lithophile elements, e.g. Sr) versus HFSE (high-field-strength elements, e.g. Zr) compared to MORB, due to LILEs high incompatibility during mantle melting and slab recycling process during subduction (McCulloch & Gamble, 1991). Fluid mobile elements other than LILE, like B and Li, are also highly enriched in subducted oceanic crust and marine sediments, and hence display increased (relative to MORB) abundances in rocks from arcs and BAB (Tomascak *et al.*, 2002; Hoog & Savov, 2018). In the following, we place the pristine B, Li and Sr isotope compositions of Brothers volcano and Snowcap lavas in the larger context of isotopic characteristics of the Southern Kermadec arc and the Manus back-arc basin and assess the reliability of the pristine rock isotope compositions, regarding potential change in composition by hydrothermal alteration.

### *Brothers volcano*

The B contents (18.7 and 19.6  $\mu\text{g/g}$ ) and  $\delta^{11}\text{B}$  compositions ( $+4.8 \pm 0.1$  and  $+5.8 \pm 0.1$  ‰) of the two unaltered dacites from Brothers volcano analyzed in this study lie between the published values of two seamounts (Rumble III and IV) to the south of Brothers volcano and the volcanic edifices of the Northern Kermadec arc (Leeman *et al.*, 2017). Furthermore, the B contents and isotopic compositions of Brothers volcano are transitional between those of rocks from volcanic centers to the south and to the north of Brothers. This is in agreement with the overall increase in B concentrations and  $\delta^{11}\text{B}$  values along the Tonga-Kermadec volcanic arc from New Zealand northwards (Leeman *et al.*, 2017). These authors attributed the variation in B systematics to a steeper thermal gradient or a greater sedimentary influence in the magma source to the south. The Sr isotopic composition of the Southern Kermadec arc ( $> 0.7038$ ), is confirmed by this study (0.703970 for Lower Cone at Brothers volcano), and likewise points to an increased influx of a sedimentary component in the southernmost Kermadec arc (Haase *et al.*, 2002).

In contrast to B, published Li concentrations (2 to 16  $\mu\text{g/g}$ ) and isotope data (+2.5 to +5.0 ‰) of pristine lavas show no distinct variations along the Kermadec arc (Brens *et al.*, 2019). The Li concentrations (11.2 and 11.9  $\mu\text{g/g}$ ) and  $\delta^7\text{Li}$  values (+4.8 and +3.6 ‰) of the two unaltered samples from Brothers volcano collected by ROV that were measured in this study fall within this range of previous published data for Tonga-Kermadec arc lavas. In contrast, the two dacitic rocks from the drill-cores of IODP 376 that were classified as unaltered based on petrographic observations and the major element compositions are significantly shifted towards more altered Li signatures of lower Li concentrations (6.2 and 0.2  $\mu\text{g/g}$ ) and higher  $\delta^7\text{Li}$  values (+6.3 and +17.5 ‰) than the unaltered rocks collected by ROV. This indicates that Li was mobilized from those samples by circulation of high-temperature fluids, even without any noticeable mineralogical changes. A similar case of cryptic alteration and Li loss from basaltic rocks was previously described for young oceanic crust of the EPR (East Pacific Rise) and further confirmed by experiments (Brant *et al.*, 2012). The experiments demonstrated that w/r exchange at 125 °C is sufficient to lead to an extensive and rapid diffusive Li loss out of plagioclase without noticeable mineralogical modification. This especially underlines the importance of careful sample selection and preparation to measure the pristine composition of highly fluid mobile elements like Li (and also B) in submarine collected rock samples that were exposed to seawater and potentially affected by hydrothermal alteration.

### *Snowcap, PACMANUS*

The Manus back-arc basin exhibits a complicated tectonic geometry, with the inactive Manus trench to the north and the actively subducting New Britain Trench to the south (*Figure 5.2-1*). The Southeast Rifts (SER), of which Pual Ridge with the Snowcap hydrothermal area is a part of, were suggested to represent BAB crust in an early rifting stage that is still influenced by subduction

magmatism especially of the active slab recycling to the south based on the high abundances of Pb and LILEs (Park *et al.*, 2010; Beier *et al.*, 2015). The unaltered dacitic sample from Snowcap with a relatively high B content of 21.7  $\mu\text{g/g}$  and a  $\delta^{11}\text{B}$  value of  $+6.8 \pm 0.1 \text{ ‰}$  also indicates significant contribution from the subducting slab, similar to other volcanic edifices of the SER that showed B of 11.8 to 23.7  $\mu\text{g/g}$  and  $\delta^{11}\text{B}$  in a range of  $+6.5$  to  $+8.3 \text{ ‰}$  (Wilckens *et al.*, 2018). The B content of the unaltered rock (21.7  $\mu\text{g/g}$ ) is close to the highest ever measured B content at the SER.

The B, Li and Sr signatures of the unaltered rock samples of Brothers volcano and Snowcap collected by ROV represent pristine rock compositions with minor affection by alteration. The relatively high B and Li abundances and B, Li and Sr isotopic compositions of the lavas are typical for magmatism at volcanic arcs or rather the immature rifting stage of an opening BAB that is strongly influenced by slab recycling processes. The two petrographic fresh looking rocks from the IODP 376 drill cores are significantly shifted in their Li content and Li isotopic composition towards more altered signatures and should not be used as a reference of the pristine Li and  $\delta^7\text{Li}$  lava composition.

### 5.6.2. Signatures of altered oceanic crust

#### 5.6.2.1. Lithium concentrations and isotopes

Lithium is a highly fluid mobile element with the affinity to preferentially partition into the fluid phase at elevated alteration temperatures ( $> 150 \text{ }^\circ\text{C}$ ), while Li is enriched in the solid phase at low-temperatures ( $< 150 \text{ }^\circ\text{C}$ , Seyfried *et al.*, 1984). The fractionation of Li isotopes depends on temperature, w/r-ratio and the assemblage of secondary minerals. The  $\delta^7\text{Li}$  values of rocks typically increase during hydrothermal alteration at low-T and high-T, due to exchange of Li in pristine oceanic crust ( $\delta^7\text{Li}$  usually  $\leq +5 \text{ ‰}$ ) and Li in seawater-derived fluids that have high initial  $\delta^7\text{Li}$  values of  $+31 \text{ ‰}$ .

As expected in high-T fluid-rock interactions, all altered rocks from Brothers volcano show depletion in Li ( $< 0.1$  to  $6.2 \text{ } \mu\text{g/g}$ ) compared to the fresh rocks (on average  $11.5 \text{ } \mu\text{g/g}$ , **Figure 5.5-3C**). Chlorite-rich samples are moderately depleted in Li (3 to 6  $\mu\text{g/g}$  remained), whereas rocks rich in illite, pyrophyllite and pyrophyllite-diaspora show more pronounced Li losses ( $< 1 \text{ } \mu\text{g/g}$  remained). The higher retention of Li in Mg-rich altered rocks (chlorite abundance) can be explained by the affinity of Li to substitute for Mg due to similar ionic radii of the two elements (Berger *et al.*, 1988). A distinction between seawater-derived versus magmatic fluid-dominated alteration fluids is not possible, due to similarly extensive Li losses for the illite-rich (seawater dominated) and the pyrophyllite-rich (magmatic fluid-dominated) alteration (**Figure 5.5-3C**).

Lithium isotopic compositions of altered rocks from Brothers volcano ( $+4.1 \pm 0.4$  to  $+26.8 \pm 0.7 \text{ ‰}$ ) range between values for fresh rock (around  $+4 \text{ ‰}$ ) to nearly seawater compositions ( $+31 \text{ ‰}$ ). The  $\delta^7\text{Li}$  values of chlorite-rich rocks show only slightly elevated  $\delta^7\text{Li}$  values relative to fresh rocks.

This either points to an overall small extent of alteration or relatively low alteration temperatures. The other alteration types at Brothers volcano, typical for seawater alteration (illite) and magmatic fluid contribution, show low as well as high  $\delta^7\text{Li}$  values and no systematic differences between alteration types that would point to a characteristic signature of magmatic fluid- versus seawater-dominated alteration (**Figure 5.5-3C**).

The data indicate that altered rock Li contents are sensitive to the type of secondary minerals and show less depletion in rocks with abundant chlorite. A systematic variation in Li isotopic compositions of altered rocks was not recognized, most likely because  $\delta^7\text{Li}$  values result from a complex interplay of varying secondary mineralogy, temperatures and w/r-ratios. A similar conclusion that  $\delta^7\text{Li}$  isotopic signatures of hydrothermal systems are the result of a combination of changing w/r-ratios, temperatures and basement alteration was also drawn based on the discharging fluid  $\delta^7\text{Li}$  compositions from the Eastern Manus Basin (Wilckens *et al.*, 2019). Furthermore, the altered rock compositions may also reflect mixed signatures of different stages of alteration that were characterized by various temperatures, fluid compositions and potential mineralogical changes over time. This is likely given that caldera systems most likely have several generations of eruptions, floor down drop, and fluid movement.

#### 5.6.2.2. Strontium concentrations and isotopes

The Sr isotopic composition of fresh arc and back-arc crust in our work areas (0.7040) are expected to become increasingly enriched by hydrothermal alteration because of interaction with more radiogenic seawater (0.70917). This trend is indeed observed in the altered samples at Brothers volcano that all show more radiogenic Sr isotopic compositions than the unaltered rocks (**Figure 5.5-2, Figure 5.5-3B,D**). The Sr isotope exchange depends on the alteration extent and w/r-ratios but is irrespective of any temperature or mineral dependent isotope fractionation effects and therefore the  $^{87}\text{Sr}/^{86}\text{Sr}$  composition of altered crust and hydrothermal fluids is commonly used as a tracer for w/r-ratios. The simplified relation of  $^{87}\text{Sr}/^{86}\text{Sr}$  values and w/r-ratios under closed-system conditions that is valid unless extremely high w/r-ratios are reached is given by (McCulloch *et al.*, 1980; Marks *et al.*, 2015):

$$W/R \approx \frac{C_{rock(i)}^{Sr} \cdot ((^{87}\text{Sr}/^{86}\text{Sr}_{rock(f)}) - (^{87}\text{Sr}/^{86}\text{Sr}_{rock(i)}))}{C_{fluid(i)}^{Sr} \cdot ((^{87}\text{Sr}/^{86}\text{Sr}_{fluid(i)}) - (^{87}\text{Sr}/^{86}\text{Sr}_{rock(i)}))} \quad (\text{Eq.5.6-1})$$

where  $C_{rock(i)}^{Sr}$  = Sr concentration of fresh rock (220  $\mu\text{g/g}$ ),  $C_{fluid(i)}^{Sr}$  = Sr concentration of seawater (8  $\mu\text{g/g}$ ),  $^{87}\text{Sr}/^{86}\text{Sr}_{rock(i)}$  = Sr isotopic composition of fresh rock (assuming on average 0.70404, **Table 5.3-2**),  $^{87}\text{Sr}/^{86}\text{Sr}_{fluid(i)}$  = Sr isotopic composition of seawater (0.709174, Hodell *et al.*, 1990), and  $^{87}\text{Sr}/^{86}\text{Sr}_{rock(f)}$  = Sr isotopic composition of altered rock (**Table 5.3-2**). For the rim of the NW Caldera wall of Brothers volcano (Site U1527), the calculated w/r-ratios are 1 to 3 with the highest values occurring in the shallowest and deepest levels of the drill-core. Relatively high w/r-

ratios (of up to 13) are also found in the topmost basement cored at NW Caldera wall based on the high  $^{87}\text{Sr}/^{86}\text{Sr}$  found there (Site U1530, **Figure 5.5-2D**) and (with w/r ratios up to 12) at the summit of the Upper Cone site (Site U1528, **Figure 5.5-2C**). These data point to enhanced ingress of seawater at shallower levels as frequently reported from the topmost part of the upper volcanic zone, e.g. also for Snowcap (e.g. Kawahata *et al.*, 2001; Bach *et al.*, 2003; Lackschewitz *et al.*, 2004; Bach *et al.*, 2003). The  $^{87}\text{Sr}/^{86}\text{Sr}$  values of the altered rocks closer to the fresh rock composition and the lower calculated w/r-ratios of 1 to 2 at deeper crust levels of Sites U1527 and U1528 indicate a more rock-controlled w/r interaction and are similar to w/r-ratios < 5 estimated for vent sites at the East Pacific Rise, the Galapagos hydrothermal system, the Central Manus Basin and the crust of the Troodos Ophiolite (Edmond *et al.*, 1979; Albarède *et al.*, 1981; Gillis *et al.*, 1992; Reeves *et al.*, 2011). The decrease in w/r-ratios from shallower to deeper crustal levels points to an evolution from a fluid towards a more rock dominated hydrothermal system with increasing depth.

The w/r-ratios we calculated for Site U1530 at the NW Caldera are mostly higher than for the other two investigated drill-cores at Brothers volcano and lie between 10 and 16. Lower w/r-ratios of 4 and 5 were calculated for a sandstone (40.40 to 40.51 mbsf) and a massive lava flow (290.86 to 290.88 mbsf) at Site U1530, which both show replacement by a chlorite dominated secondary mineral assemblage. Similarly, the lowest measured  $^{87}\text{Sr}/^{86}\text{Sr}$  value of clay mineral separates from Snowcap was also obtained for a chlorite separate at 174.58 mbsf (Lackschewitz *et al.*, 2004). However, three other chlorite-rich altered rocks of Site U1530 show w/r-ratios of 10 to 15 that are similar as high as w/r-ratios of the other alteration types at Site U1530 and there is hence no evidence for a simple relationship between w/r-ratios and a specific alteration mineral assemblage. In any case, calculated w/r-ratios for Site U1530 have to be considered with care because of the high variability of Sr concentrations of the altered whole rocks towards higher values at the stockwork zone as well as much lower values < 40 mbsf than the precursor (**Table 5.3-2, Figure 5.5-2D**). Changes in Sr concentration of altered versus fresh rocks are not regarded by equation (Eq.5.6-1) and therefore could lead to invalid results of calculated w/r-ratios. Variability of Sr concentrations in altered whole rocks can either be attributed to destruction of primary Sr host phases (especially plagioclase, e.g. Berndt *et al.*, 1988) or precipitation and dissolution of Sr-bearing secondary phases, like anhydrite that is present in significant amounts, and barite at Site U1530 (de Ronde *et al.*, 2019c; Berndt *et al.*, 1988). Precipitation and dissolution of anhydrite affecting Sr isotopic systematics were also suggested for the Eastern Manus Basin based on the extensive Sr losses from solutions and unreasonably low  $^{87}\text{Sr}/^{86}\text{Sr}$  isotopic end-member values of discharging fluids (Reeves *et al.*, 2011), the variability of Sr concentrations of altered whole rocks (Paulick *et al.*), and the considerable shifts towards more radiogenic  $^{87}\text{Sr}/^{86}\text{Sr}$  values of anhydrite compared to clay mineral separates from similar depth of ODP drill-cores at Snowcap and Roman Ruins (Roberts *et al.*, 2003; Lackschewitz *et al.*, 2004). Anhydrite is also an abundant phase at the Upper Cone site of Brothers volcano (Site U1528, de Ronde *et al.*, 2019b). But in contrast to Site U1530

and the Eastern Manus Basin, the low variability in Sr concentrations of altered whole rocks compared to the unaltered rocks at Site U1528 (**Table 5.3-2**) suggests that the portion of Sr hosted in anhydrite is small and therefore has a minor impact on the whole rock Sr isotopic composition.

The Sr concentrations and isotopic compositions give evidence that rock alteration changes from a fluid to a more rock dominated environment from shallower to deeper crustal levels at the rim of the NW Caldera (Site U1527) and at the Upper Cone (Site U1528). At both drilling sites, anhydrite precipitation or dissolution seems to have a minor control on the Sr isotope systematics of the altered rocks. In contrast, at Site U1530 and the Eastern Manus Basin anhydrite appears to be a main Sr host mineral of the altered rocks and to majorly affect the Sr isotopic systematics.

#### 5.6.2.3. *Boron concentrations and isotopes*

Boron tends, similar to Li, to partition into the fluid phase at higher temperatures ( $> 150$  °C) and into the solid phase at lower temperatures by reaction with felsic rocks ( $<150$  °C). The  $\delta^{11}\text{B}$  fractionation by fluid-rock interaction is controlled by variations in temperature, secondary mineralogy and w/r-ratios (Spivack & Edmond, 1987). The potential pH effect on  $\delta^{11}\text{B}$  fractionation is negligible in hydrothermal systems that are hosted in basaltic or even more felsic crust because of the generally high acidity of interacting fluids ( $\text{pH} < 5$ ). High- and low-temperature altered rocks usually show an increase in  $\delta^{11}\text{B}$  values by progressive alteration compared to fresh oceanic crust ( $\leq +16$  ‰) due to interaction with seawater-derived fluids, which start with high  $\delta^{11}\text{B}$  values of  $+40$  ‰. In addition, B also has a moderately volatile character leading to the suggestion that it is a potential tracer for magma degassing in seafloor hydrothermal systems. Based on discharging fluid  $\delta^{11}\text{B}$  data from vent sites at divergent plate boundaries in the Western Pacific, a shift of magma degassing influenced fluids towards lower  $\delta^{11}\text{B}$  for the dedicated B concentrations and estimated w/r-ratios was noticed compared to solely seawater affected fluids (Wilckens *et al.*, 2018).

#### *Impact of seawater versus magmatic fluid contributions*

Boron contents of altered rocks from Brothers volcano and Snowcap are depleted compared to the unaltered rock and usually have  $\leq 5$   $\mu\text{g/g}$ , corresponding to a B loss of  $\geq 75$  % (**Figure 5.5-1; Figure 5.5-2; Figure 5.5-3A**). The two advanced argillic altered rocks recovered from Snowcap have slightly higher B concentrations (up to  $7.8$   $\mu\text{g/g}$ ) relative to the other altered samples, potentially because of slightly better preservation of the fresh lava signal due to more channelized fluid flow directly under the fresh dacitic lava cap at Snowcap (Roberts *et al.*, 2003). Besides, no systematic differences between alteration types and B concentrations could be found as well as no relation between alteration types, B values or  $\delta^{11}\text{B}$  compositions was recognized (**Figure 5.5-3A**).

The missing imprint of magmatic fluid signatures on the rock B contents and  $\delta^{11}\text{B}$  compositions, could be explained by three potential reasons: (1) the magmatic fluid and seawater-derived fluid have similar  $\delta^{11}\text{B}$  values, (2) overprint of the magmatic fluid signal of the altered rocks due to

extensive dilution by high seawater fluxes, (3) overprint by low-temperature (< 150 °C) alteration. A seawater like  $\delta^{11}\text{B}$  value of the magmatic fluid is implausible, as a lowering in  $\delta^{11}\text{B}$  of magma degassing affected fluids versus solely seawater affected fluids was previously observed (Wilckens *et al.*, 2018) and the altered rocks tend towards higher  $\delta^{11}\text{B}$  values with decreasing B concentrations (**Figure 5.5-3A**). More likely is a combination of strong dilution of the magmatic fluid by high fluid fluxes of seawater-derived hydrothermal fluids, locally accompanied by a low-temperature alteration overprint. Low-temperature overprint is evident by the occurrence of smectites throughout all three investigated drillcores of Brothers volcano (de Ronde *et al.*, 2019e) and by the abundance of corrensite at intermediate depth at Snowcap (**Figure 5.5-1**). Although, the generally low B concentrations of the altered rocks points to that high-T alteration was still the dominating processes and the affection of B rock systematics by low-T overprint was less extensive. One altered rock sample from the uppermost rock column of Site U1527 at the NW Caldera of Brothers volcano point to a more extensive low-temperature overprint due to especially low B depletion (15.6  $\mu\text{g/g}$  remained; 185 mbsf) compared to the unaltered rock (**Figure 5.5-3**).

The B systematics of altered crust is minor affected by different fluid sources (seawater versus magmatic fluid contribution) or different secondary minerals, most likely due to dilution of the magmatic fluid by high fluxes of a seawater-like fluid with a high  $\delta^{11}\text{B}$  composition, as well as in some cases due to a low-temperature alteration overprint.

#### *Impact of water-to-rock-ratios and alteration temperatures*

The secondary mineralogy and different fluid sources seem to have a negligible effect on B systematics of altered rocks at Brothers volcano and Snowcap, instead B is potentially more strongly affected by alteration temperatures and w/r-ratios, as discussed in the following chapter.

The low B concentrations of altered compared to the fresh rocks and high  $\delta^{11}\text{B}$  values of altered rocks up to  $+23.2 \pm 0.1 \text{ ‰}$  at Snowcap and  $+17.4 \pm 0.1 \text{ ‰}$  at Brothers volcano point to extensive high-temperature fluid-rock interaction with a seawater-derived fluid (**Figure 5.5-3A**, previous subchapter). The significant positive correlation ( $R^2=0.6$ ,  $p \ll 0.05$ ) between Sr isotopes that are mainly controlled by w/r-ratios (**Chapter 5.6.2.2**) and  $\delta^{11}\text{B}$  values suggest that w/r-ratios may also strongly control B isotope signatures (**Figure 5.5-3B**). To test the impact of various w/r-ratios on the B contents and  $\delta^{11}\text{B}$  values of altered rocks for different temperatures, we modified a model calculation that was established by Yamaoka *et al.* (2015) to estimate the change in altered rock composition with increasing reaction progress (**Figure 5.6-2**). The calculation is based on reaction of multiple batches of fluids in equilibrium with a progressively altered rock portion by assuming closed system conditions. The changing B concentration of the altered rock ( $C_R$ ) can be calculated by using the following mass balance, assuming a distribution coefficient between rock and fluid B concentrations ( $C_F$ ) of  $D_B$  that is defined as  $D_B = C_R/C_F$ :

$$C_R + (W/R)C_F = C_R^i + (W/R)C_F^i \quad (\text{Eq.5.6-2})$$

where  $C_R^i$  is the B concentration of the fresh rock (20.0  $\mu\text{g/g}$ , average B concentration of fresh rocks from Brothers volcano and Snowcap),  $C_F^i$  is the B concentration of seawater (4.5  $\mu\text{g/g}$ ), and  $W/R$  depicts the w/r-ratio. The  $D_B$  values were chosen as 0.5 for 150 °C, 0.15 for 250 °C, and 0.05 for 350 °C, based on Yamaoka *et al.* (2012). The changing B isotope ratio of the altered rock ( $^{11/10}B_R$ ) is based on a mass balance assuming a B isotopic fractionation factor,  $\alpha$ -, between the B isotope ratio of the rock and fluid ( $^{11/10}B_F$ ) that is defined as  $\alpha = ^{11/10}B_R / ^{11/10}B_F$ :

$$\begin{aligned} & [C_R^{11/10}B_R + \left(\frac{W}{R}\right)C_F^{11/10}B_F] / [C_R + (W/R)C_F] \\ & = \left[ C_R^{i\frac{11}{10}}B_R + \left(\frac{W}{R}\right)C_F^{i\frac{11}{10}}B_F \right] / [C_F^i + \left(\frac{W}{R}\right)C_F^i] \end{aligned} \quad (\text{Eq.5.6-3})$$

where  $^{11/10}B_R^i$  is the B isotope ratio of the fresh rock (+5.8 ‰, deduced from the average  $\delta^{11}\text{B}$  value of fresh rocks from Brothers volcano and Snowcap), and  $^{11/10}B_F^i$  is the B isotope ratio of seawater (+39.6 ‰, Foster *et al.*, 2010). The  $\alpha$  values for different temperature conditions (0.979 for 150 °C, 0.984 for 250 °C, 0.987 for 350 °C) were calculated based on the empirical investigations of mineral-fluid B isotope fraction compiled by Wunder *et al.* (2005).

The results of the model calculations show that increased  $\delta^{11}\text{B}$  values of altered rocks are either caused by higher w/r-ratios or increased alteration temperatures (**Figure 5.6-2**). These results further demonstrate that alteration temperatures as low as 150 °C are insufficient to explain the extensive leaching of B from the unaltered rock measured at Brothers volcano and Snowcap (**Figure 5.6-2A**). This is in accordance with estimated alteration temperatures of the seawater dominated alteration ( $\leq 250$  °C) and the advanced argillic alteration potentially influenced by magma degassing (230-350 °C), constrained based on secondary minerals at Brothers volcano (de Ronde *et al.*, 2019d) and  $\delta^{18}\text{O}$  of clay minerals at Snowcap (Lackschewitz *et al.*, 2004). Measured  $\delta^{11}\text{B}$  values that are close to or lower than fresh rock values point to low w/r-ratios of  $<3$  at 350 °C, and  $<5$  at 250 °C (**Figure 5.6-2B,C**), similar to the lower range of w/r-ratios calculated by  $^{87}\text{Sr}/^{86}\text{Sr}$  (**Chapter 5.6.2.2**). At Brothers volcano, lower  $\delta^{11}\text{B}$  were found for the upper part of Site U1527, the lower part of Site U1528 and several intervals of Site U1530, with Site U1530 generally showing the highest variability in  $\delta^{11}\text{B}$  (**Figure 5.5-2**). At Snowcap, the nine measured  $\delta^{11}\text{B}$  values of altered rocks span a whole range from lower than fresh values up to a maximum value of  $+23.2 \pm 0.1$  ‰ for a magnetite and corrensite-rich layer at ca. 150 to 190 mbsf (**Figure 5.5-1**), potentially caused by higher w/r-ratios or increased alteration temperatures. Moderate to significantly increased  $\delta^{11}\text{B}$  values that point to w/r-ratios of  $>5$  and up to 50 (depending on estimated temperatures), were detected in rocks of the deformed zone in deeper levels of Site U1527, in the top section of Site U1528 and in various zones of Site U1530 (**Figure 5.5-2**).

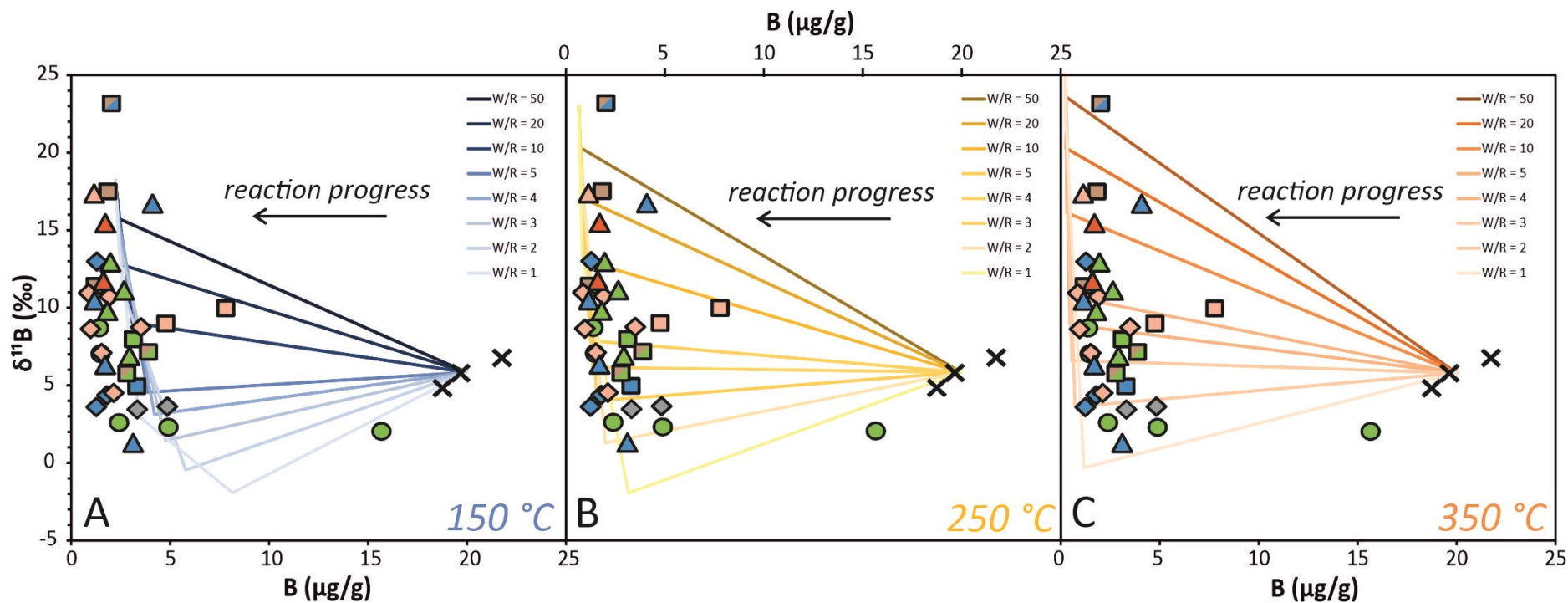


**Figure 5.6-2:** Model calculations adapted from Yamaoka et al. (2015) that predicts the B contents and isotopic compositions of progressively altered crust for w/r-ratios in a range from 1 to 50, using the average fresh rock composition of Brothers volcano and Snowcap (20.0  $\mu\text{g/g}$  and +5.8 ‰) and unaltered bottom seawater (4.5  $\mu\text{g/g}$  and +39.6 ‰) as starting materials (for further details, see **Chapter 5.6.2.3**). Overlying, the fresh and altered rock B and  $\delta^{11}\text{B}$  compositions of Brothers volcano and Snowcap are shown with the same symbols as in **Figure 5.5-3**. (A) for 150 °C ( $D_B=0.5$ ,  $\alpha=0.979$ ), (B) for 250 °C ( $D_B=0.15$ ,  $\alpha=0.984$ ), (C) for 350 °C ( $D_B=0.05$ ,  $\alpha=0.987$ ).

Limitations of w/r-ratio constraints based on the model calculations are: (1) inappropriate temperature assumptions could lead to an underestimation of w/r-ratios, (2) modification of the interacting fluid  $\delta^{11}\text{B}$  towards lower values than seawater along the reaction pathway are not regarded by the model but would also cause underestimation of w/r-ratios, and (3) we did not consider potential variations of the  $D_{\text{B}}$  and  $\alpha$  values for different alteration minerals that would also affect  $\delta^{11}\text{B}$  altered rock values. Summarized, estimated w/r-ratios based on  $\delta^{11}\text{B}$  compositions have to be assumed as minimal values because the model tends to underestimate the effective w/r-ratios based on the made assumptions. It should also be realized that w/r-ratios computed on the basis of isotopic mass balances do not represent physical ratios of water and rock (instantaneous or time-integrated) in the system. Nevertheless, the w/r-ratio sensitivity interlinked with a temperature dependency of B distribution and  $\delta^{11}\text{B}$  fractionation makes it a useful complement to other traces for w/r-ratio variations, like Sr isotopes. Furthermore, in terms of the typical occurring mineral phases in seafloor hydrothermal systems (clay minerals, sulfides, and sulfates), B is predominantly hosted in clay minerals that show similar B isotopic fractionation factors (Wunder *et al.*, 2005) and mineralogical effects on w/r-ratio calculations can therefore be estimated to be of minor importance.

#### 5.6.2.4. *Oxygen isotopes and temperature constraints*

The in-situ  $\delta^{18}\text{O}$  composition of quartz separates from Hole U1530A at the NW Caldera site of Brothers volcano were used to make constraints of shifts in alteration temperatures with depth and over time. The stockwork zone that occurs at shallower depth (seafloor to 31.28 mbsf) of Hole U1530A, displays uniform and relatively low alteration temperatures (278 to 315 °C) based on the  $\delta^{18}\text{O}$  data of the quartz separates most likely due to extensive entrainment of unmodified seawater close to the surface (**Figure 5.6-1**, **Figure 5.6-3**). Fluctuating proportions of low-T seawater ingress and pulses of increased hydrothermal activity and high-T fluid up flow led to a high variability in alteration temperatures (269 to 425 °C) in the chlorite-altered lava flow underlying the stockwork zone but with an overall tendency towards higher temperatures. Following this trend, quartz separates from a dominantly chlorite replaced lava flow at deeper portions of Hole U1530A point to relatively high and in this case uniform alteration temperatures (334 to 400 °C) compared to highly variable but lower temperatures (262 to 353 °C) in the volcanoclastic zones above and below. This relation points to high permeability contrasts between the more coherent lava flows and surrounding volcanoclastic rocks that led to increased alteration temperatures in the less permeable lava flows compared to lower alteration temperatures in the volcanoclastics of higher permeability (**Figure 5.6-3**). Indeed, a change in  $\delta^{18}\text{O}$  values from the interior towards the rim of quartz separates from deeper levels of Hole U1530A (**Figure 5.6-1**) indicate a shift from lower (minimum 262 °C) towards higher (maximum 380 °C) alteration temperatures over time. The evolution from lower to higher alteration temperatures can either be explained by sealing of the crust by newly formed minerals that led to a decrease in w/r-ratios or potentially by pulses of higher-T fluids that affected these zones in later stages of alteration.

### 5.6.3. Implications for subsurface processes in hydrothermal systems

The previous discussion chapters elucidated that w/r-ratios (or the time-integrated fluid flux they are a rough gauge of) are a leading factor controlling the Sr (**Chapter 5.6.2.2**) and B isotopic composition (**Chapter 5.6.2.3**) of altered crust, in which B isotopes are also affected by changing temperatures and Sr isotopes are affected if anhydrite is a major Sr host of the secondary mineral assemblage. Oxygen isotope data on quartz separates pointed to significant variance in alteration temperatures with depth at Hole U1530A of Brothers volcano and also indicated changes in reaction temperatures over time at deeper depth intervals. In the following chapter, we combine the implications of Sr, B and O isotope data to make constraints on w/r-ratios and temperatures with depth and potential reasons for variations.

For Brothers volcano, the Sr and B isotopic compositions of altered rocks with depth at the Upper Cone (Site U1528) both show increased values in the top sections (< 70 mbsf) and a sharp decrease at deeper crustal levels (**Figure 5.5-2**). This points to an evolution from more fluid-dominated to more rock-dominated alteration conditions with depth (**Figure 5.6-3**). Temperature variations appear to have a minor effect on B isotopic compositions of the altered rocks at the Upper Cone site. The drill-core from the rim of the NW Caldera displays overall relatively low w/r-ratios. However, a plastically deformed zone at 220.98 to 226.49 mbsf (**Figure 5.3-1B**) exhibits increased  $\delta^{11}\text{B}$  values but no variations in  $^{87}\text{Sr}/^{86}\text{Sr}$  ratios compared to the rest of the rock column. This may be indicative of increased alteration temperatures under low w/r-ratios. The basement at the slope at the NW Caldera (Site U1530) shows high variability in Sr and B isotopic compositions, in which Sr isotopes at Site U1530 are potentially modified by precipitation and dissolution of anhydrite that is bearing a significant amount of the whole rock Sr based on highly variable Sr concentrations of whole rocks (**Chapter 5.6.2.2, Table 5.3-2**). Noticeable are the shifts towards higher  $\delta^{11}\text{B}$  values just below alteration type boundaries at 65.30 and 191.38 mbsf, while the  $\delta^{11}\text{B}$  values in between show a significant decrease at Site U1530 (**Figure 5.5-2D**). A suggestion is that the rapid shifts in  $\delta^{11}\text{B}$  compositions are the result of changing w/r-ratios due to permeability contrasts between massive lava flows that could serve like a sealing cap that leads to increased w/r-ratios in the underlying volcanoclastic material (**Figure 5.6-3**). This assumption is supported by temperature constraints based on  $\delta^{18}\text{O}$  data of quartz separates that indicated increased alteration temperatures within a lava flow at 290.86 to 290.88 mbsf compared to the over- and underlying volcanoclastic rocks (**Figure 5.6-1**). In deeper parts of the basement at the NW Caldera the  $\delta^{18}\text{O}$  data further point to an increase in alteration temperatures over time. This increase in temperature may be explained by sealing of the crust by precipitation of secondary minerals that led to a more channelized fluid flow along fractures (e.g. Dobson *et al.*, 2003, Heap *et al.*, 2017) or by pulses of increased hydrothermal activity that caused ingress of higher temperature fluids. Overall, Site U1530 experienced a complex alteration history as already indicated by the occurrence of seawater- as well as magmatic fluid-influenced alteration within the core, influenced by multiple stages of alteration

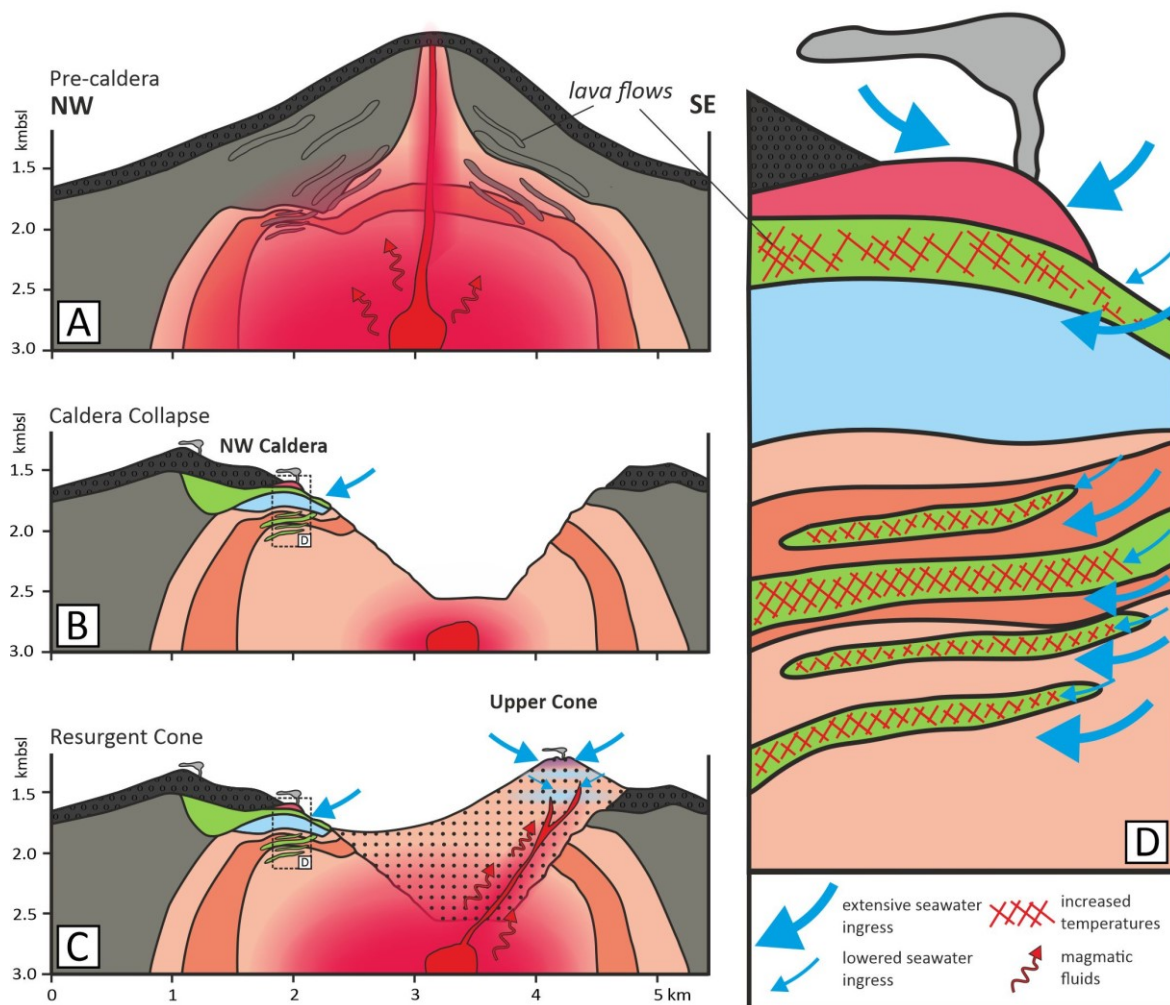


**Figure 5.6-3:** Alteration evolution at Brothers volcano. Alteration types are the same as in **Figure 5.5-2**. The formation steps from (A) Pre-caldera, over (B) Caldera collapse to (C) resurgent cone were adapted from de Ronde et al. (2019d) established based on observations of the IODP Expedition 376 drill cores (de Ronde et al., 2019e). In the pre-caldera stage (A), the dacitic basement was replaced by an advanced argillic alteration assemblage, in which more coherent lava flows were not affected by alteration. After collapse of the caldera (B and C), an increased seawater ingress was initiated and replacement by a chlorite- and/or illite-rich secondary mineral assemblage occurred (also of the more coherent lava flows). A more detailed section of Hole UI530A at the NW Caldera Site (D) shows that the more coherent lava-flows act as permeability barriers and exhibit low extents of seawater ingress and increased alteration temperatures (up to 425 °C) compared to the surrounding volcanoclastics that experienced increased seawater ingress and lower alteration temperatures (262 to 353 °C). Indeed in deeper zones, temperatures increased over time either due to sealing of veins and fractures by newly formed minerals or onset of increased hydrothermal activity over time. At the Upper Cone site (C), increased seawater ingress occurs at the topmost part that decreases with depth.

and influenced by diverse alteration factors (e.g. reaction temperatures and w/r-ratios).

For Snowcap (Site 1188), the higher retention of B concentrations of the altered rocks directly under the dacitic cap points to more channelized fluid flow and following lesser overall alteration extents (**Figure 5.5-1**, Roberts et al., 2003); the  $\delta^{11}\text{B}$  values indicate moderate w/r-ratios of 5 to 10

(**Figure 5.6-2**). The by far highest  $\delta^{11}\text{B}$  compositions were measured for a magnetite- and corrensite-rich layer between 160 and 190 mbsf, potentially caused by high w/r-ratios up to 50 or an increase in alteration temperatures. An increase in alteration temperatures of the respective depth interval is unlikely as  $\delta^{18}\text{O}$  measurements of clay minerals (Lackschewitz *et al.*, 2004) point to a lower alteration temperature than above and below. Reconstructions of volcanic facies at Snowcap (Paulick & Herzig, 2003; Paulick *et al.*, 2004; Paulick & Bach, 2006) showed that the basement exhibits distinct boundaries between more coherent volcanic lavas and primary as well as re-sedimented hyaloclastites, most likely also accompanied by distinct differences in permeability (**Figure 5.6-4**). Following, the high  $\delta^{11}\text{B}$  values of the magnetite- and corrensite-rich layer between 160 and 190 mbsf at Snowcap may best be explained by alteration under increased w/r-ratios close to permeability barriers represented by overlying more coherent lava flows, similar as it was observed at the NW Caldera of Brothers volcano (**Figure 5.6-3**, **Figure 5.6-4**). Indeed, it has to be regarded that this interpretation is in discord to Sr isotope data of clay minerals from Snowcap (Lackschewitz *et al.*, 2004) that showed the lowest measured  $^{87}\text{Sr}/^{86}\text{Sr}$  values of the whole drill-site

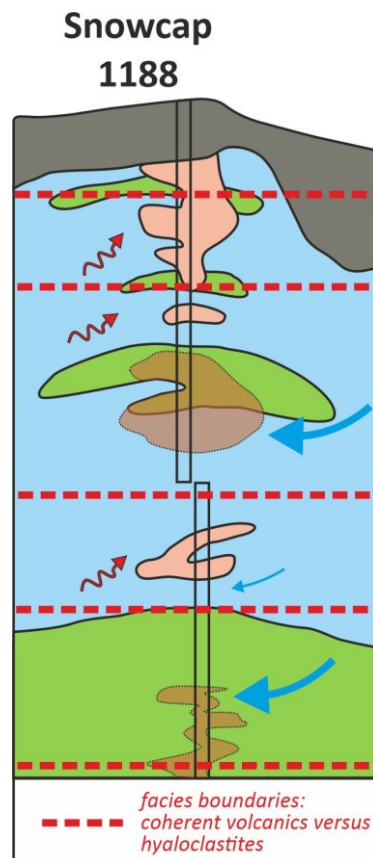


**Figure 5.6-4:** Alteration characteristics at Snowcap, Manus Basin. Alteration types are the same as in **Figure 5.5-1**; symbols of fluid ingress are the same as in **Figure 5.6-3**. The red dashed horizontal lines show facies boundaries between coherent volcanics versus hyaloclastites (primary or re-sedimented) published in Paulick & Bach (2006) based on reconstructions by Paulick *et al.* (2004) and Paulick & Herzig (2003). An increase in fluid ingress in the magnetite-rich zones (brown) is assumed based on increase  $\delta^{11}\text{B}$  values in those zones.

for the magnetite- and corrensite-rich layers and following point to relatively low w/r-ratios but may be modified due to precipitation of other secondary phases (e.g. sulfates) of shifted Sr isotopic compositions relative to the whole rocks.

### **5.7. Conclusions**

Seafloor hydrothermal systems host significant amounts of economical relevant base metals, in which systems at divergent plate boundaries often host especially large and Au-rich deposits comparable to porphyry-type and epithermal ore deposits on-land. Characterization of subsurface process in hydrothermal systems are therefore of major interest. In this study, we investigated the applicability of B, Sr and Li concentrations and isotopes of altered rocks and O isotopes on quartz separates as tracers for w/r-ratios, temperatures, secondary mineralogy and different fluid sources. The results indicate that the combination of Sr, B and O isotope systematics is a useful approach to investigate variations in w/r-ratios and temperatures of seafloor hydrothermal systems with depth. The Li isotopic compositions of altered crust in contrast did not display a simple relationship relative to secondary mineralogy, w/r-ratios or temperatures and are most likely influenced by all of them to a certain extent. A difference in B, Sr, and Li isotopic composition between seawater- and advanced argillic-dominated alteration was not recognized.

For Brothers volcano, our investigations suggest a strong control of w/r-ratios at the rim of the NW Caldera (Site U1527) and at the Upper Cone (Site U1528) and furthermore an evolution from a more rock to a more fluid dominated system with increasing depth at the Upper Cone. A plastically deformed zone at deeper levels of Site U1527 seems to be influenced by a higher-temperature alteration. Site U1530 at the NW Caldera indicates dependence on permeability contrasts between more coherent lava flows and more permeable volcanoclastic rocks but also exhibits a complicated alteration history of several stages of hydrothermal activity that led to advanced argillic alteration in early stages of alteration followed by a heated seawater-derived alteration by chlorite and illite in later stages. For Snowcap, most noticeable is the increased  $\delta^{11}\text{B}$  value of an oxide-rich layer between 160 and 190 mbsf that may be caused by rock alteration under increased w/r ratios, close to volcanic facies boundaries also accompanied by differences in permeability. Summarized, the data underline the high impact of permeability contrasts on fluid pathways and changes in alteration temperatures.

### **Acknowledgements**

The authors thank the shipboard participants of ODP Expedition 193, IODP Expedition 376 and of SO-216 and SO-253, including the crews and pilots of *MARUM QUEST*. We also thank P. Brandl, M. Portnyagin, D. Garbe-Schönberg, and F. Hauff for providing the rock powders and performing the Sr concentration measurements of the two unaltered drill-core samples from Brothers volcano.

Further, we thank J. Valley for support conducting the oxygen isotope measurements. This research was funded by the GIF Grant I-1357-301.8/2016.

## References

- Albarède F., Michard A., Minster J. F. and Michard G. (1981)  $^{87}\text{Sr}/^{86}\text{Sr}$  ratios in hydrothermal waters and deposits from the East Pacific Rise at  $21^\circ\text{N}$ . *Earth Planet. Sci. Lett.* **55**, 229–236.
- Audétat A. (2019) The Metal Content of Magmatic-Hydrothermal Fluids and Its Relationship to Mineralization Potential. *Econ. Geol.* **114**, 1033–1056.
- Bach W., Peucker-Ehrenbrink B., Hart S. R. and Blusztajn J. S. (2003) Geochemistry of hydrothermally altered oceanic crust. *Geochem. Geophys. Geosyst.* **4**, 119.
- Ballance P. F., Ablaev A. G., Pushchin I. K., Pletnev S. P., Biryulina M. G., Itaya T., Follas H. A. and Gibson G. W. (1999) Morphology and history of the Kermadec trench–arc–backarc basin–remnant arc system at  $30$  to  $32^\circ\text{S}$ . *Mar. Geol.* **159**, 35–62.
- Beier C., Bach W., Turner S., Niedermeier D., Woodhead J., Erzinger J. and Krumm S. (2015) Origin of Silicic Magmas at Spreading Centres—an Example from the South East Rift, Manus Basin. *J. Petrol.* **56**, 255–272.
- Berger G., Schott J. and Guy C. (1988) Behavior of Li, Rb and Cs during basalt glass and olivine dissolution and chlorite, smectite and zeolite precipitation from seawater. *Chem. Geol.* **71**, 297–312.
- Berndt M. E., Seyfried W. E. and Beck J. W. (1988) Hydrothermal alteration processes at mid-ocean ridges. *J. Geophys. Res.* **93**, 4573–4583.
- Brant C., Coogan L. A., Gillis K. M., Seyfried W. E., Pester N. J. and Spence J. (2012) Lithium and Li isotopes in young altered upper oceanic crust from the East Pacific Rise. *Geochim. Cosmochim. Acta* **96**, 272–293.
- Brens R., Liu X.-M., Turner S. and Rushmer T. (2019) Lithium isotope variations in Tonga-Kermadec arc-Lau back-arc lavas and Deep Sea Drilling Project (DSDP) Site 204 sediments. *Island Arc* **28**, e12276.
- Caratori Tontini F., Davy B., de Ronde C. E. J., Embley R. W., Leybourne M. and Tivey M. A. (2012) Crustal Magnetization of Brothers Volcano, New Zealand, Measured by Autonomous Underwater Vehicles. *Econ. Geol.* **107**, 1571–1581.
- de Ronde C. E. J., Hannington M. D., Stoffers P., Wright I. C., Ditchburn R. G., Reyes A. G., Baker E. T., Massoth G. J., Lupton J. E., Walker S. L., Greene R. R., Soong C. W. R., Ishibashi J., Lebon G. T., Bray C. J. and Resing J. A. (2005) Evolution of a Submarine Magmatic-Hydrothermal System. *Econ. Geol.* **100**, 1097–1133.
- de Ronde C. E. J., Humphris S. E., Höfig T. W., Brandl P. A., Cai L., Cai Y., Caratori Tontini F., Deans J. R., Farough A., Jamieson J. W., Kolandaivelu K. P., Kutovaya A., Labonté J. M., Martin A. J., Massiot C., McDermott J. M., McIntosh I. M., Nozaki T., Pellizari V. H., Reyes A. G., Roberts S., Rouxel O., Schlicht L. E. M., Seo J. H., Straub S. M., Strehlow K., Takai K., Tanner D., Tepley III F. J. and Zhang C. (2019a) Expedition 376 summary. In *Proc. Int. Ocean Disc. Progr. Vol 376* (eds. C. E. J. de Ronde, S. E. Humphris, T. W. Höfig and the Expedition 376 Scientists). College Station, TX.
- de Ronde C. E. J., Humphris S. E., Höfig T. W., Brandl P. A., Cai L., Cai Y., Caratori Tontini F., Deans J. R., Farough A., Jamieson J. W., Kolandaivelu K. P., Kutovaya A., Labonté J. M., Martin A. J., Massiot C., McDermott J. M., McIntosh I. M., Nozaki T., Pellizari V. H., Reyes A. G., Roberts S., Rouxel O., Schlicht L. E. M., Seo J. H., Straub S. M., Strehlow K., Takai K., Tanner D., Tepley III F. J. and Zhang C. (2019b) Site U1528. In *Proc. Int. Ocean Disc. Progr. Vol 376* (eds. C. E. J. de Ronde, S. E. Humphris, T. W. Höfig and the Expedition 376 Scientists). College Station, TX.
- de Ronde C. E. J., Humphris S. E., Höfig T. W., Brandl P. A., Cai L., Cai Y., Caratori Tontini F., Deans J. R., Farough A., Jamieson J. W., Kolandaivelu K. P., Kutovaya A., Labonté J. M., Martin A. J., Massiot C., McDermott J. M., McIntosh I. M., Nozaki T., Pellizari V. H., Reyes A. G., Roberts S., Rouxel O., Schlicht L.

- E. M., Seo J. H., Straub S. M., Strehlow K., Takai K., Tanner D., Tepley III F. J. and Zhang C. (2019c) Site U1530. In *Proc. Int. Ocean Disc. Progr. Vol 376* (eds. C. E. J. de Ronde, S. E. Humphris, T. W. Höfig and the Expedition 376 Scientists). College Station, TX.
- de Ronde C. E. J., Humphris S. E., Höfig T. W., Reyes A. G. and the IODP Expedition 376 Scientists (2019d) Critical role of caldera collapse in the formation of seafloor mineralization. *Geology* **47**, 762–766.
- de Ronde C. E. J., Humphris S. E., Höfig T. W. and the Expedition 376 Scientists (eds.) (2019e) *Proc. Int. Ocean Disc. Progr. Vol 376*, College Station, TX.
- de Ronde C. E. J., Massoth G. J., Butterfield D. A., Christenson B. W., Ishibashi J., Ditchburn R. G., Hannington M. D., Brathwaite R. L., Lupton J. E., Kamenetsky V. S., Graham I. J., Zellmer G. F., Dziak R. P., Embley R. W., Dekov V. M., Munnik F., Lahr J., Evans L. J. and Takai K. (2011) Submarine hydrothermal activity and gold-rich mineralization at Brothers Volcano, Kermadec Arc, New Zealand. *Miner. Deposita* **46**, 541–584.
- Deniel C. and Pin C. (2001) Single-stage method for the simultaneous isolation of lead and strontium from silicate samples for isotopic measurements. *Anal. Chim. Acta* **426**, 95–103.
- Diehl A. (2019) Causes for variable hydrothermal vent fluid compositions in intraoceanic arcs - Insights from fluid compositions and mineral precipitates of the South Kermadec Arc. dissertation, University of Bremen.
- Dobson P. F., Kneafsey T. J., Hulen J. and Simmons A. (2003) Porosity, permeability, and fluid flow in the Yellowstone geothermal system, Wyoming. *J. Volcanol. Geotherm. Res.* **123**, 313–324.
- Edmond J. M., Measures C., McDuff R. E., Chan L. H., Collier R., Grant B., Gordon L. I. and Corliss J. B. (1979) Ridge crest hydrothermal activity and the balances of the major and minor elements in the ocean. *Earth Planet. Sci. Lett.* **46**, 1–18.
- Embley R. W., Ronde C. E. J. de, Merle S. G., Davy B. and Tontini F. C. (2012) Detailed Morphology and Structure of an Active Submarine Arc Caldera. *Econ. Geol.* **107**, 1557–1570.
- Foster G. L., Pogge von Strandmann P. A. E. and Rae J. W. B. (2010) Boron and magnesium isotopic composition of seawater. *Geochem. Geophys. Geosyst.* **11**.
- Foustoukos D. I. and Seyfried W. E. (2007) Fluid Phase Separation Processes in Submarine Hydrothermal Systems. *Rev. Mineral. Geochem.* **65**, 213–239.
- Gamo T., Okamura K., Charlou J.-L., Urabe T., Auzende J.-M., Ishibashi J., Shitashima K., Chiba H. and Cruise S. S. P. o. t. M. (1997) Acidic and sulfate-rich hydrothermal fluids from the Manus back-arc basin, Papua New Guinea. *Geology* **25**, 139–142.
- Gillis K. M., Ludden J. N. and Smith A. D. (1992) Mobilization of REE during crustal aging in the Troodos Ophiolite, Cyprus. *Chem. Geol.* **98**, 71–86.
- Haase K. M., Stroncik N., Garbe-Schönberg D. and Stoffers P. (2006) Formation of island arc dacite magmas by extreme crystal fractionation. *J. Volcanol. Geotherm. Res.* **152**, 316–330.
- Haase K. M., Worthington T. J., Stoffers P., Garbe-Schönberg D. and Wright I. (2002) Mantle dynamics, element recycling, and magma genesis beneath the Kermadec Arc-Havre Trough. *Geochem. Geophys. Geosyst.* **3**, 1–22.
- Hansen C. T., Meixner A., Kasemann S. A. and Bach W. (2017) New insight on Li and B isotope fractionation during serpentinization derived from batch reaction investigations. *Geochim. Cosmochim. Acta* **217**, 51–79.
- Heap M. J., Kennedy B. M., Farquharson J. I., Ashworth J., Mayer K., Letham-Brake M., Reuschlé T., Gilg H. A., Scheu B., Lavallée Y., Siratovich P., Cole J., Jolly A. D., Baud P. and Dingwell D. B. (2017) A multidisciplinary approach to quantify the permeability of the Whakaari/White Island volcanic hydrothermal system (Taupo Volcanic Zone, New Zealand). *J. Volcanol. Geotherm. Res.* **332**, 88–108.
- Heck P. R., Huberty J. M., Kita N. T., Ushikubo T., Kozdon R. and Valley J. W. (2011) SIMS analyses of silicon and oxygen isotope ratios for quartz from Archean and Paleoproterozoic banded iron formations. *Geochim. Cosmochim. Acta* **75**, 5879–5891.

- Hodell D. A., Mead G. A. and Mueller P. A. (1990) Variation in the strontium isotopic composition of seawater (8 Ma to present). *Chem. Geol.* **80**, 291–307.
- Honnorez J. J., Alt J. C. and Humphris S. E. (1998) Vivisection and autopsy of active and fossil hydrothermal alterations of basalt beneath and within the TAG hydrothermal mound. In *Proc. Ocean Drill. Progr. Sci. Res., Vol. 158* (eds. P. M. Herzig, S. E. Humphris, D. J. Miller and R. A. Zierenberg), pp. 231–254.
- Hoog J. C. de and Savov I. P. (2018) Boron Isotopes as a Tracer of Subduction Zone Processes. In *Boron Isotopes* (eds. H. Marschall and G. Foster), pp. 217–247.
- James R. H., Allen D. E. and Seyfried W. E. (2003) An experimental study of alteration of oceanic crust and terrigenous sediments at moderate temperatures (51 to 350°C). *Geochim. Cosmochim. Acta* **67**, 681–691.
- Kawahata H., Nohara M., Ishizuka H., Hasebe S. and Chiba H. (2001) Sr isotope geochemistry and hydrothermal alteration of the Oman ophiolite. *J. Geophys. Res.* **106**, 11083–11099.
- Kelly J. L., Fu B., Kita N. T. and Valley J. W. (2007) Optically continuous silcrete quartz cements of the St. Peter Sandstone. *Geochim. Cosmochim. Acta* **71**, 3812–3832.
- Lackschewitz K. S., Asada R. and Paulick H. Data Report: Summary of revised alteration phases for PACMANUS hydrothermal field - X-Ray Diffraction Analyses of altered felsic volcanic rocks from Holes 1188A, 1188F, 1189A, and 1189B. In *Proc. Ocean Drill. Progr. Sci. Res.* (eds. F. J. A. S. Barriga, R. A. Binns, D. J. Miller and P. M. Herzig).
- Lackschewitz K. S., Devey C. W., Stoffers P., Botz R., Eisenhauer A., Kummert M., Schmidt M. and Singer A. (2004) Mineralogical, geochemical and isotopic characteristics of hydrothermal alteration processes in the active, submarine, felsic-hosted PACMANUS field, Manus Basin, Papua New Guinea. *Geochim. Cosmochim. Acta* **68**, 4405–4427.
- Leeman W. P., Tonarini S. and Turner S. (2017) Boron isotope variations in Tonga-Kermadec-New Zealand arc lavas. *Geochem. Geophys. Geosyst.* **18**, 1126–1162.
- Marks N., Zierenberg R. A. and Schiffman P. (2015) Strontium and oxygen isotopic profiles through 3 km of hydrothermally altered oceanic crust in the Reykjanes Geothermal System, Iceland. *Chem. Geol.* **412**, 34–47.
- Marschall H. (2018) Boron Isotopes in the Ocean Floor Realm and the Mantle. In *Boron Isotopes* (eds. H. Marschall and G. Foster), pp. 189–215.
- Marschall H. R., Wanless V. D., Shimizu N., Pogge von Strandmann P. A., Elliott T. and Monteleone B. D. (2017) The boron and lithium isotopic composition of mid-ocean ridge basalts and the mantle. *Geochim. Cosmochim. Acta* **207**, 102–138.
- Martinez F. and Taylor B. (1996) Backarc spreading, rifting, and microplate rotation, between transform faults in the Manus Basin. *Mar. Geophys. Res.* **18**, 203–224.
- McCulloch M. T. and Gamble J. A. (1991) Geochemical and geodynamical constraints on subduction zone magmatism. *Earth Planet. Sci. Lett.* **102**, 358–374.
- McCulloch M. T., Gregory R. T., Wasserburg G. J. and Taylor Jr. H. P. (1980) A neodymium, strontium, and oxygen isotopic study of the Cretaceous Smail ophiolite and implications for the petrogenesis and seawater-hydrothermal alteration of oceanic crust. *Earth Planet. Sci. Lett.* **46**, 201–211.
- Moriguti T. and Nakamura E. (1998) High-yield lithium separation and the precise isotopic analysis for natural rock and aqueous samples. *Chem. Geol.* **145**, 91–104.
- Park S.-H., Lee S.-M., Kamenov G. D., Kwon S.-T. and Lee K.-Y. (2010) Tracing the origin of subduction components beneath the South East rift in the Manus Basin, Papua New Guinea. *Chem. Geol.* **269**, 339–349.
- Paulick H. and Bach W. (2006) Phyllosilicate Alteration Mineral Assemblages in the Active Subsea-Floor Pacmanus Hydrothermal System, Papua New Guinea, ODP Leg 193. *Econ. Geol.* **101**, 633–650.
- Paulick H. and Herzig P. M. (2003) Volcanic facies controls on mass transfer at the active, dacite-hosted Pacmanus hydrothermal system, Manus basin, Papua New Guinea (Ocean Drilling Program Leg 193). In

- Mineral exploration and sustainable development* (eds. G. D. Eliopoulos and et al.). Millpress. Rotterdam, pp. 167–170.
- Paulick H., Herzig P. M. and Hoernes S. Data Report: A comprehensive geochemical, mineralogical, and isotopic data set of variably altered dacitic volcanic rocks from the subsurface of the PACMANUS hydrothermal field (ODP Leg 193). In *Proc. Ocean Drill. Prog. Sci. Res.* (eds. F. J. A. S. Barriga, R. A. Binns, D. J. Miller and P. M. Herzig).
- Paulick H., Vanko D. A. and Yeats C. J. (2004) Drill core-based facies reconstruction of a deep-marine felsic volcano hosting an active hydrothermal system (Pual Ridge, Papua New Guinea, ODP Leg 193). *J. Volcanol. Geotherm. Res.* **130**, 31–50.
- Penniston-Dorland S., Liu X.-M. and Rudnick R. L. (2017) Lithium Isotope Geochemistry. In *Advances in Lithium Isotope Geochemistry* (eds. P. B. Tomascak, T. Magna and R. Dohmen), pp. 165–217.
- Reeves E. P., Seewald J. S., Saccocia P., Bach W., Craddock P. R., Shanks W. C., Sylva S. P., Walsh E., Pichler T. and Rosner M. (2011) Geochemistry of hydrothermal fluids from the PACMANUS, Northeast Pual and Vienna Woods hydrothermal fields, Manus Basin, Papua New Guinea. *Geochim. Cosmochim. Acta* **75**, 1088–1123.
- Roberts S., Bach W., Binns R. A., Vanko D. A., Yeats C. J., Teagle D., Blacklock K., Blusztajn J. S., Boyce A. J., Cooper M. J., Holland N. and McDonald B. (2003) Contrasting evolution of hydrothermal fluids in the PACMANUS system, Manus Basin. *Geology* **31**, 805.
- Romer R. L., Meixner A. and Hahne K. (2014) Lithium and boron isotopic composition of sedimentary rocks — The role of source history and depositional environment. *Gondwana Res.* **26**, 1093–1110.
- Seewald J. S., Reeves E. P., Bach W., Saccocia P. J., Craddock P. R., Shanks W. C., Sylva S. P., Pichler T., Rosner M. and Walsh E. (2015) Submarine venting of magmatic volatiles in the Eastern Manus Basin, Papua New Guinea. *Geochim. Cosmochim. Acta* **163**, 178–199.
- Seewald J. S., Reeves E. P., Bach W., Saccocia P. J., Craddock P. R., Walsh E., Shanks W. C., Sylva S. P., Pichler T. and Rosner M. (2019) Geochemistry of hot-springs at the SuSu Knolls hydrothermal field, Eastern Manus Basin. *Geochim. Cosmochim. Acta* **255**, 25–48.
- Seyfried W. E., Janecky D. R. and Mottl M. J. (1984) Alteration of the oceanic crust. *Geochim. Cosmochim. Acta* **48**, 557–569.
- Sharp Z. and Kirschner D. (1994) Quartz-calcite oxygen isotope thermometry. *Geochim. Cosmochim. Acta* **58**, 4491–4501.
- Shipboard Scientific Party (2002) Leg 193 Summary. In *Proc. Ocean Drill. Progr. Init. Rep.* (eds. R. A. Binns, F. J. A. S. Barriga and D. J. Miller).
- Spivack A. and Edmond J. (1987) Boron isotope exchange between seawater and the oceanic crust. *Geochim. Cosmochim. Acta* **51**, 1033–1043.
- Stoiber R. E. and Rose W. I. (1974) Fumarole incrustations at active central american volcanoes. *Geochim. Cosmochim. Acta* **38**, 495–516.
- Taran Y., Hedenquist J. W., Korzhinsky M. A., Tkachenko S. I. and Shmulovich K. I. (1995) Geochemistry of magmatic gases from Kudryavy volcano, Iturup, Kuril Islands. *Geochim. Cosmochim. Acta* **59**, 1749–1761.
- Thal J., Tivey M., Yoerger D., Jöns N. and Bach W. (2014) Geologic setting of PACManus hydrothermal area — High resolution mapping and in situ observations. *Mar. Geol.* **355**, 98–114.
- Tomascak P. B., Widom E., Benton L. D., Goldstein S. L. and Ryan J. G. (2002) The control of lithium budgets in island arcs. *Earth Planet. Sci. Lett.* **196**, 227–238.
- Whitney J. A. (1975) Vapor generation on a quartz monzonite magma; a synthetic model with application to porphyry copper deposits. *Econ. Geol.* **70**, 346–358.

- Wilckens F. K., Reeves E. P., Bach W., Meixner A., Seewald J. S., Koschinsky A. and Kasemann S. A. (2018) The influence of magmatic fluids and phase separation on B systematics in submarine hydrothermal vent fluids from back-arc basins. *Geochim. Cosmochim. Acta* **232**, 140–162.
- Wilckens F. K., Reeves E. P., Bach W., Seewald J. S. and Kasemann S. A. (2019) Application of B, Mg, Li, and Sr Isotopes in Acid-Sulfate Vent Fluids and Volcanic Rocks as Tracers for Fluid-Rock Interaction in Back-Arc Hydrothermal Systems. *Geochem. Geophys. Geosyst.* **20**, 5849–5866.
- Williams-Jones A. E. and Heinrich C. A. (2005) 100<sup>th</sup> Anniversary Special Paper. *Econ. Geol.* **100**, 1287–1312.
- Wunder B., Meixner A., Romer R. L., Wirth R. and Heinrich W. (2005) The geochemical cycle of boron. *Lithos* **84**, 206–216.
- Yamaoka K., Ishikawa T., Matsubaya O., Ishiyama D., Nagaishi K., Hiroyasu Y., Chiba H. and Kawahata H. (2012) Boron and oxygen isotope systematics for a complete section of oceanic crustal rocks in the Oman ophiolite. *Geochim. Cosmochim. Acta* **84**, 543–559.
- Yamaoka K., Matsukura S., Ishikawa T. and Kawahata H. (2015) Boron isotope systematics of a fossil hydrothermal system from the Troodos ophiolite, Cyprus. *Chem. Geol.* **396**, 61–73.
- Yang K. and Scott S. D. (1996) Possible contribution of a metal-rich magmatic fluid to a sea-floor hydrothermal system. *Nature* **383**, 420–423.
- Yeats C. J., Bach W., Vanko D. A., Roberts S., Lackschewitz K. S., Paulick H. and Shipboard Scientific Party (2001) Fluid-dacite interaction in the PACMANUS subseafloor hydrothermal system preliminary results from secondary mineral chemistry and geochemical modeling (abstract no. S011A-0346). *Eos* **82**.



## CHAPTER 6:

### CONCLUSIONS AND OUTLOOK

---

Fluid-rock interaction in seafloor hydrothermal systems results in vast changes in ocean and oceanic crust chemistry, is an important ore forming process and accomplishes environments that host a variety of highly specialized life forms. The characteristics of hydrothermal fluid-rock exchange are indeed highly diverse in differing geological settings due to variations in fluid temperature and acidity, host rock and alteration phase compositions, and basement structures. The investigation of seafloor hydrothermal systems is therefore of major importance to learn more about the processes that drive changes in the mode of fluid-rock exchange and to make constraints on global geochemical budgets.

In the scope of this thesis three stand-alone manuscripts were drafted that focus on four different settings of hydrothermal activity; reaching from slow-spreading mid-ocean ridges (*Chapter 3*), over the matured ridge flanks (*Chapter 4*) to arc and back-arc environments that are closely associated with subduction zone processes (*Chapter 5*). For investigations, the stable isotope ( $\delta^{11}\text{B}$ ,  $\delta^7\text{Li}$  and  $\delta^{18}\text{O}$ ) and  $^{87}\text{Sr}/^{86}\text{Sr}$  compositions of hydrothermal fluids and fresh as well as altered rocks from the four settings were examined. The sensitivity of these four isotope systems for different aspects of fluid-rock exchange varies and following their combination enables to study exchange processes from different perspectives. Boron and Li show a mass dependent isotopic fractionation between fluids and rocks that strongly depends on temperature but also on host rock and alteration phase mineralogy;  $\delta^{11}\text{B}$  fractionation is also sensitive to fluid pH shifts and the interconnected change in fluid B speciation. Furthermore, the high diversity in B and Li elemental and isotopic compositions of interacting earth's reservoirs leads to distinct alterations in fluid and rock compositions in dependence on w/r-ratios. The  $^{87}\text{Sr}/^{86}\text{Sr}$  ratio in hydrothermal fluids and altered rocks is controlled by the  $^{87}\text{Sr}/^{86}\text{Sr}$  signatures of the source rocks and fluids in relation to the w/r-ratios but is insensitive for changing temperatures or differences in mineralogy and fluid pH due to the rather small relative mass difference of  $^{87}\text{Sr}$  and  $^{86}\text{Sr}$ . The  $\delta^{18}\text{O}$  fractionation between fluids and quartz is additionally a well-calibrated paleo-thermometer. The aim of the multi-proxy approach that was used in this thesis was to test the applicability of  $\delta^{11}\text{B}$ ,  $\delta^7\text{Li}$ ,  $\delta^{18}\text{O}$  and  $^{87}\text{Sr}/^{86}\text{Sr}$  systematics as tracers for hydrothermal fluid-rock interaction processes, to study the differing characteristics of hydrothermal activity in the four investigated settings and to make assumptions on the impact of hydrothermal discharge in these diverse settings on seawater  $\delta^{11}\text{B}$  and  $\delta^7\text{Li}$  geochemical budgets.

In the first manuscript (*Chapter 3*), we examined the B and  $\delta^{11}\text{B}$  composition of vent fluids from four ultramafic hosted systems (Logatchev, Irinovskoe, Semenov, and Ashadze) that are located between the 15°20'N and the Marathon Fracture Zones of the slow-spreading Mid-Atlantic Ridge.

The investigations of the natural fluid samples were undergirded by experimental data on B and  $\delta^{11}\text{B}$  exchange between ultramafic material and seawater-like fluids that were conducted under representative conditions for natural hydrothermal systems (100 to 300 °C, 40 MPa, Hansen *et al.*, 2017 and study in **Chapter 3**). Furthermore, careful assessments of the in-situ pH and B speciation in the experimental solutions were performed by thermodynamic modeling. From previous experiments (Seyfried & Dibble, 1980; Janecky, 1982; Janecky & Seyfried, 1986) and observations in nature (e.g. Boschi *et al.*, 2008) it was already supposed that ultramafic hosted hydrothermal systems are characterized by B partitioning towards the solid phase even at elevated temperatures (<300 °C). This is also in line with our natural fluid and experimental results. The data availability on  $\delta^{11}\text{B}$  fractionation during fluid-rock exchange in ultramafic systems is in contrast very sparse but a lowering in  $\delta^{11}\text{B}$  fractionation was supposed compared to mafic or felsic hosted systems due to the increase in fluid pH and the increase in the relative abundance of the tetrahedral B species in solution by alteration of ultramafic rocks (Foustoukos *et al.*, 2008; Hansen *et al.*, 2017). This assumption arose from that  $\delta^{11}\text{B}$  fractionation between solids and fluids occurs due to the exchange of tetrahedral and trigonal coordinated B species, hence a higher abundance of the tetrahedral B species in solution that is also the dominating B species in the interacting solid (clay minerals) should result in a decrease in  $\delta^{11}\text{B}$  fractionation (Kakihana *et al.*, 1977; Wunder *et al.*, 2005; Kowalski *et al.*, 2013). Our experimental data support a decrease in  $\delta^{11}\text{B}$  fractionation with increasing abundance of the tetrahedral species in solution. However, the absolute lowering in  $\delta^{11}\text{B}$  fractionation was significantly more extensive than previously supposed based on theoretical predictions (Kowalski *et al.*, 2013) and following more research on these systematics is necessary. In particular, experimental studies on B and  $\delta^{11}\text{B}$  exchange conducted under alkaline conditions over a wider temperature range and including a careful evaluation of the in-situ fluid pH and B speciation are needed.

The natural fluids that were collected from the ultramafic systems at the slow-spreading Mid-Atlantic Ridge indeed displayed a less fractionated, higher  $\delta^{11}\text{B}$  signature ( $+35 \pm 3 \text{ ‰}$ , **Chapter 3**) than fluids from basaltic hosted vent sites at slow-spreading ridges ( $27 \pm 7 \text{ ‰}$ , James *et al.*, 1995). However, the fluid pH of the examined ultramafic systems were rather acidic (pH 4.0 to 6.7) probably due to the high basement reaction temperatures (>340 °C) that enabled the formation of talc-tremolite in the basement and resulted in an increase of fluid pH values. Following, the less  $\delta^{11}\text{B}$  fractionated signals of the ultramafic fluids most likely reflect the very low initial B concentrations of the ultramafic rocks (<0.02  $\mu\text{g/g}$ ) and the resulting major dominance of the high  $\delta^{11}\text{B}$  composition of the interacting seawater (+39.6 ‰) and were not caused by a decrease in  $\delta^{11}\text{B}$  fractionation due to a shift in fluid pH and B speciation. Interestingly, we identified a distinct shift towards lower  $\delta^{11}\text{B}$  values of fluids in basaltic hosted systems at slow- ( $27 \pm 7 \text{ ‰}$ ) versus fast-spreading ( $33 \pm 4 \text{ ‰}$ , Spivack & Edmond, 1987; James *et al.*, 1995) ridges. We assume this discrepancy arises from the differing tectonic structures and thermal regimes at slow- compared to

fast-spreading ridges. The longer fluid pathways at the more structure controlled slow-spreading ridges hence could lead to a relative decrease in w/r-ratios and following to a lower, more rock dominated  $\delta^{11}\text{B}$  composition of the fluids.

Furthermore, we used the compilation of the new B and  $\delta^{11}\text{B}$  fluid data from the ultramafic hosted hydrothermal systems together with literature fluid data on basaltic hosted systems at slow- and fast-spreading ridges, as well as data on subduction influenced systems at convergent margins to make constraints on the total B hydrothermal mass flux and its  $\delta^{11}\text{B}$  composition. Our comparison showed that in modern oceans the total B hydrothermal mass flux corresponds to 30% of the river influx and displays a B isotopic composition of  $+29 \pm 6 \text{ ‰}$ ; all four settings of high-temperature fluid discharge accumulated. As already mentioned, basaltic hosted systems at slow- compared to fast-spreading ridges show distinctly lower  $\delta^{11}\text{B}$  values most likely due to the longer fluid pathways and lower w/r-ratios at the highly structure controlled slow-spreading ridges. This discrepancy influences the  $\delta^{11}\text{B}$  of the total B hydrothermal mass flux today but further may also have important implications for the  $\delta^{11}\text{B}$  of past B hydrothermal mass fluxes and seawater composition that is an important input parameter for ocean pH reconstructions (e.g. Foster & Rae, 2016). Several authors estimated pronounced pulses of globally rapid seafloor spreading to explain sea level high-stands and increased atmospheric  $\text{CO}_2$  productions in certain periods over the Phanerozoic (e.g. Conrad & Lithgow-Bertelloni, 2007; Seton *et al.*, 2009). If those periods of rapid seafloor spreading in the past were characterized by a less tectonic dominated regime at the ridge axes, the total B hydrothermal mass flux therefore may showed distinctly higher  $\delta^{11}\text{B}$  values than today based on our budget constraints. However, some B hydrothermal mass fluxes and  $\delta^{11}\text{B}$  are not well defined so far and need further studying by continued sampling and analyzing of fluids. In particular, B and  $\delta^{11}\text{B}$  signatures of vent fluids issuing from convergent plate margin settings, ultra-slow-spreading divergent margins and especially the impact of lower temperature hydrothermal systems of more alkaline fluid composition (e.g. Lost City) are not well constrained and need more research in prospective studies.

In the second manuscript (**Chapter 4**), we investigated the  $\delta^7\text{Li}$  and  $^{87}\text{Sr}/^{86}\text{Sr}$  compositions of discharging fluids and the  $\delta^{11}\text{B}$ ,  $\delta^7\text{Li}$  and  $^{87}\text{Sr}/^{86}\text{Sr}$  compositions of fresh and altered rocks that were collected from “Dorado Outcrop”, a low-temperature ridge flank hydrothermal system at 18.5 to 23 Ma crust of the Cocos Plate. Dorado Outcrop is believed to be the first sampled ridge flank hydrothermal system that is representative for flank systems in general, regarding discharging fluid temperatures ( $12.3^\circ\text{C}$ ), sediment cover thickness (around 500m), and the short residence time of fluids in the basement of a few years only (e.g. Fisher & Wheat, 2010). Fluid circulation in the flanks is driven by mining of lithospheric heat and occurs between recharging and discharging outcrops that are up to tens of km apart from each other, while the surrounding basement is buried by a thick sediment cover. The absolute changes in fluid compositions compared to seawater are

minimal due to the low reaction temperatures in the basement (approximately 13.2 °C) but the large water fluxes circulating through the flanks (Stein & Stein, 1994; Mottl, 2003) leading to a major impact of those systems on seawater isotopic composition of certain elements (e.g. B and Li). Regarding  $\delta^7\text{Li}$ , it has long been recognized that seawater  $\delta^7\text{Li}$  composition is not reflecting the simple weighted average of input fluxes by rivers, high-temperature hydrothermal systems and fluid expulsion at subduction zones but has to be significantly modified by additional output fluxes, like low-temperature basalt alteration and sorption to marine sediments (recently re-assessed mass balance by Misra & Froelich, 2012). The depletion in Li concentration and increase in  $\delta^7\text{Li}$  composition of the end-member fluid at Dorado Outcrop versus seawater indicated that low-temperature basalt alteration can account for 7 to 27 % of the observed shift in seawater  $\delta^7\text{Li}$  composition expected based on input flux compositions. The impact could be even higher if global ridge flank alteration temperatures are on average lower compared to Dorado Outcrop. Strontium isotopic compositions of the Dorado Outcrop fluids are not changed compared to seawater and gave no evidence for a significant impact of ridge flank hydrothermal alteration on seawater  $^{87}\text{Sr}/^{86}\text{Sr}$  composition. Discrete fluids collected at Dorado Outcrop are nevertheless the first samples that depict interaction with a “typical” ridge flank hydrothermal system. The data allow first constraints on Li output fluxes based on fluid data and on potential shifts in seawater  $\delta^7\text{Li}$  composition caused by low-temperature basalt alteration but consolidations can only come with further sampling of representative ridge flank systems.

Altered rocks collected at the surface of Dorado Outcrop showed the typical enrichment of B and Li compared to the unaltered rocks, caused by uptake of both elements by low-temperature basalt alteration. B and Li isotopic compositions are increased in the altered versus unaltered rocks due to interaction with seawater of much higher isotopic composition compared to the unaltered rocks. The  $\delta^7\text{Li}$  end-member value of the altered rocks at Dorado is nevertheless lower than previously published data on low-temperature altered rocks collected from the seafloor (Chan *et al.*, 1992). We assumed that the low  $\delta^7\text{Li}$  values of the altered rocks from Dorado Outcrop resulted from interaction with seawater at the time of formation of the outcrop (18.5 to 23 Ma) of lower  $\delta^7\text{Li}$  composition than in modern oceans (Misra & Froelich, 2012). Similar estimates were already made based on low-temperature altered crust of the Troodos Ophiolite of Cretaceous times (Coogan *et al.*, 2017). The  $\delta^{11}\text{B}$  of seawater showed minor variations over the last 20 Myr (e.g. Pearson & Palmer, 2000), and following no change in alteration phase  $\delta^{11}\text{B}$  composition is expected. If low-temperature basalt alteration products indeed reflect the seawater  $\delta^7\text{Li}$  composition at the time of their formation (and potentially also  $\delta^{11}\text{B}$  compositions, in case of fluctuation in seawater composition before 20 Ma) could be tested by systematic sampling of low-temperature altered oceanic crust of varying ages, e.g. from seamounts that reach over the surrounding sediment cover of known formation times.

In the third manuscript (*Chapter 5*), we investigated the  $\delta^{11}\text{B}$  signatures of fresh and altered rocks at the Manus back-arc basin (ODP 193) and the  $\delta^{11}\text{B}$ ,  $\delta^7\text{Li}$  and  $^{87}\text{Sr}/^{86}\text{Sr}$  systematics in fresh and altered rocks or rather  $\delta^{18}\text{O}$  in quartz separates from the Brothers arc volcano (IODP 376). Both systems point to significant affection by subduction processes in the Western Pacific area that is expressed by the appearance of acid-sulfate fluids and advanced argillic alteration patterns resulting from up rise of magmatic fluids. Magmatic fluids typically occur in shallower water depth at convergent plate margins and are further assumed to enhance formation of especially large and gold-rich ore bodies that are comparable to porphyry-type and epithermal ore deposits on-land (e.g. Audétat, 2019). The combination of  $\delta^{11}\text{B}$ ,  $\delta^7\text{Li}$  and  $^{87}\text{Sr}/^{86}\text{Sr}$  altered whole rock data indicated that more coherent lava flows that are embedded between more heterogeneous volcanoclastic rocks act as permeability barriers, leading to lower w/r-ratios and higher reaction temperatures within the more coherent lava flows compared to higher w/r-ratios and comparable lower alteration temperatures in the volcanoclastic zones. Detailed investigations of the change in w/r-ratios and temperatures at those permeability boundaries in seafloor hydrothermal systems based on high-resolution sampling and measuring of  $\delta^{11}\text{B}$ ,  $\delta^7\text{Li}$  and  $^{87}\text{Sr}/^{86}\text{Sr}$  could lead to a deeper understanding of fluid pathways in the sub-seafloor, also important for ore formation process. The  $\delta^7\text{Li}$  composition of altered rocks at Brothers volcano seemed to reflect a complex interplay of changing temperatures, w/r-ratios and mineralogical differences. The impact of single parameters on the  $\delta^7\text{Li}$  values of the hydrothermally altered rocks could not be disassembled and need further research. In particular the impact of mineralogical differences (e.g. sulfates) on Li isotopic fractionation should be investigated in more detail.

Summarized, the research conducted in this thesis underlined the usefulness of  $\delta^{11}\text{B}$ ,  $\delta^7\text{Li}$ ,  $\delta^{18}\text{O}$  and  $^{87}\text{Sr}/^{86}\text{Sr}$  signatures as proxies for fluid-rock interaction processes in seafloor hydrothermal systems. Deeper understanding of hydrothermal water-to-rock interaction processes is important to estimate the impact of hydrothermal exchange on the seawater and altered crust compositions and to study fluid pathways in the basement. Information on these processes are necessary to make constraints on shifts in paleo-seawater values due to varying compositions of input and output fluxes, to estimate the elemental charge that is transported to the mantle by subduction of matured crust, and to get deeper insights to ore forming processes in seafloor hydrothermal systems. Nevertheless, a large number of hydrothermal systems were not identified so far, Beaulieu *et al.* (2015) estimated 75% of the global vent systems still have to be discovered, and refinement of the made assumptions will only come with research on further systems, accompanied by tailored experimental approaches that realistically mimic the fluid-rock exchange conditions in nature.

## **References**

Audétat A. (2019) The Metal Content of Magmatic-Hydrothermal Fluids and Its Relationship to Mineralization Potential. *Econ. Geol.* **114**, 1033–1056.

- Beaulieu S. E., Baker E. T. and German C. R. (2015) Where are the undiscovered hydrothermal vents on oceanic spreading ridges? *Deep Sea Research Part II: Topical Studies in Oceanography* **121**, 202–212.
- Boschi C., Dini A., Früh-Green G. L. and Kelley D. S. (2008) Isotopic and element exchange during serpentinization and metasomatism at the Atlantis Massif (MAR 30°N). *Geochim. Cosmochim. Acta* **72**, 1801–1823.
- Chan L., Edmond J. M., Thompson G. and Gillis K. (1992) Lithium isotopic composition of submarine basalts. *Earth Planet. Sci. Lett* **108**, 151–160.
- Conrad C. P. and Lithgow-Bertelloni C. (2007) Faster seafloor spreading and lithosphere production during the mid-Cenozoic. *Geology* **35**, 29.
- Coogan L. A., Gillis K. M., Pope M. and Spence J. (2017) The role of low-temperature (off-axis) alteration of the oceanic crust in the global Li-cycle. *Geochim. Cosmochim. Acta* **203**, 201–215.
- Fisher A. and Wheat C. G. (2010) Seamounts as Conduits for Massive Fluid, Heat, and Solute Fluxes on Ridge Flanks. *Oceanog.* **23**, 74–87.
- Foster G. L. and Rae J. W. (2016) Reconstructing Ocean pH with Boron Isotopes in Foraminifera. *Annu. Rev. Earth Planet. Sci.* **44**, 207–237.
- Foustoukos D. I., Savov I. P. and Janecky D. R. (2008) Chemical and isotopic constraints on water/rock interactions at the Lost City hydrothermal field, 30°N Mid-Atlantic Ridge. *Geochim. Cosmochim. Acta* **72**, 5457–5474.
- Hansen C. T., Meixner A., Kasemann S. A. and Bach W. (2017) New insight on Li and B isotope fractionation during serpentinization derived from batch reaction investigations. *Geochim. Cosmochim. Acta* **217**, 51–79.
- James R. H., Elderfield H. and Palmer M. R. (1995) The chemistry of hydrothermal fluids from the Broken Spur site, 29°N Mid-Atlantic ridge. *Geochim. Cosmochim. Acta* **59**, 651–659.
- Janecky D. R. (1982) Serpentinization of peridotite within the oceanic crust; experimental and theoretical investigations of seawater-peridotite interaction at 200C and 300C, 500 bars. *Thesis, University of Minnesota at Minneapolis, MN, USA.*
- Janecky D. R. and Seyfried W. E. (1986) Hydrothermal serpentinization of peridotite within the oceanic crust. *Geochim. Cosmochim. Acta* **50**, 1357–1378.
- Kakahana H., Kotaka M., Satoh S., Nomura M. and Okamoto M. (1977) Fundamental Studies on the Ion-Exchange Separation of Boron Isotopes. *B. Chem. Soc. Jpn.* **50**, 158–163.
- Misra S. and Froelich P. N. (2012) Lithium isotope history of Cenozoic seawater. *Science (New York, N.Y.)* **335**, 818–823.
- Mottl M. (2003) *Partitioning of energy and mass fluxes between mid-ocean ridge axes and flanks at high and low temperature, in Energy and mass transfer in submarine hydrothermal systems.* Dahlem University Press, Berlin, Germany.
- Pearson P. N. and Palmer M. R. (2000) Atmospheric carbon dioxide concentrations over the past 60 million years. *Nature* **406**, 695–699.
- Seton M., Gaina C., Muller R. D. and Heine C. (2009) Mid-Cretaceous seafloor spreading pulse. *Geology* **37**, 687–690.
- Seyfried W. E. and Dibble W. E. (1980) Seawater-peridotite interaction at 300°C and 500 bars. *Geochim. Cosmochim. Acta* **44**, 309–321.
- Spivack A. and Edmond J. (1987) Boron isotope exchange between seawater and the oceanic crust. *Geochim. Cosmochim. Acta* **51**, 1033–1043.
- Stein C. A. and Stein S. (1994) Constraints on hydrothermal heat flux through the oceanic lithosphere from global heat flow. *J. Geophys. Res.* **99**, 3081–3095.
- Wunder B., Meixner A., Romer R. L., Wirth R. and Heinrich W. (2005) The geochemical cycle of boron. *Lithos* **84**, 206–216.

## ACKNOWLEDGMENTS

---

First of all, I would like to thank my supervisor Wolfgang Bach for his constant support over the last years. He always had time for last minute corrections whenever necessary, was open minded for any wild ass guesses and mostly found the right words to motivate me.

I also highly appreciate that Horst Marschall agreed to review this dissertation.

Further, I would like to thank our collaboration partners Yaron Katzir and Stephen Fox from the Ben Gurion University of the Negev for the joined research. I enjoyed the two field trips to Cyprus that we went on together a lot and will keep the Cyprus coffee always in good memory. Many thanks also to Steve for conducting the CL and the oxygen isotope measurements.

In this context, I also want to thank the GIF for funding this joined research and for the organization of the Young Scientist Meeting (GYSM) in Bremen, October 2019.

Further, I am also very thankful for the financial support by GLOMAR.

Special thanks go to Simone Kasemann, Anette Meixner and Friedrich Lucassen for a lot of support in the isotope geochemistry lab and for always welcoming me in the Isotope Geochemistry group, to Christian Hansen for support conducting and evaluating the exchange experiments, to Petra Witte and Andreas Türke for helping me with the SEM, to Patrick Monien for help with the LA-ICP-MS, and to Stefan Sopke for support conducting the EMPA analyses. Besides, also many thanks to Geoffrey Wheat (University of Alaska-Fairbanks) and Eoghan Reeves (University of Bergen) for providing sample materials related to this thesis and for their suggestions for improvement of the manuscripts.

Further, I am also very thankful for the time on the Joides resolution (IODP 376) and would like to thank all participants for the great time on board and in Japan. Special thanks go to Olivier Rouxel (IFREMER, Brest) for performing the elemental and isotopic measurements in his lab and to Jeremy Deans (University of Southern Mississippi) for his interest in my research and his great ideas for improvements of the manuscript.

Many thanks also to all not already mentioned present or past colleagues from the Petrology of the Ocean Crust group; Alex, Andreas K., Bastian, Elmar, Florian, Janis, Karen, Leslie, Tony and Wolf.

I also would like to thank Tina, Rene and Nele for the numerous coffee breaks and lunchtimes; within the university and outside. These breaks were always an important source of refreshment!

Finally, I would like to thank my friends and family outside of sciences for the support over the last years, especially my mother and father, his wife, Felix, and the cats. I could always count on your open ear and could find some rest in your company.



## APPENDIX

---

### *A.1. Supplementary material to thesis chapter 3*

#### *A.1.1 Materials and methods*

##### *A.1.1.1 Natural fluid collection procedure*

The natural fluid samples analyzed in this study were collected from four vent fields (Ashadze II, Irinovskoe, Logatchev, and Semenov-2, **Figure A. 1-1**) between 12 °N and 15 °N along the Mid-Atlantic Ridge (MAR) by the remotely operated vehicle (ROV) *MARUM QUEST* equipped with titanium isobaric gas-tight (IGT) samplers (Seewald *et al.*, 2002) during the *RV METEOR* Expedition M126 in April and May 2016. Per discrete fluid discharge site, two or three fluid samples were taken and in total 19 fluid samples were collected in this study. The water depth the fluids were sampled from ranged from 2433 to 3281 meters below sea level (mbsl). The maximum measured temperatures (uncertainty  $\pm 2$  °C, 2sd) during collection were detected in real-time by a thermocouple temperature probe that was attached to the IGT samplers. The pH values (at 25 °C, 0.1 MPa, uncertainty  $\pm 0.02$ , 2sd) of the discrete fluid samples were determined potentiometric onboard of the ship based on an Ag/AgCl combination reference electrode. In addition to the discrete hydrothermal fluids, also two bottom seawater samples (in 2700 and 3282 mbsl) were collected during the cruise by a rosette sampler equipped with a conductivity-temperature-depth (CTD) logger that was lowered from the ship by a heaver to determine the background signal of unmodified seawater. Fluid aliquots of discrete fluid and bottom seawater samples that were intended for further analyses onshore (Mg, B and  $\delta^{11}\text{B}$  compositions) were stored in acid-cleaned high-density polyethylene (HDPE) Nalgene<sup>TM</sup> bottles.

##### *A.1.1.2 Natural fluid sampling locations*

The discrete fluid samples analyzed in this study were all collected at high-temperature ( $\geq 300$  °C) fluid discharge sites that are located along the MAR between the Marathon and the 15°20' N Fracture Zone. This ridge segment shows extensive hydrothermal activity despite of the low-magma budget supposed for the area (Petersen *et al.*, 2009). Hydrothermal circulation in this segment is suggested to be mainly structure controlled and commonly is associated with the corrugated surfaces of ultramafic and gabbroic mantle lithologies that were tectonically uplifted along large-scale detachment faults, (Fouquet *et al.*, 2010), so called oceanic core complexes (OCC). All here investigated vent fields (Ashadze II, Irinovskoe, Logatchev, and Semenov-2) show evidence for fluid-rock interaction with ultramafic rocks but specific signatures of hydrothermal activity (e.g. temperatures, alteration mineralogy, fluid pH and composition) are rather variable between the

different discharge locations. Details regarding the sampling sites investigated in this study are given in the following sections.

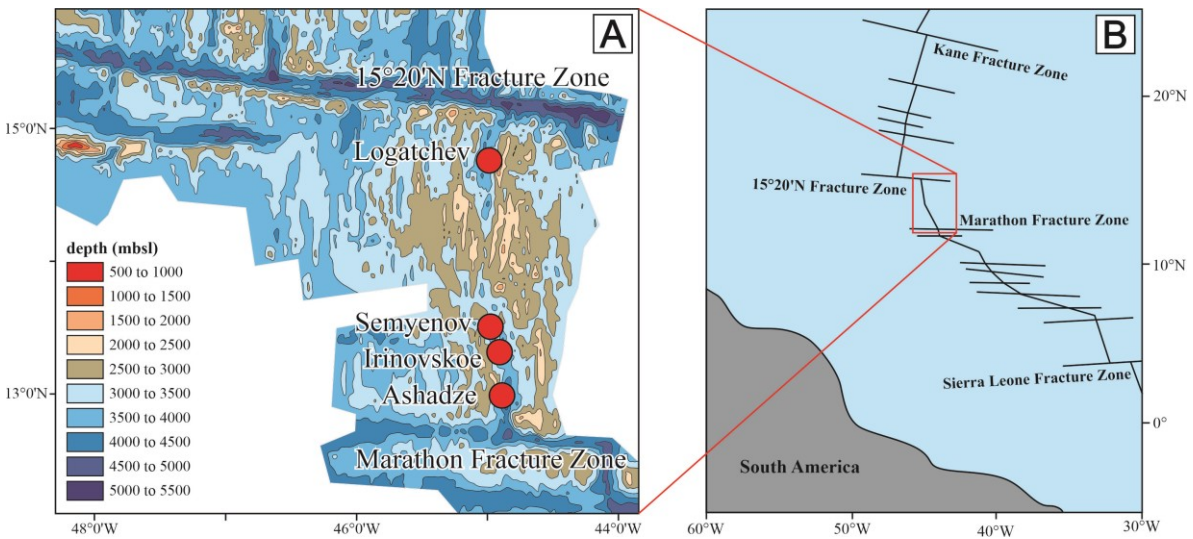


**Figure A. 1-1:** Locations of the investigated vent fields along the MAR between the Marathon and 15°20'N Fracture Zones. (A) The bathymetric map was modified after Ondréas *et al.* (2012), and (B) the overview map showing the progression of the MAR ridge axis and fracture zones was modified after Melekestseva *et al.* (2010).

### Logatchev

The Logatchev hydrothermal field (LHF) at 14°45'N on the MAR is situated on the eastern flank around 7 km apart from the MAR axis on a plateau beneath a 350 m elevated cliff in 3060 to 2910 m water depth (Petersen *et al.*, 2009). The LHF comprises of seven high-temperature fluid discharge sites, in which three of them were studied in here (Site 'A' and 'B', 'IRINA II'). The vent sites Site 'A' and 'IRINA II' are characterized by exiting of high-temperature (up to 358 °C) fluids from black smoker chimneys that are placed on top of up to 15 m elevated hydrothermal mounts relative to the surrounding seafloor (Petersen *et al.*, 2009). In contrast, hot fluid discharge (up to 360 °C) at Site 'B' arises from the bottom of so-called 'smoking craters'; 2 to 5 m deep local depressions encircled by 1 to >5 m high craters. The primary host rocks at LHF are dunites, harzburgites and grabbronorites (Augustin *et al.*, 2008; Petersen *et al.*, 2009) that are extensively serpentinized and replacement by serpentine (mainly the lizardite polymorph, Augustin *et al.*, 2008) and magnetite. Brucite that would also be typically for a mineral assemblage produced by serpentinization is lacking from altered rocks collected from the seafloor surface at LHF, potentially due to destabilization of brucite by interaction with bottom seawater (Snow & Dick, 1995; Augustin *et al.*, 2012). The interaction of high-temperature fluids with ultramafic lithologies is also evident by the very high dissolved methane and hydrogen concentrations reported for discharging fluids at the LHF (Schmidt *et al.*, 2007; Schmale *et al.*, 2012). Furthermore, the escaping end-member fluids at the LHF have  $^{87}\text{Sr}/^{86}\text{Sr}$  compositions that are pronounced less radiogenic than of the serpentinites,

pointing to additional fluid-rock exchange with mafic lithologies in the basement (Augustin *et al.*, 2012). The local replacement of serpentine by talc is probably resulting from Si-metasomatism triggered by irruption of gabbroic intrusions to shallower levels (Petersen *et al.*, 2009).

### *Semenov*

The actively fluid discharging Semenov hydrothermal field -2 (SHF-2, 13°31.13'N, 44°58.03'W) is hosted within an OCC west of the MAR in a water depth of 2500 to 2500 m (Beltenev *et al.*, 2007). We investigated hydrothermal fluids from three vent sites of the SHF-2 (Ash Lighthouse, Michelangelo, Yellow Submarine) that showed a milky white color and discharge temperatures up to 313 °C. The OCC consists of serpentinized harzburgite, in which transformation of serpentine to talc locally occurs, altered gabbroic rocks, dolerites, basalts, amphibolites, plagiogranites, tonalities, and diorites (Beltenev *et al.*, 2007; Beltenev *et al.*, 2009; Pertsev *et al.*, 2012). The rocks exposed at the surface of the SHF-2 are basalts (Beltenev *et al.*, 2007), however geochemical signatures of massive sulfides give evidence for ultramafic (high Au contents) as well as mafic (high SiO<sub>2</sub> contents) contributions to hydrothermal activity (Melekestseva *et al.*, 2017). Some authors also suggested contributions of magmatic fluids at the Semenov hydrothermal district due to the high Au contents of massive sulfides accompanied by the occurrence of silicic rock types (Melekestseva *et al.*, 2017) and the high volatile contents of fluid inclusions in barite (Melekestseva *et al.*, 2014).

### *Irinovskoe*

The Irinovskoe hydrothermal field (IHF) is situated at 13°20'N, in 5 km distance to the MAR spreading axis and in water depth between 2700 and 2850 m (Escartín *et al.*, 2017). The IHF is hosted at an OCC that consists of ultramafic and gabbroic rocks that were hydrothermally altered to varying extents. Fluid discharge of black smoke occurs at two vent sites at the IHF (Active Pot and Pinnacle Ridge) with temperatures up to 365 °C that were both investigated in this study.

### *Ashadze*

The Ashadze hydrothermal district (AHD) at 12°58'N along the MAR is part of an OCC consisting of serpentinized peridotites, altered gabbroic rocks and trondhjemites that is located to the western flank of the axial valley (Beltenev *et al.*, 2003; Silantyev *et al.*, 2011). The district comprises two active black smoker hydrothermal fields (AHF-1 and -2) in which only fluid samples from AHF-2 were investigated in this study. The AHF-2 is located 9 km off-axis in a water depth of 3260 m in a N-S trending linear depression that is restricted to the east by a faulted gabbroic body and to the west by a N-S oriented ridge (Fouquet *et al.*, 2010; Ondréas *et al.*, 2012). Fluid discharge at the AHF-2 occurs from hydrothermal craters that are up to 5 m deep and 40 m wide that are situated in serpentinized ultramafic lithologies, similar to the craters observed at the Logatchev hydrothermal district (Fouquet *et al.*, 2008). Ondréas *et al.* (2012) suggested that those craters formed by

submarine explosions accompanied by geyser-like fluid venting. The maximum measured discharging fluid temperatures were 296°C (Ondréas *et al.*, 2012), however in-situ temperatures were probably higher but difficult to determine by ROV due to the depressions fluids were arising from. Fluids that were investigated in this study were taken from the actively venting crater-shaped edifice ‘Main Crater’ within the AHF-2 and showed maximum temperatures of 283 °C measured by ROV (258 °C by IGT sampler), but were probably also closer to the direct vent discharge site.

#### *A.1.1.3 Experimental setup*

In this study, we conducted a batch experiment using a Dickson-type reactor (introduced by Dickson *et al.*, 1963 and modified by Seyfried *et al.*, 1987) at the University of Bremen to investigate the B distribution and isotopic fractionation between fresh olivine and a seawater-like fluid at 300 °C and 40 MPa. The setup was chosen to simulate conditions as they typically occur in ultramafic hosted seafloor hydrothermal systems. Furthermore, the experimental setup was installed in analogy to the previous research conducted by Hansen *et al.* (2017) who already investigated the B distribution and isotopic fraction between fresh olivine and a seawater-like fluid at 100 and 200 °C (at 40 MPa) by using the same Dickson-type reactor and the same starting materials as in this study. A detailed description of the experimental setup is given in Hansen *et al.* (2017) but in the following the important factors and divergent parameters compared to the previously conducted experiments are summarized.

The initial solid phase was represented by pre-tumbled and polished olivine crystals separated from peridotitic rocks and received from an Austrian wholesale mineral trader (Mineraliengroßhandel Hausen GmbH). A fraction of purest looking olivine grains were handpicked and finely ground by an agate mortar, followed by wet sieving to receive a grain-size fraction of 50 to 100 µm. The initial fluid phase was a synthetic seawater-like fluid on the basis of ultrapure water (MilliQ<sup>®</sup>) that was prepared to match 3.2 wt.% NaCl adjusted by suprapure sodium chloride (Merck<sup>®</sup>). In contrast to seawater, the synthetic solution was lacking Mg and sulfate because the formation of Mg-hydroxide sulfate hydrate most likely would lead to clogging of the sampling line. The B concentration was pre-adjusted by using an Alfa Aesar<sup>®</sup> plasma standard solution (Spec-pure<sup>®</sup>) of known B concentration (10 µg/ml) and B isotopic composition ( $-0.6 \pm 0.1$  ‰).

For the experimental run, the grounded fresh olivine (4.58 g) was transferred to a flexible gold bag ( $V \approx 100$  ml) that was pre-conditioned by 6 M HCl and 14 M HNO<sub>3</sub> to generate a protective inert Ti-oxide layer. Following, 75 ml of the synthetic seawater-like solution was added. A stream of N<sub>2</sub> gas purged dissolved oxygen from solution and was used to replace the air in the headspace of the cell. The gold bag was placed into a stainless steel (T316) high P-T (maximum 400 °C, 56.5 MPa) vessel and was heated up to 300 °C at an isostatic pressure inside of the reaction cell of 40 MPa for a total runtime of 152 days. An initial fluid sample was received before heating of the system.

During the experimental run, multiple fluid samples were extracted from the reaction cell while keeping P-T conditions constant. After determination of the experiment, one final fluid sample was taken directly before and one directly after cooling of the system. All extracted fluid samples were split in aliquots for determination of pH, salinity, dissolved element concentration (Mg, B) and  $\delta^{11}\text{B}$  compositions. In addition, the solid reaction product was quantitatively retrieved from the gold cell after ending of the experiment, repeatedly purged with ultrapure water (MilliQ<sup>®</sup>) and centrifuged. After that, the solid reaction product was dried in a drying oven at 45 °C. Two aliquots of the solid reaction product were created that were grounded by an agate mortar to (1) a fine grain size for chemical analyses and (2) to a slightly coarser grain size for mineralogical characterization.

#### *A.1.1.4 Scanning electron microscopy (SEM) with energy dispersive X-ray spectroscopy (EDX)*

The morphologies of mineral phases that were contained in the solid reaction product after determination of the experiment were investigated by SEM by using a Zeiss SUPRA 40 FESEM at the University of Bremen in the backscatter electron mode. The instrument was additionally equipped with a Bruker Modell XFlash 6 | 30 EDX system that was used to determine semi-quantitative chemical compositions of the newly formed mineral phases and to perform elemental mapping for distinctive image sections. A beam diameter of 1  $\mu\text{m}$  and an acceleration voltage of 15 kV for were used. Before measurements, the solid reaction product was slightly crushed by a hand mortar to create a coarser grained powder that was pasted on a graphite stamp and pre-sputtered with a thin graphite layer.

#### *A.1.1.5 Thermogravimetry (TG) and differential scanning calorimetry (DSC)*

The fractions of hydrous mineral phases in the solid reaction product were determined by a NETZSCH STA 449 F3 Jupiter<sup>®</sup> analyzer hosted in the Crystallography working group at the University of Bremen. Evaluation of the data was performed by using the NETZSCH Proteus<sup>®</sup> Thermal Analysis software package.

For measurements, one  $\text{Al}_2\text{O}_3$  crucible was filled with approximately 30 mg of the finely powdered solid reaction product and one empty  $\text{Al}_2\text{O}_3$  crucible was used for background calibration. Both crucibles were heated simultaneously using a heating program from 30-to-1440-to-30 °C at a heating/cooling rate of 5 °C/min and were evaluated by combination of TG and DSC at a resolution of  $\pm 1 \mu\text{g/g}$ . A mixture of synthetic air consisting of  $\text{N}_2$  and  $\text{O}_2$  (80:20) was used as purging (50 ml/min) and protective (20 ml/min) gas. In addition, one identical run was performed by using two empty  $\text{Al}_2\text{O}_3$  crucibles for reference.

#### *A.1.1.6 Alternating gradient field magnetometer (AGFM) analyses*

The fraction of ferromagnetic mineral phases (in this case we estimate solely represented by magnetite) of the solid reaction product were quantified by using a Princeton MicroMag<sup>™</sup> 2900

AGFM in the Marine Geophysics working group at the University of Bremen. Measurement was performed from a custom-made cup that was filled with finely powdered rock material of the solid reaction product (10 to 20 mg), fixated by an instant adhesive. The cup was attached to a cantilevered rod equipped with a piezoelectric element. Following, the cup was exposed to an alternating gradient field between +300 and -300 mT, sufficient to produce complete hysteresis loops. Saturation magnetization ( $M_s$ ) was derived from the loops opening. The fraction of magnetite in the sample was quantified in reference to the established  $M_s$  of pure magnetite (62.2 Am<sup>2</sup>/kg, after Peters & Dekkers, 2003) under the assumption that magnetite is present as multi-domain crystals and  $M_s$  of magnetite is therefore independent from grain size.

#### *A.1.1.7 Fluid pH and salinity*

The fluid samples that were taken from the reaction cell before, during and after the experimental run were screened for salinity changes that would point to potential leakage within the reaction cell by using an Atago<sup>®</sup> Master-S/Mill $\alpha$  refractometer. In addition, the pH at 25 °C of each fluid was determined directly after sampling by using a micro-pH combined with a A-157 electrode that was attached to a Schott<sup>®</sup> Instruments Lab 850 device (<0.3 RSD%) based on a Silamid<sup>®</sup> Ag/AgCl reference electrode and using 3 M KCl solution as electrolyte. Viability of pH measurements was ensured by 3-point-calibration (pH 4.01, 7.00 and 10.01 at 25 °C) with buffer solution prior to sample measurements.

The in-situ pH of the fluid samples was calculated based on thermodynamic modeling as explained in detail in *Chapter A.1.1.10*.

#### *A.1.1.8 Boron and magnesium concentrations*

The B and Mg concentrations of the natural fluids and bottom seawater collected from different sites along the MAR were determined on-shore by Inductively Coupled Plasma Optical Emission Spectrometry (ICP-OES, Thermo Scientific iCAP 7000) at the Bergen Geoanalytical Facility. We used unacidified aliquots that were diluted with a 2 wt.% HNO<sub>3</sub> solution prior to measurements. The analytical uncertainties for Mg and B are  $\pm 2\%$  (2sd), based on the reproducibility of several sample dilutions. The bottom seawater samples gave values of 0.413 mmol/kg. This B concentration is lower than seawater B values of 0.450 mmol/kg received from Logatchev (Schmidt *et al.*, 2007) but within error of average ocean seawater (0.416 mmol/kg; Spivack & Edmond, 1987) and deep ocean waters from the North Atlantic and Caribbean (approximately 0.400 to 0.420 mmol/kg; Noakes & Hood, 1961; Seyfried *et al.*, 2015).

The B and Mg concentrations of the fluids derived from the batch experiment were measured by a double focusing magnetic sector field Thermo Finnigan Element2<sup>™</sup> Inductively Coupled Plasma – Mass Spectrometry (ICP-MS) at the University of Bremen. Prior to measurements, aliquots of the

fluid samples were diluted 1:10 with 0.48 M HNO<sub>3</sub>. A single element standard solution from Alfa Aesar was used as B reference (10 µg/ml). We used a medium resolution ( $m/\Delta m=4000$ ) and <sup>115</sup>In as internal standard for <sup>24</sup>Mg, and <sup>9</sup>Be as internal standard for <sup>11</sup>B for measurements. Between every sample, one run with 5 % NH<sub>4</sub>OH and one run with blank solution were performed. The internal precision (<1% RSD for B) and accuracy relative to the expected values of the reference solution (<1% RSD for B) were monitored by repeated measurements of the reference solution. Mg was always under detection limit in the reference solution, but duplicate measurements of sample solutions give an internal precision of <1% RSD for Mg.

The B concentration of the solid reaction product was determined from the same solution and by the same instrument that was used to determine the B isotopic composition (for details on the procedure see *Chapter A.1.1.9*). The uncertainty of B concentration of the solid was ±2 % (2sd) based on the internal reproducibility of repeatedly measured solutions (samples and standard materials). The B concentration received for the basaltic reference material IAEA-B-5 that was measured along with the sample was  $9.4 \pm 0.0$  µg/g (n=1) and agrees well with a concentration of  $9.3 \pm 0.5$  µg/g (2sd, n=4) published by Wilckens *et al.* (2018) and with the range of 8.36 to 11.9 µg/g that is given by the GEOREM database (25. March 2020).

#### *A.1.1.9 Boron isotopic compositions*

The B isotopic composition of natural fluids and of fluids as well as of the solid reaction product that were received from the experiments were measured by a ThermoFischer Scientific Neptune Plus Multi collector – Inductively Coupled Plasma – Mass Spectrometry (MC-ICP-MS) coupled to a stable introduction system (SIS) and a high-efficiency x-cone in the Isotope Geochemistry Laboratory at the MARUM, University of Bremen.

Purification of B in solution prior to measurement of the isotopic composition of the natural fluids was performed by a sublimation procedure after Wang *et al.* (2010). An aliquot of 45 µl of the fluid and 5 µl 7 N HNO<sub>3</sub> were placed in the lid of a 5 ml conical Savillex<sup>®</sup> beaker. The beaker was closed tightly lid-down, wrapped in aluminum foil and placed on a hotplate at 98 °C for 18 hours. Afterwards, the aluminum foil was removed, the beaker was carefully turned upright and the cooled condensate was diluted in 2 % HNO<sub>3</sub> for measurements.

The purification of B of the experimental fluids and of the solid reaction product were performed by a two-step ion exchange (for the fluids only the cation exchange step was used) procedure after Romer *et al.* (2014) that was modified after Tonarini *et al.* (1997) and Kasemann *et al.* (2001), see *Appendix A.2.1*. Prior to purification, the B hosted in the solid reaction product was transferred to solution by alkaline fusion of the rock powder (190.9 mg) with K<sub>2</sub>CO<sub>3</sub> as fluxing agent (1:4) in Pt-crucibles followed by dissolution with ultrapure water (MilliQ<sup>®</sup>). The received solution was passed to a first column separation step based on anion exchange with Amberlit IRA 743. Afterwards an

appropriate amount of mannitol (1 µg B : 20 µg mannitol) was added to ensure stability of B in solution. A second cation exchange step (in case of the experimental fluids the first and only step) was performed by using AG 50W-X8 (mesh 200-400). Potential loss of B during procedure was monitored by measuring the B concentrations in the pre- and post-carriages and were always < 0.01 % of the total B amount in solution and therefore negligible.

For measurements, the purified sample solutions dissolved in 2 % HNO<sub>3</sub> were closely matched to 50 ppb B and repeatedly analyzed in the standard – sample – standard bracketing mode using the boric acid reference solution NIST SRM 951. Measurements were supplemented by baseline determinations between every single run. The B isotopic composition is given in the δ<sup>11</sup>B (‰) notation:  $[\delta^{11}\text{B} = \{[(^{11}\text{B}/^{10}\text{B})_{\text{sample}} / (^{11}\text{B}/^{10}\text{B})_{\text{NIST SRM 951}}] - 1\} \times 1000]$ . The uncertainties of B isotopic measurements performed in this study are always given as ±2sd. In case of the solid, a complete procedural blank was processed (including the K<sub>2</sub>CO<sub>3</sub> fluxing agent) and yield a B amount of 11.7 ng for the amount of K<sub>2</sub>CO<sub>3</sub> used for the sample, corresponding to 0.5 % of the total B in sample solution and showed a δ<sup>11</sup>B value of -5.0 ± 0.2 ‰. The NIST SRM 951 solutions processed together with the samples showed a δ<sup>11</sup>B value of 0.1±0.1 ‰ for the sublimation technique, -0.1±0.0 ‰ for the solid phase and -0.1±0.1 ‰ for the cation exchange technique used for the experimental fluids and point to negligible fractionation during procedure. In addition, one of the natural fluid samples (M126/554-12-IGT-3) was measured as duplicate using the sublimation and cation exchange technique to ensure comparability of results and gave conform δ<sup>11</sup>B values of +36.3±0.2 ‰ and +36.1 ± 0.1 ‰. The basaltic reference material IAEA-B-5 displayed a δ<sup>11</sup>B value of -4.3±0.1 ‰ (n=1) in agreement with previously published values of -4.3±0.2 ‰ (n=3, Hansen *et al.*, 2017), and -4.2±0.2 ‰ (n=4, Wilckens *et al.*, 2018). A laboratory internal seawater standard (bottom seawater collected from SuSu Knolls, Western Pacific) gave a δ<sup>11</sup>B value of +39.7±0.2 ‰ (n=1) by the sublimation and +39.5±0.1 ‰ (n=1) for the cation exchange technique. Both δ<sup>11</sup>B values are in good agreement with previously measured compositions of the seawater standard of +39.7±0.3 ‰ (n=8, Wilckens *et al.*, 2018) and also with average seawater composition of +39.61±0.04 ‰ (2SD<sub>mean</sub>, Foster *et al.*, 2010).

#### A.1.1.10 Thermodynamic modeling

Similar to the experimental setup itself, also the thermodynamic modeling (1) to calculate the in-situ pH of reaction and (2) to estimate the speciation of B in solution was conducted in analogy to the modeling performed by Hansen *et al.* (2017). The thermodynamic modeling was based on the EQ3/6 software package Version 8.0 (Wolery, 1992) combined with a tailor-made database for 40 MPa created with the software code SUPCRT92 (Johnson *et al.*, 1992) and by entering information on dissolved aqueous species that were derived from ICP-MS and measured pH.

Calculation of the in-situ pH of the fluids is necessary due to the strong temperature dependence of pH and the great difference in temperatures during pH measurements of the experimental fluids (at 25 °C) compared to reaction (at 300 °C). Furthermore, the pH in solution has a significant impact on B isotopic fraction between solid and fluid because the occurrence of distinctive B species depends on pH and the different B species show varying B isotopic compositions (Hansen *et al.*, 2017). We therefore also modeled the speciation of B in solution with increasing reaction progress.

Thermodynamic modeling was conducted: (1) by using the software code EQ3NR, the abundance of aqueous species derived from ICP-MS measurements and the measured pH values to create a basic thermodynamic state of the aqueous solution regarding the occurrence of aqueous species and their activities; (2) by using the output file created with EQ3NR as initial parameterization for modeling fluid-rock interactions with the software code EQ6. Therefore, a heating of solution up to 300 °C was simulated while precipitation of mineral phases was suppressed. The thermodynamic database (0 to 400 °C, constant 40 MPa) used for modeling was created using the software code SUPCRT92 (Johnson *et al.*, 1992) but modified after Klein *et al.* (2013) to make adjustments regarding serpentization reactions and further tailored after Akinfiyev *et al.* (2006) to integrate thermodynamic information on different B species. Indeed, the  $\text{BO}_2^-$  species was removed from the database because it is not thermodynamic stable in aqueous solutions ( $\text{BO}_2^- + 2\text{H}_2\text{O} \leftrightarrow \text{B}[\text{OH}]_4^-$ ). The species considered in the used database are  $\text{B}[\text{OH}]_{3(\text{aq})}$ ,  $\text{B}[\text{OH}]_4^-$ ,  $\text{NaB}[\text{OH}]_{4(\text{aq})}$ , and  $\text{B}[\text{OH}]_3\text{Cl}$ .

### *A.1.2 Results of the natural fluid samples*

#### *A.1.2.1 Calculation of the fluid end-member composition*

The discrete fluids from all four investigated hydrothermal fields (Ashadze II, Irinovskoe, Logatchev, and Semenov-2) show depletion in B concentrations and a decrease in  $\delta^{11}\text{B}$  compositions compared to bottom seawater (**Table A. 1-1**, **Figure A. 1-2**). The decrease in B concentrations in the fluids versus seawater points to uptake of B by alteration mineral phases, like it is typically observed for high-temperature fluid-rock interaction with ultramafic rocks (Mével, 2003). However, fluids that were sampled at the seafloor can expect to be mixed with bottom seawater due to the sampling procedure and potentially also because of entrainment of seawater towards shallower crust levels prior to fluid discharge (details are given in Reeves *et al.*, 2011; Wilckens *et al.*, 2018). Usually, the sampled fluids represent a two-component mixture of hydrothermal fluid and entrained seawater. The commonly observed formation of Mg-bearing secondary mineral phases (e.g. chlorite, smectite, serpentine, brucite) by hydrothermal alteration of ocean crust leads to a virtual complete removal of Mg in the interacting fluid, also confirmed by experimental approaches for different primary lithologies (e.g. Seyfried & Bischoff, 1981, Hajash & Chandler, 1982). The “end-member” (EM) composition of the pure hydrothermal fluid prior to mixture with seawater can therefore be calculated by extrapolation to a zero-Mg composition by using a linear least squares regression. **Figure A. 1-2** shows that the B concentrations and  $\delta^{11}\text{B}$

compositions versus Mg concentrations of individual fluid discharge sites of the four hydrothermal sites show common linear trends between seawater and a hydrothermal EM. Therefore, we calculated one EM B and EM  $\delta^{11}\text{B}$  composition per hydrothermal field by linear extrapolation to zero-Mg composition forced to seawater composition (*Table A. 1-2*).

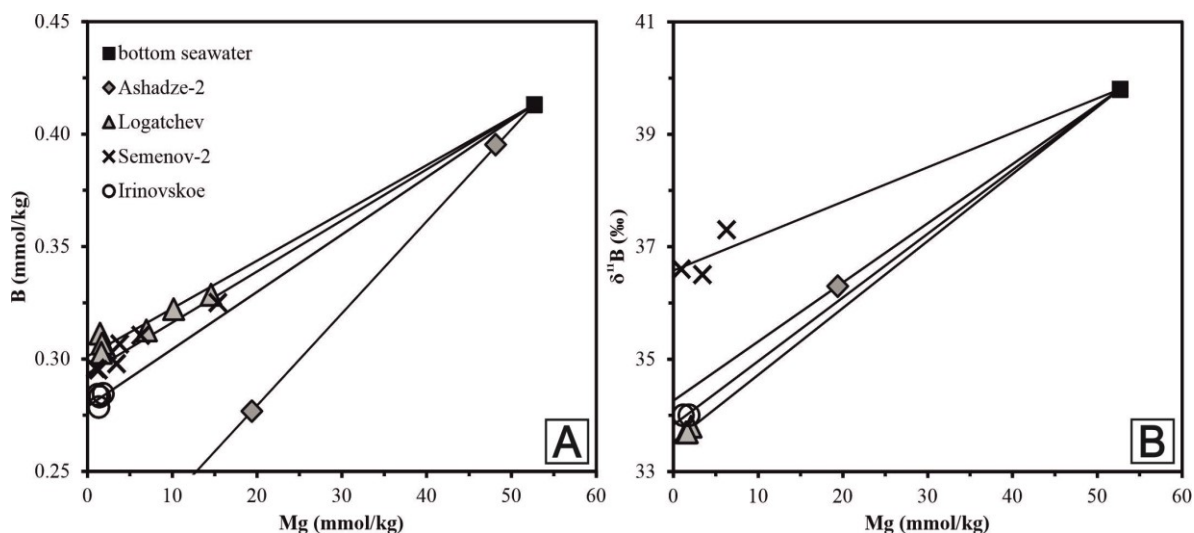


**Figure A. 1-2:** Compositions of hydrothermal fluid samples collected from four different vent fields and bottom seawater. (A) Mg versus B concentrations, (B) Mg versus  $\delta^{11}\text{B}$  compositions. The lines represent linear regression for each vent field, forced to run through the seawater composition and were used for the hydrothermal fluid end-member (EM) calculation.

#### A.1.2.2 Description of the fluid end-member composition

In *Figure A. 1-3* the EM B concentrations and isotopic compositions of the four vent fields and are shown in comparison to bottom seawater (0.41 mmol/kg,  $+39.8 \pm 0.1$  ‰). The EM B concentrations of Logatchev, Semenov-2 and Irinovskoe lie in a narrow range of 0.28 to 0.30 mmol/kg, while Ashadze-2 shows a slightly more depleted signature of 0.20 mmol/kg compared to the other three sites. The stronger depletion in B of the fluids at the Ashadze-2 vent field indicate a more extensive uptake of B by alteration mineral phases than for the other three sides, although all four sites show the typical depletion of B in solution observed for ultramafic hydrothermal systems. The EM  $\delta^{11}\text{B}$  compositions also plot in a narrow range from  $+33.5$  to  $+34.3$  ‰ for three hydrothermal fields but in this case for Logatchev, Irinovskoe and Ashadze-2, while Semenov-2 displays a higher  $\delta^{11}\text{B}$  value of  $+36.6$  ‰ compared to the other vent sites. The Semenov-2 hydrothermal field is the only of the four here investigated fields that shows basaltic rocks at the surface and also more silicic rock types (plagiogranites, tonalities and diorites) in the area in general beside the direct discharge sites (Beltenev *et al.*, 2007), while the other three hydrothermal fields are directly hosted within serpentinized ultramafic lithologies. Nevertheless, the depletion of B from solution versus seawater points to exchange of the fluids with ultramafic rocks also within the basement at Semenov-2.

**Table A. 1-1:** Chemical and isotopic composition of hydrothermal fluids and bottom seawater collected between the Marathon and 15°20'N Fracture Zones.

vent field	vent site	Sample ID	depth mbsl	T <sub>max</sub> (ROV) °C	T <sub>max</sub> (IGT) °C	pH at 25 °C	Mg* mmol/kg	B* mmol/kg	δ <sup>11</sup> B** ‰	±2sd ‰
<i>Ashadze-2</i>	Main crater	M126/554-11 (IGT-2)	3281	283	258	6.7	48.15	0.395		
	Main crater	M126/554-12 (IGT-3) duplicate†	3281	283	243	4.8	19.41	0.277	36.3 36.1	0.2 0.2
<i>Logatchev</i>	IRINA II	M126/527-1 (IGT-2)	3018	353	358	4.2	2.10	0.305	33.8	0.1
	IRINA II	M126/527-6 (IGT-3)	3018	190	197	4.7	10.18	0.322		
	IRINA II	M126/527-7 (IGT-1)	3019	190	198	4.9	14.61	0.328		
	Site A	M126/551-2 (IGT-3)	2928	ND	324	4.8	6.98	0.313		
	Site A	M126/551-3 (IGT-2)	2928	ND	323	4.2	1.51	0.311	33.7	0.1
	Site B	M126/544-12 (IGT-2)	2981	ND	346	4.2	1.73	0.307		
	Site B	M126/544-13 (IGT-4)	2981	ND	346	4.3	1.67	0.303	33.7	0.1
<i>Semenov-2</i>	Ash Lighthouse	M126/511-7 (IGT-2)	2444	ND	309	4.6	3.81	0.307		
	Ash Lighthouse	M126/511-6 (IGT-4)	2444	ND	305	4.7	6.29	0.310	37.3	0.1
	Michelangelo	M126/518-7 (IGT-4)	2433	317	312	4.6	0.95	0.296	36.6	0.1
	Michelangelo	M126/532-4 (IGT-2)	2433	ND	310	4.9	15.38	0.325		
	Yellow Submarine	M126/538-10 (IGT-3)	2439	ND	311	4.7	3.45	0.298	36.5	0.1
	Yellow Submarine	M126/538-11 (IGT-4)	2442	317	313	4.6	1.30	0.295		
<i>Irinovskoe</i>	Pinnacle Ridge	M126/514-2 (IGT-1)	2774	362	355	4.1	1.36	0.279		
	Pinnacle Ridge	M126/514-1 (IGT-2)	2774	362	356	4.1	1.18	0.284	34.0	0.1
	Active Pot	M126/541-6 (IGT-1)	2791	362	359	4.1	1.46	0.283		
	Active Pot	M126/541-5 (IGT-2)	2790	362	357	4.0	1.87	0.284	34.0	0.2
<i>Semenov</i>		bottom seawater (CTD)	3282				52.83	0.413	39.8	0.1
<i>Irinovskoe</i>		bottom seawater (CTD)	2700				52.56	0.413		

\*Mg and B concentrations were measured by ICP-OES at the Bergen Geoanalytical Facility.

\*\*B isotopic compositions were measured by MC-ICP-MS at the MARUM, University of Bremen.

†B in solution used for B isotope determination of the duplicate was purified by cation exchange (just like for the fluids derived from the batch experiment).

Except of the dupliacte, B purification of the natural fluids necessary for B isotope determination was performed by sublimation (see **Chapter A.1.1.9**)

ND= not determined; T<sub>max</sub> (ROV) = maximal temperature measured by ROV; T<sub>max</sub> (IGT) = maximal temperature measured by IGT sampler.

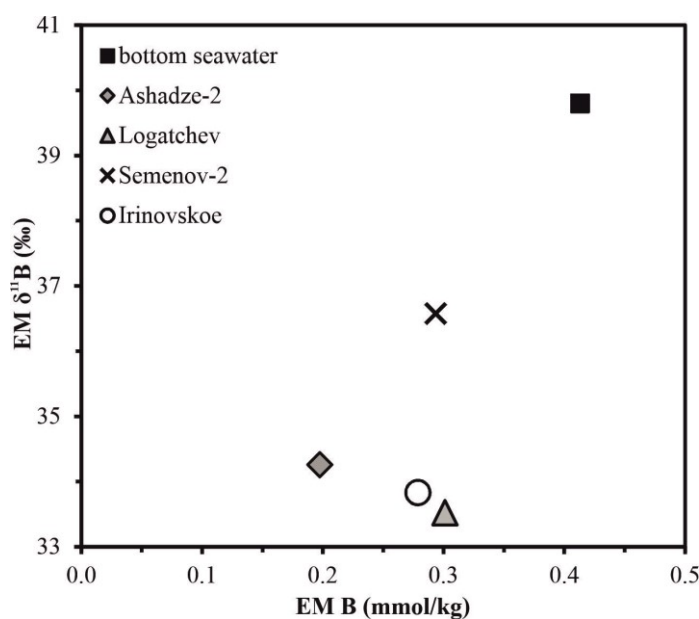


**Figure A. 1-3:** End-member (EM) B and  $\delta^{11}\text{B}$  compositions of the four investigated vent fields (calculated by linear extrapolation to zero-Mg), in comparison to bottom seawater composition.

**Table A. 1-2:** B and  $\delta^{11}\text{B}$  end-member compositions (extrapolation to zero-Mg) of hydrothermal fluid samples collected between the Marathon and 15°20'N Fracture Zones and of bottom seawater.

vent field	EM B mmol/kg	EM $\delta^{11}\text{B}$ ‰
Ashadze-2	0.20	34.3
Logatchev	0.30	33.5
Semenov-2	0.29	36.6
Irinovskoe	0.28	33.8
bottom seawater	0.41	39.8

### A.1.3 Results of the experiment

#### A.1.3.1 Characterization of the experimental solid phase

The fresh olivine crystals that were used as initial solid phase for the experiment were characterized as forsterite-rich ( $\text{Mg}_{1.83}\text{Fe}_{0.17}\text{SiO}_4$ ) by Hansen *et al.* (2017) based on LA-ICP-MS measurements. The solid reaction product that was collected after determination of the experiment showed strong modifications in the mineral assemblage and the chemical composition compared to the initial olivine. The types and compositions of newly formed mineral phases were identified by SEM and EDX analyses (**Figure A. 1-4; Table A. 1-3; Table A. 3-1**). Measurements revealed the replacement of the initial olivine by fine needles of serpentine ( $\text{Mg}_{2.96}\text{Fe}_{0.04}\text{Si}_2\text{O}_5(\text{OH})_4$ , most likely chrysotile) that also overgrew the adjacent secondary mineral phases of tabular anhedral brucite crystals ( $\text{Mg}_{0.97}\text{Fe}_{0.03}(\text{OH})_2$ ) and euhedral to subhedral magnetite crystals that partially showed dissolution textures; some relict olivine was still present.

**Table A. 1-3:** Major element compositions of silicate phases in the solid reaction product of the 300 °C experiment based on SEM-EDX analyses and calculated mineral formula (all data points are documented in **Table A. 3-1**).

mineral phase	olivine*	chrysotile	brucite
average of analyses	6	7	10
<i>oxides</i>			
SiO <sub>2</sub>		38.51	1.48
MgO		35.65	55.38
FeO		1.08	3.93
<b>total</b>		<b>75.24</b>	<b>60.78</b>
<i>cations</i>			
Si <sup>4+</sup>		1.68	0.01
Mg <sup>2+</sup>		3.6	0.95
Fe <sup>2+</sup>		0.05	0.03
<b>total</b>		<b>5.33</b>	<b>0.99</b>
<i>tetrahedral cations normed</i>			
Si <sup>4+</sup>		2.00	
<i>octahedral cations normed to:</i>			
		<i>Mg+Fe=3</i>	<i>Mg+Fe=1</i>
Mg <sup>2+</sup>		2.96	0.97
Fe <sup>2+</sup>		0.04	0.03
<b>formula</b>	<b>Mg<sub>1.83</sub>Fe<sub>0.17</sub>SiO<sub>4</sub></b>	<b>Mg<sub>2.96</sub>Fe<sub>0.04</sub>Si<sub>2</sub>O<sub>5</sub>(OH)<sub>4</sub></b>	<b>Mg<sub>0.97</sub>Fe<sub>0.03</sub>(OH)<sub>2</sub></b>

\*measurements of the initial olivine reactant by LA-ICP-MS were published by Hansen *et al.*, (2017).

**Table A. 1-4:** Mineral phase proportions in the solid reaction product of the 300 °C experiment.

mineral phase	initial solid		solid reaction product			total
	olivine	olivine	serpentine	brucite	magnetite	
proportions (wt.%)	100.0	24.8*	61.0	8.5	5.7	<b>100.0</b>
formula	Mg <sub>1.83</sub> Fe <sub>0.17</sub> SiO <sub>4</sub>	Mg <sub>1.83</sub> Fe <sub>0.17</sub> SiO <sub>4</sub>	Mg <sub>2.96</sub> Fe <sub>0.04</sub> Si <sub>2</sub> O <sub>5</sub> (OH) <sub>4</sub>	Mg <sub>0.97</sub> Fe <sub>0.03</sub> (OH) <sub>2</sub>	Fe <sub>3</sub> O <sub>4</sub>	
M (g/mol)	146.05	146.05	278.37	59.26	231.53	
total amounts (g)**	4.588	1.280	3.152	0.470	0.244	<b>5.146</b>
<b>Reaction turnover (mol%***)</b>	<b>72.1</b>					
<b>Reaction turnover (wt%)</b>	<b>75.1</b>					

\*calculated based on missing fraction (F) to reach 100 wt.% :  $F_{olivine} = 100 - (F_{chrysotile} + F_{brucite} + F_{magnetite})$

\*\*calculated by mass balance calculation.

\*\*\*calculated based on equation (Eq.A.1-1).

The mineral proportions of the solid reaction product were quantified by TG and AGFM analyses (**Table A. 1-4; Table A. 3-2**). The TG analysis was used to detect the abundances of hydrous mineral phases and identified two distinct signals. The first signal (300 to 450 °C) was represented by a mass reduction of 2.57 % relative to the initial sample weight that is characteristic for the dehydroxylation of brucite (Tritschack *et al.*, 2014; Hansen *et al.*, 2017). This corresponds to a total brucite fraction of 8.5 wt.%, calculated based on the measured water loss relative to the

stoichiometric water content of pure brucite and the previously identified brucite composition by SEM-EDX (*Table A. 1-3*). A second signal (460 to 770 °C) showed a mass reduction of 7.90 % and typically occurs due to dehydroxylation of chrysotile (Trittschack *et al.*, 2014). This indicates a total chrysotile abundance of 61.0 wt.%, calculated by relative water loss. The magnetite fraction of 5.7 wt.% was determined by AGFM analysis. The fraction of relict olivine of 24.8 % arose from the difference between 100 % and the sum of fractions (%) of the other mineral phases.

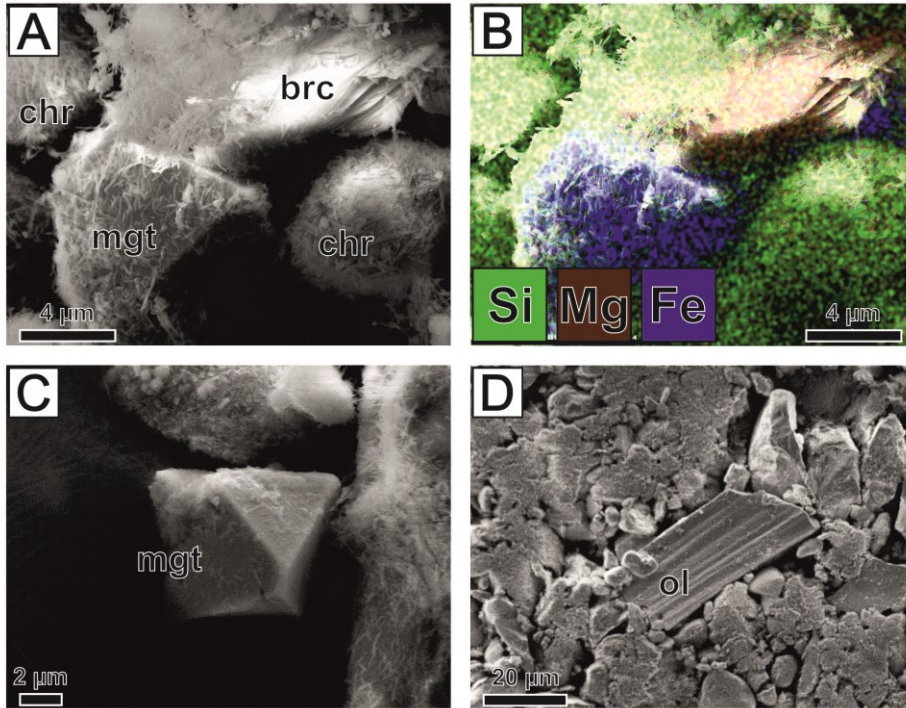


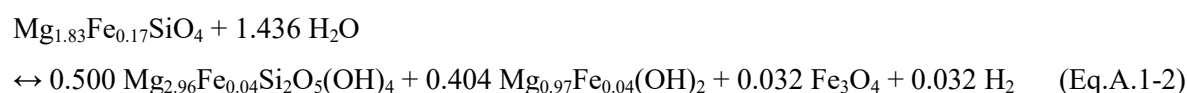
**Figure A. 1-4:** Appearance of mineral phases of the solid reaction product based on SEM. (A) subhedral magnetite (mgt) crystal and tabular brucite (brc) crystal that are overgrown by fine needles of chrysotile (chr) and surrounded by agglomerates of chrysotile needles; (B) additionally shows elemental mapping results by SEM-EDX. (C) Euhedral magnetite crystal. (D) Relict olivine (ol) crystal that shows dissolution lineations within agglomerates of chrysotile needles.

The still present olivine relicts show that the replacement of the solid reaction product by secondary mineral phases was not complete. To estimate the chemical fluid-rock exchange rates it is important to consider the reaction turnover of the experiment. Since chrysotile is the only Si containing secondary mineral phase, the reaction turnover can be calculated based on the proportion of moles chrysotile and relict olivine, derived from quantification and composition of both mineral phases. Stoichiometry gives that two moles of chrysotile ( $n_{chr}$ ) relates to one mole of olivine ( $n_{ol}$ ) and therefore it follows:

$$reaction\ turnover\ (mol\%) = \left( \frac{2 \cdot n_{chr}}{n_{ol} + 2 \cdot n_{chr}} \right) \cdot 100 \quad (Eq.A.1-1)$$

The calculation gives a reaction turnover of 72.1 mol% for the 300 °C experiment.

In an additional step the actual present amounts of the mineral phases within the solid reaction product were calculated, because it can be expected that the initial amount of solid introduced to the system (4.588 g) experienced distinct changes due to reaction. Direct weighing of the retrieved solid reaction product was considered insufficient due to potential loss of material by incomplete transfer from the reaction cell. The calculation was conducted by mass balance calculation based on the expected serpentinization reaction (Hansen *et al.*, 2017), the measured compositions of the mineral phases:



by regarding the initial sample weight of fresh olivine and the total reaction turnover. It gives individual sample weights within the solid reaction product of 3.152 g for serpentine, 0.470 g for brucite, 0.244 for magnetite and 1.280 g for relict olivine; a total sample weight of 5.146 g was calculated (**Table A. 1-4**). The reaction turnover equals to 75.1 wt.%.

**Table A. 1-5:** B and  $\delta^{11}\text{B}$  compositions of the solid phases of the experiment based on MC-ICP-MS analyses.

sample	B μg/g	$\delta^{11}\text{B}$ ‰	2sd ‰
initial olivine*	0.02	-14	2
reaction product	12.4	-5.0	0.1

\*analyzed by Hansen *et al.*, (2017).

The B and  $\delta^{11}\text{B}$  compositions of the initial olivine were 0.02 μg/g and  $-14 \pm 2$  ‰ (2sd, Hansen *et al.*, 2017). The solid reaction product was measured as a whole because of difficulties to separate the finely intergrown newly formed mineral phases and showed an increased B content of 12.4 μg/g and an increased  $\delta^{11}\text{B}$  value of  $-5.0 \pm 0.1$  ‰, compared to the initial olivine (**Table A. 1-5**).

#### A.1.3.2 Characterization of the experimental fluid phase

The initial synthetic seawater-like fluid showed distinct geochemical changes (Mg, B,  $\delta^{11}\text{B}$  compositions and pH) with increasing reaction progress, monitored by repeated fluid sampling over the whole run time of the experiment of 152 days.

The initial fluid was designed to be devoid of Mg to prevent clogging of the sampling line but Mg concentrations immediately increased after introducing the fluid to the system in the cool state (**Table A. 1-6**). However, already after heating up the system to the anticipated temperature of 300 °C, Mg concentrations in the fluid started to decrease and the next sample taken seven days after the start of the experiment was Mg-free again. A slight increase in Mg concentrations was detected after the final cooling of the system at the end of the experiment.

**Table A. 1-6:** Data of fluid samples taken during reaction progress of the 300 °C experiment.

time (days)	description	V <sub>left</sub> * (ml)	W/R	Mg (µg/ml)	B (µg/ml)	Mg (mmol/kg)	B (mmol/kg)	δ <sup>11</sup> B (‰)	2sd (‰)	pH <sub>@25°C</sub>	pH <sub>insitu</sub> **
0.0	stock solution	75.11	16.7	0.0	9.9	0.00	0.93	-0.6	0.1	3.6	
0.1	initial cool	64.14	14.3	2.8	10.0	0.12	0.95	-0.5	0.1	4.6	5.0
0.2	initial hot	58.09	12.9	1.3	9.8	0.06	0.93	-0.6	0.1	6.2	5.5
7.0	hot	55.45	12.3	0.0	9.9	0.00	0.93	-0.3	0.1	9.0	7.3
14.0	hot	52.87	11.8	0.0	9.6	0.00	0.90	-0.9	0.2	9.8	7.5
32.0	hot	50.34	11.2	0.0	9.4	0.00	0.89	-0.5	0.1	10.7	7.8
56.0	hot	47.78	10.6	0.0	9.2	0.00	0.87	-0.3	0.1	11.0	8.0
94.0	hot	45.29	10.1	0.0	9.0	0.00	0.85	-0.1	0.1	11.1	8.1
152.0	hot	39.70	8.8	0.0	8.6	0.00	0.82	0.0	0.2	10.8	7.9
152.2	final cool	35.96	8.0	0.6	8.2	0.03	0.78	-0.1	0.2	10.1	

\*fluid volume that remained in the Au container after each sampling step.

\*\*calculated.

**Table A. 1-7:** Calculations of the change in B concentration and isotopic composition of the fluid (F) over time and the resulting estimate of the composition of the solid reaction product (S). The final cooling stage (gray characters) was excluded for calculations.

time (days)	V <sub>F(left)</sub> * (ml)	V <sub>F(removed)</sub> * (ml)	B <sub>F</sub> * (µg/ml)	B <sub>F(left)</sub> (µg)	B <sub>F(removed)</sub> (µg)	B <sub>F(total)</sub> (µg)	B <sub>S(uptake)</sub> (µg)	δ <sup>11</sup> B <sub>F</sub> * (‰)	[ <sup>11</sup> B]/[ <sup>10</sup> B] <sub>F</sub>
0.0	75.11	-	9.9	742.51	-	742.51	-	-0.6	4.041010
0.1	64.14	10.98	10.0	643.04	110.04	753.08	-10.57	-0.5	4.041469
0.2	58.09	6.04	9.8	569.56	59.25	628.81	14.23	-0.6	4.040996
7.0	55.45	2.65	9.9	547.48	26.14	573.61	-4.06	-0.3	4.042263
14.0	52.87	2.58	9.6	505.66	24.66	530.32	17.15	-0.9	4.039981
32.0	50.34	2.53	9.4	472.40	23.75	496.15	9.51	-0.5	4.041608
56.0	47.78	2.56	9.2	439.20	23.55	462.75	9.64	-0.3	4.042585
94.0	45.29	2.49	9.0	406.58	22.33	428.91	10.29	-0.1	4.043224
152.0	39.70	5.59	8.6	342.52	48.20	390.73	15.86	0.0	4.043764
152.2	35.96	3.74	8.2	295.39	30.73	326.12	16.40	-0.1	4.043404
<b>total</b>		<b>35.41</b>			<b>337.93</b>		<b>62.05</b>		

\*measured input data.

n <sup>11</sup> B <sub>F(total)</sub> [mol]	n <sup>10</sup> B <sub>F(total)</sub> [mol]	m <sup>11</sup> B <sub>F(total)</sub> [µg]	m <sup>10</sup> B <sub>F(total)</sub> [µg]	n <sup>11</sup> B <sub>F(left)</sub> [mol]	n <sup>10</sup> B <sub>F(left)</sub> [mol]	m <sup>11</sup> B <sub>F(left)</sub> [µg]	m <sup>10</sup> B <sub>F(left)</sub> [µg]
5.51E-05	1.36E-05	606.14	136.36	5.51E-05	1.36E-05	606.14	136.36
5.59E-05	1.38E-05	614.79	138.29	4.77E-05	1.18E-05	524.95	118.08
4.67E-05	1.15E-05	513.33	115.48	4.23E-05	1.05E-05	464.96	104.60
4.26E-05	1.05E-05	468.30	105.32	4.06E-05	1.01E-05	446.96	100.52
3.94E-05	9.74E-06	432.91	97.41	3.75E-05	9.29E-06	412.78	92.88
3.68E-05	9.11E-06	405.04	91.11	3.51E-05	8.67E-06	385.65	86.75
3.43E-05	8.50E-06	377.80	84.96	3.26E-05	8.06E-06	358.57	80.63
3.18E-05	7.87E-06	350.18	78.74	3.02E-05	7.46E-06	331.95	74.64
2.90E-05	7.17E-06	319.01	71.72	2.54E-05	6.29E-06	279.65	62.87
2.42E-05	5.99E-06	266.25	59.86	2.19E-05	5.42E-06	241.17	54.22

m <sup>11</sup> B <sub>S(uptake)</sub> [µg]	m <sup>10</sup> B <sub>S(uptake)</sub> [µg]	n <sup>11</sup> B <sub>S(uptake)</sub> [mol]	n <sup>10</sup> B <sub>S(uptake)</sub> [mol]	[ <sup>11</sup> B]/[ <sup>10</sup> B] <sub>S</sub>	δ <sup>11</sup> B <sub>S</sub> (‰)
-	-	-	-	-	-
-8.64	-1.93	-7.86E-07	-1.93E-07	4.073928	7.5
11.63	2.60	1.06E-06	2.60E-07	4.062462	4.7
-3.34	-0.72	-3.03E-07	-7.18E-08	4.226946	45.3
14.05	3.10	1.28E-06	3.10E-07	4.113889	17.4
7.74	1.78	7.03E-07	1.78E-07	3.956572	-21.5
7.86	1.79	7.14E-07	1.79E-07	3.995140	-12.0
8.39	1.90	7.63E-07	1.90E-07	4.016093	-6.8
12.94	2.92	1.18E-06	2.92E-07	4.029976	-3.4
13.40	3.01	1.22E-06	3.01E-07	4.050919	1.8
<b>50.61</b>	<b>11.44</b>	<b>4.60E-06</b>	<b>1.14E-06</b>	<b>4.021217</b>	<b>-5.5</b>

The B concentration of the fluid (initially 10  $\mu\text{g/ml}$ ) showed a steady decrease with increasing reaction progress until the final sample was taken under hot conditions (8.6  $\mu\text{g/g}$ ), followed by an immediate drop in B concentration after cooling of the system (8.2  $\mu\text{g/g}$ , *Table A. 1-6, Figure A. 1-5B*). The decrease in B concentration of the fluid points to uptake of B by the newly formed mineral phases during reaction.

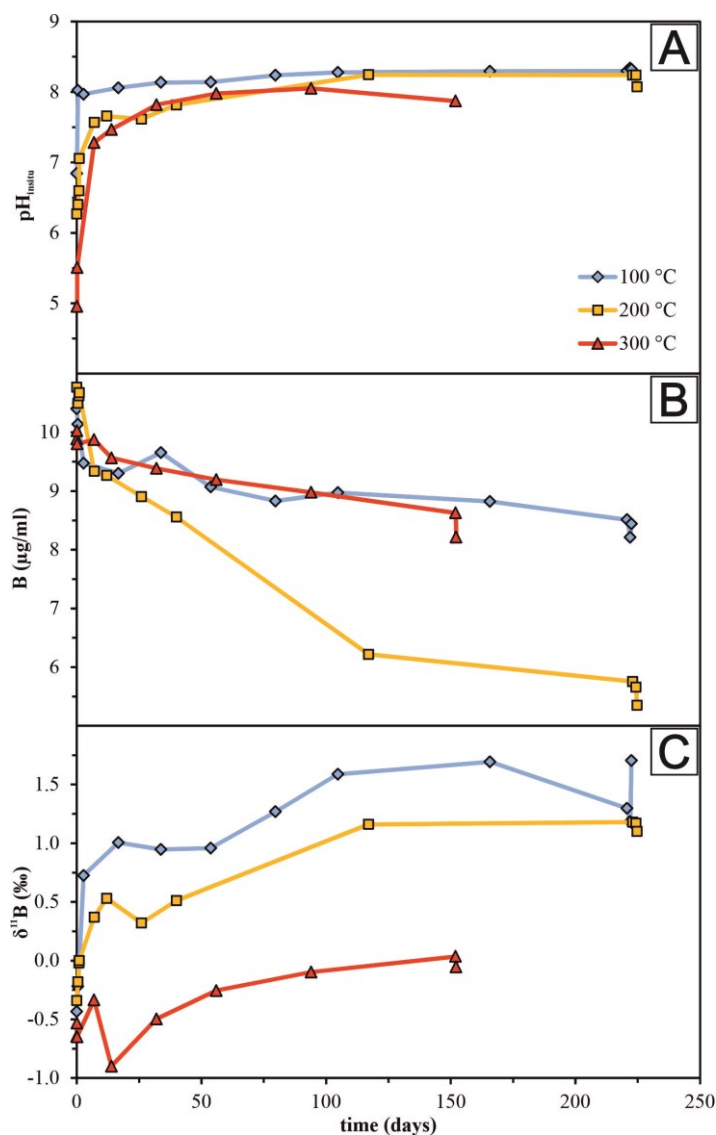


**Figure A. 1-5:** Change in fluid composition over time of the 300 °C experiment, in comparison to the experiments at 100 and 200 °C conducted by Hansen et al. (2017). (A) In-situ pH calculated by EQ3/6, (B) B concentrations, (C)  $\delta^{11}\text{B}$  compositions versus time. Differences of the reaction turnover are not considered in this illustration.

The  $\delta^{11}\text{B}$  composition of the fluid (initially  $-0.6 \pm 0.1$  ‰) showed some fluctuation towards higher and lower values at the start of the experiment but then steadily increased until the final hot sample was taken ( $0.0 \pm 0.2$  ‰, Figure *Figure A. 1-5C*). The drop between the hot ( $0.0 \pm 0.2$  ‰) and the cool ( $-0.1 \pm 0.1$  ‰) sample taken on the last day of the experiment, was within the error of

measurements. The overall increase in  $\delta^{11}\text{B}$  values of the fluid with increasing reaction progress indicates a preferential uptake of the lighter isotope  $^{10}\text{B}$  by the secondary mineral phases.

The pH of the fluid rapidly increased within the first week of the experiment and reached steady state after around 32 days ( $\text{pH}@_{25^\circ\text{C}}=10.7$ ,  $\text{pH}@_{300^\circ\text{C}}=7.8$ , **Figure A. 1-5A**). Hansen *et al.* (2017) already stated the importance to consider the temperature dependence of pH of hydrothermal fluids (in-situ pH of reaction) due to the high impact of pH on B speciation in aqueous solution ( $^{[3]}\text{B}$ - or  $^{[4]}\text{B}$ -coordinated species), linked to distinct differences in B isotopic fractionation.

The B speciation of the experimental fluid with increasing reaction progress was modeled based on the software code EQ3/6 and the measured geochemical input data (**Figure A. 1-6**). The  $^{[3]}\text{B}$ -coordinated species  $\text{B}(\text{OH})_{3(\text{aq})}$  is the most dominant one over the whole run time of the 300 °C experiment but with decreasing fraction from start (92 %) till the end (75 %) of the experiment. The abundance of the other  $^{[3]}\text{B}$ -coordinated species  $\text{B}(\text{OH})_3\text{Cl}^-$  stays relatively stable and represents a fraction in a range from 6 to 8 % in solution. The total fraction of the  $^{[4]}\text{B}$ -coordinated species  $\text{B}(\text{OH})_4^-$  and  $\text{NaB}(\text{OH})_{4(\text{aq})}$  rises from initially not present in the fluid to 18 % (both taken together) at the end of the experiment, in accordance with the increase in pH with ongoing reaction progress.

#### A.1.3.3 Boron distribution coefficient ( $D_{S-F}^{\text{B}}$ ) and isotopic fractionation factor ( $\Delta^{11}\text{B}_{S-F}$ )

The distinct shifts in B and  $\delta^{11}\text{B}$  compositions of the experimental fluid over time were used to estimate the B distribution and isotopic fractionation between the solid and fluid by fluid-rock interaction at 300 °C, in accordance to the 100 and 200 °C experiments published by Hansen *et al.* (2017). For calculations, we only considered fluid samples that reacted at the anticipated temperature of 300 °C and excluded the sample obtained after cooling of the system and experienced a shift in alteration conditions. The composition of the solid reaction product was not used for calculations because of potential changes in B and  $\delta^{11}\text{B}$  composition of the solid: (1) due to potential changes after cooling and opening of the system, and (2) due to possible loss of the finest grained solid fraction by incomplete retrieving of the material from the reaction cell.

The total B fraction that was taken up by the solid phase of 62  $\mu\text{g}$  B prior to the final cooling stage was quantified by calculating the total amount of B removed from the fluid and subtracting the amount of B that was already removed by each sampling step (**Table A. 1-7**). Assuming a sample weight of the solid reaction product of 5.146 g received from mass balance calculation (see **Chapter A.1.3.1**), a B concentration of 12.0  $\mu\text{g/g}$  of the solid reaction product could be expected in excellent agreement with the actual measured value of 12.4  $\mu\text{g/g}$  by MC-ICP-MS (**Table A. 1-5**). If it is considered that the reaction was incomplete and that the reaction turnover equaled 75.1 wt.%, a B concentration of 16.0  $\mu\text{g/g}$  is calculated solely regarding the reacted part of the solid and by assuming a negligible portion of B that is hosted in the unreacted olivine (0.02  $\mu\text{g/g}$  B).

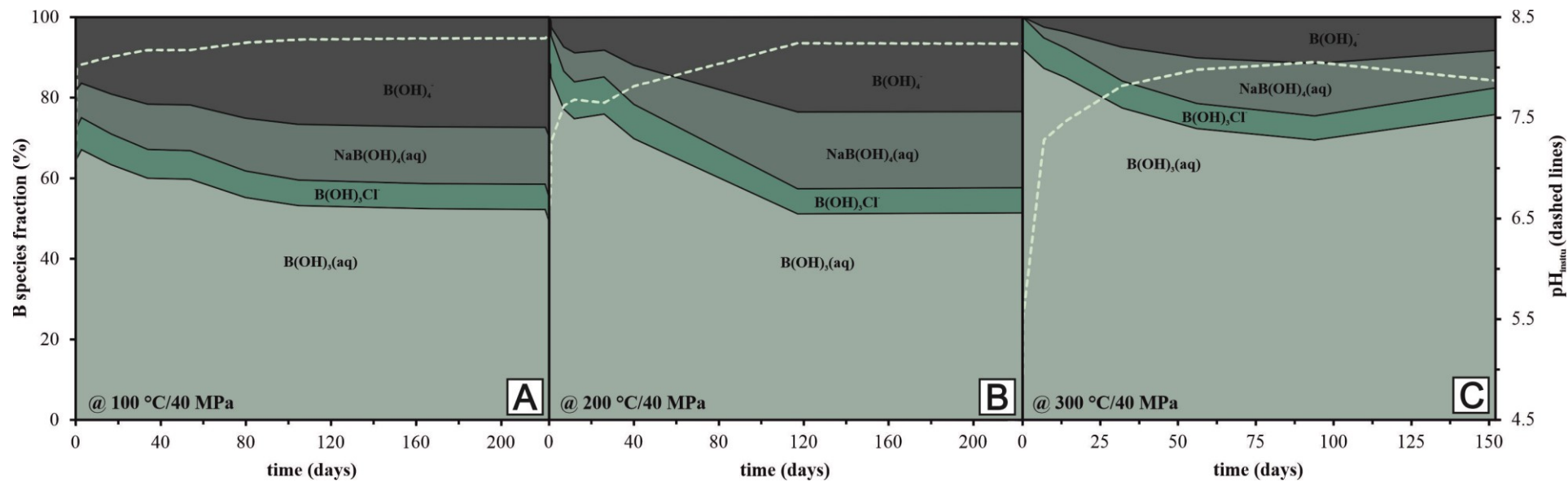


**Figure A. 1-6:** Fractions of B species in aqueous solution calculated by EQ3/6 versus time (A) at 100 °C, (B) 200 °C (both taken from Hansen et al., 2017), and (C) at 300 °C (this study). The light green dashed lines show the in-situ pH of solution versus time.

The distribution coefficient between solid and fluid ( $D_{S-F}^B$ ) was calculated by the following equation (Eq.A.1-3) after Spivack & Edmond (1987), assuming a weight fraction  $F$  of 0.751, a B content of the solid reaction product  $cB_{S-product}$  of 12.0  $\mu\text{g/g}$ , an initial B content of fresh olivine  $cB_{S-initial}$  of 0.02  $\mu\text{g/g}$ , and a B concentration of the final sampled interacting fluid  $cB_{F-final}$  of 8.8  $\mu\text{g/g}$ :

$$D_{S-F}^B = \frac{(cB_{S-product} - (1-F) \cdot cB_{S-initial})/F}{cB_{F-final}} \quad (\text{Eq.A.1-3})$$

and gives a  $D_{S-F}^B = 1.82$  for the 300 °C experiment.

The B isotopic compositions of the repeatedly taken fluid samples were used to calculate the absolute fractions of the two isotopes  $^{11}\text{B}$  and  $^{10}\text{B}$  in each sampled fluid and within the complete system, and were finally used to predict the fractions of  $^{11}\text{B}$  and  $^{10}\text{B}$  in the solid reaction product by mass balancing (**Table A. 1-7**). We calculated a  $\delta^{11}\text{B}$  composition of the solid reaction product of -5.5 ‰ by this procedure, in very close approximation to the actual measured  $\delta^{11}\text{B}$  value of  $-5.0 \pm 0.1$  ‰ by MC-ICP-MS (**Table A. 1-5; Table A. 1-7**). The B isotopic fractionation factor ( $\Delta^{11}\text{B}_{S-F}$  or  $\alpha_{S-F}^B$ ) was calculated by the following equation (Eq.A.1-4) based on the difference in B isotopic composition of the calculated solid ( $\delta^{11}\text{B}_S$ ) of -5.5 ‰ and the finally sampled fluid ( $\delta^{11}\text{B}_F$ ) of  $0.0 \pm 0.2$  ‰ and the isotope ratios  $^{11}\text{R}_S$  and  $^{11}\text{R}_F$ , respectively:

$$\Delta^{11}\text{B}_{S-F} = \delta^{11}\text{B}_S - \delta^{11}\text{B}_F = 1000 \cdot \ln \alpha_{S-F}^B$$

$$\text{with } \alpha_{S-F}^B = (^{11}\text{B}/^{10}\text{B})_S / (^{11}\text{B}/^{10}\text{B})_F \quad (\text{Eq.A.1-4})$$

and gives  $\Delta^{11}\text{B}_{S-F} = -5.5$  ( $\alpha_{S-F}^B = 0.9944$ ) for the 300 °C experiment.

A summary of the calculated B distribution coefficient and isotopic fractionation factor derived from the 300 °C experiment (this study) is given in **Table A. 1-8**, in comparison to the results of the 100 and 200 °C experiments (Hansen *et al.*, 2017).

#### A.1.4 Summary of the experimental results of this and the previous study

The 300 °C serpentinization experiment conducted in this study is a follow-up of two previously executed, basically identical experiments but with reaction temperatures of 100 and 200 °C by Hansen *et al.* (2017). Therefore, in the following section we will give a brief comparison of the new and the previous results to get a more precise picture how changing reaction temperatures affect mineralogical aspects, as well as B distribution and isotopic fraction by serpentinization and how this is related to changing pH conditions and B speciation in aqueous solution.

First, we looked at differences regarding mineralogical aspects and chemical variations of the solid reaction products between the three experiments that were conducted at differing temperatures. For

all three experiments, an alteration mineral assemblage occurred as it is also typically produced by serpentinization processes at the seafloor (Bach *et al.*, 2004, Früh-Green *et al.*, 2017), consisting of serpentine, brucite and magnetite. But the absolute and relative abundances of the three mineral phases varied between the three experiments and also slight compositional variations were observed. The deviating absolute abundances of the alteration mineral phases between the three reaction temperatures are due to the large differences of the total reaction turnovers (11.7 mol% for the 100 °C experiment, and 69.1 or rather 72.1 mol% for the 200 and 300 °C experiments) but also the relative abundances vary (**Figure A. 1-7**). Most noticeable is the increase of the magnetite fraction with increasing reaction temperatures, accompanied by an increase of the Mg# (Mg# = Mg/[Mg+Fe]) of brucite (0.87 to 0.97) and serpentine (0.97 to 0.99). This relation indicates that a larger portion of the mobilized Fe is taken up by the higher abundant magnetite fraction at increased reaction temperatures and following a smaller portion of Fe substitutes with the octahedral bounded Mg in the serpentine and brucite structures.

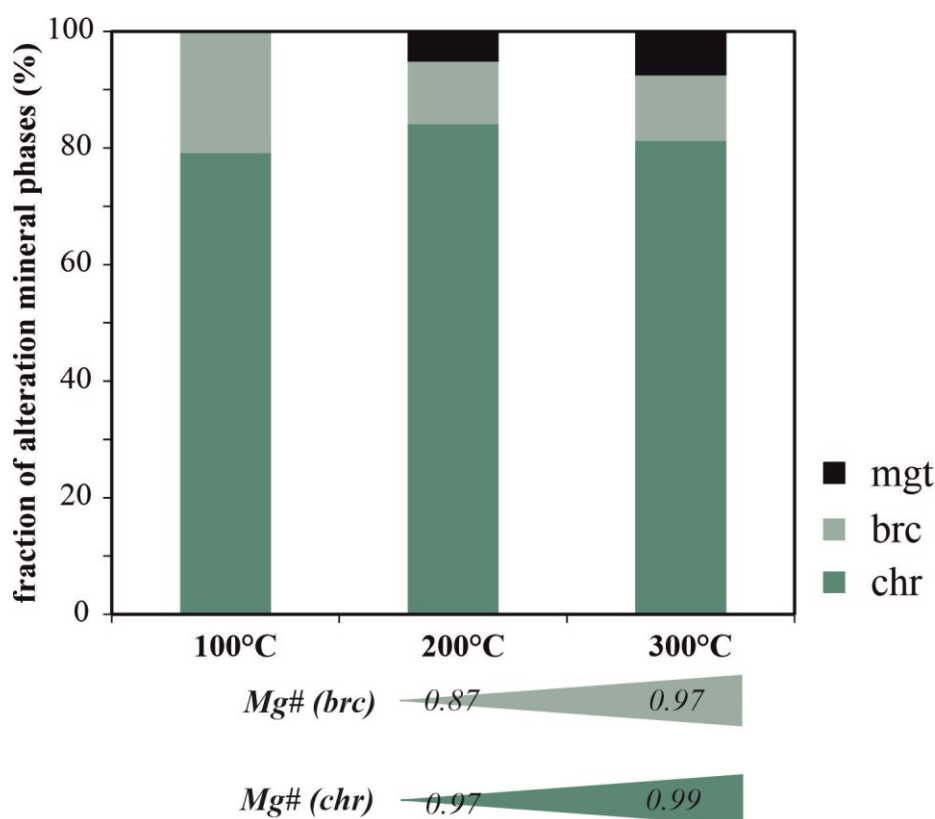


**Figure A. 1-7:** Comparison of fractions of alteration mineral phases contained in the solid reaction products and Mg# (Mg# = Mg/[Mg+Fe]) with varying reaction temperatures (this study, and Hansen *et al.*, 2017). Mgt=magnetite, brc=brucite, chr=chrysotile.

The B concentrations of the solid reaction products corrected for the reaction turnover ( $B_{S(\text{reacted})}$ , **Table A. 1-8**) show the highest B concentrations for the 100 °C experiment (195.9 µg/g) and a steady decrease in concentration with increasing reaction temperatures for 200 °C (76.5 µg/g) and 300 °C (16.0 µg/g). It can be estimated that the main B fraction within in the solid reaction product

is hosted at the tetrahedral sites of serpentine, and brucite; subordinated sorption to oxide surfaces may also occur. High B concentrations of serpentized rocks and serpentine separates with maximum concentrations close to 100  $\mu\text{g/g}$  were previously reported for natural samples (e.g. Boschi *et al.*, 2008).

The calculated  $\delta^{11}\text{B}$  composition of the solid reaction products of the experiments vary between -2.3 ‰ (200 °C) and -8.7 ‰ (100 °C) and is generally higher compared to the fresh olivine (-14  $\pm$  2 ‰) due to interaction with a fluid of higher  $\delta^{11}\text{B}$  composition ( $\geq$  -0.9 ‰, **Table A. 1-7**). It can be estimated that the bulk solid  $\delta^{11}\text{B}$  value equals the  $\delta^{11}\text{B}$  composition of the altered portion due to the negligible small portion of B hosted within the relict olivine phase (0.02  $\mu\text{g/g}$ ) but may experience shifts in composition due to additional fluid-rock interaction at decreasing temperatures at the end of the experiment.

**Table A. 1-8:** Summary of the results of the 300 °C experiment (this study) compared to the 100 and 200 °C experiments published by Hansen *et al.* (2017).

	$\delta^{11}\text{B}_F^*$ (‰)	$\delta^{11}\text{B}_S$ (‰)	RT** (mol.%)	$B_{S(\text{total})}$ ( $\mu\text{g/g}$ )	$B_{S(\text{reacted})}$ ( $\mu\text{g/g}$ )	$D_{S-F}^B$	$\Delta^{11}\text{B}_{S-F}$	$\alpha_{S-F}^B$
100 °C	1.3	-8.7	11.7	25.3	195.9	23.0	-10.0	0.9900
200 °C	1.2	-2.3	69.4	55.6	76.5	13.3	-3.5	0.9965
300 °C	0.0	-5.5	72.1	12.0	16.0	1.8	-5.5	0.9944

\*measured

\*\*RT = reaction turnover

$B_{S(\text{total})}$  = B content calculated for the whole solid reaction product.

$B_{S(\text{reacted})}$  = B content calculated for the solid reaction product also regarding the reaction turnover.

The fluid samples that were repeatedly taken over the run time of the experiments revealed some distinct variations regarding the chemical (Mg, B) and isotopic ( $\delta^{11}\text{B}$ ) compositions, as well as of fluid pH and B speciation in aqueous solution (**Figure A. 1-5; Figure A. 1-6**). A sharp initial change in Mg, B,  $\delta^{11}\text{B}$  compositions and pH in the fluids right at the beginning of the experiments was observed for all reaction temperatures (100, 200 and 300 °C, **Figure A. 1-5**). Hansen *et al.* (2017) attributed this rapid change to an enhanced reactivity of the system in the beginning of the experiments due to immediate reaction of the very fine-grained solid fraction with the fluid. They furthermore suggested that after this initial stage, Mg concentrations and pH values are buffered by formation of secondary mineral phases, mainly serpentine minerals and brucite. The fluid pH (at 25 °C and in-situ) values (**Figure A. 1-5A; Figure A. 1-6**) indicated that the main reaction progress was completed for all reaction temperatures latest after around 50 days of reaction, and definitely after ending of the experiments.

Modeling results revealed distinct differences in B species abundances in solution between the three conducted reaction temperatures and over the experimental runtimes, mainly influenced by changing pH and T conditions (**Figure A. 1-6**). The relative fractions of total  $\text{B}^{[3]}$  ( $\text{B}[\text{OH}]_3(\text{aq})$  and  $\text{B}[\text{OH}]_3\text{Cl}^-$ ) versus  $\text{B}^{[4]}$  ( $\text{B}[\text{OH}]_4^-$  and  $\text{NaB}[\text{OH}]_4(\text{aq})$ ) species in the equilibrated fluids of the 100

equals the 200 °C experiment (42 % B<sup>[4]</sup>), although the absolute abundance of NaB(OH)<sub>4(aq)</sub> is slightly higher at 200 than 100 °C. In contrast, at 300 °C the B<sup>[4]</sup> fraction in solution (finally 18 %) is significantly smaller compared to 100 and 200 °C.

The solid-fluid B distribution coefficient ( $D_{S-F}^B$ , **Table A. 1-8**) increases with decreasing reaction temperatures, considering the total reaction turnovers. Boron isotopic fractionation ( $\Delta^{11}B_{S-F}$ ) was largest at the lowest reaction temperature as it can be expected based on previous experiments (e.g. Wunder *et al.*, 2005). Unexpectedly based on previous experiments, we obtained a higher extent of B isotopic fractionation at 300 °C than at 200 °C (**Table A. 1-8**), pointing to that additional factors besides temperature influencing the fractionation in our experiments. One likely factor leading to shifts in  $\Delta^{11}B_{S-F}$  is the variability in B<sup>[4]</sup> fractions in solution in our experiments (**Figure A. 1-6**), while most previous experiments were conducted under acidic conditions with B<sup>[3]</sup> in solution only (Spivack & Edmond, 1987, Hervig *et al.*, 2002; Wunder *et al.*, 2005). The fluid of the 200 °C experiment contained a larger final fraction of B<sup>[4]</sup> (42 %) than at 300 °C (18 %) and hence this most likely caused the lower B isotopic fractionation at 200 vs. 300 °C. Detailed explanations regarding the  $\Delta^{11}B_{S-F}$  versus temperature relation with respect of B speciation in solution can be found in the main text (**Chapter 3.3**).

## References

- Akinfiev N. N., Voronin M. V., Zotov A. V. and Prokof'ev V. Y. (2006) Experimental investigation of the stability of a chloroborate complex and thermodynamic description of aqueous species in the B-Na-Cl-O-H system up to 350°C. *Geochem. Int.* **44**, 867–878.
- Augustin N., Lackschewitz K. S., Kuhn T. and Devey C. W. (2008) Mineralogical and chemical mass changes in mafic and ultramafic rocks from the Logatchev hydrothermal field (MAR 15°N). *Mar. Geol.* **256**, 18–29.
- Augustin N., Paulick H., Lackschewitz K. S., Eisenhauer A., Garbe-Schönberg D., Kuhn T., Botz R. and Schmidt M. (2012) Alteration at the ultramafic-hosted Logatchev hydrothermal field. *Geochem. Geophys. Geosyst.* **13**.
- Bach W., Garrido C. J., Paulick H., Harvey J. and Rosner M. (2004) Seawater-peridotite interactions. *Geochem. Geophys. Geosyst.* **5**.
- Beltenev V., Ivanov V., Rozhdestvenskaya I., Cherkashov G., Stepanova T., Shilov V., Davydov M., Laiba A., Kaylio V., Narkevsky E., Pertsev A., Dobretzova I., Gustaytis A., Popova Y., Amplieva Y., Evrard C., Moskalev L. and Gebruk A. (2009) New data about hydrothermal fields on the Mid-Atlantic Ridge between 11° - 14°N: 32<sup>nd</sup> Cruise of R/V Professor Logatchev. *InterRidge News* **18**, 13–17.
- Beltenev V., Ivanov V., Rozhdestvenskaya I., Cherkashov G., Stepanova T., Shilov V., Pertsev A., Davydov M., Egorov I., Melekesteva I., Narkevsky E. and Ignatov V. (2007) A new hydrothermal field at 13°30' N on the Mid-Atlantic Ridge. *InterRidge News* **16**, 9–10.
- Beltenev V., Nescheretov A., Shilov V., Ivanov V., Shagin A., Stepanova T., Cherkashev G., Batuev B., Samovarov M., Rozhdestvenskaya I., Andreeva I., Fedorov I., Davydov M., Romanova L., Rumyantsev A., Zaharov V., Luneva N. and Artemeva O. (2003) New discoveries at 12°58'N, 44°52'W, MAR: Professor Logatchev-22 cruise, initial results. *InterRidge News* **12**, 13–14.
- Boschi C., Dini A., Früh-Green G. L. and Kelley D. S. (2008) Isotopic and element exchange during serpentinization and metasomatism at the Atlantis Massif (MAR 30°N). *Geochim. Cosmochim. Acta* **72**, 1801–1823.

Dickson F. W., Blount C. W. and Tunell G. (1963) Use of hydrothermal solution equipment to determine the solubility of anhydrite in water from 100 degrees C to 275 degrees C and from 1 bar to 1000 bars pressure. *Am. J. Sci.* **261**, 61–78.

Escartín J., Mével C., Petersen S., Bonnemains D., Cannat M., Andreani M., Augustin N., Bezos A., Chavagnac V., Choi Y., Godard M., Haaga K., Hamelin C., Ildefonse B., Jamieson J., John B., Leleu T., MacLeod C. J., Massot-Campos M., Nomikou P., Olive J. A., Paquet M., Rommevaux C., Rothenbeck M., Steinfuhrer A., Tominaga M., Triebe L., Campos R., Gracias N. and Garcia R. (2017) Tectonic structure, evolution, and the nature of oceanic core complexes and their detachment fault zones (13°20'N and 13°30'N, Mid Atlantic Ridge). *Geochem. Geophys. Geosyst.* **18**, 1451–1482.

Foster G. L., Pogge von Strandmann P. A. E. and Rae J. W. B. (2010) Boron and magnesium isotopic composition of seawater. *Geochem. Geophys. Geosyst.* **11**.

Fouquet Y., Cambon P., Etoubleau J., Charlou J. L., Ondréas H., Barriga, Fernando J. A. S., Cherkashev G., Semkova T., Poroshina I., Bohn M., Donval J. P., Henry K., Murphy P. and Rouxel O. (2010) Geodiversity of Hydrothermal Processes Along the Mid-Atlantic Ridge and Ultramafic-Hosted Mineralization: a New Type Of Oceanic Cu-Zn-Co-Au Volcanogenic Massive Sulfide Deposit. *Geophys. Monogr. Ser.* **188**, 321–367.

Fouquet Y., Cherkashov G., Charlou J. L., Ondréas H., Birot D., Cannat M., Bortnikov N. S., Silantyev S., Sudarikov S., Cambon-Bonavita M. A., Desbruyères D., Fabri M. C., Querellou J., Hourdez S., Gebruk A., Sokolova T., Hoisé E., Mercier E., Kohn C., Donval J. P., Etoubleau J., Normand A., Stephan M., Briand P., Crozon J., Fernagu P. and Buffier E. (2008) Serpentine cruise - ultramafic hosted hydrothermal deposits on the Mid-Atlantic Ridge: First submersible studies on Ashadze 1 and 2, Logatchev 2 and Krasnov vent fields. *InterRidge News* **17**, 16–21.

Früh-Green G. L., Orcutt B. N., Green S. L., Cotterill C., Morgan S., Akizawa N., Bayrakci G., Behrmann J.-H., Boschi C., Brazleton W. J., Cannat M., Dunkel K. G., Escartin J., Harris M., Herreo-Bervera E., Hesse K., John B., Lang S. Q., Lilley M. D., Liu H.-Q., Mayhew L. E., McCaig A. M., Menez B., Morono Y., Quéméneur M., Rouméjon S., Sandaruwan Ratnayake A., Schrenk M. O., Schwarzenbach E. M., Twing K. I., Weis D., Whattham S. A., Williams M. and Zhao R. (2017) Expedition 357 summary. In *Proceedings of the International Ocean Discovery Program Volume 357* (eds. G. L. Früh-Green, B. N. Orcutt, S. L. Green and C. Cotterill), pp. 1–34.

Hajash A. and Chandler G. W. (1982) An experimental investigation of high-temperature interactions between seawater and rhyolite, andesite, basalt and peridotite. *Contr. Mineral. and Petrol.* **78**, 240–254.

Hansen C. T., Meixner A., Kasemann S. A. and Bach W. (2017) New insight on Li and B isotope fractionation during serpentinization derived from batch reaction investigations. *Geochim. Cosmochim. Acta* **217**, 51–79.

Hervig R. L., Moore G. M., Williams L. B., Peacock S. M., Holloway J. R. and Roggensack K. (2002) Isotopic and elemental partitioning of boron between hydrous fluid and silicate melt. *Amer. Miner.* **87**, 769–774.

Johnson J. W., Oelkers E. H. and Helgeson H. C. (1992) SUPCRT92 - A software package for calculating the standard molal thermodynamic properties of minerals, gases, aqueous species, and reactions from 1 to 5000 bar and 0 to 1000°C. *Comput. Geosci.* **18**, 899–947.

Kasemann S., Meixner A., Rocholl A., Vennemann T., Rosner M., Schmitt A. K. and Wiedenbeck M. (2001) Boron and Oxygen Isotope Composition of Certified Reference Materials NIST SRM 610/612 and Reference Materials JB-2 and JR-2. *Geostand. Geoanal. Res.* **25**, 405–416.

Klein F., Bach W. and McCollom T. M. (2013) Compositional controls on hydrogen generation during serpentinization of ultramafic rocks. *Lithos* **178**, 55–69.

Melekestseva I. Y., Kotlyarov V. A., Khvorov P. V., Ivanov V. N., Beltenev V. E. and Dobretsova I. G. (2010) Noble-metal mineralization in the Semenov-2 hydrothermal field (13°31'N), mid-atlantic ridge. *Geol. Ore Deposits* **52**, 800–810.

Melekestseva I. Y., Maslennikov V. V., Tret'yakov G. A., Nimis P., Beltenev V. E., Rozhdestvenskaya I. I., Maslennikova S. P., Belogub E. V., Danyushevsky L., Large R., Yuminov A. M. and Sadykov S. A. (2017)

- Gold- and Silver-Rich Massive Sulfides from the Semenov-2 Hydrothermal Field, 13°31.13'N, Mid-Atlantic Ridge. *Econ. Geol.* **112**, 741–773.
- Melekestseva I. Y., Tret'yakov G. A., Nimis P., Yuminov A. M., Maslennikov V. V., Maslennikova S. P., Kotlyarov V. A., Beltenev V. E., Danyushevsky L. V. and Large R. (2014) Barite-rich massive sulfides from the Semenov-1 hydrothermal field (Mid-Atlantic Ridge, 13°30.87' N). *Mar. Geol.* **349**, 37–54.
- Mével C. (2003) Serpentinization of abyssal peridotites at mid-ocean ridges. *Comptes Rendus Geoscience* **335**, 825–852.
- Noakes J. E. and Hood D. W. (1961) Boron-boric acid complexes in sea-water. *Deep Sea Research (1953)* **8**, 121–129.
- Ondréas H., Cannat M., Fouquet Y. and Normand A. (2012) Geological context and vents morphology of the ultramafic-hosted Ashadze hydrothermal areas (Mid-Atlantic Ridge 13°N). *Geochem. Geophys. Geosyst.* **13**, 6.
- Pertsev A. N., Bortnikov N. S., Vlasov E. A., Beltenev V. E., Dobretsova I. G. and Ageeva O. A. (2012) Recent massive sulfide deposits of the Semenov ore district, Mid-Atlantic Ridge, 13°31' N. *Geol. Ore Deposits* **54**, 334–346.
- Peters C. and Dekkers M. J. (2003) Selected room temperature magnetic parameters as a function of mineralogy, concentration and grain size. *Physics and Chemistry of the Earth, Parts A/B/C* **28**, 659–667.
- Petersen S., Kuhn K., Kuhn T., Augustin N., Hékinian R., Franz L. and Borowski C. (2009) The geological setting of the ultramafic-hosted Logatchev hydrothermal field (14°45'N, Mid-Atlantic Ridge) and its influence on massive sulfide formation. *Lithos* **112**, 40–56.
- Reeves E. P., Seewald J. S., Saccocia P., Bach W., Craddock P. R., Shanks W. C., Sylva S. P., Walsh E., Pichler T. and Rosner M. (2011) Geochemistry of hydrothermal fluids from the PACMANUS, Northeast Pual and Vienna Woods hydrothermal fields, Manus Basin, Papua New Guinea. *Geochim. Cosmochim. Acta* **75**, 1088–1123.
- Romer R. L., Meixner A. and Hahne K. (2014) Lithium and boron isotopic composition of sedimentary rocks — The role of source history and depositional environment. *Gondwana Res.* **26**, 1093–1110.
- Schmale O., Walter M., Schneider von Deimling J., Sültenfuß J., Walker S., Rehder G. and Keir R. (2012) Fluid and gas fluxes from the Logatchev hydrothermal vent area. *Geochem. Geophys. Geosyst.* **13**.
- Schmidt K., Koschinsky A., Garbe-Schönberg D., Carvalho L. M. de and Seifert R. (2007) Geochemistry of hydrothermal fluids from the ultramafic-hosted Logatchev hydrothermal field, 15°N on the Mid-Atlantic Ridge. *Chem. Geol.* **242**, 1–21.
- Seewald J. S., Doherty K. W., Hammar T. R. and Liberatore S. P. (2002) A new gas-tight isobaric sampler for hydrothermal fluids. *Deep Sea Research Part I: Oceanographic Research Papers* **49**, 189–196.
- Seyfried W. and Bischoff J. (1981) Experimental seawater-basalt interaction at 300°C, 500 bars, chemical exchange, secondary mineral formation and implications for the transport of heavy metals. *Geochim. Cosmochim. Acta* **45**, 135–147.
- Seyfried W. E., Janecky D. R. and Berndt M. E. (1987) Rocking Autoclaves for Hydrothermal Experiments II. - The Flexible Reaction-Cell System. In *Hydrothermal Experimental Techniques* (eds. G. C. Ulmer and H. L. Barnes). A Wiley-Interscience Publication, pp. 216–239.
- Seyfried W. E., Pester N. J., Tutolo B. M. and Ding K. (2015) The Lost City hydrothermal system. *Geochim. Cosmochim. Acta* **163**, 59–79.
- Silantyev S. A., Krasnova E. A., Cannat M., Bortnikov N. S., Kononkova N. N. and Beltenev V. E. (2011) Peridotite-gabbro-trondhjemite association of the Mid-Atlantic Ridge between 12°58' and 14°45'N. *Geochem. Int.* **49**, 323–354.
- Snow J. E. and Dick H. J. (1995) Pervasive magnesium loss by marine weathering of peridotite. *Geochim. Cosmochim. Acta* **59**, 4219–4235.

- Spivack A. and Edmond J. (1987) Boron isotope exchange between seawater and the oceanic crust. *Geochim. Cosmochim. Acta* **51**, 1033–1043.
- Tonarini S., Pennisi M. and Leeman W. P. (1997) Precise boron isotopic analysis of complex silicate (rock) samples using alkali carbonate fusion and ion-exchange separation. *Chem. Geol.* **142**, 129–137.
- Trittschack R., Grobéty B. and Brodard P. (2014) Kinetics of the chrysotile and brucite dehydroxylation reaction. *Phys. Chem. Minerals.* **41**, 197–214.
- Wang B.-S., You C.-F., Huang K.-F., Wu S.-F., Aggarwal S. K., Chung C.-H. and Lin P.-Y. (2010) Direct separation of boron from Na- and Ca-rich matrices by sublimation for stable isotope measurement by MC-ICP-MS. *Talanta* **82**, 1378–1384.
- Wilckens F. K., Reeves E. P., Bach W., Meixner A., Seewald J. S., Koschinsky A. and Kasemann S. A. (2018) The influence of magmatic fluids and phase separation on B systematics in submarine hydrothermal vent fluids from back-arc basins. *Geochim. Cosmochim. Acta* **232**, 140–162.
- Wolery T. J. (1992) EQ3/6 - A Software Package for Geochemical Modeling of Aqueous Systems. *Package Overview and Installation Guide (Version 7.0)*.
- Wunder B., Meixner A., Romer R. L., Wirth R. and Heinrich W. (2005) The geochemical cycle of boron. *Lithos* **84**, 206–216.

## **A.2. Procedures and isotopic reference materials**

### **A.2.1 Purification procedures**

Purification of B prior to  $\delta^{11}\text{B}$  measurements was performed by ion exchange chromatography after Romer *et al.* (2014) that was modified after Tonarini *et al.* (1997) and Kasemann *et al.* (2001):

#### **1. stage: Anion exchange with Amberlite IRA 743, mesh 20-50**

**(PE-BIORAD Biospin columns)**

- (1) Conditioning and cleaning of the columns**  
6.6 M HCl (full reservoir)  
2 x H<sub>2</sub>O (full reservoir)  
0.5 ml 2M NH<sub>4</sub>OH  
3 x 1 ml H<sub>2</sub>O
- (2) Addition of sample solution and resin**
- (3) Rinsing**  
2 x 1 ml H<sub>2</sub>O  
2 x 1 ml 2M NH<sub>4</sub>OH  
4 x 1 ml H<sub>2</sub>O
- (4) Elution (collection of the main fraction)**  
24 x 0.5 ml 0.5 M HCl
- (5) Tail**  
2 x 1 ml 0.5 M HCl
- (6) Addition of 0.2 % mannitol solution,**  
adjusted to the B concentration in solution (1:20)
- (7) Cleaning of the column and discarding of the resin**
- (8) Drying (T ≤ 65 °C)**

#### **2. stage: Cation exchange with Biorad Resin AG 50WX-8, mesh 200-400**

**(PE-BIORAD Biospin columns)**

- (1) Stir up the resin**
- (2) Cleaning of the columns and resin**  
2 x 6.2 M HCl (full reservoir)
- (3) Conditioning**  
4 x 1 ml 0.02 M HCl
- (4) Addition of sample solution (collection of the main fraction)**  
(dissolved in 1 ml 0.02 M HCl)  
4 x 0.25 ml
- (5) Elution (collection of the main fraction)**  
2 x 0.25 ml 0.02 M HCl (wash sample beaker)  
7 x 0.5 ml 0.02 M HCl  
4 x 1ml 0.02 M HCl
- (6) Tail**  
2 x 1 ml 0.02 M HCl
- (7) Cleaning of the column and resin**
- (8) Drying (T ≤ 65 °C)**

Purification of Li prior to  $\delta^7\text{Li}$  measurements was performed by ion exchange chromatography that was modified after Moriguti & Nakamura (1998):

**1. stage: Biorad Resin AG 50WX-8, mesh 200-400**

**(PE-BIORAD Biospin columns)**

- (1) Stir up the resin**
- (2) Cleaning of the columns and resin**  
2 x 6 M HCl (full reservoir)  
1 x H<sub>2</sub>O (full reservoir)
- (3) Conditioning**  
2 x 1 ml 0.15 M HCl
- (4) Addition of the sample solution**  
(dissolved in 2 ml 0.15 M HCl)  
8 x 0.25 ml
- (5) Rinsing**  
1 x 0.5 ml 0.15 M HCl (wash sample beaker)  
1 x 0.5 ml 0.15 M HCl  
1 x 1 ml 0.15 M HCl
- (6) Elution (collection of the main fraction)**  
4 x 5 ml 0.15 M HCl  
2 x 4 ml 0.15 M HCl
- (7) Tail**  
2 x 1 ml 0.15 M HCl
- (8) Cleaning of the columns and resin**  
2 x 6 M HCl (full reservoir)  
1 x H<sub>2</sub>O (full reservoir)
- (9) Drying (T ≤ 95 °C)**

**2. stage: Biorad Resin AG 50WX-8, mesh 200-400**

**(PE-BIORAD Biospin columns)**

- (1) Stir up the resin**
- (2) Cleaning**  
6 x 6 M HCl (full reservoir)  
3 x H<sub>2</sub>O (full reservoir)
- (3) Conditioning**  
1 x 1ml 0.15 M HCl
- (4) Addition of the sample solution**  
(dissolved in 1 ml 0.15 M HCl)  
4 x 0.25 ml
- (5) Rinsing**  
1 x 0.5 ml 0.5 M HCL in 50 % Ethanol (wash sample beaker)  
1 x 0.5 ml 0.5 M HCL in 50 % Ethanol
- (6) Elution (collection of the main fraction)**  
1 x 0.5 ml 0.5 M HCL in 50 % Ethanol  
12 x 1 ml 0.5 M HCL in 50 % Ethanol
- (7) Tail**  
2 x 1 ml 0.5 M HCL in 50 % Ethanol
- (8) Cleaning of the column and resin**  
3 x H<sub>2</sub>O (full reservoir)  
6 x 6 M HCl (full reservoir)
- (9) Drying (T ≤ 95 °C)**

Purification of Sr prior to  $^{87}\text{Sr}/^{86}\text{Sr}$  measurements was conducted by ion exchange that was adapted from Deniel & Pin (2001):

***Separation based on Sr-spec resin***

***(handmade columns out of Pasteur pipettes)***

- (1) Loading of the resin (70  $\mu\text{l}$ ) onto the columns with Milli-Q**
- (2) Cleaning and conditioning of the resin**
  - 2 x 500  $\mu\text{l}$  Milli-Q
  - 2 x 500  $\mu\text{l}$  2 M  $\text{HNO}_3$
- (3) Addition of the sample solution in 100  $\mu\text{l}$  steps**  
(dissolved in 500 - 1000  $\mu\text{l}$  2 M  $\text{HNO}_3$ )
- (4) Rinsing of the resin**
  - 12 x 100  $\mu\text{l}$  2 M  $\text{HNO}_3$
  - 2 x 500  $\mu\text{l}$  7 M  $\text{HNO}_3$  (for Ba-rich samples)
  - 3 x 100  $\mu\text{l}$  2 M  $\text{HNO}_3$  (for Ba-rich samples)
- (5) Elution (collect ion of the main fraction)**
  - 5 x 200  $\mu\text{l}$  0.05 M  $\text{HNO}_3$
- (6) Cleaning of the column and discarding of the resin**
- (7) Addition of 40  $\mu\text{l}$  0.1 M  $\text{H}_3\text{PO}_4$  to the beaker, drying at 120  $^\circ\text{C}$**
- (8) Addition of 40  $\mu\text{l}$  conc.  $\text{HNO}_3$  to the beaker, drying at 120  $^\circ\text{C}$**
- (9) Addition of 40  $\mu\text{l}$   $\text{H}_2\text{O}_2$  to the beaker, drying at 120  $^\circ\text{C}$**

A.2.2 Reference materials

**Table A. 2-1:** B and  $\delta^{11}\text{B}$  compositions of the reference solution and standard materials that were measured along the sample materials.

standard material	series number	series location	series sample material	B ( $\mu\text{g/g}$ )	$\pm 2\text{sd}^\dagger$	$\delta^{11}\text{B}$ (‰)	$\pm 2\text{sd}^{\dagger\dagger}$
<i>reference solution</i>							
NIST-SRM-951	LS-BSi-2016-1	Dorado Outcrop	silicates			0.0	0.0
NIST-SRM-951	LS-BSi-2017-1	Snowcap, PACMANUS	silicates			0.0	0.1
NIST-SRM-951	LS-BSi-2019-1	Brothers volcano	silicates			-0.2	0.1
NIST-SRM-951	LS-BSi-2019-2	Brothers volcano & solid reaction product*	silicates			-0.1	0.0
NIST-SRM-951	LS-BSi-2019-3	Brothers volcano	silicates			-0.1	0.1
NIST-SRM-951	LS-BSo-2019-1	initial & reacted fluids*	solutions			-0.1	0.1
NIST-SRM-951	LS-BSo-2019-2	vent fluids from the MAR**	solutions			0.1	0.1
NIST-SRM-951	LS-BSo-2019-3	Brothers volcano	borehole fluids			-0.3	0.0
			<b>average/2sd<sub>mean</sub></b>			<b>-0.1</b>	<b>0.2</b>
<i>basaltic reference material</i>							
BHVO-2	LS-BSi-2016-1	Dorado Outcrop	silicates	<b>2.36</b>	<b>0.02</b>	<b>-2.8</b>	<b>0.3</b>
IAEA-B5	LS-BSi-2016-1	Dorado Outcrop	silicates	6.56	0.02	-3.9	0.1
IAEA-B5	LS-BSi-2017-1	Snowcap, PACMANUS	silicates	9.44		-4.3	0.1
IAEA-B5	LS-BSi-2019-1	Brothers volcano	silicates	9.46	0.04	-4.3	0.1
IAEA-B5	LS-BSi-2019-2	Brothers volcano & solid reaction product*	silicates	9.37	0.04	-4.3	0.1
IAEA-B5	LS-BSi-2019-3	Brothers volcano	silicates	8.81	0.07	-3.6	0.1
			<b>average/2sd<sub>mean</sub></b>	<b>8.73</b>	<b>2.48</b>	<b>-4.1</b>	<b>0.7</b>
<i>granitic reference material</i>							
IAEA-GM	LS-BSi-2017-1	Snowcap, PACMANUS	silicates	4.86		-0.1	0.1
IAEA-GM	LS-BSi-2019-1	Brothers volcano	silicates	4.89	0.02	0.0	0.0
IAEA-GM	LS-BSi-2019-2	Brothers volcano & solid reaction product*	silicates	4.88	0.01	-0.2	0.0
IAEA-GM	LS-BSi-2019-3	Brothers volcano	silicates	4.59	0.02	0.5	0.0
			<b>average/2sd<sub>mean</sub></b>	<b>4.81</b>	<b>0.29</b>	<b>0.0</b>	<b>0.6</b>
<i>seawater reference material</i>							
BSW SuSu Knolls#	LS-BSo-2019-1	initial & reacted fluids*	solutions	5.15		39.5	0.1
BSW SuSu Knolls#	LS-BSo-2019-2	vent fluids from the MAR**	solutions			39.7	0.2
BSW SuSu Knolls#	LS-BSo-2019-3	Brothers volcano	borehole fluids	4.86		39.7	0.0
BSW SuSu Knolls#	LS-BSo-2019-3	Brothers volcano	borehole fluids	4.91		39.6	0.1
			<b>average/2sd<sub>mean</sub></b>	<b>4.97</b>	<b>0.30</b>	<b>39.7</b>	<b>0.1</b>
NASS-6	LS-BSo-2019-3	Brothers volcano	borehole fluids	<b>4.16</b>		<b>39.5</b>	<b>0.2</b>

$^\dagger 2 \times$ Standard deviation (2sd) based on at least three measurements of the same solution.

$^\dagger\dagger 2 \times$ Standard deviation (2sd) based on at least 10 repeated measurements of the standard solution and at least 5 measurements for other reference materials.

\*serpentinization experiment.

\*\*natural vent fluid samples from Logatchev, Semenov, Irinovskoe and Ashadze.

#Laboratory internal bottom seawater standard from the Manus Back-arc Basin, Western Pacific.

**Table A. 2-2:** Li and  $\delta^7\text{Li}$  compositions of the reference solution and standard materials that were measured along the sample materials.

standard material	series number	series location	series sample material	Li ( $\mu\text{g/g}$ )	$\pm 2\text{sd}^\dagger$	$\delta^7\text{Li}$ (‰)	$\pm 2\text{sd}^{\dagger\dagger}$
<i>standard solution</i>							
NIST-RM-8545	LS-LiSi-2016-1	Dorado Outcrop	silicates			0.0	0.2
NIST-RM-8545	LS-LiSo-2016-1	Dorado Outcrop	solutions			-0.2	0.2
NIST-RM-8545	LS-LiSo-2018-1	Brothers volcano	borehole fluids			0.0	0.1
NIST-RM-8545	LS-LiSi-2019-1	Brothers volcano	silicates			-0.3	0.2
NIST-RM-8545	LS-LiSi-2019-2	Brothers volcano	silicates			-0.2	0.1
NIST-RM-8545	LS-LiSi-2019-3	Brothers volcano	silicates			-0.2	0.1
NIST-RM-8545	LS-LiSi-2019-4	Brothers volcano	silicates			-0.1	0.1
			<b>average/2sd<sub>mean</sub></b>			<b>-0.2</b>	<b>0.2</b>
<i>basaltic reference material</i>							
BHVO-2	LS-LiSi-2016-1	Dorado Outcrop	silicates	4.39	0.02	4.4	0.3
BHVO-2	LS-LiSi-2019-1	Brothers volcano	silicates	4.39	0.04	4.3	0.2
			<b>average/2sd<sub>mean</sub></b>	<b>4.39</b>	<b>0.00</b>	<b>4.3</b>	<b>0.2</b>
IAEA-B5	LS-LiSi-2016-1	Dorado Outcrop	silicates	8.18	0.12	4.7	0.3
IAEA-B5	LS-LiSi-2019-2	Brothers volcano	silicates	8.18	0.09	4.9	0.3
IAEA-B5	LS-LiSi-2019-4	Brothers volcano	silicates	8.01	0.05	3.9	0.1
			<b>average/2sd<sub>mean</sub></b>	<b>8.12</b>	<b>0.19</b>	<b>4.5</b>	<b>1.1</b>
<i>granitic reference material</i>							
IAEA-GM	LS-LiSi-2019-3	Brothers volcano	silicates	<b>45.57</b>	<b>0.82</b>	<b>-0.7</b>	<b>0.1</b>
<i>seawater reference material</i>							
BSW SuSu Knolls#	LS-LiSo-2016-1	Dorado Outcrop	solutions	0.18		31.2	0.2
BSW SuSu Knolls#	LS-LiSo-2018-1	Brothers volcano	borehole fluids	0.18	0.00	30.7	0.1
			<b>average/2sd<sub>mean</sub></b>	<b>0.18</b>	<b>0.01</b>	<b>30.9</b>	<b>0.7</b>

$^\dagger 2 \times$  Standard deviation (2sd) based on at least three measurements of the same solution.

$^\dagger\dagger 2 \times$  Standard deviation (2sd) based on at least 10 repeated measurements of the standard solution and at least 5 measurements for other reference materials.

#Laboratory internal bottom seawater standard from the Manus Back-arc Basin, Western Pacific.

**Table A. 2-3:**  $^{87}\text{Sr}/^{86}\text{Sr}$  values of the standard solution that was measured along the sample materials.

standard material	series number	series location	series sample material	$^{87}\text{Sr}/^{86}\text{Sr}$	$\pm 2\text{sd}$
NIST-SRM-987	LS-Sr-2016-1	Dorado Outcrop	silicates & fluids	0.710246	0.000007
NIST-SRM-987	LS-Sr-2016-2	Dorado Outcrop	silicates & fluids	0.710248	0.000005
NIST-SRM-987	LS-Sr-2019-1	Brothers volcano	silicates	0.710247	0.000004
			<b>average/2se</b>	<b>0.710247</b>	<b>0.000005</b>

## References

Deniel C. and Pin C. (2001) Single-stage method for the simultaneous isolation of lead and strontium from silicate samples for isotopic measurements. *Anal. Chim. Acta* **426**, 95–103.

Kasemann S., Meixner A., Rocholl A., Vennemann T., Rosner M., Schmitt A. K. and Wiedenbeck M. (2001) Boron and Oxygen Isotope Composition of Certified Reference Materials NIST SRM 610/612 and Reference Materials JB-2 and JR-2. *Geostand. Geoanal. Res.* **25**, 405–416.

Moriguti T. and Nakamura E. (1998a) High-yield lithium separation and the precise isotopic analysis for natural rock and aqueous samples. *Chem. Geol.* **145**, 91–104.

Romer R. L., Meixner A. and Hahne K. (2014) Lithium and boron isotopic composition of sedimentary rocks — The role of source history and depositional environment. *Gondwana Res.* **26**, 1093–1110.

Tonarini S., Pennisi M. and Leeman W. P. (1997) Precise boron isotopic analysis of complex silicate (rock) samples using alkali carbonate fusion and ion-exchange separation. *Chem. Geol.* **142**, 129–137.

### **A.3. Overview of the electronic appendix**

Larger tables are documented in the electronic appendix. In the following, descriptions of the additional content are given:

**Table A. 3-1:** Major element compositions (wt.%) of the solid reaction product of the serpentinization experiment (**Chapter A.1.1.4; Table A. 1-3**) determined by SEM. Measurements that are displayed in gray were excluded for average calculations due to interferences from adjacent mineral phases that caused shifts in composition.

**Table A. 3-2:** The calculated magnetite content (%) of the solid reaction product (serpentinization experiment, **Chapter A.1.1.6 and A.1.3.1; Table A. 1-4**) based on repeated AGFM measurements on the same sample powder.

**Table A. 3-3:** Major element compositions (wt.%) of a vein sample (Dorado Outcrop, **Chapter 4.3.2; Table 4.5-3**) determined by SEM. Measurements marked with a star were not used for average calculations due to higher variations in concentrations than 2sd.

**Table A. 3-4:** Major element compositions (wt.%) of secondary mineral phases determined by EMPA (Dorado Outcrop, **Chapter 4.3.3; Table 4.5-3**). Measurements marked with a star were not used for average calculations due to higher variations in concentrations than 2sd.

**Table A. 3-5:** Major element compositions (wt.%) of reference materials used to test the accuracy of sample measurements (EMPA). The materials were provided by the Smithsonian Institution, Washington D.C., USA.

**Table A. 3-6:** Trace element compositions ( $\mu\text{g/g}$ ) of secondary mineral phases determined by LA-ICP-MS (Dorado Outcrop, **Chapter 4.3.4 and 4.5.2.2**).

**Table A. 3-7:** Trace element compositions ( $\mu\text{g/g}$ ) of reference materials that were determined by LA-ICP-MS.

**Table A. 3-8:** Oxygen isotope measurements on quartz that were conducted by SIMS on sample material (IODP Exp. 376, Brothers volcano, **Chapter 5.5.3; Table 5.6-1**) and the reference material UWQ-1. The position of the measuring points is projected to the CL images (F level) of the quartz separates.